

Usability of polymer film heat exchangers in the chemical industry

vom Fachbereich Maschinenbau und Verfahrenstechnik der
Technischen Universität Kaiserslautern zur Verleihung
des akademischen Grades

Doktor-Ingenieur (Dr.-Ing.)

genehmigte

Dissertation

von
Herrn
Dipl.-Ing. Dmitrij Laaber
aus Kaliningrad

Dekan: Prof. Dr.-Ing. Bernd Sauer

Prüfungskommission:

Prüfungsvorsitzender: Prof. Dr.-Ing. Michael Günthner
1. Berichterstatter: Prof. Dipl.-Ing. Dr. techn. Hans-Jörg Bart
2. Berichterstatter: Prof. Dr.-Ing. Siegfried Ripperger

Eingereicht am: 18.06.2016

Tag der mündlichen Prüfung: 12.12.2016

Kaiserslautern 2017

Dedicated to my wife

and

in loving memory of my mother

PREFACE

This research work was carried out in a cooperation project with the industrial partners Calorplast GmbH and Merck KGaA. The project was supported by the Federal Ministry of Education and Research (BMBF). The presented work was done at the Department of Separation Science and Technology of the University of Kaiserslautern during the years 2011 – 2014.

First, I would like to thank Prof. Hans-Jörg Bart for the challenging research tasks and the great supervision and support. Furthermore, I would also like to thank both project partners, Mr. Frank Scholz from Calorplast and Mr. Klaus Marschar from Merck KGaA for their instant and productive input. I also would like to thank the entire staff of the department for the pleasant working atmosphere and the productive ideas. A very special thank you goes to Mr. Markus Lichti for his help with the experimental setup. Apart from that, I would like to thank all the supervised students for their contributions to this work.

Finally, I would like to thank my wonderful wife for the great support and her patience.

Cologne, January 2017

Dmitrij Laaber

ABSTRACT

The main goal of this work was the study of the applicability of a polymer film heat exchanger concept for the applications in the chemical industry, such as the condensation of organic solvents. The polymer film heat exchanger investigated is a plate heat exchanger with very thin (0.025 – 0.1 mm) plates or films, which separate the fluids and enable the heat transfer. After a successful application of this concept to seawater desalination in a previous work, a further step is in chemical engineering, where the good chemical resistance of polymers in aggressive fluids is the challenge.

Two approaches were performed in this work. The first one was experimental and included the study of the chemical and mechanical resistance of preselected films, made of polymer materials, such as polyimide (PI), polyethylene terephthalate (PET) and polytetrafluoroethylene (PTFE). To simulate realistic operating conditions in a heat exchanger the films were exposed to a combined thermal (up to 90°C) and mechanical pressure loads (4-6 bar) with permanent contact with the relevant organic solvents, such as toluene, hexane, heptane and tetrahydrofuran (THF). Furthermore, a lab-scale apparatus and a full-scale demonstrator were manufactured in cooperation with two industrial partners. These were used for the investigation of the heat transfer performance for operating modes with and without phase change.

In addition to the experimental work, a coupled finite element –computational fluid dynamics (FEM-CFD)-model was developed, based on the fluid-structure-interaction (FSI). Two major tasks had to be solved here. The first one was the modelling of the condensation process, based on available mathematical models and energy balances. The second one was the consideration of the partially reversible deformation of the used film during operation. Since this deformation changes the geometry of the fluid channels also has an influence on the overall performance of the apparatus, a coupled FEM-CFD model was developed.

During the experimental study of the chemical resistance of the films, the PTFE film showed the best performance, and hence can be used for all four tested solvents. For the polyimide film, failures while exposed to THF were observed, and the PET film can only be used with water and hexane. With the used lab-scale heat exchanger and the full-scale demonstrator competitive overall heat transfer coefficients between 270 W/m²K and 700 W/m²K could be reached for the liquid-liquid (water-water, water-hexane) operation mode without phase change. For the condensation process, overall heat transfer coefficients of up to 1700/m²K could be obtained.

The numerical approach led to a well-functioning coupled model in a very small scale (1 cm²). An upscale, however, failed due to enormous hardware resources necessary required for the simulation of the entire full-scale demonstrator. The main reason for this is the very low thickness of the films,

which leads to tiny mesh element sizes (<0.05 mm) necessary to model the deformation of the film. The modelling of the liquid-liquid heat transfer provided an acceptable accuracy (approx. 10%), but at very low rates the deviations were then higher (over 30%). The results of the condensation modelling were ambivalent. On the one hand a physically plausible model was developed, which could map the entire condensation process. On the other hand, the corresponding energy balance revealed major inaccuracy and hence could not be used for the determination of the overall heat transfer and showed the current limits of the FEM-CFD approach.

KURZFASSUNG

Das Ziel dieser Arbeit war die Untersuchung der Anwendbarkeit von auf Polymerfolien basierten Wärmeübertragern in der chemischen Industrie, für zum Beispiel solche Aufgaben wie die Kondensation organischer Lösungsmittel. Ein solcher Wärmeübertrager ist im Grunde wie ein Plattenwärmeübertrager aufgebaut, statt starrer Platten kamen hier allerdings sehr dünne (0.025 – 0.1 mm) Kunststofffolien zum Einsatz, die die beiden Fluide voneinander trennen und den Wärmeübergang ermöglichen. Nach einer erfolgreichen Anwendung im Bereich der Meerwasserentsalzung, wurde in dieser Folgearbeit versucht den Anwendungsbereich auf die chemische Industrie zu erweitern, wo die teils sehr gute chemische Beständigkeit von Polymeren vor allem bei aggressiven Medien Vorteile bieten kann.

Das gestellte Ziel der Arbeit wurde auf zwei Ebenen verfolgt. Zum einen experimentell, was die Untersuchungen der chemischen und der mechanischen Beständigkeit der vorausgewählten Folien aus Polyimid (PI), Polyethylterephthalat (PET) und Polytetrafluorethylen (PTFE) einschloss. Um möglichst realistische Betriebsbedingungen im späteren Einsatz abzubilden, wurden die Folien einer kombinierten thermischen (bis 90°C) und mechanischen Druckbelastung (4-6 bar) bei ständigem Kontakt mit einem organischen Lösungsmittel ausgesetzt. Verwendet wurden hierfür Toluol, Hexan, Heptan und Tetrahydrofuran (THF). Darüber hinaus wurden ein kleinerer Wärmeübertrager im Labormaßstab und ein Demonstrator in anwendungsrelevanter Größe in Zusammenarbeit mit zwei Industriepartnern hergestellt. Mit Hilfe dieser Apparate wurde der Wärmeübergang experimentell untersucht, und zwar sowohl für mit und ohne Phasenwechsel (mit und ohne Kondensation).

Zusätzlich zu den experimentellen Arbeiten, wurde ein gekoppeltes Modell aus FEM (Finite Element Methode) und CFD (Computational Fluid Dynamics) entwickelt, das auf dem Prinzip der Fluid-Struktur-Interaktion (FSI) basiert, das die Durchströmung und den Wärmeübergang in den Apparaten beschreibt. Hierzu mussten zwei Aufgaben gelöst werden. Zum einen wurde auf der Basis mathematischer Modelle und Energiegleichungen der Kondensationsprozess abgebildet. Zum anderen wurde die Verformung der Folien im Betrieb und dessen Auswirkungen auf die Leistungsfähigkeit der Wärmeübertragers betrachtet, was insgesamt zum kombinierten FEM-CFD Modell führt.

Bei den experimentellen Untersuchungen der chemischen Beständigkeit zeigte die PTFE-Folie die besten Eigenschaften und kann uneingeschränkt für alle vier Lösungsmittel verwendet werden. Die Polyimidfolie erreichte ähnliche Ergebnisse, versagte allerdings bei THF. Die PET-Folie zeigte nur bei Wasser und Hexan eine ausreichende Beständigkeit. Mit den untersuchten Apparaten konnten zu gängigen metallischen Wärmeübertragern konkurrenzfähige Gesamtwärmeübergangszahlen zwischen 270 W/m²K und 700W/m²K für den Flüssig-flüssig-Betrieb erreicht werden und zwar sowohl

mit nur Wasser als auch mit der Paarung Hexan-Wasser. Bei der Kondensation konnten im Demonstrator bis zu $1700\text{W}/\text{m}^2\text{K}$ erreicht werden.

Die numerischen Untersuchungen ergaben ein im kleinen Maßstab (1 cm^2) funktionierendes gekoppeltes Modell. Es scheiterte die Maßstabsvergrößerung an den enormen Ressourcenanforderungen der Software, die für die Anwendung auf den finalen Demonstrator benötigt wurden. Dies lag hauptsächlich daran, dass die Folien sehr dünn waren und dadurch winzig kleine Netzgrößen ($<0.05\text{mm}$) gewählt werden mussten, um die Verformung realistisch abzubilden. Die Modellierung des Flüssig-flüssig-Wärmeübergangs konnte mit einer akzeptablen Abweichung von rund 10% für höhere Volumenströme umgesetzt werden. Bei kleineren Volumenströmen allerdings nahmen die Abweichungen auf bis zum 30% zu. Die Ergebnisse der Kondensationsmodellierung zeigten die Limits des Simulationsansatzes. Es wurde ein physikalisch plausibles Modell erstellt, das den Kondensationsprozess an sich abbildete. Allerdings wurde die entsprechende Energiebilanz beziehungsweise der Wärmeübergang nicht sinnvoll berechnet, jedoch konnten die Strömungsverhältnisse sehr gut abgebildet werden.

LIST OF TABLES

Table 1: Thermal conductivity values of polymers and metals	32
Table 2: Maximum long-term application temperatures for selected polymers and metals	33
Table 3: Coefficients for the COSTALD-method	48
Table 4: Parameter set for the corrections factor F defined in (2.118).....	74
Table 5: Main properties of the used polymers (Sources: (Goodfellow GmbH), (Elsner et al. 2012; DuPont Teijin Films))	79
Table 6: Chemical resistance data of selected polymers as provided from manufacturers or suppliers	79
Table 7: Properties of the selected polymer films	80
Table 8: Main fluid properties of the used organic solvents, sources: (GESTIS 2015), (VDI 2006)	82
Table 9: Parameters for the main polymer film testing at constant load	91
Table 10: Operating points (OPW) for the full-scale heat exchanger	93
Table 11: Specifications of the used PC-systems	94
Table 12: Mesh settings for the lab-scale heat exchanger model	101
Table 13: Parameters of mesh evaluation simulation runs.....	102
Table 14: Dimensionless parameters for material property approximation equations (liquid state)	111
Table 15: Material properties of the PET polymer film.....	112
Table 16: Parameters for material property (gas state) approximation equations (2.47) to (2.50)...	116
Table 17: Testing results for demonstrator 1.....	136
Table 18: Results of the condensation modelling with Ansys CFX®	142
Table 19: Experimental data obtained with the lab-scale heat exchanger: liquid water - water with polyimide film	157
Table 20: Experimental data obtained with the lab-scale heat exchanger: liquid water - water with PTFE film	159
Table 21: Experimental data obtained with the lab-scale heat exchanger: liquid hexane - water with polyimide film	161
Table 22: Experimental data obtained with the lab-scale heat exchanger: liquid hexane – water with PTFE film	163
Table 23: Experimental data obtained with the lab-scale heat exchanger: gaseous hexane – water with polyimide film	165
Table 24: Experimental data obtained with the lab-scale heat exchanger: gaseous hexane – water with PTFE film	167
Table 25: Experimental data obtained with the full-scale heat demonstrator 2: water – water with PET film.....	169

Table 26: Experimental data obtained with the full-scale heat demonstrator 2: gaseous hexane –
water with PET film..... 171

LIST OF FIGURES

Figure 1: Definition of the Young's modulus E	29
Figure 2: Influence of temperature on the shear modulus for amorphous and semi-crystalline polymers, Source: (Elsner et al. 2005), modified	30
Figure 3: Dependency of Young's modulus on the temperature for semi-crystalline polyamide PA6, Source: (Serban et al. 2013)	31
Figure 4: Discrete fluid volume with equations for mass conservation balance. Source: (Lechler 2011), modified.....	36
Figure 5: Forces in x-direction on a discrete volume element. Source: (Lechler 2011), modified	37
Figure 6: Energy balance of a discrete volume element. Source: (Lechler 2011), modified.....	38
Figure 7: Classification of turbulence models. Source: (Martin 2011).....	42
Figure 8: Turbulent pipe flow. Source: (von Böckh, Wetzel 2014).....	52
Figure 9: Natural convection at a vertical plane, source: (von Böckh, Wetzel 2014)	55
Figure 10: Natural convection at an inclined plane, source: (Herwig, Moschallski 2014), modified....	55
Figure 11: Diagram for the critical Raleigh number, source: (von Böckh, Wetzel 2014)	56
Figure 12: Natural convection at a horizontal plane, source: (Herwig, Moschallski 2014), modified ..	57
Figure 13: Thermal conductivity through plane walls in Cartesian (a) and cylindrical (b) coordinate systems.....	58
Figure 14: Example of heat transition through a wall. Source: (Baehr, Stephan 2008), modified	59
Figure 15: Film condensation at a vertical plane, source: (Herwig, Moschallski 2014), modified.....	62
Figure 16: Force equilibrium for a single droplet, source: (Herwig, Moschallski 2014), modified	63
Figure 17: Temperature curves for different flow configurations	66
Figure 18: Temperature distribution in a cross-flow labyrinth heat exchange, source: (StrykerTECH LLC)	66
Figure 19: A simplified sketch of a plate heat exchanger, source: (WilTec Wildanger Technik GmbH 2015).....	68
Figure 20: Bonded polymer film heat exchanger, source: (Perry et al.), modified	70
Figure 21: Cross-corrugated polymer films	70
Figure 22: Cell method principle, source (VDI 2006), modified	72
Figure 23: Structural formula of polyethylene terephthalate monomer (Gooch 2007)	75
Figure 24: Structural formula of a polyimide monomer, source: (Gooch 2007).....	76
Figure 25: Structural formula of PTFE, source: (Gooch 2007).....	77
Figure 26: Structural formula of PEEK, source (Elsner et al. 2012), modified.....	77
Figure 27: Structural formula of PMMA.....	78
Figure 28: Chemical formula of toluene.....	81

List of Figures	12
Figure 29: Chemical formulas of n-hexane and n-heptane.....	81
Figure 30: Structural formula of tetrahydrofuran.....	81
Figure 31: Pressure pipe for material behaviour investigation.....	83
Figure 32: Measured deformation height of the films.....	83
Figure 33: Test rig for polymer film samples.....	84
Figure 34: Test rig for condensation studies.....	85
Figure 35: Milled flow channels as the film supporting structure.....	86
Figure 36: Schematic sketch of the lab scale heat exchanger.....	87
Figure 37: The CAD sketch of the full-scale heat exchanger with four fluid chambers.....	88
Figure 38: Operating mode of the testing procedures with the demonstrator 1.....	89
Figure 39: Operating mode of the testing procedures with the demonstrator 2.....	90
Figure 40: Simple sketch and picture of the stabilising structure in the heat exchanger.....	90
Figure 41: Heat transfer test rig with the large demonstrator mounted on it.....	92
Figure 42: Model domains for the lab-scale heat exchanger, condensation domain - left, cooling domain - right.....	97
Figure 43: Fluid volumes of the used full-scale heat exchanger model.....	98
Figure 44: An example of mesh refinement (entire geometry – left; mesh without refinement – center; refined mesh –right).....	101
Figure 45: Mesh quality example at the inlet area of the lab-scale heat exchanger.....	103
Figure 46: Test geometry and a mesh example for the FEM mesh study (green: hot fluid volume, grey: cooling volume).....	103
Figure 47: Mesh study results for the FEM modelling.....	104
Figure 48: Deformed shapes of the deformed film (side view).....	105
Figure 49: Model scheme for the serial non-coupled model in Ansys Workbench®.....	114
Figure 50: A block diagram of a FSI principle.....	115
Figure 51: Comparison of the deformation heights for the polyimide film.....	117
Figure 52: Deformation heights of six polyimide samples exposed to tetrahydrofuran.....	119
Figure 53: Microscope pictures of the polyimide film before (left) and after the exposure (right) ...	119
Figure 54: Colour change of the solvents: toluene - left, tetrahydrofuran - right.....	120
Figure 55: Comparison of the deformation heights for the PTFE-glass fibre film.....	121
Figure 56: Deformation heights of the PTFE-glass fibre samples exposed to tetrahydrofuran (left) and toluene (right).....	122
Figure 57: Inner structure of the PTFE-glass fibre compound; left: 20x magnification; right: 100x magnification.....	122

Figure 58: Time-based comparison of the material behaviour for different load types; left: PTFE - glass fibre - compound, right: polyimide.....	123
Figure 59: Comparison of the performance of the polyimide film and the PTFE-glass fibre compound at pulsating pressure loads.....	124
Figure 60: Deformed shape of the lab-scale heat exchanger after FEM analysis.....	126
Figure 61: Deformed shape of the mesh received with errors by CFX®	126
Figure 62: Single element of the full-scale heat exchanger	127
Figure 63: Overall heat transfer coefficients and the corresponding logarithmic temperatures for the experiments with water on the polyimide film.....	129
Figure 64: Overall heat transfer coefficients and the corresponding logarithmic temperatures for the experiments with water on the PTFE-Glass fibre compound.....	130
Figure 65: Thermal image of a low rate flow on the hot side with the polyimide film.....	131
Figure 66: A qualitative comparison of the wetting behaviour of PTFE and PI films.....	131
Figure 67: Overall heat transfer coefficients and the corresponding logarithmic temperatures for the experiments with non-condensing hexane on the PI film.....	132
Figure 68: Overall heat transfer coefficients and the corresponding logarithmic temperatures for the experiments with non-condensing hexane on the PTFE-glass fibre compound	133
Figure 69: Overall heat transfer coefficients and the corresponding logarithmic temperatures for the experiments with condensing hexane on the polyimide film	134
Figure 70: Overall heat transfer coefficients and the corresponding logarithmic temperatures for the experiments with condensing hexane on the PTFE-glass fibre compound.....	134
Figure 71: Comparison of the simulated and experimental results for water-water heat transfer in the lab-scale heat exchanger	135
Figure 72: Comparison of the heat transfer results at the highest flow rates with different fluid flow models	136
Figure 73: Overall heat transfer coefficients and the corresponding logarithmic temperature differences for testing procedures with water in demonstrator 2	137
Figure 74: Overall heat transfer coefficients and the corresponding logarithmic temperature differences for testing procedures with hexane condensation in demonstrator 2	138
Figure 75: Damaging of the sealing material at the gas inlet.....	139
Figure 76: A comparison of the sealing damage at the inlet (left) and at the outlet (right).....	140
Figure 77: Comparison of the available fluid models.....	141
Figure 78: Condensation lines for the used models.....	143
Figure 79: Temperature distribution with $\lambda=0.25$ W/m ² K	143
Figure 80: Temperature distribution with $\lambda=0.05$ W/m ² K	144

Figure 81: Temperature distribution with $\lambda=0.05$ W/m²K and additional wall heat transfer model.. 144

LIST OF SYMBOLS***Latin symbols***

Symbol	Unit	Definition
a	m/s^2	Acceleration
A, B, C, D	-	Dimensionless material specific constants for the gas polynomial
a_1	-	SST-model constant
A_{full}	m^2	Entire polymer film surface area
A_i	m^2	Surface area
A_m	m^2	Average surface area
A_{red}	m^2	Reduced polymer film surface area
$b_1 \dots b_3$	m/kg	Constants for the general cubic equation of state
C_μ	-	Turbulence constant
c_p	J/kg	Isobaric heat capacity
c_v	J/m^3	Isochoric heat capacity
dV	m^3	Differential volume
E	N/m^2	Young's modulus
e	J	Inner energy
E_{tot}	J	Total energy
F	N	Force
f_i		Specific function for the heat transfer determination
g	m/s^2	Gravitational constant
h	J/kg	Specific enthalpy

H°_T	J/mol	Molar enthalpy
Δh_v	J/kg	Phase transition enthalpy
k	–	Kinetic energy (in k-epsilon equation)
k	J/m ² K	Overall heat transfer coefficient
k_m	J/m ² K	Mean heat transfer coefficient
L	m	Characteristic length
m	kg	Mass
\dot{m}	kg/s	Mass flow
n°_i	–	Constants for the ideal gas part of the IAPWS-function
p	Pa	Pressure
p_c	Pa	Critical pressure
p_s	Pa	Saturation pressure
q	W/m ²	Heat flux density
\dot{q}	W	Heat radiation
Q	J	Heat
r	m or rad	Spatial coordinate for the thermal conduction equation
R	J/kg K	Specific gas constant
R_w	J/kg K	Specific gas constant of water
S°_T	J/mol K	Molar entropy
t	s	Time
T	K	Temperature

T_c	K	Critical temperature
T_g	K	Glass transition temperature
T_s	K	Saturation temperature
ΔT_s	K	Mean temperature
u, v, w	m/s	Velocities in x, y, and z directions
v	m ³ /kg	Specific volume
v_c	m ³ /kg	Critical volume
v_m	m ³ /mol	Specific molar volume
V	m ³	Volume
\vec{G}	m/s (for each scalar)	Diffusion vector
W	J	Mechanical work
W	J/K	Heat capacity flux
Z	–	Real gas factor

Greek symbols

α	J/m^2	Heat transfer coefficient
$\alpha(T)$	J/kg	Temperature dependent parameter for the general cubic equation of state
β	m^3/K	Volumetric expansivity
$\beta(T)$	J/kg	Temperature dependent parameter for the general cubic equation of state
Δ_{ij}	–	Kronecker symbol
δ_{ϑ}	m	Thickness of the temperature boundary layer
ε	m^2/s^2	Turbulence eddy dissipation
ε_m	m	Mechanical strain
ζ	–	Darcy friction factor
η	Pa s	Dynamic viscosity
ϑ	K	Temperature
λ	$\text{W}/\text{m K}$	Thermal conductivity
μ	m^2/K	Thermal diffusivity
ν	m^2/s	Kinematic viscosity
ρ	kg/m^3	Density
σ_{fg}	Pa	Interface tension between the liquid and the gas phase
σ_{wet}	Pa	Wetting tension
σ_{wf}	Pa	Interface tension between the wall and the liquid phase

σ_{wg}	Pa	Interface tension between the wall and the gas phase
τ_{ii}	Pa	Normal stress in i -direction
τ_{ij}	Pa	Shear stress in the ij -plane
Φ^o	–	Ideal gas part of the IAPWS function
Φ_r	–	Residual part of the IAPWS function
ω	$1/s$	Turbulence frequency
ω	–	Acentric factor

Dimensionless symbols

Gr_L	$Gr_L = \frac{g \cdot \beta (T_s - T_\infty) L^3}{\nu^2}$	Grashof number for vertical plates
Nu	$Nu_L = \frac{h \cdot L}{k}$	Nusselt number
NTU	$NTU = \frac{k \cdot A}{C_{\min}}$	Number of transfer units
p^+	$p^+ = \frac{p}{p_c}$	Pressure coefficient
P_i	$P_i = \frac{T'_i - T''_i}{T'_i - T'_{i+1}}$	Mass flux temperature gradient
Pr	$Pr = \frac{\nu}{\alpha}$	Prandtl number
Ra	$Ra = Gr \cdot Pr$	Rayleigh number
Re	$Re = \frac{\rho \cdot c \cdot L}{\mu} = \frac{c \cdot L}{\nu}$	Reynolds number
R_i	$R_i = \frac{\dot{W}_i}{\dot{W}_{i+1}}$	Heat capacity flux quotient
∇	$\nabla = \left(\frac{\partial}{\partial x_1}, \dots, \frac{\partial}{\partial x_n} \right) = \sum_{i=1}^n \vec{e}_i \frac{\partial}{\partial x_i}$	Nabla Operator
η_t	$\eta_t = C_\mu \cdot \rho \cdot \frac{k^2}{\varepsilon}$	Turbulence parameter
θ	$\theta = \frac{\Delta T_m}{T'_1 - T'_2}$	Mean temperature gradient

LIST OF PUBLICATIONS

- D. Laaber, H.-J. Bart, „Energieeffiziente Wärmeübertrager“, Abschlussband zur BMBF-Förderinitiative „Technologien für Nachhaltigkeit und Klimaschutz“, 2016 in press
- D. Laaber, H.-J. Bart, "Chemical Resistance and Mechanical Stability of Polymer Film Heat Exchangers", Chem. Ing. Tech., 2015, 87, No. 1–2, 1–7
- D. Laaber, H.-J. Bart, "Polymerfilm-Wärmeübertrager für chemische Prozesse", Begleitheft zur ProcessNet Jahrestagung 2014, Aachen
- D. Laaber, H.-J. Bart, "Hochflexibel Wärme übertragen" CIT Plus 2014, 3, 28 - 29
- D. Laaber, H.-J. Bart, "Chemical and pressure stress resistance of polymer films", Polymer Testing 40 (2014) 280-285, doi:10.1016/j.polymertesting.2014.09.018
- D. Laaber, H.-J. Bart, "Untersuchung des Langzeitverhaltens von Kunststofffolien für den Einsatz in Wärmeübertragern", Chemie Ingenieur Technik 2013, 85, 9, 1467, DOI: 10.1002/cite.201250736
- D. Laaber, H.-J.-Bart, "CFD-Simulation der Strömungskanäle in einem polymeren Wärmeübertrager " Chemie Ingenieur Technik 2013, 85, 9, 1383, DOI: 10.1002/cite.201250653

LIST OF LECTURES

- H.-J. Bart, D. Laaber, " Collaborative project:Energy efficient polymer film heat exchangers ", Abschlussseminar zur BMBF-Fördermaßnahme "Chemische Prozesse und stoffliche Nutzung von CO₂", 21. – 22.04.2015, Berlin
- D. Laaber, H.-J. Bart, "Verbundprojekt: Energieeffiziente Wärmeübertrager", 4. Statusseminar zur BMBF-Fördermaßnahme "Chemische Prozesse und stoffliche Nutzung von CO₂", 08.04.2014, Königswinter
- D. Laaber, H.-J. Bart, "Untersuchung des Wärmeübergangs in einem Polymerfilm-Wärmeübertrager", Jahrestreffen der Fachgruppen Mehrphasenströmungen und Wärme- und Stoffübertragung, 24.03.-25.03.2014, Fulda
- D. Laaber, H.-J. Bart, "Fluid-Structure-Kopplung für die Berechnung des Wärmeübergangs in einem Polymerfilm-Wärmeübertrager", Jahrestreffen der Fachgruppen Computational Fluid Dynamics, Mischvorgänge und Rheologie, Würzburg, 24.02. – 26.02.2014
- D. Laaber, H.-J. Bart, "Einfluss organischer Lösungsmittel auf die Festigkeit von Polymeren Werkstoffen für den Einsatz in Wärmeübertragern", Jahrestreffen der Fachgruppe Wärme- und Stoffübertragung, 20.03. - 21.03.2013, Baden-Baden

- D. Laaber, H.-J.-Bart, "Verbundprojekt: Energieeffiziente Polymerwärmeübertrager", 3. Statusseminar zur BMBF-Fördermaßnahme "Chemische Prozesse und stoffliche Nutzung von CO₂", 09.04. - 10.04.2013, Berlin

LIST OF POSTERS

- D. Laaber, H.-J. Bart, "Polymerfilm-Wärmeübertrager für chemische Prozesse", ProcessNet-Jahrestagung und 31. DECHEMA-Jahrestagung der Biotechnologen 2014, 30.09.-02.10.2014, Aachen
- D. Laaber, H.-J. Bart, "Numerische Untersuchungen des Wärmeübergangs in einem Polymerfilm-Wärmeübertrager", Jahrestreffen der Fachgruppen Computational Fluid Dynamics, Mischvorgänge und Rheologie, 24.02. – 26.02.2014, Würzburg
- D. Laaber, H.-J. Bart, "Verbundprojekt: Energieeffiziente Wärmeübertrager", 4. Statusseminar zur BMBF-Fördermaßnahme "Chemische Prozesse und stoffliche Nutzung von CO₂", 08.04.2014, Königswinter
- D. Laaber, H.-J. Bart, "Chemical stability of polymer film heat exchangers for highly corrosive applications", Bring On The Heat Europe Conference, 14.11.-15.11.2013, Frankfurt/Main
- D. Laaber, H.-J.-Bart, "Verbundprojekt: Energieeffiziente Polymerwärmeübertrager", 3. Statusseminar zur BMBF-Fördermaßnahme "Chemische Prozesse und stoffliche Nutzung von CO₂", 09.04. - 10.04.2013, Berlin
- D. Laaber, H.-J. Bart, "CFD-Simulation der Strömungskanäle in einem polymeren Wärmeübertrager", Jahrestreffen der Fachgemeinschaft Fluidodynamik und Trenntechnik, 25.09. - 27.09.2013, Würzburg
- D. Laaber, H.-J. Bart, "Untersuchung des Langzeitverhaltens von Kunststofffolien für den Einsatz in Wärmeübertragern", Jahrestreffen der Fachgemeinschaft Fluidodynamik und Trenntechnik, 25.09. - 27.09.2013, Würzburg

LIST OF CONTENTS

PREFACE	4
ABSTRACT	5
KURZFASSUNG	7
LIST OF TABLES.....	9
LIST OF FIGURES	11
LIST OF SYMBOLS.....	15
LIST OF PUBLICATIONS	21
LIST OF LECTURES	21
LIST OF POSTERS.....	22
LIST OF CONTENTS	23
1. INTRODUCTION AND MOTIVATION	27
2. THEORETICAL BACKGROUND	29
2.1. THEORETICAL BASICS	29
2.1.1. <i>Physical properties of materials</i>	29
2.1.1.1. Definition of the mechanical properties.....	29
2.1.1.2. Mechanical strength of polymers.....	30
2.1.1.3. Thermal and thermodynamic properties	31
2.1.1.4. Chemical resistance.....	33
2.2. BASICS OF FLUID DYNAMICS	34
2.2.1. <i>Characteristic length</i>	34
2.2.2. <i>Dimensionless quantities</i>	34
2.2.3. <i>Fluid flow models</i>	35
2.2.3.1. General balance equations.....	35
2.2.3.2. Navier-Stokes-Equations	39
2.2.3.3. Turbulence modelling.....	41
2.2.3.4. Fluid properties determination	43
2.3. HEAT TRANSFER	51
2.3.1. <i>Convection</i>	51
2.3.1.1. Forced convection	51
2.3.1.2. Natural convection	53
2.3.2. <i>Thermal conduction</i>	58
2.3.3. <i>Thermal radiation</i>	59
2.3.4. <i>Heat transition</i>	59
2.3.5. <i>Phase transition (Condensation)</i>	61
2.3.5.1. Film condensation	61
2.3.5.1. Droplet condensation.....	63
2.3.5.1. Stream condensation.....	64
2.4. HEAT EXCHANGERS	65

2.4.1.	<i>Basic heat exchanger classification</i>	65
2.4.2.	<i>Plate heat exchangers</i>	67
2.4.1.	<i>Polymer heat exchangers</i>	68
2.4.1.1.	Design and materials for polymer heat exchangers	68
2.4.1.2.	Polymer film heat exchangers	69
2.4.2.	<i>Models for heat exchanger design and calculation</i>	71
2.4.2.1.	Cell method	71
2.4.2.2.	Short-cut correlations for standardised heat exchangers	73
3.	METHODS	75
3.1.	EXPERIMENTAL STUDIES	75
3.1.1.	<i>Polymers</i>	75
3.1.1.1.	Polyethylene terephthalate.....	75
3.1.1.2.	Polyimide.....	76
3.1.1.3.	Polytetrafluoroethylene	76
3.1.1.1.	Polyether ether ketone	77
3.1.1.2.	Poly(methylmethacrylate).....	78
3.1.1.3.	General properties of used polymers	78
3.1.2.	<i>Preselection of films</i>	79
3.2.	ORGANIC SOLVENTS	80
3.3.	EXPERIMENTAL SET-UP	82
3.3.1.	<i>Pressure test rig</i>	82
3.3.1.	<i>Heat exchanger test rig</i>	84
3.4.	HEAT EXCHANGER DESIGN	86
3.4.1.	<i>Polymer film supporting structure</i>	86
3.4.2.	<i>Lab scale heat exchanger</i>	87
3.4.3.	<i>Full-scale demonstrator</i>	88
3.4.3.1.	Demonstrator 1	89
3.4.3.2.	Demonstrator 2	89
3.4.4.	<i>Testing procedures with the pressure test rig</i>	91
3.4.5.	<i>Testing procedures for the determination of the heat transfer</i>	92
3.5.	NUMERICAL METHODS.....	94
3.5.1.	<i>Hardware</i>	94
3.5.2.	<i>Software</i>	94
3.5.3.	<i>Geometry</i>	96
3.5.3.1.	Geometry mapping of the lab-scale heat exchanger.....	96
3.5.3.2.	Geometry mapping of the full-scale demonstrator	97
3.5.4.	<i>Meshing</i>	98
3.5.4.1.	Meshing parameters	99
3.5.4.1.	Basic meshing	100
3.5.4.2.	Meshing of the lab-scale heat exchanger	101

3.5.4.3.	Meshing of the full-scale demonstrator	102
3.5.4.4.	Mesh studies	102
3.5.5.	<i>Modelling of the mechanical deformation</i>	105
3.5.6.	<i>Fluid dynamics modelling</i>	106
3.5.6.1.	Domains.....	106
3.5.6.2.	Outlet types.....	108
3.5.6.3.	Opening types.....	108
3.5.6.4.	Wall types.....	109
3.5.6.5.	Interfaces.....	109
3.5.6.6.	Materials.....	110
3.5.7.	<i>Flow and heat transfer modelling</i>	110
3.5.7.1.	Simple, one-phase, stationary heat transfer model	110
3.5.7.2.	Extended one-phase model with geometry deformation	112
3.5.7.3.	Coupled fluid-structure-interaction model.....	114
3.5.7.4.	Phase transition heat transfer model	115
4.	RESULTS AND DISCUSSION	117
4.1.	MECHANICAL STABILITY AND CHEMICAL RESISTANCE	117
4.1.1.	<i>Static pressure load</i>	117
4.1.1.1.	Main test results for the polyimide film	117
4.1.1.2.	Main test results of the PTFE-glass fibre compound	120
4.1.2.	<i>Pulsating pressure load</i>	123
4.1.3.	<i>Deformation modelling for coupled FSI-models</i>	125
4.2.	RESULTS OF THE HEAT TRANSFER DETERMINATION.....	128
4.2.1.	<i>Lab-scale heat exchanger</i>	128
4.2.1.1.	Experimental results for water-water heat transfer.....	129
4.2.1.2.	Experimental results for liquid hexane-water heat transfer	132
4.2.1.3.	Experimental results for hexane condensation with water cooling	133
4.2.1.1.	Numerical results of the heat transfer in the lab-scale apparatus	134
4.2.2.	<i>Full-scale demonstrator</i>	136
4.2.2.1.	Experimental results for the water - water heat transfer.....	136
4.2.2.2.	Experimental results for hexane condensation heat transfer	137
4.2.2.3.	Design and sealing difficulties	138
4.2.2.4.	Results of the numerical modelling of the condensation process.....	140
5.	SUMMARY AND OUTLOOK	146
5.1.	CONCLUSIONS.....	146
5.2.	OUTLOOK.....	149
	PUBLICATION BIBLIOGRAPHY	151
6.	APPENDIX	157
6.1.	EXPERIMENTAL DATA OBTAINED WITH THE LAB-SCALE HEAT EXCHANGER.....	157

6.2. EXPERIMENTAL DATA OBTAINED WITH THE FULL-SCALE DEMONSTRATOR 2	169
SUPERVISED THESES	173
CURRICULUM VITAE.....	174

1. INTRODUCTION AND MOTIVATION

On 11th December 2015, a climate agreement was signed in Paris by all 191 countries participating in the 2015 United Nations Climate Change Conference. The main goal of this agreement was the significant reduction of the climate changing emissions, primarily CO₂ (United Nations 2015). Though the agreement is not binding, the leading industrial countries already are and will enforce their efforts to reduce the carbon dioxide emission. The importance of taking actions has been proven again.

One of the primary methods for this is the increase of the energy effectivity of industrial processes, electricity generation and transportation. About 50 million tonnes of CO₂ were emitted by industrial processes in Germany in the year 2013 (German Federal Environment Agency 2015). Although these emissions are moderate, for example compared to the electricity generation, there is still a major potential for the reduction of the human impact on the climate by the decrease of the emitted CO₂.

The German government also supports scientists and researchers, who optimise processes, machines and apparatuses to make them more energy efficient. In 2010, the German Ministry of Education and Research initiated a research program for "Technologies for Sustainability and Climate Protection". Within this program several projects were launched in cooperation with the chemical industry, in order to enhance the energy efficiency of chemical processes (BMBF 2010).

One of the possible methods to reduce the energy consumption of a chemical process is the optimisation of the energy exchanging processes, such as the heat transfer. Here, heat losses must be compensated by more, mostly fossil, fuel. Hence, an increase of the efficiency would automatically lead to a reduction of the fuel consumption and to reduced carbon dioxide emissions.

In most cases, heat exchangers made of metals are being used, due to the excellent heat conductivity and thermal as well as mechanical properties of metals. For some applications, however, metals cannot be used. These are the handling with highly corrosive fluids or in the pharmaceutical industry, where a contamination of the product with metals cannot be accepted. In such cases, breakable and costly heat exchangers made of glass or ceramics are used. These materials provide sufficient chemical resistance and are thermally stable, but the required wall thickness make them heavy and ineffective for the heat transfer.

During the last 20 to 30 years, the usage of polymeric heat exchangers has been constantly growing. Polymers have an enormous weight advantage, compared with metals or glass, and provide sufficient chemical resistance. Another very important factor are the costs of polymer materials, compared to metals and ceramics (Zaheed, Jachuck 2004). However, most of polymer heat exchangers are built as tubed types, which leads to low heat transfer rates. Polymers have a very low thermal conductivity. While for metals the values range goes from 10 W/m K to almost 200 W/m K, for unfilled, pure

polymers the corresponding values are below 0.5 W/m K (T'Joel et al. 2009). Since polymers also are mechanically weak, compared with metals, the tubed heat exchangers must have thick walls or support structures, to provide a sufficient mechanical durability. Higher wall thickness increases the thermal resistance, which leads to a less effective operating of the apparatus.

A possible solution for this problem was developed at the Chair of Separation Science and Technology of the University of Kaiserslautern. In 2010, an apparatus design with very thin polymer films (25 μm) for water desalination was successfully tested and competitive overall heat transfer coefficients could be reached (Christmann et al. 2012). An attempt to apply this design to various chemical processes was made in the following years. The special application, describe in this work, was the condensation of organic solvents, such as hexane, toluene or tetrahydrofuran.

For this, an extensive experimental work was done including research on the chemical resistance at high temperatures, the mechanical strength and the heat transfer efficiency. The results of this research are presented in this thesis. Furthermore, the flow in the heat exchanger and the heat transfer was modelled with a commercial multiphysics software package Ansys Workbench[®]. In these models, it was tried not only to simulate the flow through a static geometry, but also to describe the interaction between the thin polymer films and the fluids by the means of the fluid-solid-interaction (FSI) models.

2. THEORETICAL BACKGROUND

2.1. THEORETICAL BASICS

2.1.1. Physical properties of materials

2.1.1.1. Definition of the mechanical properties

In the material science, several material properties are defined to describe the mechanical behaviour. The most important of them are presented in this chapter. The focus lies on the properties, which are relevant for polymers, hence no phenomena specific for metals or ceramics are mentioned here.

All materials, metals as well as ceramics and polymers, show reversible elastic behaviour at least for minor stress loads (Hornbogen et al. 2012). In most cases, this is the working range of the material, since no damage occurs in operation and all deformations are reversible.

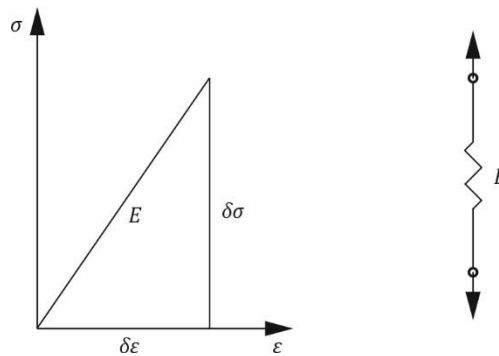


Figure 1: Definition of the Young's modulus E

The characteristic quantity for the reversible elastic behaviour is the Young's modulus E . It can be easily derived from the simplified stress-strain diagram, s. Figure 1, where ε denotes the strain and σ the stress. Then the Young's modulus E is (Czichos et al. 2014):

$$E = \frac{\delta\sigma}{\delta\varepsilon_m} \quad (2.1)$$

This behaviour is also known as the Hooke's law, which describes the linear force-elongation correlation of a spring, as shown on the left-hand side of Figure 1.

If the stress load is higher, than the limit of the elastic zone, the plastic, non-reversible deformation begins. This causes a deformation, which can lead to the failure of the material. Therefore, in technical applications materials shouldn't be exposed to higher stress than the maximum elasticity. In some cases, like screws, however, minor plastic deformation is accepted. For polymer film used in the heat exchanger investigated in this work, plastic deformation should be avoided, as this would permanently change the geometry of the channels and hence influence the flow significantly. For polymers, the

material response to mechanical stress is different to the one of metals and is described in the next section.

2.1.1.2. Mechanical strength of polymers

All polymers are viscoelastic (Elsner et al. 2012). This means that the elastic stress region is not permanent, but time dependent. Because of the relaxation of the chain configurations, especially amorphous polymers can reduce inner stress with the time, which must not necessarily lead to material failure.

Likewise with metals, higher temperatures reduce the mechanical strength, but this phenomenon can be seen already at ambient temperature. However, there is quite a difference between the different types of polymers. For amorphous polymers, the glass transition temperature T_g has an enormous influence on the mechanical strength, as can be seen in Figure 2. Below this temperature, the materials show a very low ductility, they have a high mechanical strength and shear modulus. Above T_g the material is very weak, the shear modulus decreases with the factor of up to 1000, as does the strength as well. For the temperature range 'III' the material properties are similar to those of highly viscous liquids. Amorphous polymers can easily be transformed and reshaped above T_g and keep the shape after cooling down (Elsner et al. 2012).

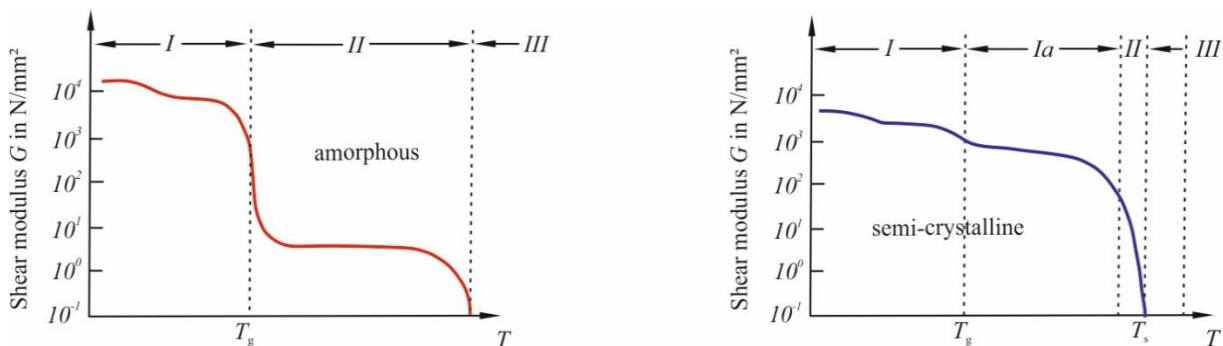


Figure 2: Influence of temperature on the shear modulus for amorphous and semi-crystalline polymers, Source: (Elsner et al. 2005), modified

Semi-crystalline polymers also have a dependency on the temperature. Below the glass transition temperature, they are brittle with high mechanical strength. With the glass transition, however, the shear modulus does not decrease as fast as for the amorphous polymers. Here the typical decrease factors are about 10. For temperatures within the range 'I', the amorphous and the crystalline parts are solid. Above the glass transition temperature within the range 'Ia' the crystalline parts remain solid, while the amorphous parts become thermo-elastic. For a short temperature range the crystals are melting, which significantly decreases the inner structure stability (Elsner et al. 2012). Serban et al. confirmed the amorphous behaviour for polyamide PA6, as shown in Figure 3.

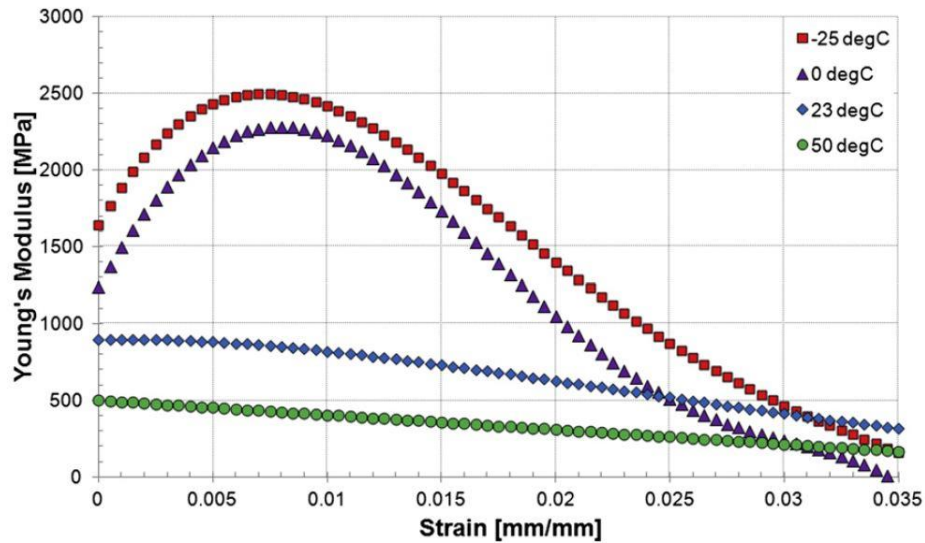


Figure 3: Dependency of Young's modulus on the temperature for semi-crystalline polyamide PA6, Source: (Serban et al. 2013)

The second significant material property is the dynamic hardening. It is also typical for the viscoelastic behaviour and yields in much higher mechanical strength at fast impacts. Serban et al. (Serban et al. 2013) showed that the mechanical strength of a semi-crystalline polyamide from almost 25 MPa at strain rates of 2 mm/min up to over 35 MPa at 2000mm/min. Shi et al. (Shi et al. 2002) also observed similar behaviour for PET. This aspect is very convenient for applications with dynamic loads, as it offers higher resistance for fast pulsating loads.

2.1.1.3. Thermal and thermodynamic properties

From all known thermal and thermodynamic properties of polymers two are of most importance for the suitability of polymer films as heat transfer walls. The first one is the thermal conductivity, which has a significant influence on the overall thermal transfer. The second one is the thermal stability, which limits the application temperature range.

Thermal conductivity

For all unfilled polymers, it can be said, that the thermal conductivity is much lower than for metals. Because of it, polymers are often used as insulators. In Table 1, the relevant values for a selection of common polymers as well as for three metals, commonly used for heat exchangers, are given.

The thermal conductivity is dependent on the chain segment orientation, as the energy transport along the chain is much more effective than from one chain to another. For this reason, the thermal conductivity of amorphous polymers, such as PET is lower than those of semi-crystalline polymers (Yang 2007).

Table 1: Thermal conductivity values of polymers and metals

Material	Thermal conductivity λ in W/m K	Reference
Polyethylene terephthalate (PET)	0.15	(Yang 2007)
Poly(methyl methacrylate), PMMA	0.21	(Yang 2007)
Poly ether ether ketone (PEEK)	0.15	(Yang 2007)
Polytetrafluoroethylene	0.25	(Yang 2007)
Polyethylene, low density (PE-LD)	0.33	(Yang 2007)
Polyethylene, high density (PE-HD)	0.52	(Yang 2007)
Polypropylene (PP)	0.12 – 02	(Yang 2007)
Polyimide (PI)	0.11	(Yang 2007)
Aluminium (Al)	209	(Baehr, Stephan 2008)
Copper (Cu)	399	(Baehr, Stephan 2008)
Steel (SS)	13 – 48	(Baehr, Stephan 2008)

The thermal conductivity can be significantly improved by reinforcing the polymer matrix with fillers, such as carbon, metal oxides or glass fibres. For polyethylene with up 25% (vol.) of aluminium oxide, the thermal conductivity can be increased to 1.6 W/m² K. However, despite the possibility of the usage of fillers the thermal conductivity always remains much lower than for metals.

Thermal stability

The thermal stability can be described as the ability of the material structure to withstand specific temperatures without any damages to its structure. For most construction materials, like metals, polymers or ceramics the relevant detailed data can be obtained from manufacturers or suppliers. However, the information on the maximum application temperature is not always useful, as mechanical loads in combination with higher temperatures set additional limits to the usage of a material. As confirmed during this work, the temperature limits provided by manufacturers can only be used as a preliminary selection criterion. For the final confirmation of a material as appropriate for an application, a specific testing is inevitable.

In Table 2 maximum, long-term application temperatures provided by manufacturers or suppliers are given. The corresponding values for three metals are also given as reference for heat exchanger applications.

Table 2: Maximum long-term application temperatures for selected polymers and metals

Material	Maximum, long-term application temperature in °C	Reference
Polyethylene terephthalate (PET)	115 - 170	(Goodfellow GmbH)
Poly(methyl methacrylate) (PMMA)	50 - 90	(Goodfellow GmbH)
Poly ether ether ketone (PEEK)	~ 250	(Goodfellow GmbH)
Polytetrafluoroethylene (PTFE)	180 - 260	(Goodfellow GmbH)
Polyethylene, low density (PE-LD)	50 - 90	(Goodfellow GmbH)
Polyethylene, high density (PE-HD)	55 - 120	(Goodfellow GmbH)
Polypropylene (PP)	90 - 120	(Goodfellow GmbH)
Polyimide (PI)	250 - 320	(Goodfellow GmbH)
Aluminium, EN AW 5083	120	(Gleich 2015)
Copper (Cu 99.5/Te 0.5)	350	(Goodfellow GmbH)
Steel (EN1.5415)	>500	(ThyssenKrupp)

2.1.1.4. Chemical resistance

In general, the chemical resistance of polymers is considered good in comparison with metals. However, it is very difficult to obtain reliable data on the chemical resistance of polymers, especially for long-term exposure or at higher temperatures. Different polymers have very different chemical resistances for various fluids, acids or organic solvents. The chemical resistance highly depends on the molecular structure and on the build-in non-organic groups. Halogens like fluorine increase the chemical resistance significantly. The best example is polytetrafluoroethylene (PTFE) which is known as the polymer with the highest possible chemical resistance (Elsner et al. 2005).

In most sources for the chemical properties of polymers like (HERA AG), one can find data for the common reference temperatures between 20 and 25 °C. Some others, like (Bürckle GmbH 2011) or (Rotert GmbH) provide data at 50°C. For higher temperatures, no data could be found during the research period between 2011 and 2014.

Apart from that, some sources appeared to provide contradictory data. For the chemical resistance of PET at contact with water for instance, some sources, like (HERA AG) or (Gehr GmbH) mention that problems might appear due to hydrolysis. (Thermoquick Engineering) however considers PET to have an excellent resistance to hot water. A similar problem appeared for polyamide (PA6) as can be seen

as discussed in section 3.1.1.3. In most cases, no maximum exposure time or duration of the testing procedure is provided in the data sets. Generally, three or four categories from resistant to soluble are used to indicate the chemical behaviour.

2.2. BASICS OF FLUID DYNAMICS

2.2.1. Characteristic length

For a better characterisation of fluid flows, dimensionless quantities are often used. Since the physical problems vary with the geometry, it is important to define standardised geometry dimensions in order to enable the comparability of real physical problems with the standard models. Therefore, the characteristic length L is used (Herwig, Schmandt 2015).

The most important purpose of the characteristic length is the comparability of similar geometries. The definition of this dimensioned variable highly depends on the type of the geometry. For pipes and tubes, the inner diameter is normally taken, for plates it is the length in the flow direction. For more complex geometries, specific characteristic variables must be defined (Herwig, Schmandt 2015). Such new definitions can be challenging since the characteristic length has a significant influence on the value of the dimensionless quantities (s. section 2.2.2). A wrong characteristic length can lead to false descriptions of the flow, such as errors in the laminar or turbulent differentiation.

2.2.2. Dimensionless quantities

According to the Π -theory every physical process or system can be described by a set of dimensionless quantities. In general, physical problems can be modelled by equations with appropriate dimensions. The usage of correct dimensions is inevitable for a successful solution. If this condition is fulfilled, the dimensioned variables can be combined to dimensionless quantities. This can be used to compare physical systems or processes as well as for the characterisation of problems (Herwig, Moschallski 2014).

A very common dimensionless quantity is the *Reynolds number* Re . It is one of the most important identifiers for fluid flows and is defined by

$$Re = \frac{\rho \cdot c \cdot L}{\eta} \quad \text{or} \quad Re = \frac{c \cdot L}{\nu} \quad (2.2)$$

with the density ρ , the mean flow velocity c , the characteristic length L , the dynamic viscosity η and the kinematic viscosity ν (Herwig, Schmandt 2015). It also can be described as the quotient of the inertia force and the friction force (Oertel et al. 2014).

The *Reynolds number* is most commonly used to characterise the flow, especially to determine its type: turbulent or laminar. For pipes and liquid flows, the critical Reynolds number value is ~ 2300 while for flat plates it is $5 \cdot 10^5$.

The next important dimensionless quantity is the *Prantl number*. It describes the quotient of the thicknesses of the laminar flow boundary layer and the temperature boundary layer. For gases, an approximated value of 0.7 can be used, for liquids it varies highly. The mathematical definition of the *Prantl number* Pr is

$$Pr = \frac{v \cdot \rho \cdot c_p}{\lambda} \quad (2.3)$$

with the isobaric heat capacity c_p and the thermal conductivity λ .

The *Grashof number* describes the quotient of the buoyancy and the friction forces

$$Gr = \frac{g \cdot L^3 \cdot \beta \cdot (\vartheta_w - \vartheta_0)}{\nu^2} \quad (2.4)$$

with the gravitational potential g , the volumetric thermal expansion coefficient β , the wall surface temperature ϑ_w and the bulk temperature ϑ_0 it highly depends on the temperature.

The Prantl number and the Grashof number can be combined to a single quantity the Raleigh number:

$$Ra = Pr \cdot Gr \quad (2.5)$$

2.2.3. Fluid flow models

2.2.3.1. General balance equations

All available fluid flow models are based on the three conservation equations for the mass, the momentum and the energy. Because the understanding of these are essential for the later CFD modelling, they are explained here. All CFD solvers use these equations for the determination of the required flow parameters. For all three equations the differential form is given, as it is mathematically simpler (Lechler 2011).

Mass conservation

As for all conservation equations, the physical model considers a discrete volume element, as shown in Figure 4.

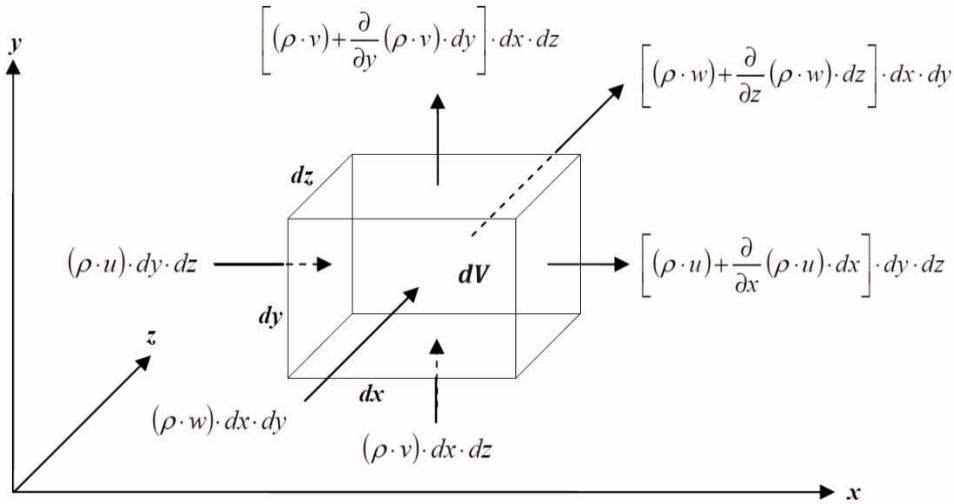


Figure 4: Discrete fluid volume with equations for mass conservation balance. Source: (Lechler 2011), modified

The density ρ and the velocity components u , v and w in x , y and z directions respectively are dependent on the position and the time. The mass change of the volume element with the time is:

$$\frac{\partial}{\partial t}(m) = \frac{\partial}{\partial t}(\rho \cdot V) = \frac{\partial}{\partial t}(\rho \cdot dx \cdot dy \cdot dz) \quad (2.6)$$

With the mass flux equations given in Figure 4, the mass balance can be written as:

$$\frac{\partial}{\partial t}(\rho) + \frac{\partial}{\partial t}(\rho \cdot u) + \frac{\partial}{\partial t}(\rho \cdot v) + \frac{\partial}{\partial t}(\rho \cdot w) = 0 \quad (2.7)$$

This means that the sum of the mass change with the time and of the mass fluxes equals zero. A shorter divergence form also exists

$$\frac{\partial}{\partial t}(\rho) + \vec{\nabla}(\rho \cdot \vec{u}) = 0 \quad (2.8)$$

with the divergence $\vec{\nabla}(\rho \cdot \vec{u})$

$$\vec{\nabla}(\rho \cdot \vec{u}) = \frac{\partial}{\partial t}(\rho \cdot u) + \frac{\partial}{\partial t}(\rho \cdot v) + \frac{\partial}{\partial t}(\rho \cdot w) \quad (2.9)$$

and the velocity vector \vec{u}

$$\vec{u} = u \cdot i + v \cdot j + w \cdot k \quad (2.10)$$

where i, j, k are the coordinates in the Cartesian coordinate system (Lechler 2011).

Momentum conservation

The momentum conservation is based on Newton's second law, according to which the force equals mass times acceleration. In Figure 5 an exemplary force balance in x -direction is given. Here, the position and time dependent forces are (Lechler 2011):

- Pressure: $p = f(x, y, z, t)$
- Normal stress: $\tau_{xx} = f(x, y, z, t)$
- Normal stress: $\tau_{xx} = f(x, y, z, t)$
- Shear stress along the y-axis: $\tau_{yx} = f(x, y, z, t)$
- Shear stress along the z-axis: $\tau_{zx} = f(x, y, z, t)$

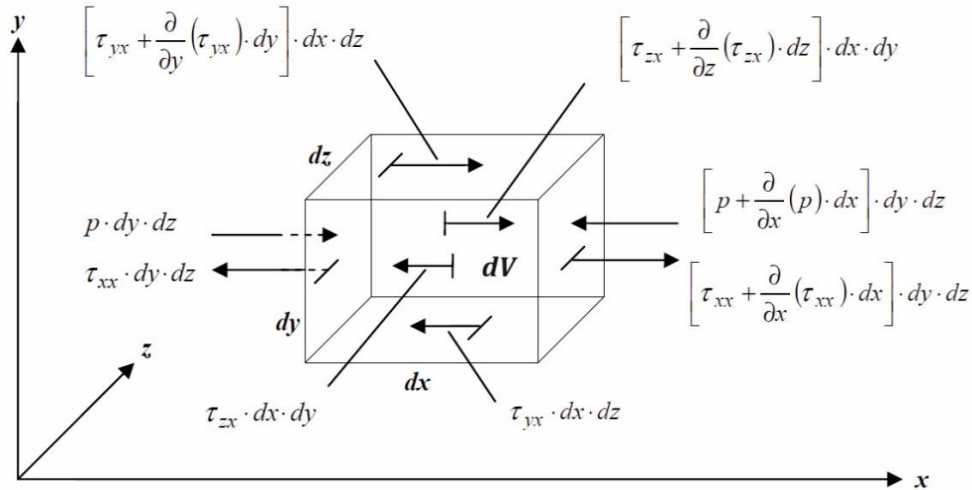


Figure 5: Forces in x-direction on a discrete volume element. Source: (Lechler 2011), modified

With the total force in x-direction

$$F_x = \left[\frac{\partial}{\partial x}(\tau_{xx}) + \frac{\partial}{\partial y}(\tau_{yx}) + \frac{\partial}{\partial z}(\tau_{zx}) - \frac{\partial p}{\partial x} + \rho \cdot g_x \right] dx dy dz \quad (2.11)$$

and the total deviation of the velocity with the time

$$a_x = \frac{\partial u}{\partial t} + u \cdot \frac{\partial u}{\partial x} + v \cdot \frac{\partial u}{\partial y} + w \cdot \frac{\partial u}{\partial z} \quad (2.12)$$

the momentum conservation in x-direction is

$$\frac{\partial}{\partial t}(\rho \cdot u) + \frac{\partial}{\partial x}(\rho \cdot u^2 + p - \tau_{xx}) + \frac{\partial}{\partial y}(\rho \cdot u \cdot v - \tau_{yx}) + \frac{\partial}{\partial z}(\rho \cdot u \cdot w - \tau_{zx}) - \rho \cdot g_x = 0 \quad (2.13)$$

with gravitation component g_x , the shear stress components τ_{ij} and the velocity components u , v and w .

Similar equations can also be derived for the y and z directions (Lechler 2011).

Energy conservation

The principle of the energy conservation also is known as the 1st law of thermodynamics:

$$\frac{d E_{\text{tot}}}{dt} = \dot{W} + \dot{Q} \quad (2.14)$$

The power \dot{W} is the mechanical component of the total energy E_{tot} while \dot{Q} is the thermal one. According to Figure 6 for the x -direction, the sum of the powers in all Cartesian directions can be written as:

$$\begin{aligned} \dot{W} = & \left[\rho \cdot (u \cdot g_x + v \cdot g_y + w \cdot g_z) - \frac{\partial}{\partial x}(u \cdot p) - \frac{\partial}{\partial y}(v \cdot p) - \frac{\partial}{\partial z}(w \cdot p) \right. \\ & - \frac{\partial}{\partial x}(u \cdot \tau_{xx} + v \cdot \tau_{xy} + w \cdot \tau_{xz}) - \frac{\partial}{\partial y}(u \cdot \tau_{yx} + v \cdot \tau_{yy} + w \cdot \tau_{yz}) \\ & \left. - \frac{\partial}{\partial z}(u \cdot \tau_{zx} + v \cdot \tau_{zy} + w \cdot \tau_{zz}) \right] dx dy dz \end{aligned} \quad (2.15)$$

For the second part of the total energy, which determines the heat flux, the equation (2.16) can be used:

$$\dot{Q} = \left[\rho \cdot \dot{q}_s - \frac{\partial}{\partial x}(\lambda \cdot \frac{\partial T}{\partial x}) - \frac{\partial}{\partial y}(\lambda \cdot \frac{\partial T}{\partial y}) - \frac{\partial}{\partial z}(\lambda \cdot \frac{\partial T}{\partial z}) \right] dx dy dz \quad (2.16)$$

Here \dot{q}_s denotes the heat radiation, λ the thermal conductivity and T the temperature of the volume element.

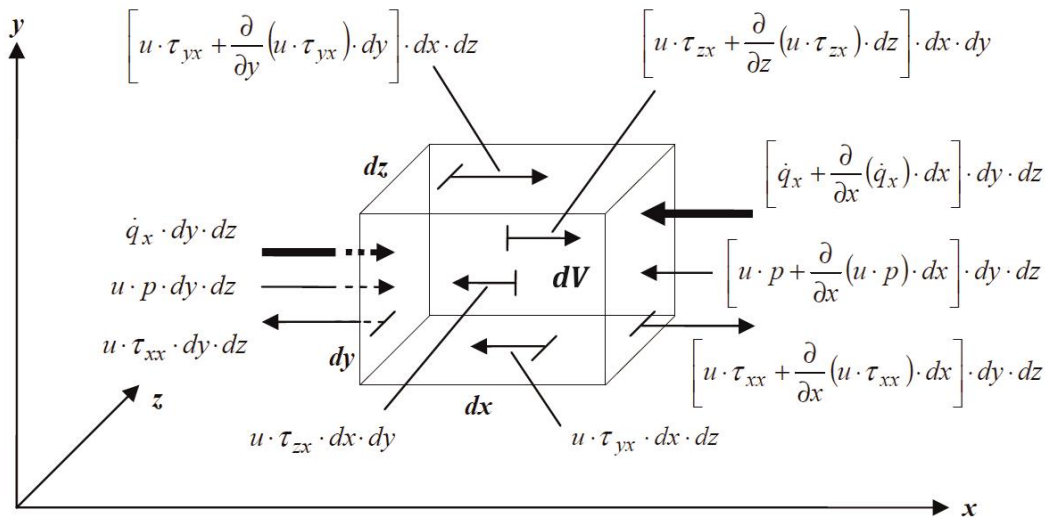


Figure 6: Energy balance of a discrete volume element. Source: (Lechler 2011), modified

The complete differential energy conservation equation in the Cartesian coordinate system is:

$$\begin{aligned}
& \frac{\partial}{\partial t} \left[\rho \left(e + \frac{1}{2} \vec{u}^2 \right) \right] \\
& + \frac{\partial}{\partial x} \left[\rho \cdot u \left(h + \frac{1}{2} \vec{u}^2 \right) - (u \cdot \tau_{xx} + v \cdot \tau_{xy} + w \cdot \tau_{xz}) - \lambda \cdot \frac{\partial T}{\partial x} \right] \\
& + \frac{\partial}{\partial y} \left[\rho \cdot v \left(h + \frac{1}{2} \vec{v}^2 \right) - (u \cdot \tau_{yx} + v \cdot \tau_{yy} + w \cdot \tau_{yz}) - \lambda \cdot \frac{\partial T}{\partial y} \right] \\
& + \frac{\partial}{\partial z} \left[\rho \cdot w \left(h + \frac{1}{2} \vec{w}^2 \right) - (u \cdot \tau_{zx} + v \cdot \tau_{zy} + w \cdot \tau_{zz}) - \lambda \cdot \frac{\partial T}{\partial z} \right] \\
& - \rho \cdot (u \cdot g_x + v \cdot g_y + w \cdot g_z) - \rho \cdot \dot{q}_s = 0
\end{aligned} \tag{2.17}$$

The first line denotes the time derivation of the inner energy e and the kinetic energy $\frac{1}{2} \vec{u}^2$, the next three lines describe the derivation of the enthalpy and the mechanical forces while the last line summarises the potential energy and the radiation (Lechler 2011).

Additional auxiliary equations for the diffusion and dissipation exist and can be found in (Herwig, Schmandt 2015).

2.2.3.2. Navier-Stokes-Equations

The Navier-Stokes-Equations are the basic general equations for the determination of fluid flow parameters (LAURIEN et al. 2011). Two main fluid flow types can be defined: the compressible and the incompressible flow.

Incompressible flows

The incompressible flows are easier to describe, because fluid parameters like the density ρ , the thermal conductivity λ and the kinematic viscosity ν are assumed to be constant. For liquids at low pressures, the flow can be considered incompressible, as the dependence of the density on the pressure is very low compared to its dependence on the temperature. The compact, vector based form of the Navier-Stokes-Equations for incompressible flows is (LAURIEN et al. 2011):

$$\begin{aligned}
& \nabla^T \cdot \vec{u} = 0 \\
& \frac{\partial \vec{u}}{\partial t} + (\vec{u}^T \cdot \nabla) \cdot \vec{u} = -\frac{1}{\rho} \cdot \nabla p + \nu \cdot \nabla^2 \vec{u} \\
& \frac{\partial T}{\partial t} + (\vec{u}^T \cdot \nabla) \cdot T = a \cdot \nabla^2 T
\end{aligned} \tag{2.18}$$

with the differential vector operator ∇ and the velocity vector \vec{u} in Cartesian coordinates

$$\nabla = \begin{bmatrix} \frac{\partial}{\partial x} \\ \frac{\partial}{\partial y} \\ \frac{\partial}{\partial z} \end{bmatrix} \quad \vec{u} = \begin{bmatrix} u \\ v \\ w \end{bmatrix} \quad (2.19)$$

The thermal diffusivity a is computed as:

$$a = \frac{\lambda}{\rho \cdot c_p} \quad (2.20)$$

with the thermal conductivity λ , the density ρ and the isobaric heat capacity c_p .

Apart from this form, several other forms of this equations exist and can be found in (Herwig, Schmandt 2015).

Compressible flows

Almost all gas flows and many liquid applications must be considered compressible. In this case, the fluid properties like the density depend on the temperature as well as on the pressure. The pressure influence for gases is very high and hence cannot be neglected.

For the compact, vector based form, the position vector \vec{x} and the velocity vector \vec{u} must be declared in the Cartesian coordinate system:

$$\vec{x} = [x_1 \ x_2 \ x_3]^T \quad \vec{u} = [u_1 \ u_2 \ u_3]^T \quad (2.21)$$

With this vector definition, the complete compact vector form is:

$$\frac{\partial \vec{U}}{\partial t} + \sum_{m=1}^3 \frac{\partial \vec{F}_m}{\partial x_m} + \sum_{m=1}^3 \frac{\partial \vec{G}_m}{\partial x_m} = \vec{0} \quad (2.22)$$

Here \vec{U} is the vector of state, which contains the conservative variables, \vec{F}_m the convection vector and \vec{G}_m the diffusion vector. These are defined as follows:

$$\vec{U} = [\rho \ \rho u_1 \ \rho u_2 \ \rho u_3 \ \rho e_{tot}]^T$$

$$\vec{F}_m = \begin{bmatrix} \rho u_m \\ \rho u_m u_1 + \delta_{m1} \cdot p \\ \rho u_m u_2 + \delta_{m2} \cdot p \\ \rho u_m u_3 + \delta_{m3} \cdot p \\ u_m (\rho e_{tot} + p) \end{bmatrix} \quad \vec{G}_m = \begin{bmatrix} 0 \\ -\tau_{m1} \\ -\tau_{m2} \\ -\tau_{m3} \\ -\sum_{l=1}^3 u_l \tau_{lm} + q_m \end{bmatrix} \quad (2.23)$$

With the inner energy e

$$e = e_{tot} - \frac{1}{2} \vec{u}^2 \quad (2.24)$$

and the isochoric heat capacity c_v the temperature T can be computed as:

$$T = \frac{e}{c_v} \quad (2.25)$$

The *Kronecker symbol* δ_{ij} is defined as:

$$\delta_{ij} = \begin{cases} 1 & \text{if } i = j \\ 0 & \text{if } i \neq j \end{cases} \quad (2.26)$$

With the equation of state for ideal gases the pressure p is

$$p = \rho \cdot R \cdot T \quad (2.27)$$

where R denotes the specific gas constant.

For the friction based stress, τ_{ij} , the Stoke's friction law can be used

$$\tau_{ij} = \mu \left(\frac{\partial u_i}{\partial x_j} + \frac{\partial u_j}{\partial x_i} \right) - \frac{2}{3} \mu \delta_{ij} \sum_{k=1}^3 \frac{\partial u_k}{\partial x_k} \quad (2.28)$$

with the dynamic toughness μ . The first part of the equation denotes the normal and shear stress, while the second part describes the friction caused by compression or expansion.

The heat flux density q_m in the m -direction is:

$$q_m = -\lambda \frac{\partial T}{\partial x_m} \quad (2.29)$$

As can be seen, the equation system used for the definition of these three vectors, consists of three parts: the continuity equation, the momentum equations for each Cartesian direction and the energy equation.

2.2.3.3. Turbulence modelling

Several models exist for the determination of a turbulent flow. In Figure 7 the available model groups are given. For technical applications the averaged basic equations are often used, as they provide sufficient accuracy and the exact knowledge of every single eddy is not necessary (Martin 2011).

Direct numerical solution

It is also possible to use the direct numerical solution (DNS), which consists of the direct integration of the Navier-Stokes-equations; it provides a very accurate solution, but requires a very fine discretisation of the problem. The recommended distance between the grid points is less than one thousandth of the specific dimension of the flow volume. This leads to a number of elements that cannot be handled

even by modern high performance computers (HPC). Nevertheless, many researchers continue working on the DNS-method (Martin 2011).

Large Eddy Simulation

The Large Eddy Simulation (LES) is based on the idea of comparatively large discretisation of the numerical solution and the modelling of small scales. This method is not widely used, as it requires many unsteady simulations. The turbulence model is highly dependent on the resolution of the grid, therefore a comparison of the results obtained with two different grid sizes is not possible, which makes a grid study with validation by experimental data inevitable. By now, the LES models are mostly used in a combination with RANS models.

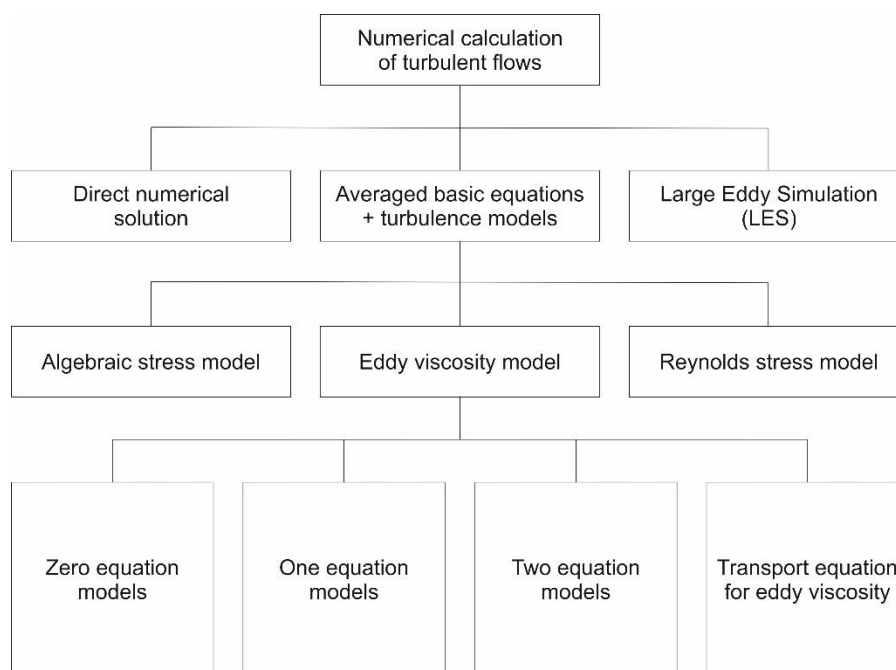


Figure 7: Classification of turbulence models. Source: (Martin 2011)

Reynolds Averaged Navier-Stokes

The *Reynolds Averaged Navier-Stokes* equations (RANS) are the most commonly used models for turbulent flows. For most applications, the exact position and time of a certain eddy is not relevant, as the information on the overall pressure loss or the global interaction of the flow with the walls is of much higher interest. Therefore, it is useful to reduce the Navier-Stokes equations to a smaller set of equations, which provide the desired information directly. This is done by the time-based averaging of the flow parameters (Herwig, Schmandt 2015). To describe the influence of the turbulence of the flow, several turbulence models can be added to the RANS equations.

In most cases, the Eddy Viscosity Model (EVM) is used. The entire information of the influence of the turbulence on the flow is combined to a single scalar parameter η_t , which is characteristic for the

isotropic eddy viscosity model. This parameter is position and time dependent and can be linked to the flow field in several ways (Herwig, Schmandt 2015).

The additional models used for the EVM can be classified according to the number of the used partial differential equations:

- The *Zero equation model* only contains algebraic equations
- The *One-equation model* links the eddy viscosity to the flow field with only one differential equation
- The *Two-equation model* uses two partial differential equations for the determination of η_t

A very popular two-equation model is the k - ε -model, which was also used in this work. Here, the partial differential equations for the turbulence kinetic energy k and the turbulence eddy dissipation ε are used. The turbulence parameter η_t is linked to k and ε as follows:

$$\eta_t = C_\mu \cdot \rho \cdot \frac{k^2}{\varepsilon} \quad (2.30)$$

The model can be adjusted to the applied problem with the constant C_μ . Further details of this model can be found in (Ansys Inc. 2014b).

For the k - ω -model the turbulence parameter is linked to the turbulence kinetic energy k and to the turbulent frequency ω via the relation:

$$\eta_t = \rho \cdot \frac{k}{\omega} \quad (2.31)$$

This model provides better results than the k - ε -model at near wall areas

The *Shear Stress Transport* model (SST) is based on the k - ω -model. It takes into account the additional shear stress caused by the turbulence τ_t . This can be formulated as follows:

$$\tau_t = \rho \cdot \sqrt{\frac{\text{Production of the kinetic energy}}{\text{Dissipation of the kinetic energy}}} \cdot a_1 \cdot k \quad (2.32)$$

Detailed information on this model can be found in (Menter 1994).

2.2.3.4. Fluid properties determination

For roughly estimated calculations of the flow and the heat transfer constant fluid properties, such as density or specific heat capacity can be used, especially if the state changes are low, e.g. temperature differences below 10 K and no occurring phase transitions. For a precise modelling of the flow parameters, the influence of the temperature on the fluid properties must be taken into account.

Especially for gases, which cannot be considered incompressible, due to their significant density changes with the pressure and temperature, the exact determination of the fluid properties is inevitable. For this, real gas and liquid equations of state are used, which are based on the thermal equations of state.

Equations of state for gases (EOS)

For ideal gases and real gases at low pressures and hence low densities, the ideal gas law (2.33) can be used (Baehr, Kabelac 2012):

$$p v = R T \Leftrightarrow \frac{p v}{R T} = Z = 1 \quad (2.33)$$

Here p denotes the absolute pressure, v the specific volume of the gas, R the specific gas constant and T is the temperature. In this case real gas coefficient $Z = 1$. For real gases, this value is different and can be computed by a series expansion containing the molar volume V_m , which is given in (2.34). Herein the virial coefficients $B(T)$, $C(T)$ etc. are functions with respect to the temperature.

$$Z = 1 + \frac{B(T)}{V_m} + \frac{C(T)}{V_m^2} + \dots = 1 + B(T) d + C(T) d^2 + \dots \text{with } d = 1/V_m \quad (2.34)$$

This series expansion enables a precise determination of the density of gases but is not suitable for liquids. Although this equation provides a very good accuracy, it is not being used for applied numerical simulations due to its complexity (Baehr, Kabelac 2012).

For most technical applications, simplified cubic equations of state are available. They are based on the general cubic equation of state, which can be written as a quotient of two polynomials:

$$p = \frac{R T v^2 + A(T)v + B(T)}{v^3 + C(T)v^2 + D(T)v + E(T)} \quad (2.35)$$

or as factorised polynomial after an applied partial fraction analysis:

$$p = \frac{R T}{v - b_1} + \frac{\alpha(T)}{(v - b_1)(v - b_2)} + \frac{\beta(T)}{(v - b_1)(v - b_2)(v - b_3)} \quad (2.36)$$

This contains the two temperature dependent parameters $\alpha(T)$ and $\beta(T)$ and the coefficients b_1 , b_2 and b_3 which in most cases are considered to be constant, though they may depend on the temperature.

One of the most commonly used equations of state for technical fluids is the Standard Redlich-Kwong-Equation (2.37) (Ansys Inc. 2014b):

$$p = \frac{R T}{v - b + c} - \frac{a(T)}{v(v - b)} \quad (2.37)$$

The parameter $a(T)$ is defined by (2.38):

$$a(T) = a_0 \left(\frac{T}{T_c} \right)^{-n} \text{ with } a_0 = \frac{0.42747 R^2 T_c^2}{p_c}, b = \frac{0.07664 R T_c}{p_c} \text{ and } n = 0.5 \quad (2.38)$$

The index 'c' denotes critical point properties, which can be obtained from various sources, like (VDI 2006). The value for exponent n is been determined experimentally and is valid for most fluids.

The Aungier-Redlich-Kwong equation is an improved expression of the Standard Redlich-Kwong-Equation (2.39), introduced by Augnier (Johnson 1998). It contains a new parameter 'c', which is a correction factor based on the critical point properties and provides better accuracy near it. The exponent 'n' is a function with respect to the acentric factor ω and hence depends on the used fluid.

$$p = \frac{R T}{v - b + c} - \frac{a(T)}{v(v + b)T_R^n} \quad (2.39)$$

with $T_R = \frac{T}{T_c}$ and $n = 0.4976 + 1.1735\omega + 0.4754\omega^2$. The correction factor 'c' can be computed according to equation (2.40). For the parameters a_0 and b the same equations can be used as for the Standard Redlich-Kwong model.

$$c = \frac{R T_c}{p_c + \frac{a_0}{v_c(v_c + b)}} + b - v_c \quad (2.40)$$

For the acentric factor, the equation (2.41) can be used:

$$\omega = -1 - \lg \left(\frac{p_s}{p_c} \right) \quad \text{with } p_s = p_s(T = 0.7 T_c) \quad (2.41)$$

The reference temperature point herein was set to 0.7 of the critical temperature because for many substances is corresponds with the boiling temperature at normal pressure of approx. 1 bar (VDI 2006).

In 1972 Soave published another derivate of the original Redlich-Kwong equation (Soave 1972). Good results could be achieved with non-polar fluids as well as for non-polar mixtures. The equation is given by:

$$p = \frac{R T}{v - b + c} - \frac{a(T)}{v(v + b)} \quad (2.42)$$

For the parameter b the same equation can be as in for the standard model, the temperature dependent parameter $a(T)$ is to be computed as follows:

$$a(T) = a_0 \left(1 + n \left(1 - \sqrt{\frac{T}{T_c}} \right) \right)^2 \quad \text{with } a_0 = 0.42747 \frac{R^2 T_c^2}{p_c} \quad (2.43)$$

For the exponent 'n' a polynomial expression similar to the one in the Aungier-Redlich-Kwong model must be used:

$$n = 0.470 + 1.574\omega - 0.176\omega^2 \quad (2.44)$$

The Peng Robinson model (2.45) is also based on the cubic expression (2.36) .

$$p = \frac{RT}{v - b + c} - \frac{a(T)}{v^2 - 2bv + b^2} \quad (2.45)$$

With the same parameters $a(T)$ and n as in the Soave-Redlich-Kwong model, the Peng-Robinson model is distinguished from the previous one by a different coefficient for the critical point parameter b .

$$b = 0.0777 \frac{R T_c}{p_c} \quad (2.46)$$

All of the equations described here are appropriate and can be used to describe the state of the gas with a sufficient precision for most applications. They often are implemented by default in multiphysics software packages, like Ansys CFX or Fluent (Ansys Inc. 2014a).

Equations for thermodynamic properties of gases

For the accurate numerical analysis of a flow, especially involving the evaluation of the thermal energy, precise energy models are needed. Property tables, for example, can be used for the simulations with commercial software packages like Ansys CFX or Fluent. These tables often only contain few values for most common temperature ranges or points. In this case, the values must be linearly interpolated by the solver between two given values. Depending on the distance between the values used as the interpolation basis, errors can be unacceptably big. Better results can be achieved with non-linear approximation equations. Most of the available approximation expressions for the specific capacity, the dynamic viscosity and the heat conduction are only dependent on the temperature (VDI 2006). Various mathematical models have been developed for the isobaric specific heat capacity of gases. For example, the Aly-Lee-Equation can be used. The deviations of the results obtained with it, from the experimental data is negligible (Frenkel et al. 1994).

$$\tilde{c}_p^{id} = A + B \left(\frac{C/T}{\sinh(C/T)} \right)^2 + D \left(\frac{E/T}{\cosh(E/T)} \right)^2 \quad (2.47)$$

For most applications in process engineering, a simple polynomial equation can be used with acceptable accuracy. Only for very low temperatures the deviations become higher (VDI 2006).

$$\frac{c_p^{id}}{[J/m K]} = A + B \frac{T}{[K]} + C \left(\frac{T}{[K]} \right)^2 + D \left(\frac{T}{[K]} \right)^3 + \frac{E}{\left(\frac{T}{[K]} \right)^2} \quad (2.48)$$

Similar polynomic expressions can be used for the dynamic viscosity η_{gas} (2.48) and for the thermal conductivity λ_{gas} (2.49) (VDI 2006). It must be taken into account, that for each equation a substance specific set of constants ('A' to 'E') must be used.

$$\frac{\eta^{id}}{Pa s} = A + B \frac{T}{[K]} + C \left(\frac{T}{[K]} \right)^2 + D \left(\frac{T}{[K]} \right)^3 + E \left(\frac{T}{[K]} \right)^4 \quad (2.49)$$

$$\frac{\lambda_{liq}}{[W/m K]} = A + B \frac{T}{[K]} + C \left(\frac{T}{[K]} \right)^2 + D \left(\frac{T}{[K]} \right)^3 + E \left(\frac{T}{[K]} \right)^4 \quad (2.50)$$

Equations for thermodynamic properties of liquids

Liquids are often being considered incompressible and the changes of the thermodynamic properties are negligible for many applications. For low pressures, no equations of state are normally used. However, in cases when a wide range of temperatures is being evaluated, the dependency on the temperature must be taken into account. The approximation equations with respect to the temperature are described in this section. The corresponding coefficients used in this work were taken from (VDI 2006).

As the density of the liquids is being considered independent from the pressure, both correlations consist of only one variable, the temperature. The Rackett Equation (2.51) is one of the most commonly used approximations, although it has high deviations from experimental data for low temperatures and does not provide accurate results for mixtures of different substances (Mchaweh et al.).

$$\frac{\rho_{liq}}{[kg/m^3]} = \frac{A}{B \left(1 + \frac{T/[K]}{C} \right)^D} \quad \text{or} \quad \frac{v_{liq}}{[m^3/kg]} = \frac{B}{A} \left(1 + \frac{T/[K]}{C} \right)^D \quad (2.51)$$

Another approved model is the COSTALD-method, which can be used for the approximation of the specific molar volume v_s along the boiling point curve, which is useful for the modelling of phase transitions (VDI 2006). The abbreviation COSTALD stands for **CO**rresponding **STA**te **L**iquid **D**ensity (Campbell 1992). It is more complex and hence it is rarely used. Especially the availability of the fluid

specific parameters is critical for some substances. It consists of a main equation and three additional parameter expressions:

$$v_s = \tilde{\rho}^{-1} = v^* V_R^{(0)} \left[1 - \omega_{SRK} V_R^{(\delta)} \right] \quad (2.52)$$

$$V_R^{(0)} = 1 + a(1 - T_r)^{\frac{1}{3}} + b(1 - T_r)^{\frac{2}{3}} + (1 - T_r) + d(1 - T_r)^{\frac{4}{3}} \quad (2.53)$$

$$(2241) \quad (2.54)$$

$$T_r = \frac{T}{T_{c,COSTALD}} \quad \text{with} \quad 0.25 < T_r < 0.95 \quad (2.55)$$

The values of the coefficients are given in Table 3. The substance specific parameters here are the characteristic specific volume, v^* , the critical COSTALD-temperature $T_{c,COSTALD}$ and the acentric factor ω_{SRK} . In case, these parameters are not available, the normal values for the critical point of the fluid can be used instead, without a significant loss of accuracy. The acentric factor ω_{SRK} is an optimised acentric factor based on the general Soave-Redlich-Kwong equation of state. In case this value is not available, the equation can be also used (VDI 2006).

Table 3: Coefficients for the COSTALD-method

$a = -1.52716$	$b = 1.43907$	$c = -0.71446$	$d = 0.190454$
$e = -0.296123$	$f = 0.376914$	$g = -0.0427457$	$h = -0.0470645$

For the other properties of liquids the following equations can be used, if the assumption of constant properties is not sufficient (VDI 2006). They depend only on the temperature, so the incompressibility of water is assumed.

Dynamic viscosity η_{liq} :

$$\ln \frac{\eta}{[Pa s]} = A + \frac{B}{[T/K]} + C \frac{T}{[K]} + D \left(\frac{T}{[K]} \right)^2 + E \left(\frac{T}{[K]} \right)^3$$

or

$$(2.56)$$

$$\frac{\eta}{Pa s} = e^{A + \frac{B}{[T/K]} + C \frac{T}{[K]} + D \left(\frac{T}{[K]} \right)^2 + E \left(\frac{T}{[K]} \right)^3}$$

Thermal conductivity λ_{liq}

$$\frac{\lambda_{liq}}{[W/m K]} = A + B \frac{T}{[K]} + C \left(\frac{T}{[K]} \right)^2 + D \left(\frac{T}{[K]} \right)^3 + E \left(\frac{T}{[K]} \right)^4 \quad (2.57)$$

Specific heat capacity at constant pressure (1 bar) c_p^{liq}

$$\frac{c_p^{liq}}{[J/kg K]} = A + B \frac{T}{[K]} + C \left(\frac{T}{[K]} \right)^2 + D \left(\frac{T}{[K]} \right)^3 + \frac{E}{\left(\frac{T}{[K]} \right)^2} \quad (2.58)$$

NASA Polynomials

In 1963 S. Gordon and B. McBride published the NASA Report SP-3001 in which they proposed a seven coefficient polynomial method for the calculation of the molar specific heat capacity C_p° , the enthalpy H_T° , and entropy S_T° for gases and liquids. Through decades, the coefficients have been modified in order to improve the accuracy of the polynomials and to expand the valid temperature range. Up to now, due to the demands of NASA the properties can be calculated for temperatures between 200 K and up to 6000 K depending on the substance (Burcat, Ruscic 2005).

For the complete polynomials, 15 constants are required. The first set containing seven constants is needed for the higher temperature range between 1000 K and 6000 K. The second one which also contains seven constants belongs to lower temperatures between 200 K and 1000 K (Burcat, Ruscic 2005) or (Zehe et al. 2001). In earlier sources, like (McBride, Sanford 1992) or (McBride et al. 1993) different temperature limits can be found, like 300 K to 1500 K and 1500 K to 3000 K. The last constant describes a reference state, which is in most cases the molar enthalpy $\frac{H_{297}}{R}$ at 297 K.

With the molar gas constant R the seven constants polynomials are defined as follows:

$$\frac{C_p^\circ}{R} = a_1 + a_2 T + a_3 T^2 + a_4 T^3 + a_5 T^4 \quad (2.59)$$

$$\frac{H_T^\circ}{R T} = a_1 + \frac{a_2 T}{2} + \frac{a_3 T^2}{3} + \frac{a_4 T^3}{4} + \frac{a_5 T^4}{5} + \frac{a_6}{T} \quad (2.60)$$

$$\frac{S_T^\circ}{R} = a_1 \ln T + a_2 T + \frac{a_3 T^2}{2} + \frac{a_4 T^3}{3} + \frac{a_5 T^4}{4} + a_7 \quad (2.61)$$

For very low temperatures, between 50 K and 200 K extended 9-constant polynomial system exists, which additionally provides an expression for the Gibbs enthalpy. It can be found in (Burcat and Ruscic 2005). Since temperatures below 273 K are not relevant for this work, these polynomials are not given here.

IAPWS equations

These equations were developed solely for water and steam and were first introduced in 1995 by the International Association for the Properties of Water and Steam (IAPWS). The latest revised release was published in 2014 (IAPWS 2014). In the used software package Ansys CFX® the 1997 release

equations are implemented (Ansys Inc. 2014b). The differences between the 1997 and the 2014 release are small, the temperature range was expanded down to 130 K, some coefficient values were improved and the calculation of the triple-point pressure was added. The main equations, some of which are given in this work, did not change during the last 20 years.

The equation system is based on the critical point of water, which is given with the critical temperature $T_c = 647.096$ K, the critical density $\rho_c = 322$ kg/m³ and the specific gas constant for water $R_w = 0.46151705$ kJ/kg K. The main equation is the one for the Helmholtz free energy f in its dimensionless form (IAPWS 2014):

$$\frac{f(\rho, T)}{R_w T} = \Phi(\delta, \tau) = \Phi^0(\delta, \tau) + \Phi^r(\delta, \tau) \quad (2.62)$$

with the density quotient $\delta = \rho/\rho_c$ and the temperature quotient $\tau = T/T_c$.

This equation consists of two parts, the ideal gas part Φ^0 and the residual part Φ^r :

$$\Phi^0 = \ln \delta + n_1^0 + n_2^0 \tau + n_3^0 \ln \tau + \sum_{i=4}^7 n_i^0 \ln[1 - e^{-\gamma_i^0 \tau}] \quad (2.63)$$

$$\Phi^r = \sum_{i=4}^7 n_i \delta^{d_i} \tau^{t_i} + \sum_{i=7}^{51} n_i \delta^{d_i} \tau^{t_i} e^{-\delta^{c_i}} + \sum_{i=52}^{54} n_i \delta^{d_i} \tau^{t_i} e^{-\alpha_i(\delta - \varepsilon_i)^2 - \beta_i(\tau - \gamma_i)^2} + \sum_{i=55}^{56} n_i \Delta^{b_i} \delta \psi \quad (2.64)$$

with the parameters $b_i, c_i, n_i^0, \varepsilon_i, \gamma_i^0$ and the additional expressions with the relevant constants C_i and D_i :

$$\Delta = \theta^2 + B_i [(\delta - 1)^2]^{a_i}$$

$$\theta = (1 - \tau) + A_i [(\delta - 1)^2]^{1/2\beta_i}$$

$$\psi = e^{-C_i(\delta - 1)^2 - D_i(\tau - 1)^2}$$

The reference state is the triple-point of water at 273.16 K, where the specific internal energy u'_t and the specific entropy of the saturated liquid are set to zero (IAPWS 2014). All coefficients were adjusted to meet this definition. These equations have a wide validity range from 130 K up to over 1200 K and pressures up to 1000 MPa. By now the IAPWS equations are the most commonly used equations for the determination of water properties (Ansys Inc. 2014a). As all these equations are already implemented in Ansys CFX®, no coefficient values are given here. They can be obtained from (IAPWS 2014).

2.3. HEAT TRANSFER

Three types of heat transfer are known: the convection, which occurs in fluids, the thermal conduction and the contact-free radiation. The both first types of the heat transfer require a material, either a fluid or a solid, the third one can also occur in a vacuum (Baehr, Stephan 2008). Physically, the convection and the thermal conduction are similar; the convection is defined for moving materials while thermal conductivity occurs in stationary materials. According to this definition no convection can be expected in solids (von Böckh, Wetzel 2014). In some sources the heat transfer with phase transition is defined as the fourth type of the heat transfer (Herwig, Moschallski 2014).

2.3.1. Convection

The definition of the convection is the heat transfer within a moving fluid. Two types of the convection exist: the forced convection and the natural convection. For technical applications the forced convection with thermal interaction between a fluid and a wall is the most interesting case; a closer study of the boundary layer is inevitable for the precise determination of the heat transfer (Baehr, Stephan 2008).

2.3.1.1. Forced convection

The forced convection is the most frequent heat transfer type in technical applications. The effectivity of the heat transfer depends on the temperature gradient as well as on the flow, which is initiated by a pressure gradient between the inlet and the outlet. As most of the technical flows are turbulent, this flow type is discussed here in detail.

In Figure 8 the velocity and temperature profiles in an ideal pipe are shown. The temperature boundary layer is typical for turbulent flow; here the temperature decreases from the wall temperature ϑ_w to the fluid temperature ϑ_F . Within the fluid, the temperature is nearly constant (von Böckh, Wetzel 2014).

Within the boundary layer, only thermal conduction occurs. Hence, the thermal conductivity of the fluid is the most important material parameter. In this area, the heat flux is defined as:

$$\dot{q} = \alpha \cdot (\vartheta_F - \vartheta_w) = -\lambda \left(\frac{\partial \vartheta}{\partial r} \right)_{r_w} \quad (2.65)$$

Based on (2.65) the heat transfer α can be computed by:

$$\alpha = -\lambda \cdot \frac{\left(\frac{\partial \vartheta}{\partial r} \right)_{r_w}}{(\vartheta_F - \vartheta_w)} \quad (2.66)$$

The heat transfer coefficient α then depends on the material property as well as on the partial deviation of the temperature with respect to the location and on the temperature gradient. In most cases the boundary layer is very thin and cannot be measured, hence, an assumption can be made:

$$\alpha = \frac{\lambda}{\delta_{\vartheta}} \quad (2.67)$$

The temperature distribution in the fluid is much more complex and cannot be determined analytically. The heat transfer here is highly influenced by the flow velocity and the turbulence (von Böckh, Wetzel 2014).

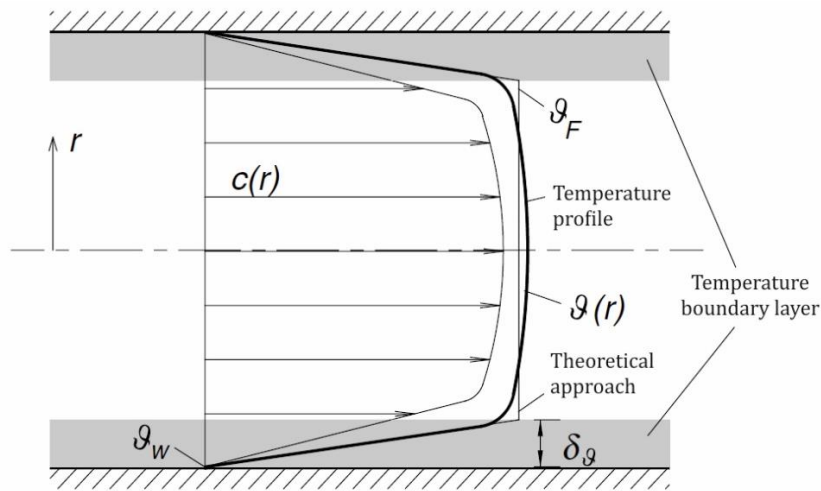


Figure 8: Turbulent pipe flow. Source: (von Böckh, Wetzel 2014)

The most frequent case of technical turbulent flows is the flow through a pipe. Based on numerous experimental results the following correlation was developed (von Böckh, Wetzel 2014):

$$Nu_{d_i,turb} = \frac{\left(\frac{\xi}{7}\right) \cdot Re_{d_i} \cdot Pr}{1 + 12.7 \cdot \sqrt{\frac{\xi}{7}} \cdot (Pr^{2/3} - 1)} \cdot f_1 \cdot f_2 \quad (2.68)$$

The Darcy friction factor ξ describes here the influence of the fluid friction in the pipe and can be computed with:

$$\xi = [1.7 \cdot \log(Re_{d_i}) - 1.5]^{-2} \quad (2.69)$$

The function f_1 allows considering the influence of the length of the pipe, as the thickness of the boundary layer increases with the length of the pipe.

$$f_1 = 1 + \left(\frac{d_i}{l}\right)^{2/3} \quad (2.70)$$

The heat flux direction also has an influence on the heat transfer value, because of the temperature dependent quantities Re and Pr . For the equation (2.68) the temperature and the speed in the very centre of the flow is used. In the boundary layer the temperature and the velocity are not the same as in the centre of the flow. Therefore, a quotient expression must be used to consider this aspect (von Böckh, Wetzel 2014):

$$f_2 = (Pr/Pr_w)^{0.11} \quad \text{for liquids} \quad (2.71)$$

$$f_2 = (\vartheta/\vartheta_w)^{0.45} \quad \text{for gases}$$

These correlations are valid for:

$$10^4 < Re_{d_i} < 10^6 \quad 0.6 < Pr < 10^3 \quad l/d_i > 1$$

For rough calculations a simplified correlation can be used (von Böckh, Wetzel 2014):

$$Nu_{d_i,turb} = (Re_{d_i}^{0.7} - 230) \cdot Pr^{0.47} \cdot f_1 \cdot f_2 \quad (2.72)$$

For f_1 and f_2 the equations (2.70) and (2.71) can be used.

2.3.1.2. Natural convection

The free convection is solely driven by temperature based density differences in the fluid. In contrast to the forced convection, the heat transfer causes the flow. A typical example for this is a heated plane wall with a stationary fluid. The flow occurs if the wall temperature is higher than the fluid temperature; this temperature gradient leads to buoyancy for fluid elements with higher temperature and hence a lower density (Herwig, Moschallski 2014). Depending on the orientation of the wall, the flow is based on the ratio between the buoyancy and the shear forces. Typically the dimensionless *Nusselt number* is being used to characterise the convection (von Böckh, Wetzel 2014):

$$Nu_L = \alpha \cdot \frac{L}{\lambda} = f(Gr, Pr, geometry) \quad (2.73)$$

with heat transfer coefficient α , the characteristic geometry length L and the thermal conductivity coefficient λ .

It also possible to compute the *Nusselt number* by the dimensionless quantities *Grashof number* and *Prantl number*. These are defined as follows (von Böckh, Wetzel 2014):

$$Gr = \frac{g \cdot L^3 \cdot \beta \cdot (\vartheta_w - \vartheta_0)}{\nu^2} \quad (2.74)$$

$$Pr = \frac{\nu \cdot \rho \cdot c_p}{\lambda} \quad (2.75)$$

with the gravitational potential g , the volumetric thermal expansion coefficient β , the wall surface temperature ϑ_w , the bulk temperature ϑ_0 , the kinematic viscosity ν , the density ρ and the isobar heat capacity c_p .

The Grashof number and the Prantl number can be combined in a single quantity, the Raleigh number Ra (von Böckh, Wetzel 2014):

$$Ra = Gr \cdot Pr \quad (2.76)$$

The characteristic length L depends on the geometry. For plane plate it is very often the length, while for tubes and pipes in most cases it is the diameter (Herwig, Moschallski 2014).

The empirical correlations for the *Nusselt number* for four common cases are presented here. For the determination of the quantities equations (2.77) - (2.79) can be used.

Vertical plane

The density of the fluid decreases with the vertical position upwards; an upward flow occurs. Because of the density and temperature differences within the boundary layer, the gravitation forces for each volume element are different. Even for laminar flows, it is not possible to deduce an analytical solution for the heat transfer in this case. Since the flow becomes turbulent after a specific height, which makes the analytical review more complex. Therefore, an empirical correlation is used to describe the flow and the heat transfer (von Böckh, Wetzel 2014).

$$Nu_L = \left(0.725 + 0.377 \cdot (Gr \cdot Pr)^{1/6} \cdot f_1(Pr) \right)^2 \quad (2.77)$$

$$\text{with: } f_1(Pr) = \left(1 + 0.671 \cdot Pr^{(-9/16)} \right)^{-7/27}$$

The characteristic length L in this case the length of the plate.

Within the boundary layer, the temperature decreases and the density increases linearly with the distance from the wall. At the contact area with the wall, the fluid has the same temperature ϑ_w as the wall and the corresponding density ρ_w . Based on this, the profile for the velocity c evolves, as shown in Figure 9. With the growing thickness of the boundary layer, this profile becomes wider which leads to turbulences in the flow. Beyond the boundary layer, the temperature in the fluid is considered constant (von Böckh, Wetzel 2014).

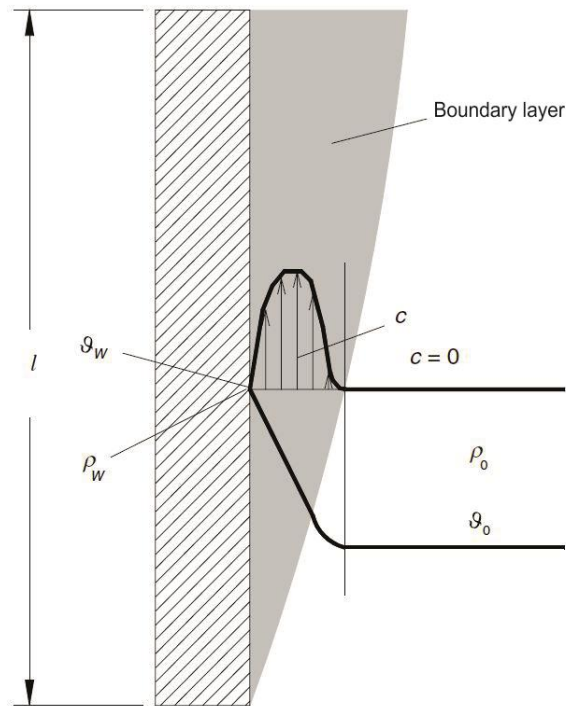


Figure 9: Natural convection at a vertical plane, source: (von Böckh, Wetzel 2014)

Inclined plane

The physical principle of the flow, which occurs at an inclined plane, is similar to that of the vertical plane. Here, the temperature based density differences are also the driving forces for the flow. For a volume element dV the density ρ_1 is higher than the density ρ_2 if $\vartheta_1 < \vartheta_2$. While the buoyancy force remains unchanged for a discrete volume element, the gravitational force decreases with the density. This force imbalance causes the flow (Herwig, Moschallski 2014).

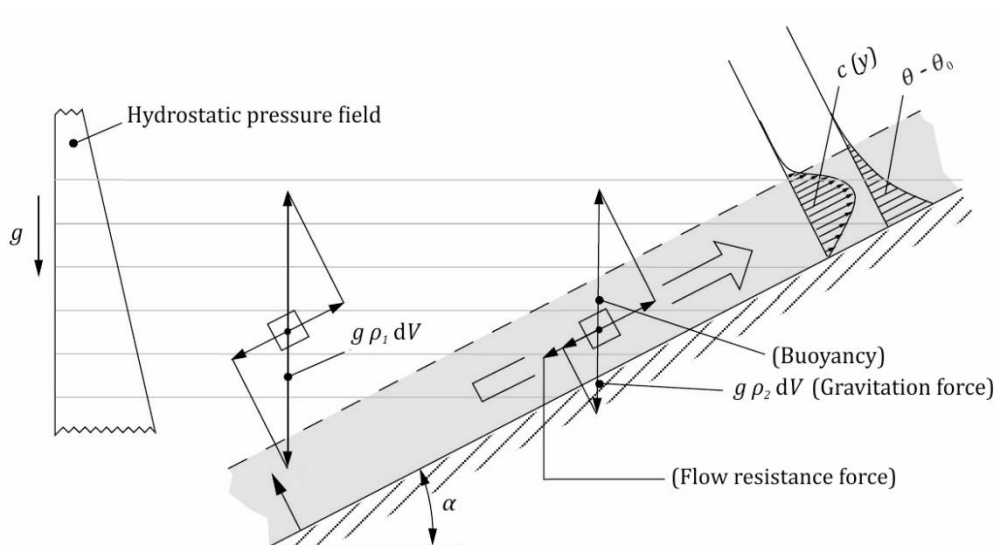


Figure 10: Natural convection at an inclined plane, source: (Herwig, Moschallski 2014), modified

For the determination of the heat transfer, the equation (2.78) with the additional condition $Ra_\alpha = Ra \cdot \cos \alpha$ can be used (von Böckh, Wetzel 2014):

$$Nu_L = 0.56 \cdot (Ra_c \cdot \cos \alpha)^{1/4} + 0.13 \cdot (Ra_\alpha^{1/3} - Ra_c^{1/3}) \quad (2.78)$$

$$Ra_\alpha = Ra \cdot \cos \alpha$$

The critical *Raleigh number* can be obtained from Figure 11:

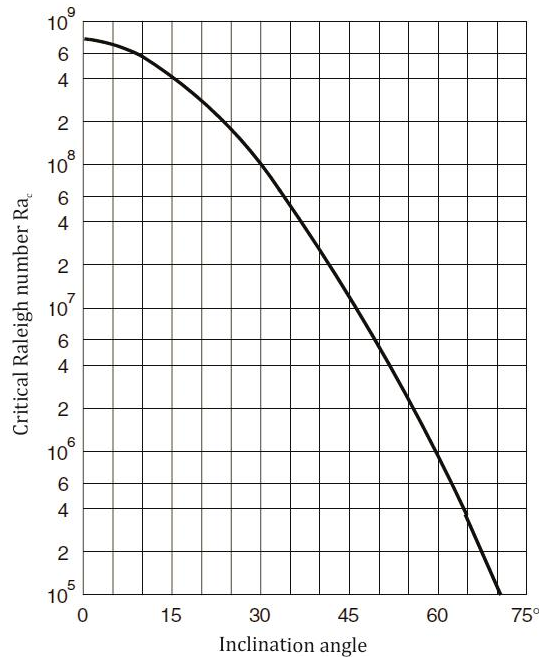


Figure 11: Diagram for the critical Raleigh number, source: (von Böckh, Wetzel 2014)

Horizontal plane

This flow has a different physical background, than the cases described previously. Here, the flow direction is normal to the gravitation force. Due to the density reduction, the isobaric lines (grey) are not parallel to the wall, but curved. Because of that, an acceleration in the horizontal direction occurs off the edge of the plate, as the curved isobaric profile only occur above the heated plate. Therefore, this type of convection is also called indirect or implied convection, because the buoyance doesn't affect the fluid molecules directly (Herwig, Moschallski 2014).

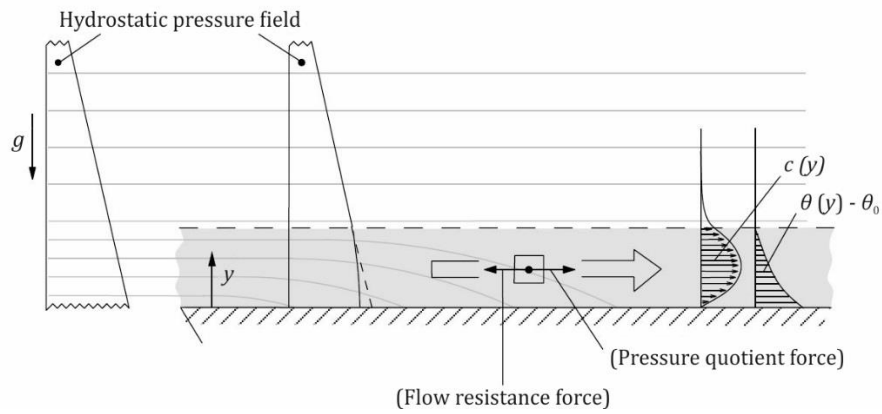


Figure 12: Natural convection at a horizontal plane, source: (Herwig, Moschallski 2014), modified

For this case, two empirical correlations were developed for the determination of the *Nusselt number*:

$$Nu_L = 0.766 \cdot [Ra \cdot f_2(Pr)]^{1/5} \quad \text{if: } Ra \cdot f_2(Pr) \leq 7 \cdot 10^4 \quad (2.79)$$

$$Nu_L = 0.15 \cdot [Ra \cdot f_2(Pr)]^{1/3} \quad \text{if: } Ra \cdot f_2(Pr) > 7 \cdot 10^4$$

The value of the additional function $f_2(Pr)$ is computed by:

$$f_2(Pr) = (1 + 0.536 \cdot Pr^{-11/20})^{-20/11} \quad (2.80)$$

These equations are only valid, if the boundary layer is not disturbed by the other effects. Apart from that the relevant area must be a part of an infinite plane (von Böckh, Wetzel 2014). The characteristic length L is $L = a \cdot b \cdot (a + b)/2$ for a rectangle with a and b as the side lengths or $L = d/4$ for circular plates with the diameter d .

Horizontal cylinder

The flow through a horizontal cylinder as well as around a cylinder with the flow direction normal to the cylinder axis is very important for technical applications, such as pipe heat exchangers. For the application studied in this work this case is not relevant, however, it is described here briefly in order to give a full overview of the empirical correlations.

For the horizontal cylinder the following correlation can be used (von Böckh, Wetzel 2014):

$$Nu_L = \left[0.752 + 0.377 \cdot Ra_L^{1/6} \cdot f_3(Pr) \right]^2 \quad (2.81)$$

$$f_3(Pr) = (1 + 0.721 \cdot Pr^{-9/16})^{-7/27}$$

The characteristic length in this case it computed by:

$$L = \pi \cdot \frac{d}{2} \quad (2.82)$$

2.3.2. Thermal conduction

Fourier law defines the stationary thermal conduction:

$$\dot{q} = -\lambda \cdot \nabla \vartheta = -\lambda \cdot \frac{d\vartheta}{dr} \quad (2.83)$$

with the materials thermal conductivity λ and the temperature gradient $\nabla \vartheta$ which is defined as the derivation of the temperature with respect to the location (von Böckh, Wetzel 2014). With the equation (2.84) the entire heat flow can be computed as:

$$\dot{Q} = \int_A \dot{q}_n \cdot dA \quad \text{with } \dot{q}_n = -\lambda \cdot \frac{d\vartheta}{dn} \quad (2.84)$$

where \dot{q}_n is the heat flux density normal to the heat exchange area and n is the normal position vector (von Böckh, Wetzel 2014). The multiplicative inverse of the thermal conductivity is the thermal resistance. Depending on the geometry of the area A , the determination of the heat flow can be complex.

The simplest case of the thermal conduction is the heat transfer through a plane wall. In a two-dimensional case, a temperature difference between the both sides of the wall is necessary for thermal conductivity to occur. Simplified sketches of plane walls in Cartesian and cylindrical coordinates are given in Figure 13.

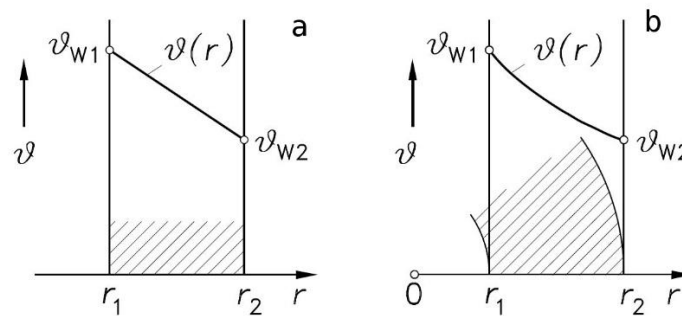


Figure 13: Thermal conductivity through plane walls in Cartesian (a) and cylindrical (b) coordinate systems

(Baehr, Stephan 2008)

According to the Fourier law, the temperature curve must be linear, the non-linear curve is caused by the cylindrical wall. In both cases the constant surface temperatures of the wall are given with the condition $\vartheta_{W1} > \vartheta_{W2}$ (Baehr, Stephan 2008). For many homogeneous materials, the thermal conductivity coefficients are known, hence the thermal conductivity can be computed easily. In fact, the thermal conductivity is not a constant, but depends on the temperature. Often a mean thermal conductivity is computed as the arithmetical average of the maximum and the minimum value. Finite element methods provide a much more precise solution, because here the local thermal conductivity

value is taken into account. For most technical applications a constant wall temperature cannot be assumed, therefore the thermal conduction have to be combined with the convection, in order to describe the overall heat transition (Baehr, Stephan 2008). For multilayer walls, the overall thermal conductivity is computed as the sum of the thermal resistances.

2.3.3. Thermal radiation

The influence of thermal radiation is of minor interest for this work, as it neither was measured or modelled. Hence, this phenomenon will be described very briefly here.

Physically thermal radiation is the emission of electromagnetic waves. In contrast to thermal conduction, thermal radiation does not require a heat transfer material, it can also occur in vacuum. The length of the electromagnetic waves varies between 0.7 and 400 μm , which is part of the ultra-red spectrum. Thermal radiation can be emitted from any solid or fluid body emits radiation if it's temperature is over the absolute zero.(von Böckh, Wetzel 2014).

2.3.4. Heat transition

In order to characterise the quality of the heat transfer process in a technical apparatus, such as a heat exchanger, the overall heat transfer coefficient k is used. It is used as a benchmark value with several reference values available in the literature, like in (VDI 2006).

The quality of the heat transition is based on at least two heat transfer types: the convection and the thermal conduction. For some applications radiation also might be important, but usually it can be neglected. For applications relevant for this work, the radiation can be neglected because the expected temperatures are moderate and the exterior walls of the frame are relatively thick, s. 3.4.3.

The heat transition can be explained with the example of a wall, which separates two fluids, as shown in Figure 14:

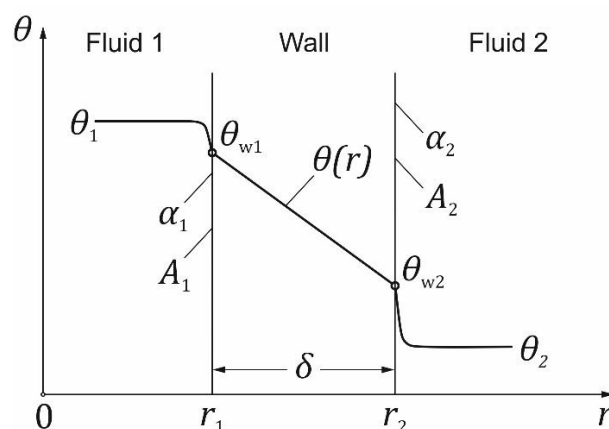


Figure 14: Example of heat transition through a wall. Source: (Baehr, Stephan 2008), modified

The wall with the thickness δ and the thermal conductivity λ separates Fluid 1 from Fluid 2. In this case, the temperature of the first fluid is higher than of the second one. Hence, the heat flux direction is from Fluid 1 towards Fluid 2. The entire heat flux can be computed with

$$\dot{Q} = k \cdot A_m \cdot (\vartheta_1 - \vartheta_2) \quad (2.85)$$

where k is the overall heat transfer coefficient and A_m the mean heat transfer surface area (Baehr, Stephan 2008). In case of a rectangular plate A_m is equivalent to the surface areas: $A_m = A_1 = A_2$. For pipes or other curved designs the surfaces areas are different due to different diameters and the mean area must be computed with as follows (Baehr, Stephan 2008):

$$A_m = \frac{A_2 - A_1}{\ln \frac{A_2}{A_1}} \quad (2.86)$$

Based on equation (2.85) the overall heat transfer coefficient is:

$$\frac{1}{k \cdot A} = \frac{1}{\alpha_1 \cdot A_1} + \frac{\delta}{\lambda_m \cdot A_m} + \frac{1}{\alpha_2 \cdot A_2} \quad (2.87)$$

The left side of the equation can also be defined as the thermal resistance R_{th} of the wall for specific fluids and temperatures with:

$$R_{th} = \frac{1}{k \cdot A} = \frac{1}{\alpha_1 \cdot A_1} + \frac{\delta}{\lambda_m \cdot A_m} + \frac{1}{\alpha_2 \cdot A_2} \quad (2.88)$$

For the convective coefficients, α_i , the equation (2.73) can be used with the corresponding correlation for the *Nusselt number*. With the equations (2.89) and (2.90) the wall temperatures can be computed:

$$\vartheta_{w1} = \vartheta_1 - \frac{k \cdot A_m}{\alpha_1 \cdot A_1} (\vartheta_1 - \vartheta_2) = \vartheta_1 - \frac{\dot{Q}}{\alpha_1 \cdot A_1} \quad (2.89)$$

$$\vartheta_{w2} = \vartheta_2 - \frac{k \cdot A_m}{\alpha_2 \cdot A_2} (\vartheta_1 - \vartheta_2) = \vartheta_2 - \frac{\dot{Q}}{\alpha_2 \cdot A_2} \quad (2.90)$$

In case of multilayer walls the thermal resistances of the wall layers must be added (Baehr, Stephan 2008):

$$R_{th_{\text{multilayer}}} = \frac{1}{k \cdot A} = \frac{1}{\alpha_1 \cdot A_1} + \sum_i \frac{\delta_i}{\lambda_{m,i} \cdot A_{m,i}} + \frac{1}{\alpha_2 \cdot A_2} \quad (2.91)$$

2.3.5. Phase transition (Condensation)

This chapter is focused on the condensation process, as it is the relevant phase transition type in this work. The physical relations for the condensation and the evaporation are similar and can be applied for both phenomena by changing some parameters.

When vapour is in contact with a wall with a temperature below the saturation temperature of the vapour, condensation occurs, which means the conversion of gas into liquid. The generated condensate is subcooled; this means that the more vapour can be condensed as the temperature of the condensation is still lower than the saturation condition. Therefore, every condensation process not only consists of heat transfer but also of mass transfer. (Baehr, Stephan 2008). Three types of condensation exist. For stationary systems droplet and film condensations are typical, while for flows a special stream condensation occurs (Herwig, Moschallski 2014).

2.3.5.1. Film condensation

The film condensation is a very common case. Condensation droplets form a film on the surface, which in case of a horizontal plane is constantly growing until the end of the condensation process. For inclined and vertical planes the film thickness remains constant at a certain position as the condensate flows downwards due to gravitation force (Herwig, Moschallski 2014). This case is shown in Figure 15.

The film starts at the edge of the wall with the width, D , at the position $x = 0$. The wall temperature T_W must be lower than the saturation temperature, T_S . For a discrete element $B \cdot dx$ the amount of the released phase transition energy flux is $\Delta h_V d\dot{m}$. This energy flux is transferred through the liquid film towards the wall by thermal conduction.

The film itself wets the wall due to adhesion conditions, which are material dependent. It is also assumed, that no shear stress occurs at the condensation boundary. With a constant temperature difference $\Delta T = T_S - T_W$, the specific heat flux density is

$$\dot{q}(x) = -\lambda_f \frac{dT}{dy} = -\lambda_f \frac{T_W - T_S}{\delta(x)} \quad (2.92)$$

with the thermal conductivity of the liquid phase λ_f and the film thickness δ with respect to the position x . With the assumption of the constant temperature difference $\dot{q}(x)$ decreases with the increasing film thickness.

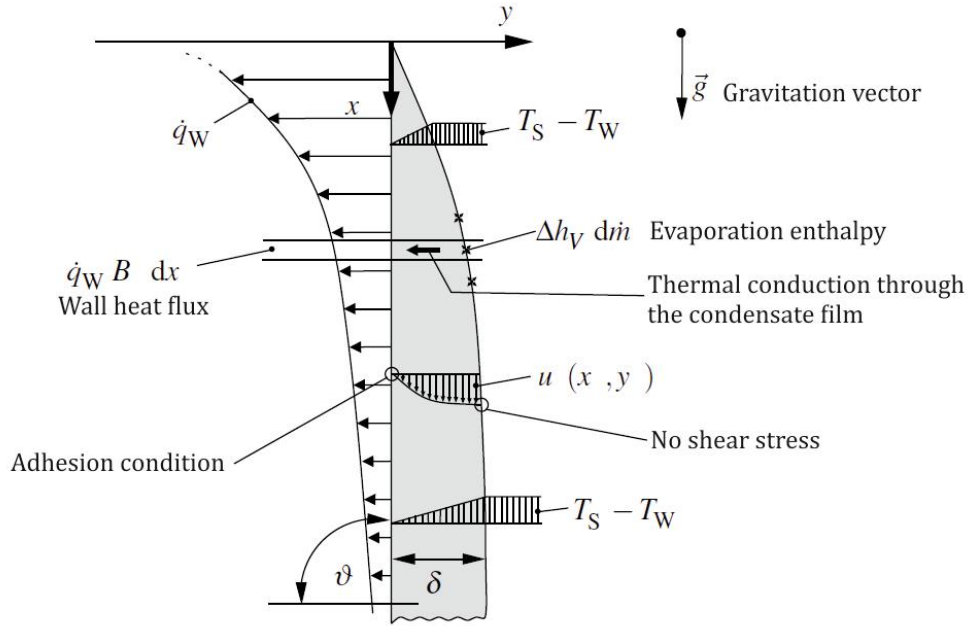


Figure 15: Film condensation at a vertical plane, source: (Herwig, Moschallski 2014), modified

According to the *Water skin theory* by Nusselt, the local *Nusselt number* $Nu(x)$ is defined for a vertical wall as

$$Nu(x) \equiv \frac{\dot{q}_w \cdot x}{\lambda_1 (T_s - T_w)} = 0.707 \left[\frac{\rho_l (\rho_l - \rho_g) g \cdot \Delta h_v \cdot x^3}{\eta_l \cdot \lambda_1 (T_s - T_w)} \right]^{1/4} \quad (2.93)$$

with the liquid and the gaseous densities ρ_l and ρ_g and the dynamic viscosity of the liquid phase η_l .

The average *Nusselt number* Nu_m can be then computed by:

$$Nu_m \equiv \frac{\dot{q}_{wm} \cdot L}{\lambda_1 (T_s - T_w)} = \frac{4}{3} Nu(L) \quad (2.94)$$

with the wall length L (Herwig, Moschallski 2014).

For more accuracy of the results, the equation (2.93) can be expanded by several additional equations, containing information on the waviness of the film surface or the temperature dependency of the fluid properties (Herwig, Moschallski 2014). The latter is discussed in detail here.

For the *Water skin theory* the following momentum equation with constant density is used

$$\eta_l \frac{\partial^2 w}{\partial y^2} = -(\rho_l - \rho_g) g \quad (2.95)$$

where w is the velocity in the vertical y -direction. For temperature dependent properties equation (2.96) can be used (Baehr, Stephan 2008):

$$\frac{\partial}{\partial y} \left[\eta_l(T) \frac{\partial w}{\partial y} \right] = -(\rho_l(T) - \rho_g)g \quad (2.96)$$

Here the gas density is still assumed to be constant. This also can be changed, but it only will significantly influence the result for very long pipes with major temperature differences with the length. This yields in the equation for the condensation heat transfer coefficient α (Baehr, Stephan 2008):

$$\frac{\alpha}{\alpha_{Nu,m}} = \left\{ \frac{1 - \eta^*}{10(1 + \lambda^*)^3} \left[5 + \lambda^*(14 - 11 \cdot \lambda^*) + \frac{\lambda^*}{\eta^*} (1 + 4 \cdot \lambda^* + 5 \cdot \lambda^{*2}) \right] \right\}^{1/4} \quad (2.97)$$

This empirical equation corresponds with equations (2.66) and (2.67). The thermal conductivity quotient λ^* and the dynamic viscosity quotient η^* are defined as:

$$\eta^* = \frac{\eta_s}{\eta_0} \quad \lambda^* = \frac{\lambda_s}{\lambda_0} \quad (2.98)$$

where the index 's' denotes the saturation temperature and the index '0' the wall temperature. For minor subcooling, e.g. $T_s - T_w < 50$ K the influence of the temperature dependency is low, about 5%, but for higher subcooling it can increase up to over 40% (Baehr, Stephan 2008).

2.3.5.1. Droplet condensation

For the droplet condensation, no wetting film occurs on the wall surface. Single drops can merge to larger drops, which due to gravity or flow are transported off their appearance position, before being able to form a closed film. The occurrence of single drops depends on the force balance, as shown in Figure 16.

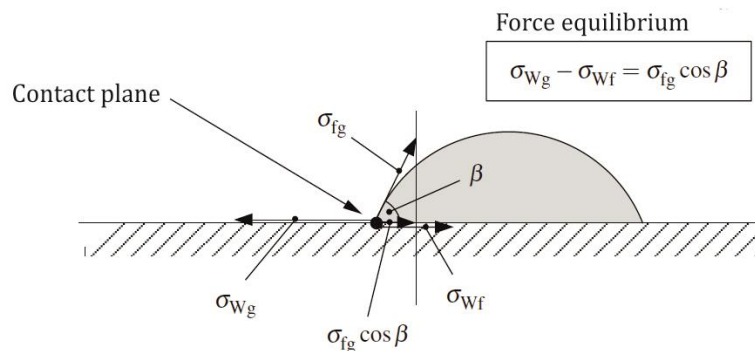


Figure 16: Force equilibrium for a single droplet, source: (Herwig, Moschallski 2014), modified

Apart from the tensions the contact angle β , which depends on the material properties of the wall and the fluid. The relevant tensions are:

σ_{Wg} : Interface tension between the wall and the gas phase

σ_{Wf} : Interface tension between the wall and the liquid phase

σ_{fg} : Interface tension between the liquid and the gaseous phase

The wetting tension σ_{wet} can be computed as:

$$\sigma_{wet} = \sigma_{Wg} - \sigma_{Wf} \quad (2.99)$$

For a stable droplet generation on the surface the tension condition must be fulfilled (Herwig, Moschalski 2014):

$$\sigma_{wet} = \sigma_{Wg} - \sigma_{Wf} < \sigma_{fg} \quad (2.100)$$

2.3.5.1. Stream condensation

For inclined planes with laminar flows, the condensation process can be described in the same way as for the film condensation. The main difference here lies in the lower film thickness. For turbulent flows, an extended approach must be used (Herwig, Moschalski 2014).

For a pipe flow, the *Nusselt number* Nu is given by this empirical equation:

$$Nu = 0.023 \cdot Re^{0.7} \cdot Pr^{0.4} \left\{ (1 - x^*)^{0.7} + \frac{3.7((1 - x^*)^{0.04}) \cdot x^{*0.76}}{p^{+0.37}} \right\} \quad (2.101)$$

with the additional equations:

$$\alpha = \frac{Nu \cdot \lambda_L}{d}, \quad Re = \frac{w_m \cdot d}{\nu_L}, \quad w_m = \frac{\dot{m}}{\rho_L \frac{\pi \cdot d^2}{4}}, \quad Pr = \frac{\nu_L}{a_L}, \quad p^+ = \frac{p}{p_c}, \quad x^* = \frac{\dot{m}_g}{\dot{m}}$$

where α is the heat transfer coefficient, λ_L the thermal conductivity of the liquid phase, d the inner pipe diameter, ν_L the kinematic viscosity of the liquid phase, \dot{m} the overall mass flux, ρ_L the density of the liquid phase, a_L the thermal diffusivity of the liquid phase, p the system pressure, p_c the critical pressure of the fluid and \dot{m}_g the gas mass flux.

The overall heat flux is then:

$$\dot{Q} = k_m \cdot A \cdot \Delta T_m \quad (2.102)$$

with the mean overall heat transfer coefficient k_m

$$\frac{1}{k_m} = \frac{1}{\alpha_{m,cond}} + \frac{\delta \cdot d}{\lambda \cdot d_m} + \frac{1}{\alpha_{m,cool}} \frac{d}{d_o} \quad (2.103)$$

Here $\alpha_{m,cond}$ and $\alpha_{m,cool}$ are the heat transfer coefficients for the condensation and the cooling side respectively, d is the inner diameter, d_m the mean diameter, d_o the outer diameter and δ the pipe wall thickness.

For the mean temperature the equation (2.104) can be used:

$$\Delta T_m = \frac{T_{out} - T_{in}}{\ln \left[\frac{T_g - T_{in}}{T_g - T_{out}} \right]} \quad (2.104)$$

with the inlet and outlet temperatures of the cooling fluid T_{in} and T_{out} and the mean gas temperature T_g .

2.4. HEAT EXCHANGERS

Several classifications of heat exchangers exist: the contact type with the fluid, additional heat conservation and the flow arrangement. For this work, plate heat exchangers with cross-flow configuration are relevant. However, for the sake of completeness, all types are described here briefly. For the most commonly used types design correlations are available and are also presented here.

2.4.1. Basic heat exchanger classification

Considering the contact with the medium two general types of heat exchangers can be named. The *direct* heat exchangers enable a direct contact of the two or more fluids, so the heat transport is combined with the mass transport. In *indirect* heat exchangers, the fluids are separated by a wall in a way that excludes any mass transport. In most cases, the heat flux is continuous and instant; these devices are *recuperators*. For some applications with interim heat conservation the heat is first transferred to a solid medium, which conserves it for some time. After a specific time period, the heat can be transferred again from the solid to the second fluid. Such devices are called *regenerators*. The differentiation with respect to the flow arrangement is not necessarily a design property, as many heat exchangers can operate with several flow arrangements. Three general cases exist (Herwig, Moschallski 2014):

- Parallel flow
- Counter-current flow
- Cross-flow

The flow configuration has a major influence on the efficiency of the heat exchanger and on the temperature distribution in the apparatus. For parallel and counter-current flows, the temperature curves are shown in Figure 17.

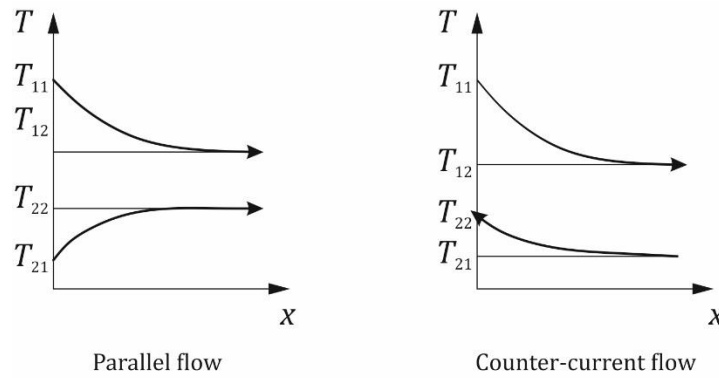


Figure 17: Temperature curves for different flow configurations

As can be seen for the parallel flow, the temperature curves are converging and can theoretically achieve the same temperature. For technical applications however, a temperature difference in the entire apparatus is desirable. This can be explained with the equation (2.102). For a very low local ΔT_m the local heat flux is also very low, hence, the effectiveness of the entire apparatus decreases. For the counter-current flow, the behaviour is different. Here the outlet temperatures T_{12} and T_{22} for the hot and the cold flow respectively cannot converge. The main advantage of this configuration is a temperature gradient, which is high enough over the entire length of the apparatus. This increases the effectiveness, thus, in many applications it is the best choice.

The third configuration, the cross-flow is also very popular. Many plate heat exchangers are operating in this mode. Here one must map the entire temperature fields to describe the temperature distribution in the apparatus. An exemplary temperature field is shown in Figure 18.

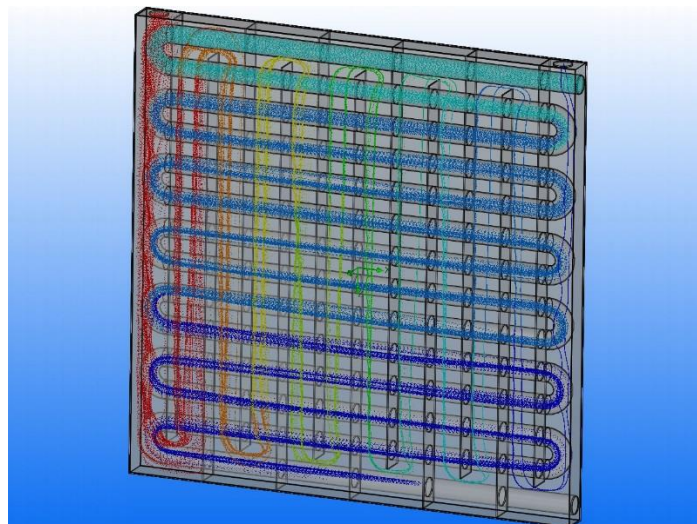


Figure 18: Temperature distribution in a cross-flow labyrinth heat exchange, source: (StrykerTECH LLC)

While the temperature of the hot flow decreases from left to the right, the cooling flow temperature increases upwards. An analytical description of such temperature fields is difficult and requires special numerical methods.

The mean temperatures for the first configuration can be easily computed with the following equation (VDI 2006):

$$\Delta T_m = \frac{\Delta T_1 - \Delta T_2}{\ln \frac{\Delta T_1}{\Delta T_2}} \quad (2.105)$$

The definitions for the temperature gradients ΔT_1 and ΔT_2 vary depending to the flow arrangement. According to Figure 17 they are:

$$\Delta T_1 = T_{11} - T_{21}, \quad \Delta T_2 = T_{12} - T_{22} \quad \text{for the parallel flow} \quad (2.106)$$

$$\Delta T_1 = T_{11} - T_{22}, \quad \Delta T_2 = T_{12} - T_{21} \quad \text{for the counter-current flow} \quad (2.107)$$

Another important classification of heat exchangers considers the design of the flow channels. In most cases, these are tubes (tubed heat exchangers) or rectangular channels (plate heat exchangers).

2.4.2. Plate heat exchangers

The plate heat exchangers are also often called compact heat exchangers, because of the large amount of flow channels per volume unit. This leads to a very high heat flux density and hence high effectivity of the apparatus (VDI 2006).

A typical plate heat exchanger is shown in Figure 19. The inner plates separate the fluids from each other and provide the heat transfer. Due to normally high flow velocities, the entire plate surface is covered with the fluid on both sides, the waved surface enhances the turbulence and hence the heat transfer. The heat exchanger shown in Figure 19 operates in the counter-current mode, but some similar heat exchangers also operate in the cross-flow configuration, which depending on the geometry of the plates is close to the counter-current low. As can be seen, the height of the plate is much larger than its width. Therefore, even for cross-flow configuration the flow field for the plate is similar to the flow field with counter-current flow. For quadratic plates, this changes and significant differences in the performance may occur.

In many cases, the plate heat exchangers are bolted and modular, so they can be expanded according to the application demands. Cleaning and replacing of the damaged plates is possible as well (VDI 2006).

Welded heat exchangers are also widely used. The main advantage of this design type is the absence of sealing problems. Thus, higher operating pressure and temperatures are possible. On the other hand, cleaning is much more difficult as the plates cannot be unmounted (VDI 2006).

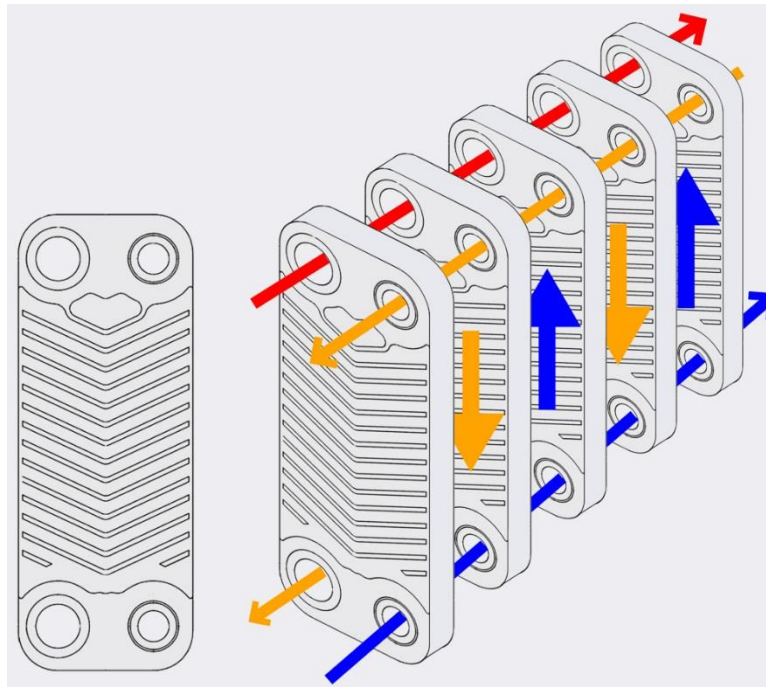


Figure 19: A simplified sketch of a plate heat exchanger, source: (WilTec Wildanger Technik GmbH 2015)

2.4.1. Polymer heat exchangers

While metals are still the most commonly used materials for heat exchangers, polymer heat exchangers (PFE) are being developed for more and more applications. Despite their excellent thermal properties, metals have several operating limitations, such as handling with highly corrosive fluids. In the chemical industry heat exchangers made of glass, ceramics or graphite are used to avoid corrosion induced apparatus damages. Apart from very good chemical properties, polymers offer several other advantages, such as low specific weight or less susceptibility to fouling (Christmann et al. 2012). Some specific production processes even exclude the usage of metallic devices, due to purity demands on the product.

2.4.1.1. Design and materials for polymer heat exchangers

The most common design types of polymer heat exchangers are:

- Plate heat exchangers
- Heat exchangers coils
- Shell and tubed heat exchangers

All three types are state of the art and in serial production. Several companies like (Calorplast GmbH), (Menerga GmbH) or (CPS Chemical Process Solutions Ltd.) are mass-producing heat exchangers made of polymers for air-conditioning applications, process and chemical engineering applications.

Several polymers have already been used as construction material for PFEs. For low temperatures up to 70°C polyethylene (PE) can be used, if the fluids contain no organic solvents or acids. PE is very cheap and has a very good availability. For moderate temperatures up to 130°C polypropylene (PP), polycarbonate (PC) or polyphenylene sulphide (PPS) are suitable. The last one also offers a very good chemical resistance in acidic conditions. For high temperatures, the fluorine containing polymers, such as polyvinylidene fluoride (PVDF) or polytetrafluoroethylene (PTFE) are used. The latter is considered to provide best chemical resistance and thermal stability, as only molten alkali metals and fluorine can attack its structure. On the other hand, PTFE has low mechanical strength, which often is enhanced by filaments like glass fibres (T'Joel et al. 2009).

The thermal conductivity of polymers is very low, compared to metals. It also can be improved by filaments like graphite. In the publication by (Derieth et al. 2008) highly filled polymers were presented, whose thermal conductivity could be increased from 0.15 – 0.5 W/m K up to 5 W/m K. Such high-tech materials enable a significant reduction of the apparatus size, due to the much more effective heat transfer performance.

2.4.1.2. Polymer film heat exchangers

Another way to reduce the influence of the low thermal conductivity of the polymers is the usage of very thin polymer films. According to the equation (2.87) the overall heat transfer depends on the thickness of the material as well as on the thermal conductivity. Hence, the thermal resistance can be reduced by decreased thickness of the fluid separating wall.

One of the first published prototypes was presented in 1973 by (Perry et al.) as a “Heat exchange apparatus having thin film flexible sheets”. The preferred thicknesses of the used PVDF films were 0.002 and 0.006 inch (0.051 mm to 0.152 mm). The individual sheets are “bonded one to another” in order to create a structure similar to honeycombs. A slightly modified sketch of the “bonded” films is given in Figure 20. On the left-hand side of the figure, the sheets with the bonding lines are shown. The film sheets are connected along these lines and hence form flow channels for the both fluids.

During the last decades, several other prototypes and demonstrators have been developed and presented in publications and as patents. In 2005 Zaheed and Jachuck introduced a compact polymer film heat exchanger (CPFHE) with cross-corrugated polymer films made of poly ether ether ketone (PEEK) or PVDF (Zaheed, Jachuck 2005).

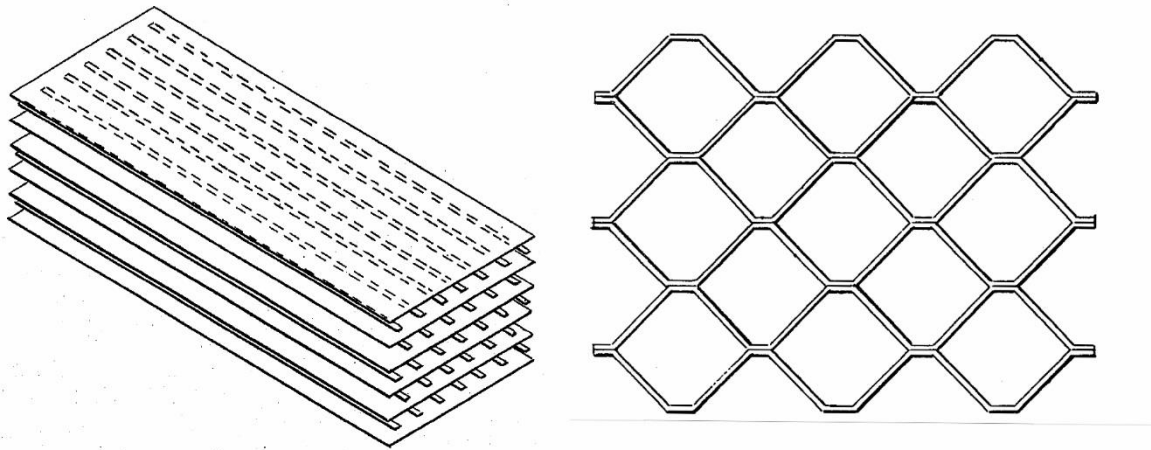


Figure 20: Bonded polymer film heat exchanger, source: (Perry et al.), modified

With a film thickness of 100 μm the apparatus was able to operate at 10 bar pressure and a temperature of 220°C. In Figure 21, the principle of the cross-corrugated polymer film heat exchanger is shown. The wave form of the heat transfer surfaces increases the effective heat transfer area on the one hand. Despite the low *Reynolds numbers*, which indicates that the flow is laminar, a good mixing could be achieved by the corrugations. On the other hand, the stiffness of the stacks could be enhanced. With the PVDF film, the overall heat transfer coefficients between 145 and 175 $\text{W}/\text{m}^2 \text{K}$ could be achieved with film thicknesses from 1 mm to 0.7 mm and cross-flow configuration. Similar heat exchangers with corrugated thin plates or films were also introduced in the 90s, but never made it to serial product.

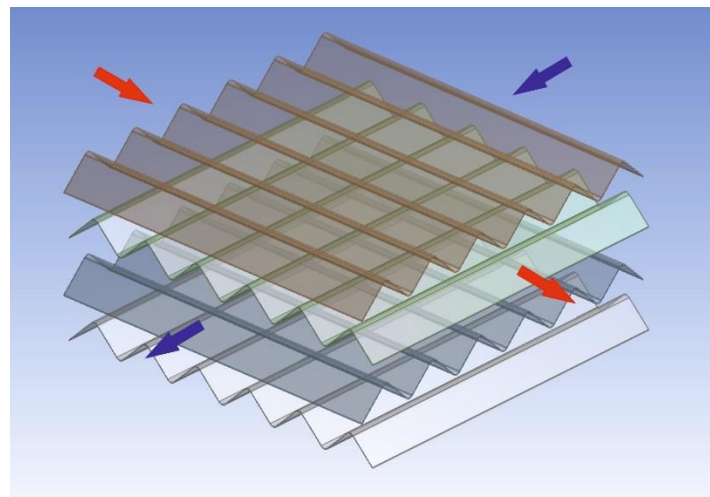


Figure 21: Cross-corrugated polymer films

Promising results could be achieved for seawater desalination applications. Here, only expensive stainless steels can be used, since the seawater is highly corrosive. Polymer films, such as PEEK withstand the operating conditions very well. Apart from that, competitive overall heat transfer coefficients could be achieved. For condensation of water over 1200 $\text{W}/\text{m}^2 \text{K}$ were determined (Christmann et al. 2012). For this apparatus films with a thickness of 25 μm were used, which were

stabilised by a grid made of stainless steel. Because of the low system pressure, the lattice spacing could be quite large (up to 50 mm). This additionally reduced weight, without affecting the mechanical stiffness. Another advantage of the flexible films is the possibility to remove scaling layers easily, by a light pressure pulse, because of the low adhesion of the films (Christmann et al. 2012).

Several prototypes have also been developed through the last decades for computer cooling, air-conditioning units or chemical industry. However, none of the patents has ever made it to a serial product. Unfortunately, no reasons for this could be found in the literature. It is possible, that polymer film heat exchangers seem not to be reliable due to the very low thickness of the films and hence a high sensitivity to external damages. For some applications, the limited operating temperature range is also an obstacle. In discussions with representatives of the chemical industry, a basic mistrust towards polymers for chemical applications or polymers as structural material was obvious. Some of the challenges linked to polymer films heat exchangers are also discussed later in this work in.

2.4.2. Models for heat exchanger design and calculation

Several methods for heat exchanger design are available. On the one hand the most accurate method is the numerical simulation with finite elements, which on the other hand is also the most extensive and complex. Due to these disadvantages, this method is rarely being applied. The cell method is much faster, easier to understand and provides a sufficient accuracy for most applications (VDI 2006).

2.4.2.1. Cell method

This section is based on the VDI Wärmeatlas (VDI 2006), Chapter C. All equations and figures were taken from this source, unless dated otherwise.

The principle of the cell method is the separation of the heat transfer surface into zones, for which the heat transfer can be computed by simple correlations. Hence, the entire apparatus can be considered as a serial or parallel connection of multiple simple heat exchangers. The outlet temperatures of the first cell are automatically the inlet temperatures of the second one. This is shown in Figure 22.

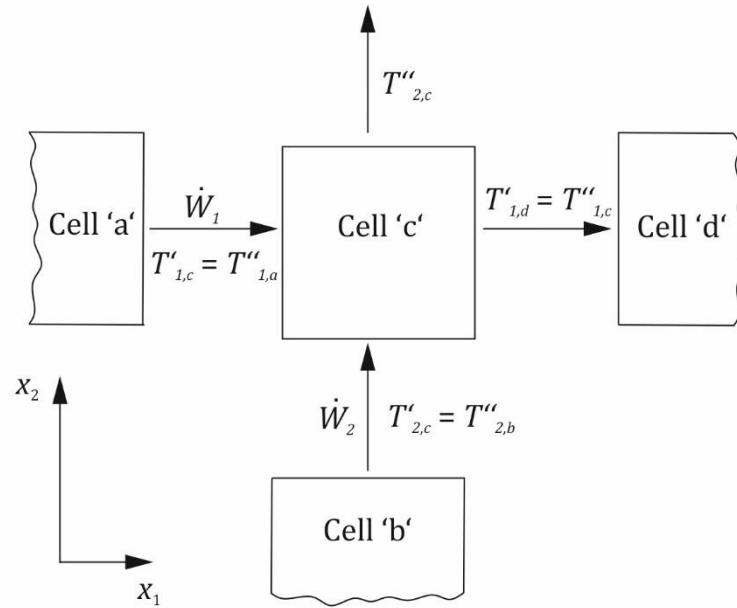


Figure 22: Cell method principle, source (VDI 2006), modified

In a two-dimensional coordinate system with the coordinates x_1 and x_2 the numbers in the indexes denote the direction of the heat capacity flux \dot{W} and the apostrophes the inlet and the outlet with one apostrophe or two respectively. The heat capacity flux is to be computed according to (2.108):

$$\dot{Q} = k \cdot A \cdot \Delta T_m = \dot{W}_1(T'_1 - T''_1) = \dot{W}_2(T''_2 - T'_2) \quad (2.108)$$

All equal cells have the same number of transfer units (NTU), which is defined as:

$$NTU_1 = \frac{k \cdot A}{\dot{W}_1}; 0 \leq NTU \leq \infty \quad (2.109)$$

With the overall heat transfer coefficient k and the heat transfer area A . The index denotes here the number of the fluid, which in most cases is either one or two. For the generalisation of the method several dimensionless quantities are used:

$$\text{Mean temperature gradient} \quad \theta = \frac{\Delta T_m}{T'_1 - T'_2}; 0 \leq \theta \leq 1 \quad (2.110)$$

$$\text{Mass flux temperature gradients} \quad P_1 = \frac{T'_1 - T''_1}{T'_1 - T'_2}; 0 \leq P_1 \leq 1 \quad (2.111)$$

$$P_2 = \frac{T''_2 - T'_2}{T'_1 - T'_2}; 0 \leq P_2 \leq 1$$

$$\text{Heat capacity flux quotients} \quad R_1 = \frac{\dot{W}_1}{\dot{W}_2}; R_2 = \frac{\dot{W}_2}{\dot{W}_1} = \frac{1}{R_1}; 0 \leq R_1 \leq \infty \quad (2.112)$$

These dimensionless quantities are linked to each other as follows:

$$\frac{P_1}{P_2} = \frac{NTU_1}{NTU_2} = \frac{1}{R_1} = R_2 \quad (2.113)$$

$$\theta = \frac{P_1}{NTU_1} = \frac{P_2}{NTU_2} \quad (2.114)$$

For n cells of the entire apparatus the overall number of transfer units $NTU_{i,ges}$ is:

$$NTU_i = \frac{NTU_{i,ges}}{n(z+1)}, i = 1, 2 \quad (2.115)$$

with the number of transverse baffles z .

The equilibrium equations for each cell are then:

$$(1 - P_1)T''_{1,a} - T''_{1,c} + P_1 = 0 \quad (2.116)$$

$$P_1 \cdot T''_{1,a} - T''_{1,c} + (1 - P_2)T''_{1,b} = 0 \quad (2.117)$$

The cell method should be applied in cases, when no analytical or empirical equations for the specific the geometry of the heat exchanger exist.

2.4.2.2. Short-cut correlations for standardised heat exchangers

For standard apparatus types, such as shell-and-tube heat exchangers, field-tube or plate heat exchangers several correlations are available. As this work focuses on plate heat exchangers, only the equations for this type, found in (VDI 2006) are presented here. Equations for other types, such as tubed heat exchangers, can be obtained from the same source.

These correlations are based on the mean temperature difference and therefore, a correction factor must be applied to consider the different flow configurations, such as cross flow or parallel flow. This factor F is defined as follows:

$$F = \frac{1}{(1 + a \cdot R_1^{db} \cdot NTU_1^b)^c} \quad (2.118)$$

with the relevant flow, dependent parameters a , b , c and $d = 0.5$. For plate heat exchangers, relevant for this work the parameter values are given in Table 4.

With the correction factor F the dimensionless temperature gradient P_1 can be computed as:

$$P_1 = \frac{1 - \exp[(R_1 - 1) \cdot NTU_1 \cdot F]}{1 - R_1 \cdot \exp[(R_1 - 1) \cdot NTU_1 \cdot F]}, \text{ if } R_1 \neq 1 \quad (2.119)$$

or

$$P_1 = \frac{NTU_1 \cdot F}{1 + NTU_1 \cdot F}, \text{ if } R_1 = 1 \quad (2.120)$$

Table 4: Parameter set for the corrections factor F defined in (2.118)

Flow configuration	a	b	c	d
Pure parallel flow, symmetrical	0.671	2.11	0.534	0.5
Pure cross flow, symmetrical	0.433	1,60	0.267	0.5
Plate heat exchanger, one pass for Fluid 1, two pass for Fluid 2	0.272	1.76	0.529	0.322
Plate heat exchanger, one pass for Fluid 1, three pass for Fluid 2 two of which in counter flow	0.211	1.75	0.572	0.292
Plate heat exchanger, one pass for Fluid 1, four pass for Fluid 2	0.244	1.90	0.577	0.323
Plate heat exchanger, one pass for Fluid 1, four pass for Fluid 2 two of which in counter flow	0.0747	1.77	0.525	0.317

Further correlations available in (VDI 2006) for plate heat exchangers are only valid for plate numbers over 40, since for smaller plate numbers boundary effects must be taken into account. Furthermore, these correlations require at least one double pass for one of the fluids. Hence, these equations are not applicable for the heat exchanger discussed in this work and therefore are not given here.

At the end of this chapter it must be said, that the presented correlations can only describe the heat transfer without any phase transitions, such as condensation or boiling. If used for phase transitions, they only provide very inaccurate results. For better accuracy numerical methods must be used (VDI 2006).

3. METHODS

3.1. EXPERIMENTAL STUDIES

3.1.1. Polymers

The polymers used during the research work presented here are briefly introduced in this chapter with the focus on chemical formula, manufacturing and the general usage. The thermal and mechanical properties of the materials as well as the chemical resistance are the most relevant aspects for this work. Hence a comparison of the relevant properties is therefore presented in a separate section.

Although only the polytetrafluoroethylene (PTFE) - glass fibre compound and the polyimide (PI) film were used for extensive studies, all four polymers, which were considered, are presented here. The polyethylene terephthalate (PET) and the polyether ether ketone (PEEK) films were excluded from further testing after they failed during the preliminary investigations.

3.1.1.1. Polyethylene terephthalate

The polyethylene terephthalate (PET) is a widely used thermoplastic polymer material for numerous applications such as the food, packing, chemical and other industries. It is a saturated, mostly crystallised polyester resin, which is gained by the condensation of ethylene glycol and terephthalic acid (Gooch 2007). The structural formula is shown in

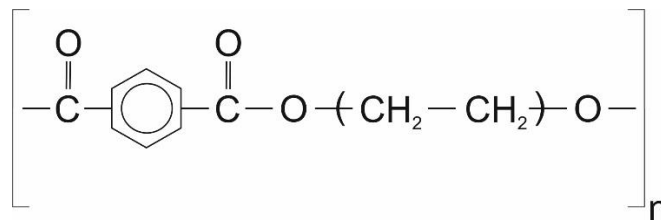


Figure 23: Structural formula of polyethylene terephthalate monomer (Gooch 2007)

PET is either transparent or white. The mean glass transition temperature is 75°C. Below it, the material has a high stiffness with a shear modulus of over 1000 N/mm²; above this temperature the stiffness decreases significantly. Therefore, PET is often enforced by glass fibres. As for most polymers, the thermal conductivity is low with 0.25 to 0.29 W/m K depending on the inner structure. Because of that, PET is also commonly used as electric insulator material. The water absorption is low, only 0.6 mass percent after 6 months of storing in water at 20°C. For higher temperatures, it barely increases while for PET with glass fibre filaments these values are lower. It also shows a good resistance to UV radiation (Elsner et al. 2012).

The four most important application for PET are: fibres for the textile industry, beverage bottles, films for the packaging and insulation and technical compounds. It can be manufactured with an amorphous

structure as well as partially crystallised. In 2010, about 40 million tons of PET were manufactured, from which about 65% as fibres and about 29% as films. It is also one of the cheaper polymeric materials (Elsner et al. 2012). For this work a Mylar® A films manufactured by DuPont (DuPont Teijin Films) with thicknesses between 50 and 150 µm were used.

3.1.1.2. Polyimide

Polyimides (PI) such as Kapton® HN by DuPont used in for this work, are high-performance polymers with excellent chemical resistance and thermal properties. It is also one the most expensive polymer materials and hence, is only used for specific applications, like high temperature electric insulation (DuPont Teijin Films 2013).

Polyimides are formed either by the condensation or by polyaddition of an organic anhydride or dianhydride with a diamine. A basic monomer is shown in Figure 24

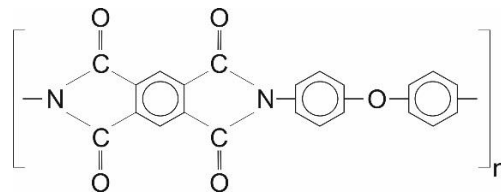


Figure 24: Structural formula of a polyimide monomer, source: (Gooch 2007)

Some polyimides can also contain aromatic rings or fluorine which widens the field of applications (Gooch 2007). It is available as thermosetting plastics or as thermoplastic resin. Polyimides are normally being glued for joining parts, welding is not possible (Elsner et al. 2012).

Kapton® films can be used for application temperatures between -269°C and +400°C. They barely burn, do not melt and have an excellent chemical resistance. They are also used for the insulation of spacesuits or spacecraft, as they show a very good resistance to UV radiation (Elsner et al. 2012).

3.1.1.3. Polytetrafluoroethylene

Polytetrafluoroethylene (PTFE) is better known as the trademark name Teflon® by DuPont. It is manufactured by the polymerisation of tetrafluoroethylene and offers the best chemical resistance of available polymers. According to (Bürckle GmbH 2011) only chlorine or fluorine containing chemicals can attack the surface of PTFE. However, sodium hydroxide appears to be able to dissolve fluorine atoms from the polymer chains. This is used to enable the usage of adhesives with PTFE (Reichelt Chemietechnik GmbH u. Co. 2015). The structural formula of the PTFE monomer is shown in Figure 25.

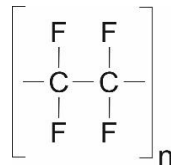


Figure 25: Structural formula of PTFE, source: (Gooch 2007)

Apart from its excellent chemical resistance, PTFE has some advantageous mechanical properties as well. Its friction coefficient is so low, that it is very often used for plain bearings or non-adhesive coatings (Gooch 2007). Furthermore, PTFE also has a wide operating temperature range from -270°C to 260°C . On the other hand its very low mechanical strength makes the usage as construction material impossible, for this PTFE is very often enforced with glass fibres (Elsner et al. 2012). Because of its chemical resistance, it is also often used for highly corrosive applications, like membranes for small seawater pumps or in chemical laboratories.

3.1.1.1. Polyether ether ketone

The polyether ether ketone (PEEK) is one of the most advanced high performance polymers. A very high glass transition temperature ($T_g = 143^{\circ}\text{C}$) allows using this polymer at temperatures above 200°C for pure material or even over 300°C in case of a glass fibre filled compound (Elsner et al. 2012).

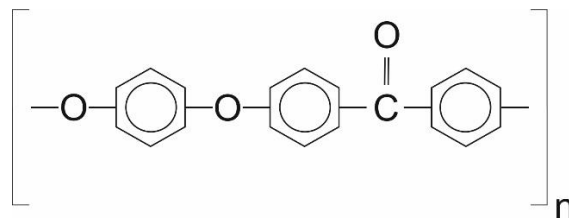


Figure 26: Structural formula of PEEK, source (Elsner et al. 2012), modified

PEEK has semi-crystalline structure with a maximum crystallinity of 45%. Apart from its outstanding thermal properties, PEEK also has a very good mechanical stability, which often is increased by glass or carbon fibres. The chemical resistance is good, too. Only concentrated sulfuric or nitric acids and some halogens containing hydrocarbons can damage PEEK. The high hydrolysis resistance enables the usage in hot water and hence this material is also applicable for heat exchangers (Elsner et al. 2005). Despite the high price, PEEK is widely used on industrial applications, especially for electric insulators, which must operate at high temperatures. It also can replace ceramics as insulation material. PEEK is available as extruded bars as well as films.

3.1.1.2. Poly(methylmethacrylate)

The poly(methylmethacrylate) (PMMA) is a transparent thermoplastic, which is often used as glass replacement. It has a good UV and weather resistance and an optical clarity of 92% (Gooch 2007). PMMA also has a good chemical resistance with non-polar solvents, weak acids or alkaline solutions. Apart from that, the mechanical strength and stiffness is very good, hence this polymer can be used as a construction material (Elsner et al. 2012). The structural formula is given in Figure 27. For this work, PMMA was used for frame and body of the lab-scale heat exchanger, due to its transparency and the sufficient chemical resistance. Because of the low ductility no thin films can be made from PMMA, hence this material was only used for the lab-scale heat exchanger.

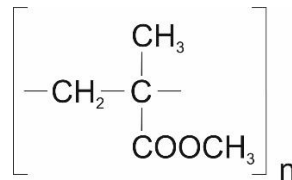


Figure 27: Structural formula of PMMA

3.1.1.3. General properties of used polymers

To select the proper materials for the heat exchanger design, a comparison of the polymer properties is inevitable. Therefore the relevant material properties are given in

Table 5. Because of a variety of materials within one polymer group, a range of values is given for each property. All values describe the material behaviour of unfilled polymers, if not mentioned otherwise.

As can be seen from

Table 5 the thermal properties such as the conductivity and the heat capacity are similar for the tested polymers. Major differences can be found in the maximum application temperatures but also in the tensile strength. Here the cheaper PET appears to be the weakest material with the lowest possible application temperatures. However, it still matches the requirements and its price makes it very interesting as a design material.

Other polymers like PEEK, PTFE and PI show a much higher thermal resistance. For PTFE even higher operating temperatures up to 300°C are possible, according to (Elsner et al. 2012). Apart from that PTFE keeps its excellent chemical resistance even at such high temperatures and practically no solvent, acid or alkaline solution can affect the material. On the other hand, PTFE has the lowest tensile strength starting at 10 MPa, which is the lowest value in this comparison. Therefore, despite its excellent thermal and chemical behaviour, the mechanical weakness must be taken into account.

Table 5: Main properties of the used polymers (Sources: (Goodfellow GmbH), (Elsner et al. 2012; DuPont Teijin Films))

Property / unit	PEEK	PET	PI	PTFE	PMMA
Density [kg/m ³]	1260 - 1320	1370 - 1400	1420	1380	1190
Glass transition [°C]	143	98	350 - 365	127	106
Max. long-term application temperature [°C]	250	100	250 - 320	180 - 260	76 - 108
Tensile strength [MPa]	70 – 100	20 - 40	70 - 110	10 - 40	20 - 80
Thermal conductivity [W/m K]	0.25	0.29	0.1 - 0.35	0.25	0.10 – 0.19
Heat capacity [J/kg]	1340	1200	1090	1000	1470-1500

The chemical resistance of the polymers requires a closer look. As explained in section 2.1.1.4, in most cases the chemical resistance is measured at maximum temperatures of 50°C. With higher temperatures, however the chemical properties can change. PTFE for example loses its resistance to fluorine containing solvents (Elsner et al. 2012).

In Table 6 an overview of the chemical resistance at 50°C for material-fluid pairs relevant for this work is given. For PET, even some contradictory data could be found, which might indicate either different testing procedures or also different types of the polymer within one group. From the table, it can be seen, that PEEK, PI and PTFE are suitable for the condensation of organic solvents, as they show a sufficient resistance to them. PET however can only be used for some solvents, like simple alkanes and toluene, but is not suitable for tetrahydrofuran. The contradiction in the hydrolysis resistance of PET must be cleared by testing, the results of which are given later. Based on own experiment results described later in this work, it can be said that some of this data appeared to be partially wrong.

Table 6: Chemical resistance data of selected polymers as provided from manufacturers or suppliers

Polymer	Water	Heptane	Hexane	Tetrahydrofuran	Toluene
PEEK	++ ^{1,2}	++ ^{1,2}	++ ^{1,2}	++ ^{1,2}	++ ^{1,2}
PET	- ^{1,5} / + ³	++ ^{1,6}	++ ^{1,6}	- ¹	++ ^{1,6}
PI	+ ⁹	++ ^{8,10}	++ ^{8,10}	++ ^{8,10}	++ ^{8,10}
PTFE	++ ^{2,3,7}	++ ^{2,3,7}	++ ^{2,3,7}	++ ^{2,3,7}	++ ^{2,3,7}

Sources: ¹ – Gehr GmbH, ² – Bürckert Fluid Control Systems, ³ – ThermoQuick Engineering, ⁴ – Hera AG Kunststofftechnik, ⁵ – Kern GmbH Technische Kunststoffteile, ⁶ – Licharz Technische Kunststoffe, ⁷ – ASV Stübbe GmbH & Co. KG, ⁸ – Krempel Group, ⁹ – Goodfellow GmbH, ¹⁰ – DuPont

3.1.2. Preselection of films

In cooperation with the industrial partners (Merck KGaA and Calorplast GmbH) a preselection of films was done for extensive testing. This was primarily based on the manufacturer data shown above but also on the experience of the project partners. Some short-term testing also was performed at the Merck facilities, which revealed some weaknesses of the PEEK film while in contact with tetrahydrofuran. During some preliminary short-term testing a tendency of cracking was observed, too. Therefore, PEEK was excluded from detailed study and hence three polymer film types were considered. Because of the non-present chemical resistance to the used organic solvents almost all other polymers had to be excluded too, especially because of tetrahydrofuran and toluene.

Hence, three films were selected. The first one was a PTFE-glass fibre compound manufactured by (Böhme Kunststofftechnik GmbH & Co. KG) with a thickness of 150 μ m. The second one was the polyimide film Kapton[®] HN by DuPont with a thickness of 75 μ m. As a cheap reference to the both premium products a simple PET film, the Mylar A with a thickness of 100 μ m was chosen. The different thicknesses of the film were mostly based on the mechanical strength of the material. Generally, a thin film is better for the heat transfer on the one hand. On the other the film still has to withstand a high-pressure load, and therefore a compromise between a sufficient expected mechanical strength and a lowest possible thickness was found for all three films. In Table 7 the basic data of the films is given. In case of the PTFE-glass fibre compound, no mechanical data could be obtained from the manufacturer.

Table 7: Properties of the selected polymer films

Property / unit		Mylar [®] A, 100 μ m	Kapton [®] HN, 75 μ m	PTFE-glass fibre 150 μ m
Tensile strength [MPa]	transversal	190	231	No data provided
	parallel	200		
Max. elongation [%]	transversal	150	82	No data provided
	parallel	120		
Max. temperature [°C]	-	130	400	200
Shrinkage at 150°C [%]	transversal	1.1	0.17	<1
	parallel	1		<1

3.2. ORGANIC SOLVENTS

Four types of organic solvents used for this work, are briefly presented here. The used solvents were toluene, hexane, heptane and tetrahydrofuran. All these solvents are commonly used in the chemical industry. Hexane and heptane represent the same solvents group and have very similar properties. Therefore, they are described in one section. All information on the solvents is taken from (GESTIS 2015).

Toluene

Toluene, also known as methyl benzene, represents the group of aromatic hydrocarbons. Its formula is given in Figure 28. It is widely used in the chemical industry and is one of the standard solvents. It is a highly inflammable liquid, which is lighter than water; its density is 0.87 g/cm^3 in the liquid state. Toluene is hazardous to health and aquatic environment. The boiling point is at 111°C .

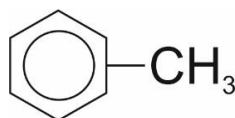


Figure 28: Chemical formula of toluene

n-Hexane / n-Heptane

The n-hexane and n-heptane are simple alkanes with six and seven C-atoms respectively. Like almost all solvents, they are highly inflammable with low ignition temperatures of approx. 220°C . The boiling points lies at 68°C and 98°C respectively. Both are hazardous to health and environment. The chemical formulas of hexane and heptane are given in Figure 29

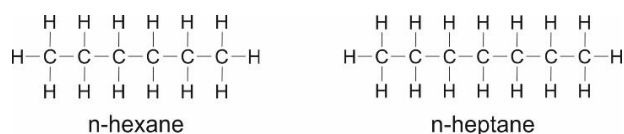


Figure 29: Chemical formulas of n-hexane and n-heptane

Tetrahydrofuran

Tetrahydrofuran is a heterocyclic compound with a boiling temperature of 64°C and an ignition temperature of 230°C . The chemical formula is shown in Figure 30. It is also highly inflammable and hazardous to health. During contact with air a formation of highly explosive peroxides occurs, which requires special precautions.

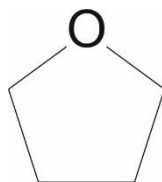


Figure 30: Structural formula of tetrahydrofuran

According to the data presented in Table 8 the maximum application temperature should not exceed 110°C , since this is the highest boiling temperature for the used solvents. In real application, however, the temperature of a thin film, which separates the hot gaseous solvent from the cooling water, is lower, as otherwise no heat transfer and hence no condensation would occur. Therefore, based on the

solvent data all three preselected film seemed to be appropriate from the temperature-based point of view.

Table 8: Main fluid properties of the used organic solvents, sources: (GESTIS 2015), (VDI 2006)

Property / unit	Hexane	Heptane	Tetrahydro- furan	Toluene
Molar mass [kg/kmol]	86.18	100.2	72.11	92.14
Liquid density at 20°C [kg/m ³]	660	680	890	870
Partial vapour pressure at 20°C [bar]	0.162	0.047	0.173	0.029
Boling point at 1 bar [°C]	68.8	98.4	65.81	110.7
Enthalpy of evaporation [kJ/kg]	334	318	29.8	362
Acentric factor [-]	0.301	0.351	0.225	0.264
Critical temperature [K]	507.6	540.3	541	591.8
Critical pressure [bar]	30.3	27.4	51.9	41.1
Critical density [kg/m ³]	323	234	320	292

3.3. EXPERIMENTAL SET-UP

3.3.1. Pressure test rig

For the determination of the material behaviour in later operating conditions in the heat exchanger, standard tensile tests are not sufficient, as they do not reflect the actual mechanical and thermal stress. Furthermore, a testing in open conditions is not possible if the tested films must stay in contact with the operating fluid during the entire testing procedure. Hence, the test rig had to provide a closed testing room, with heating and appropriate pressure load with the exposed surface of the film similar to the actual exposed area in the heat exchanger. Therefore, a pressure test rig with mounting plug for the film samples was designed, shown in Figure 31.

The bottom part of the pressure pipe has a welded screw thread ending with a rounded groove for the o-ring. For testing the film sample is being placed between the o-ring and the plug with the opening, which represents the exposure area of one film segment (s. also 3.4.2). In case of the performed experiments, the opening was 10x10 mm. The plug is being pressed against the pressure pipe by a lock nut. On the outer side of the plug, a measuring adapter can be placed to place the dial gauge at the proper position. The depth of the inner borehole of the adapter corresponds with the length of the measuring needle, so the dial gauge shows '0' when it only touches the relaxed film.

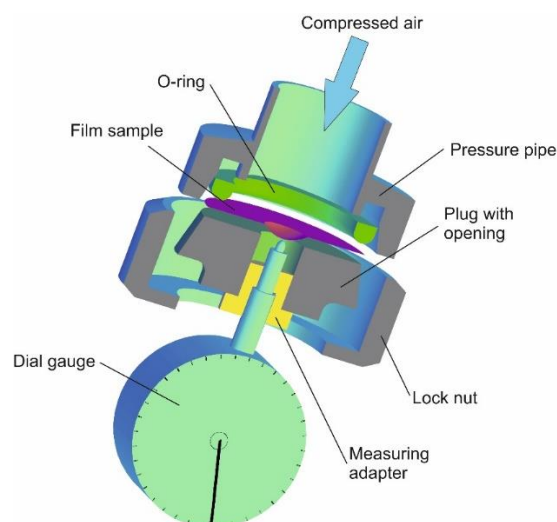


Figure 31: Pressure pipe for material behaviour investigation

The deformation of the film caused by the pressure in the pipe forces the dial gauge meter to deflect with respect to the deformation height, which is shown in Figure 32.

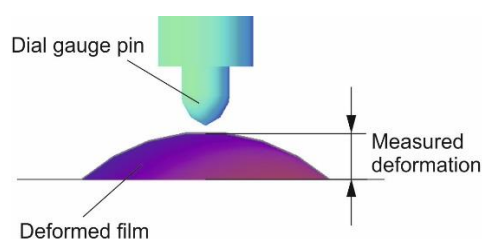


Figure 32: Measured deformation height of the films

The zero reference for the dial gauge meter was set by the appropriate height of the measuring adapter to the contact area of the film with the plug, so it indicates the non-deformed film. The dial gauge pin was centred by the adapter, so it showed the maximum deformation height, which was logged.

For testing with organic solvents, the pressure pipe was filled with a small amount of the solvent. This could be done through a small bypass pipe with a valve, which is not shown in Figure 31. Because of the upside-down position of the pipe, the solvent covers the free surface of the film and thus enables a permanent contact with the film and the liquid. During the pressure exposure, the pressure pipe ending is being placed in a heat bath with adjustable temperature. It is normally filled with water; hence it can be used with temperatures below 100°C due to the boiling point of water at normal conditions. Since the operating conditions of the heat exchanger do not exceed temperatures of 100°C, water could be used as heating fluid. The entire test rig scheme is shown in Figure 33.

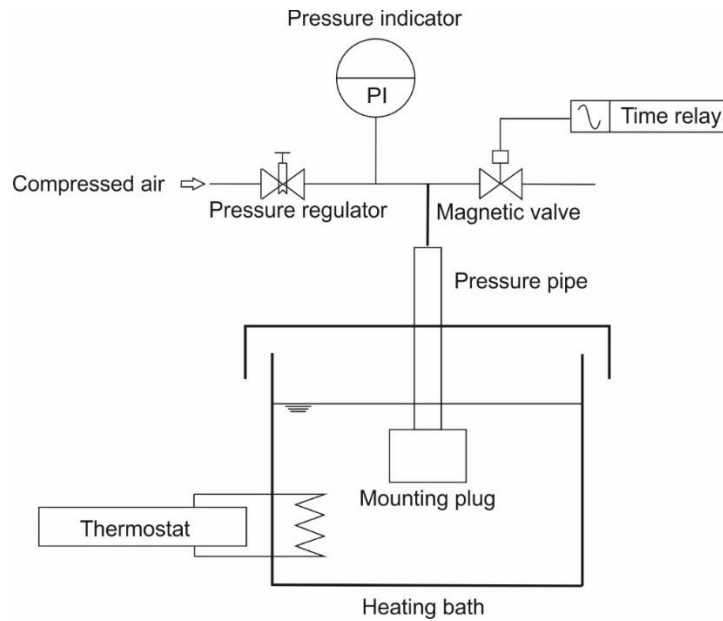


Figure 33: Test rig for polymer film samples

For higher temperatures (90°C) the pressure pipe was placed directly into the heating bath as shown in Figure 33. For lower testing temperatures, the heating was implemented by a thin copper pipe wrapped round the pressure pipe. The hot water from the heating bath flowed through the copper pipe and hence heated the test rig. The temperature in the pressure pipe was constantly monitored by means of a thermoelement placed close to the film sample.

A pressure regulator serviced by the compressed air supply of the department ensured a constant pressure load on the film. An analogue pressure meter was used for monitoring the needed pressure. For pulsating load testing, the magnetic valve was activated. The on-time and the off-time of the relay could be adjusted separately.

The accuracy of the used measuring systems was sufficient for the purpose. For the pressure meter, it was 0.1 bar and for the thermostat 0.2 K. The pressure regulator was able to hold the constant load for alternating supply pressures between 6 and 10 bar even with minor leakages in the pressure pipe. This is equivalent to changing water pressures in a cooling water supply system.

3.3.1. Heat exchanger test rig

To study the performance of the lab scale heat exchanger as well that of the demonstrator a test rig with a circuit for organic fluids was designed. This test rig had to fit both sizes of the tested heat exchangers, hence the heating section had to be dimensioned with respect to higher flow rates, too. The simplified schematic sketch of the test rig is shown in Figure 34. The apparatus is connected to two circuits. The first one is closed and contains the organic solvent. From the reservoir R1 the liquid is pumped by P1 through the preheater HE1 and the evaporator HE2. The gaseous solvent then

condenses in the test apparatus. To protect the pump from high temperatures the condensed solvent is cooled below 40°C in the cooler C1.

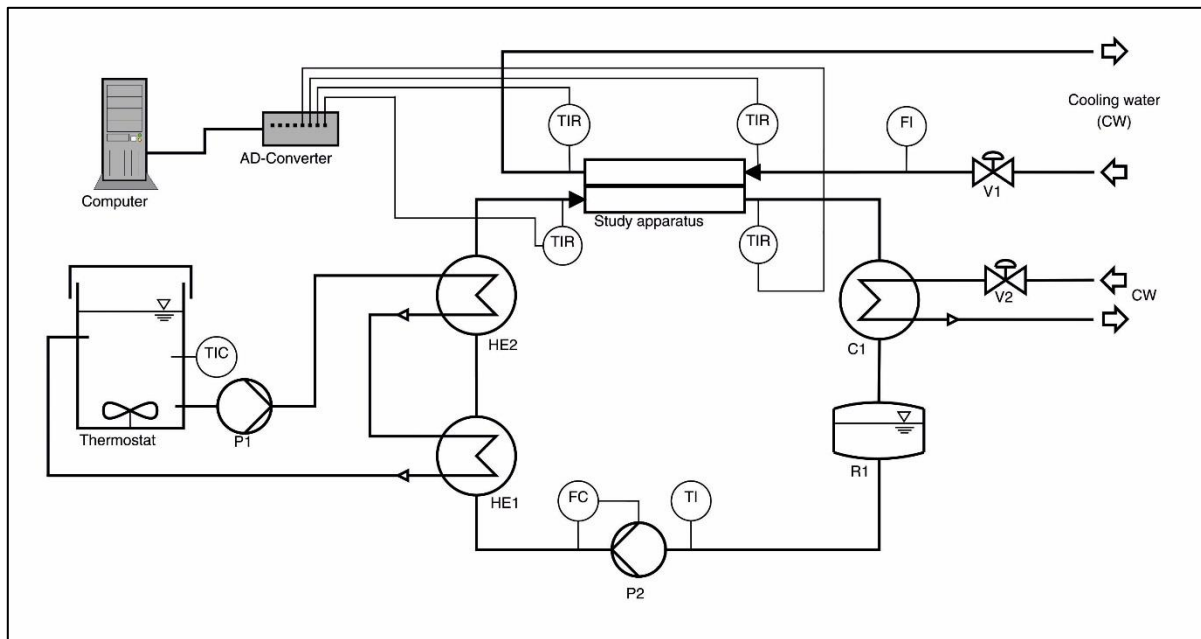


Figure 34: Test rig for condensation studies

The heat exchangers HE1 and C1 are field tube type heat exchangers made of stainless steel. For the evaporator, a tube bundle heat exchanger was used. For the heating, a hot water circuit containing a thermostat was used. The heat bath temperature could be set with an accuracy of 0.1 K. The counter flow configuration of the heating part of the test rig ensured a stable evaporation of the solvent. The thermostat itself is controlled by a P-controller, which is not the most accurate controller type, but is sufficient in this case, considering the latent mass of water and its high heat capacity. The pump P1 is built into the thermostat and could not be controlled.

For the cooling a normal domestic water connection was used, which provided temperatures between 11°C and 19°C depending on the outside temperatures. Both cooling flow rates could be set. For the main apparatus, cooling a manual valve and an analogue rotameter was used. As sufficient information on the flow determination for water was available, the expected accuracy of this analogue meter was sufficient. This was also proven during the preliminary testing.

The flow rate through the cooler C1 was also controlled by a manual valve and was set with respect to the needed temperature at the inlet of the pump. As the flow itself was not relevant for the evaluation of the tested apparatus, no flow indicator was installed.

A measurement program designed in LabView recorded four temperatures at inlets and outlets of the tested apparatus. The voltages from the used thermocouples (TYPE K) were first amplified and then converted in the AD-converter.

3.4. HEAT EXCHANGER DESIGN

3.4.1. Polymer film supporting structure

One of the main challenges about the heat exchanger design was the stabilisation of the highly flexible polymer films, which need a reliable support. Therefore, a preliminary testing was performed in order to determine the maximum possible unsupported area of the film at the required process pressure difference of approx. 6 bar. In collaboration with the industrial partner Calorplast GmbH a concept of the basic structure design was developed. To simplify the manufacturing of the later demonstrator it was decided to create the supporting block by milling rectangular crossed flow channels into the supporting plates. This led to a square unsupported surface area of the film.

After setting-up the basic design, the next step was the determination of the maximum possible width of the flow channels. This was done by preliminary testing with water at 90°C and 6 bar, which revealed, that the used films were able to withstand the pressure load with an unsupported square with a side length of 10 mm (s. section 4.1.1). To increase the reliability of the films it was decided to reduce the final free surface by a factor of five, which yielded in the selection of a 2 millimetre-milling tool. The distance between the flow channels was set to 3 mm in order to fit into the dimensions of the support plate with an integer number of flow channels. The milled support plate is given in Figure 35.

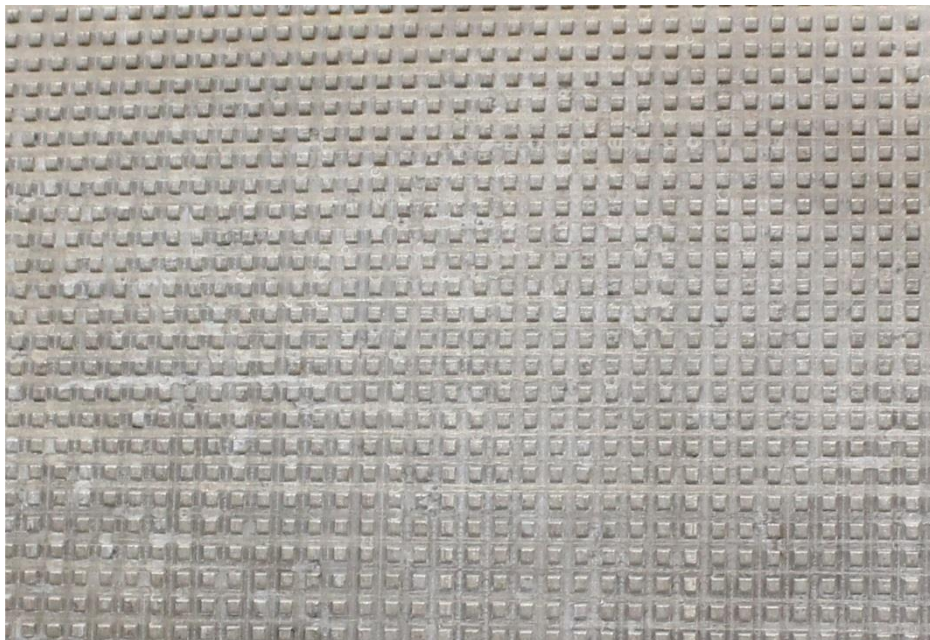


Figure 35: Milled flow channels as the film supporting structure

3.4.2. Lab scale heat exchanger

To study the heat transfer properties of the polymer films as well as the flow through the stabilising structure of the heat exchanger a small lab-scale heat exchanger was designed and built. The heat transfer area was 180 mm x 180 mm. It consisted of two different flow chambers: the smaller one with stabilisers for the condensation and the larger one for the cooling water. The design sketch of this heat exchanger is shown in Figure 36. The two fluid chambers are separated by the polymer film. As sealing material, soft fluoroelastomer (FKM) with a thickness of 3 mm was used. The cold side of the heat exchanger consists of a 20 mm thick frame, which contains inlets and outlets for the cooling water. Alternative connectors in the shape of annular distributors for the cooling water are mounted on the end plate. The hot, condensation side is much smaller, the flow channel is only 2 mm thick. The supporting plate has quadratic block placed on it, which support the polymer film, deformed by the higher pressure on the cooling side.

As the entire construction was built of poly(methylmethacrylate) (PMMA) some parts, such as the annular connectors, the frame and the end plate were joined by a special cyanoacrylate based glue. For the assembly of the heat exchanger screw connectors at the corners as well as additional ones in the centre of each side were used.

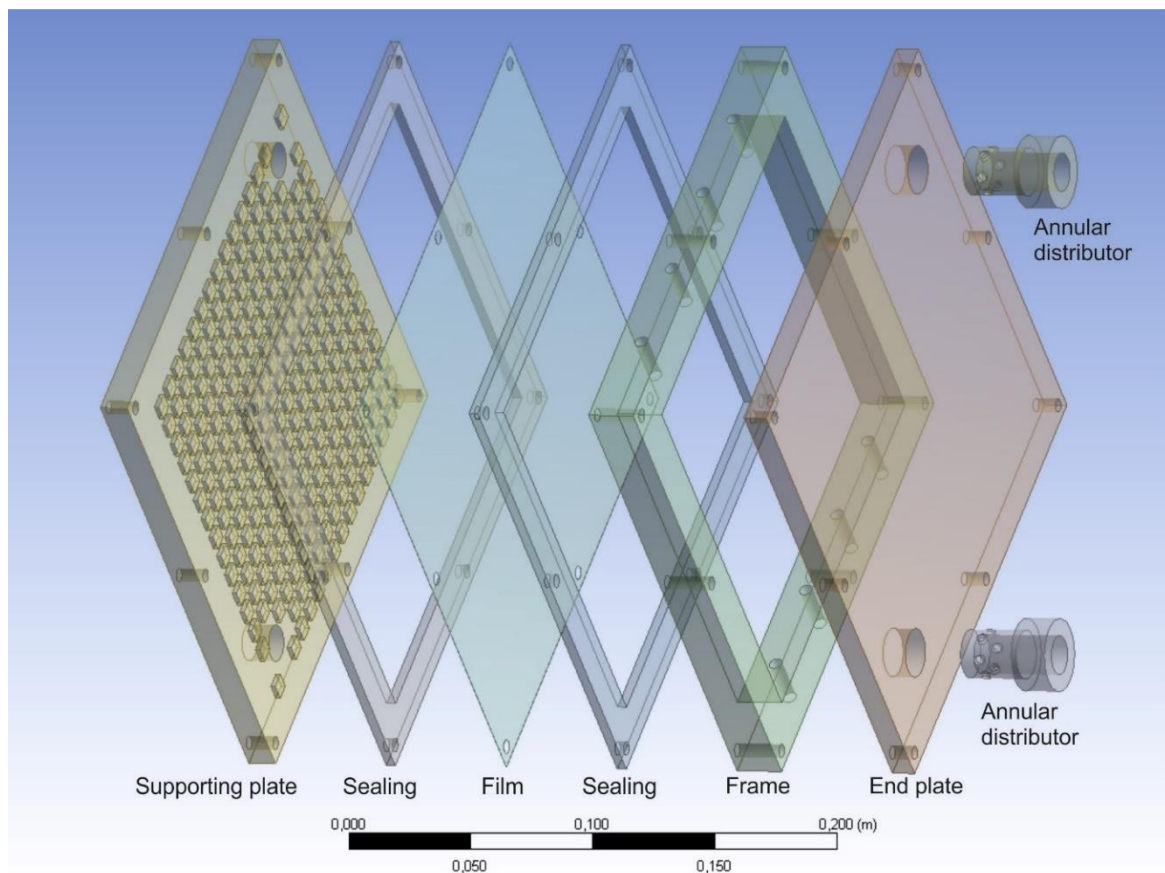


Figure 36: Schematic sketch of the lab scale heat exchanger

The design is not modular, in contrast to the later demonstrator, as the main purpose of this lab scale model is the basic study of the polymer film performance. The support structure is similar to the one used in the demonstrator. Due to the full symmetry of the heat exchanger various operation modes, such as parallel, counter and cross flow could be tested. The cold side also contains extra inlets with a higher overall cross-sectional area, to reduce the pressure loss and to improve the water distribution in the chamber.

The cooling side had a much larger volume than the warm side, because high outlet temperatures of the cooling water had to be avoided, due to the material caused limitations on the temperatures.

3.4.3. Full-scale demonstrator

The design of the full-scale heat exchanger, developed in cooperation with Calorplast GmbH, follows the same principle as the lab-scale apparatus. It follows the design of conventional plate heat exchangers with a crossed flow. Here, the modular design was implemented (s. Figure 37). Hence, the number of the middle plates, which stabilise the fluid separating polymer film, increase the required heat transfer area. The end plate and the connection plate have a thickness of 35 mm to give the entire structure the necessary stiffness.

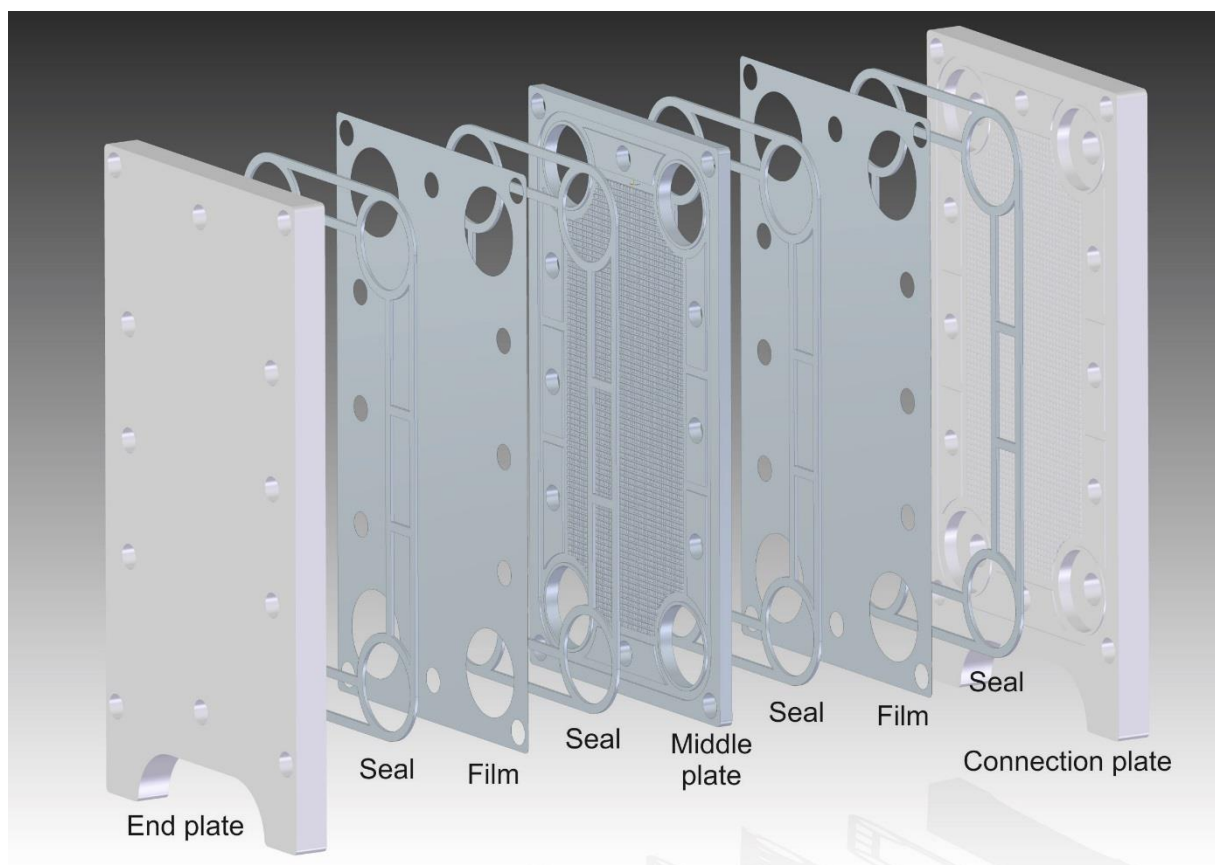


Figure 37: The CAD sketch of the full-scale heat exchanger with four fluid chambers

For the assembly, massive M24 bolts were used at the peripheral boreholes. The seal was designed as a two-line part with the inner and the outer sealing circle. The supporting structure for the film consisted of rectangular pimples, which were made by milling of narrow (2 mm) flow channels. The size of the pimples was 3 mm, which is a good compromise between a sufficient support for the film and an acceptable possible flow rate for each module.

The design of the apparatus allowed cross-flow operating mode with fluids running either upwards or downwards. The complete heat exchanger was made of polymer materials except for the end plates, for which aluminium was used to increase the stiffness. Nevertheless, it must be said that the outer plates have no contact with the product fluid, and hence this design feature is acceptable. The middle plates were made of polytetrafluoroethylene (PTFE) with 30% glass fibres and for the sealing either a PTFE-foam or fluorinated rubber was used.

3.4.3.1. Demonstrator 1

The first demonstrator, which was tested during the research process, consisted completely of polymeric materials. Due to sealing problems, which will be discussed later, only few measurements were performed with this apparatus. For the same reason, only a simple PET film with a thickness of 100 μm was used. The operating fluid was water on both sides. Both flows were in the upwards direction, so the operating mode is a combination of a cross-flow and a parallel flow, as shown in Figure 38. This mode is not suitable for the initial purpose, the condensation of organic solvents, as the condensed solvent would fill up the flow chamber. However, for the first test runs it ensured that the entire surface of the film is covered with the fluid and hence the entire area is wetted and involved in the heat transfer process.

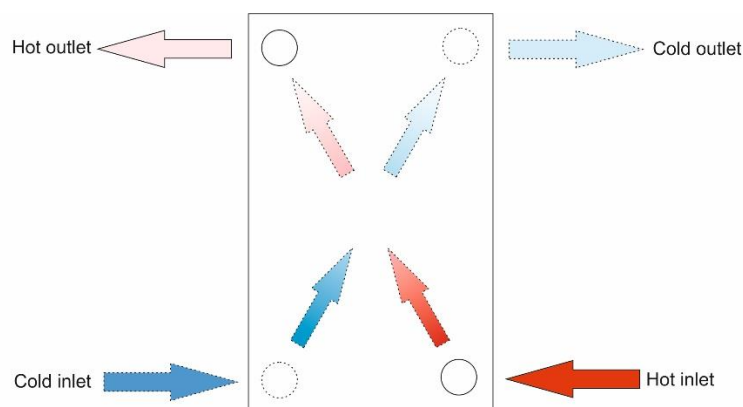


Figure 38: Operating mode of the testing procedures with the demonstrator 1

3.4.3.2. Demonstrator 2

For the enhanced demonstrator 2 a cross-flow operating mode was used, to enable the condensing hexane to flow out of the heat exchanger driven by gravitation. Based on the experience from previous

testing with the lab-scale apparatus and the first demonstrator, the cross-flow was also meant to ensure the full coverage of the heat exchanger surface by the cooling water. The operating mode is shown in Figure 39.

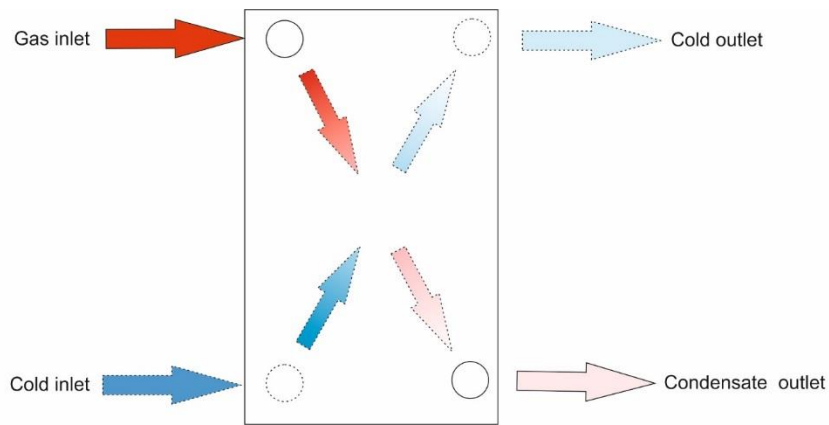


Figure 39: Operating mode of the testing procedures with the demonstrator 2

With the demonstrator 2 two different heat exchanging processes were studied. The first one was the simple water-water heat transfer without any phase transition. The second process was the condensation of the vaporised hexane with water cooling.

Due to the design of the stabilising structure of the demonstrators, a special consideration of the heat transfer area had to be done. For most applications the heat transfer, such as tubed heat exchangers the surface area is obvious, and can be computed by the arithmetical average of the outer and the inner diameter (VDI 2006). For plate heat exchangers, the situation is simple, too.

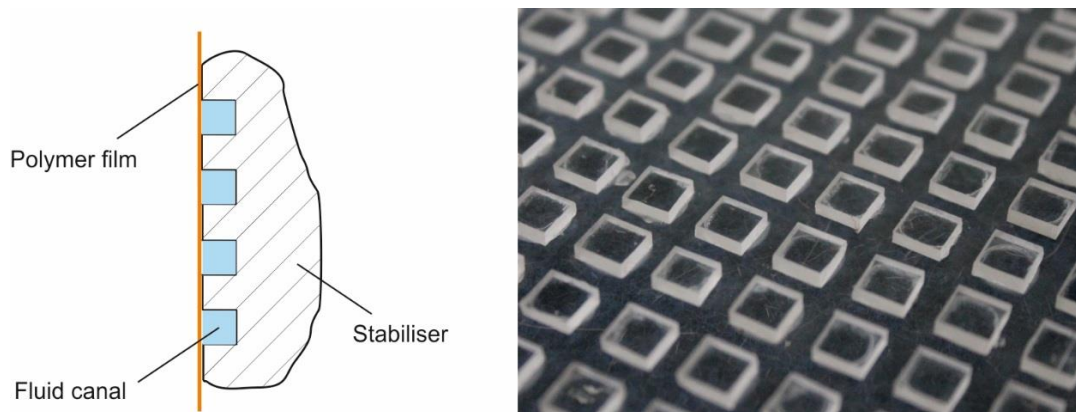


Figure 40: Simple sketch and picture of the stabilising structure in the heat exchanger

The polymer film was kept in position from both sides. Therefore, not the entire film was covered with the fluid, but only the part of it, which had no contact with the stabiliser. This is shown in Figure 40. As already said, the fluid, which flows through the areas marked in light blue, does not have any direct contact with the parts of the film. On the other hand, some minor heat transfer definitely takes place from the fluid via the stabiliser to the film. Therefore, in this work the results of the heat transfer are

presented for the full film surface as well as for the area reduced by the contact areas with the stabiliser. For one stack the areas are: the full area $A_{full} = 0.1641 \text{ m}^2$ and the reduced area $A_{red} = 0.1062 \text{ m}^2$. Such a reduction of the heat transfer area (about 35%) certainly has a not negligible influence on the overall heat transfer coefficient.

3.4.4. Testing procedures with the pressure test rig

The preliminary testing procedures were performed to define the most suitable films prior to general testing. For this, four film types were tested, such as polyethyleneterephthalate (PET), polyether ether ketone (PEEK), polyfluoroethylene (PTFE) and polyimide (PI). According to the manufacturer information, all of these materials except PET should have the required chemical resistance and thermal stability. The testing was performed for two weeks in hot water at 90° and with the pressure load of 6bar. Six samples of each film were tested for statistical reasons.

The general testing procedures consisted of two testing stages. The first major testing stage included all testing procedures at constant pressure load. These were done for all relevant combinations of polymer films and organic solvents. Reference testing with water and the polymer films were performed as well. To represent the real operating condition of the heat exchanger the testing temperatures were set to boiling temperatures of the used organic solvent. Apart from the preliminary testing, the operating pressure was set to 6 bar. The maximum testing duration was set to 2 months of permanent load and contact of the film with the solvent. An overview of the performed testing procedures of the first stage is given in Table 9.

Table 9: Parameters for the main polymer film testing at constant load

	Toluene	Hexane	Heptane	Tetrahydro-furan	Water
PET, Mylar A	90°C, 6 bar	70°C, 6 bar	90°C, 6 bar	70°C, 6 bar	90°C, 4-6 bar
PTFE – glass fibre	90°C, 6 bar	70°C, 6 bar	90°C, 6 bar	70°C, 6 bar	90°C, 4-6 bar
PI, Kapton HN	90°C, 6 bar	70°C, 6 bar	90°C, 6 bar	70°C, 6 bar	90°C, 4-6 bar
PEEK, Victrex Aptiv 1000	90°C, 6 bar	70°C, 6 bar	90°C, 6 bar	70°C, 6 bar	90°C, 4-6 bar

The second test stage had its focus on the dynamic behaviour. The tests were only performed for two polymer films, the PTFE-glass fibre compound and the polyimide film, as they already showed best performance at constant load. Due to the design characteristics of the test rig only testing with water was possible. During the dynamic pressure drop sequences the pressure pipe was periodically opened

and so the vaporised solvent could easily escape from the pipe to the work environment. For the testing two frequencies were chosen. The lower frequency of 45 load changes per hour was due to the longest adjustable time periods of the time relay. The higher frequency of 550 load changes per hour was the highest possible pulsation rate, which still enabled to fully rise the pressure to 6bar and to drop it to 1bar. These studies were performed in water at constant temperature of 90°C.

3.4.5. Testing procedures for the determination of the heat transfer

The testing procedures for both heat exchangers were similar. Preliminary testing with water was performed to gain basic information about the heat transfer and reference results for the evaluation of the CFD-model without a phase transition.

Normal domestic water supply was used for the cooling side, hence, the temperatures varied between approx. 10°C and 19°C depending on the season of the year. On this side, only the flow rates could be set. For the testing with higher flow rates on the hot side, the larger demonstrator was also connected directly to the domestic water supply. In this case, the temperature was given by the supply and could not be changed. The flow rates were varied to get appropriate operating points.



Figure 41: Heat transfer test rig with the large demonstrator mounted on it

For the condensation studies, the temperature as well as the flow rate of the organic solvent could be set. To enable the condensed liquid flow out the heat exchanger the inlet for the solvent was at the upper right connector. The cooling water inlet was at the lower right connector to enable the filling of the entire cooling chambers with the cooling water. The heat exchanger operated in the cross-flow, as can be seen in Figure 41. Here, the test rig with one evaporator (to the right of the demonstrator) is shown. This was used for smaller flow rates of the organic solvent, for higher flow rates an additional evaporator was built in, as shown in Figure 34.

The testing procedures with the corresponding fluids, flow rates and temperatures are given in Table 10 for the full-scale demonstrator. For the lab-scale heat exchanger more operating points were evaluated. Here the flow rates for water between 10 and 61 l/h for the hot side and between 55 and 127 l/h for the cooling side were set. The temperatures were varied between 70°C for liquid-liquid-testing and up to 90°C for condensation studies. The minimum and the maximum flow rates and temperatures are limited to the used range by the test rig design, but they correspond with the demands on the heat exchanger based on real industrial applications.

Table 10: Operating points (OPW) for the full-scale heat exchanger

Operating point	Fluid chambers	Fluid 1	Flow rate of fluid 1	Inlet temperature of fluid 1	Fluid 2	Flow rate of fluid 2	Inlet temperature of fluid 2
-	-	-	l/h	°C	-	l/h	°C
OPW1	6	Water	326	62,4	Water	317	14,0
OPW2	6	Water	221	61,2	Water	460	13,9
OPW3	6	Water	152	51,0	Water	497	13,7
OPW4	6	Water	474	60,7	Water	671	13,5
OPO11	2	Hexane	27,7	70,3	Water	317	15,0
OPO12	2	Hexane	27,7	77,4	Water	497	12,1
OPO13	2	Hexane	37,0	72,7	Water	317	16,5
OPO14	2	Hexane	45,6	74,5	Water	317	16,7
OPO15	2	Hexane	54,3	75,7	Water	317	16,1
OPO16	2	Hexane	54,3	75,7	Water	497	15,7
OPO17	2	Hexane	132,7	75,7	Water	497	13,9
OPO17	2	Hexane	77,5	75,7	Water	497	15,5
OPO19	2	Hexane	177	76,1	Water	497	13,9
OPO21	2	Hexane	27,7	77,4	Water	317	12,1
OPO22	2	Hexane	37,0	77,7	Water	317	12,2
OPO23	2	Hexane	47,0	77,6	Water	317	12,1
OPO24	2	Hexane	54,3	72,3	Water	317	12,1
OPO25	2	Hexane	54,3	72,4	Water	497	12,0
OPO26	2	Hexane	77,5	74,7	Water	497	12,0
OPO27	2	Hexane	132,7	74,4	Water	497	11,9
OPO27	2	Hexane	177,0	74,92	Water	497	11,7

3.5. NUMERICAL METHODS

3.5.1. Hardware

One of the goals of the model development was the possibility to use the model on standard PCs, avoiding the use of high-performance PCs or even clusters. However, the size of the geometry and the appropriate mesh element sizes set very high demands on the used hardware, especially on the memory. In Table 11 the description of the used PC-configurations is given. Though these specifications are higher than for standard computers, especially considering the memory size, they still represent affordable systems, which are much cheaper than HPC-Workstations or servers.

For all three systems, the size of the virtual working memory was set to the same size as the physically installed memory. The usage of the virtual memory makes the simulation process much slower, as the hard disk drives (HDD) or even solid state drives (SSD) cannot perform with the same speed as normal RAM-modules. However, it gives the possibility to expand the available working memory if necessary.

Table 11: Specifications of the used PC-systems

Specification	System 1	System 2	System 3
CPU	AMD FX 6300	AMD FX 6100	Intel Core i3 540
RAM	32 GB DDR3, 1600	32 GB DDR3, 1333	8 GB DDR3, 1333
HDD / SSD	SSD 120 GB	HDD 1TB	HDD 500GB
OS	Windows 7 Prof. 64 bit		
Software	Ansys Workbench 15.0	Ansys Workbench 14.7	Ansys Workbench 14.7

3.5.2. Software

Before starting-up the modelling, different software was evaluated in order to select the most appropriate FEM and CFD package for the problem. Without doubt, Ansys Workbench® (Ansys Inc. 2014d) is one of the mostly used multiphysics software packages and in many cases, it is considered to be highly reliable. This can be said for the FEM analysis as well as for the CFD fluid dynamics part. In contrast to open-source software Ansys is assigned to licencing costs and is a closed commercial program, without a possibility to access the implementation of the equations used for the solver, besides user-defined functions. However, in 2012 Ansys presented several FSI solutions successfully used in automotive industry (Ansys Inc. 2012).

Despite the popularity of Ansys there are some other packages, which can be considered as an alternative. The first one is the open-source software OpenFOAM® (OpenCFD Ltd. 2015). The main advantages of it are the possibility of making changes to the solver on the one hand and no licence

costs on the other hand. By now, it is also widely used in the research but also more and more in the product development. However, OpenFOAM® has a major disadvantage being without any graphical interface, which makes more difficult and more time-consuming to use. An attempt to model a simple heat exchanger detail was performed within this project by J. Schäfer (Schäfer 2013), but ratio of the results to the time investment was unacceptable. In addition, no published work about a successful implementation of an FSI-coupling with OpenFOAM® could be found at the beginning of the project. Therefore, it was decided not to continue its usage.

The third possible software was Hyperworks® by Altair Engineering Inc. (Altair Engineering 2014). Being a commercial multiphysics software bundle, it is similar to Ansys Workbench® considering its possibilities. It consists of a powerful mesher Hypermesh® and several solvers. This software was also tested for the coupling of FEM and CFD, but unfortunately, it failed to depict the deformation of the very thin film in a proper way (Burkey 2014).

During the literature research, some other solvers for similar tasks were found in publications, like a FEM analysis coupled with some electro-thermal equations (Taralov et al. 2012). However, such solvers were developed for a specific problem and can hardly be applied to different problems. In this case, the complete CFD-part is missing and had otherwise to be added to the solver.

For these reasons, Ansys Workbench® was selected for the development of the entire modelling, for pure CFD as well as for coupled models. As the most productive models were developed with the usage of CFX®, only this Ansys® module will be explained in detail. In principal, the boundaries are quite similar in Fluent® and CFX®. Therefore, many settings can also be applied to Fluent® as well. However, there are some differences, especially considering the detail settings of inlets and outlets. The most information presented in the following subsections is taken from the CFX-user guide (Ansys Inc. 2014a), if not mentioned otherwise.

Since Ansys Workbench® is being continuously improved, several versions of the software, from 13.0 to 15.0, were used during the development process of the model. Some major changes in the coupling and exporting of FEM-module results were introduced with the version 14.7 as well as some minor improvements with version 15.0 (Ansys Inc. 2014a). Since the final simulation runs were performed with the version 15.0 all settings, used models and modules are referred to this version.

For the models presented in this work following Ansys® modules were used:

- Ansys Design Modeller® (for importing the geometries from CAD-data)
- Ansys ICEM® (for meshing the model)
- Ansys CFX® (as main solver for the fluid flow, heat transfer and phase transitions)
- Ansys Mechanical® (transient or static analysis, deformation of the heat exchanger)

3.5.3. Geometry

The Ansys Design Modeller provides two possibilities for creating a model geometry. First, the build in CAD-functions can be used to create 2D-sketches, extrude them and define bodies and volumes. Several volume operations, such as unite and subtract are also available. The pattern function, which allows to create repeating geometry parts in a way fast and easy way, is very useful.

The second possibility is the import of the built geometry from common CAD programs, such as AutoCAD®, CATIA® or SolidEdge®. In case of AutoCAD®, the import interface is integrated into the main application of the software and can be easily imported. However, the model size and especially the number of faces are very important for the import speed and the required memory usage. Therefore, it is sometimes better to use the CAD tools built in the Design Modeller, than to import a 3D-model from a CAD program.

3.5.3.1. Geometry mapping of the lab-scale heat exchanger

The lab-scale heat exchanger, as shown in Figure 36, was modelled as a two-fluid domain geometry for most simulations. The condensation domain with the stabilising structure consists of narrow rectangular flow channels. The cooling side consists of one block without any defined flow channels with annular distributors. Both domains are shown in Figure 42.

For the extended mechanical model, the separating polymer film had to be created as a solid body. The advantage of the model containing the polymer film as a solid body is the possibility to perform the FEM-based deformations studies of the film and its influence on the flow in the heat exchanger and the overall heat transfer. This also allows simulating the part of the heat transfer caused by the heat conduction in the film areas, which are not in contact with fluids directly.

The main disadvantage of this extended modelling is the higher complexity and the non-matching contact surfaces of the film and the fluid volumes, which causes some difficulties for the CFD solver. In this case, the exact contact areas between the fluid and the film had to be declared separately and the remaining free areas had to be set as walls. Secondly, the extremely thin film in comparison with the fluid domains forces the meshing software to generate very fine meshes with element numbers that could be barely handled by the computers used for this work. This is explained in detail in section 3.5.1. Therefore, for pure CFD simulations, the domain separating polymer film was not modelled as solid body, but as a virtual thin wall. On the one hand, this was done due to enormous element numbers caused by the meshing of the film and the contact areas. On the other hand, a solid body was not necessarily needed to determine the heat transfer and the flows through the heat exchanger chambers. For the attempt to create a fully coupled FEM-CFD-Model with fluid structure interaction (FSI) the film had to be modelled as a solid with a solid material assignment.

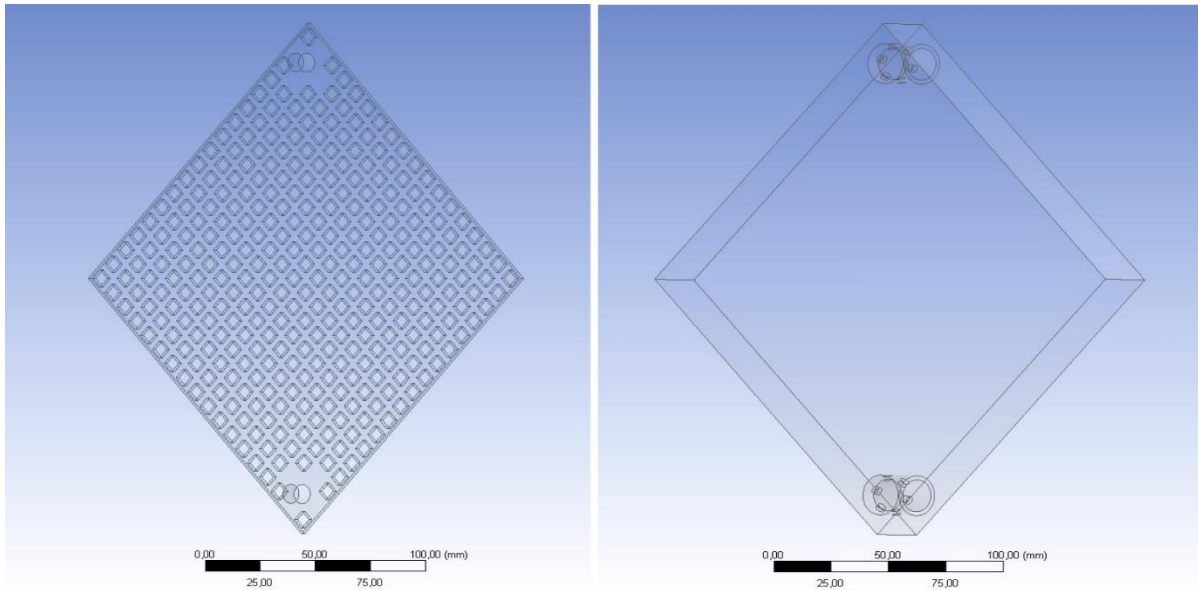


Figure 42: Model domains for the lab-scale heat exchanger, condensation domain - left, cooling domain - right

3.5.3.2. Geometry mapping of the full-scale demonstrator

The design of the demonstrator is modular with parallel flow chambers for each of the both fluids. Therefore, the basic geometry model consists of two fluid volumes with both inlets, outlets and walls and of a solid volume for the separating polymer film. To reduce the simulation time and primarily due to limited hardware resources only one pair of fluid volumes was modelled with the respectively reduced mass flow. Both of the used flow solvers (Ansys CFX® and Fluent®) allow the modelling of the contact faces between fluids and solids as well as the direct contact of two fluid volumes with a virtual thin wall (Ansys Inc. 2014a). For the modelling of the polymer film heat exchanger the last one seems to be the most appropriate way, as it significantly reduces the amount of the model elements, which generally affects the simulation time in a positive way. The created fluid volumes are shown in Figure 43. The disadvantage is the missing possibility to visualise the temperature distribution within the film. It also only allows the modelling of the static non-deforming geometry, which considering the thickness and the flexibility of the films is not the case.

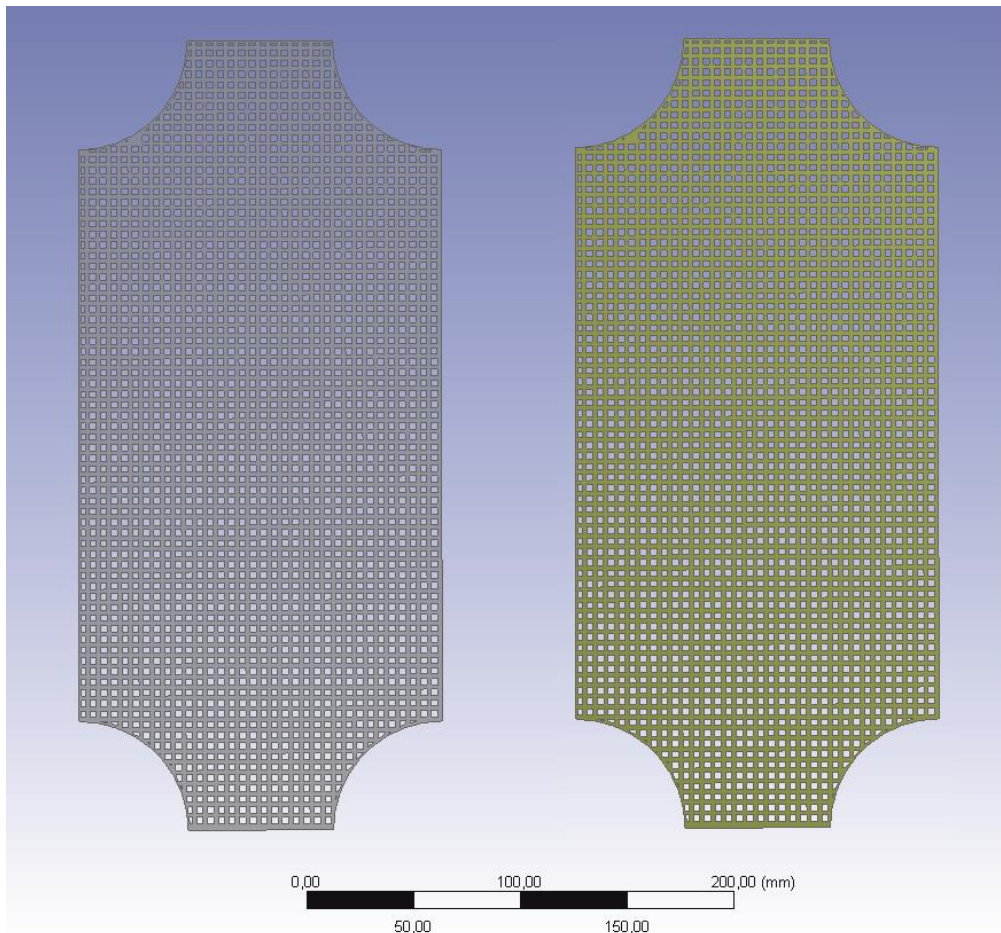


Figure 43: Fluid volumes of the used full-scale heat exchanger model

3.5.4. Meshing

The used software module 'ICEM', which is part of 'Ansys Workbench', is a user friendly and flexible mesh generator for all solvers integrated in Workbench software package. For faster meshing this module offers preconfigured options, which allow to generate a mesh within few steps with an element quality sufficient for most cases.

The choice of the geometry model described in the previous subsection has a direct influence on the meshing. Apart from the obvious higher number of elements and knots, the usage of the three-volume model (one solid and two fluid volumes) has also a secondary impact on the mesh. As the modelled polymer films are between 0.75 and 0.1 mm thick, the element size for the mesh must be lower than the thickness of the film. For the extended FEM-based model, element sizes of less than the half of the lowest thickness of the body are highly recommended for reliable results (Ansys Inc. 2014c). The size of the entire heat transfer surface and the heat exchanger dimensions has caused an unmanageable amount of mesh elements, which exceeds 10^8 elements per volume. This problem will be discussed in detail in chapter 3.5.7.3.

3.5.4.1. Meshing parameters

In this section, the meshing parameters used in this work are briefly described. All other settings which were kept to default values are not mentioned here. Further explanations can be found in the Ansys Workbench Meshing Guide (Ansys Inc. 2014c).

Solver preference

By the selection of the solver preference, which is only available for meshes created for CFD simulations, some solver specific defaults are set. Primarily these are: the inflation aspect ratio, the collision avoidance and the transition ratio. These settings were not changed and hence are not explained here. For more information please refer to (Ansys Inc. 2014c).

Relevance center

This sets the size preference for the elements according to one of the three available options: coarse, medium and fine. Depending on the geometry size and shape, the limiting values for the element size are being created by default.

Advanced size function

Four options are available for this setting. The first one is the curvature, which is normally set by default. This enables to adjust the size of the elements to fit curvatures of the geometry. The corresponding normal curvature angles, element sizes etc. can be changed by the user or kept to default values. The second one is the proximity size function. This allows to define element layers for body regions where 'gaps' between two mesh elements can occur. The function parameters can also be defined by the user or kept to the default values. The third option is the combination of the two functions described above and is supposed to deliver the best mesh quality with the highest element numbers. Finally, the fourth option sets a fixed element size, which excludes any mesh refinements. For simpler geometries and very specific cases, it could be an appropriate option. For bigger geometries, it can cause unnecessarily very high element numbers.

Smoothing

The smoothing option triggers the mesher to relocate the nodes to create a mesh better fitting to the geometry shape. The intensity of this setting can be set to low, medium or high. The highest setting also causes an increased element number, but provides a better mesh quality, especially if the geometry contains curved shapes.

Transition

This setting has an influence on the growth rate of the adjacent elements. Two options are available: fast and slow. The last one can improve the mesh quality but also slows down the meshing speed.

Span angle center¹

This is an additional setting for the curvature based mesh refinement. Depending on the selected option the span angle will be set to the value range between 12° to 36° for fine, 24° to 75° for medium and 60° to 91° for coarse respectively.

Inflation controls

In order to modify the inflation several options can be set additionally. In most cases, the 'program controlled' option is absolutely sufficient and does not require any further settings. If this option is used, especially accurate refinement is set at the edges of the bodies as well at the boundary edges and contact areas. This setting is recommended for problems with contact areas between domains and particularly for fluid-structure-interaction models.

3.5.4.1. Basic meshing

Ansys ICEM® is a very powerful tool to create high quality meshes from given geometries. It can be used either as a built-in functionality in several modules of Ansys Workbench®, such as CFX®, Fluent® or Ansys Mechanical® or as a standalone program, which provides an advanced functionality. With the latter, FEM-meshes can be created as well as VOF-meshes. Due to this integration, ICEM® creates solver specific meshes and contains various settings to improve the mesh quality, such as refinement, region specific meshing of one body, definition of element types and sizes. Refinement is a possibility to vary the size of the mesh, according to demands on the mesh quality in specific parts of the model. For smaller parts, the mesh element size can be adjusted to avoid a coarse mesh, which could lead to inaccurate results or in the worst case could cause divergences.

As can be seen in Figure 44 the exemplarily flow channel consists of two parts of a different size: the main flow channel with a quadratic cross-section and a narrow side-flow channel. The first meshing result reveals an equal distribution of the mesh element size for both parts of the body. For the smaller part, the solution might be inaccurate. In this narrow flow channel only one element fits in the limited width. To enable a detailed analysis of this small auxiliary flow channel a finer mesh must be created

¹ The American spelling here is given by the spelling used by Ansys

for this small part. The refined mesh (right) increases the element number and allows a closer look at the flow details in this area.

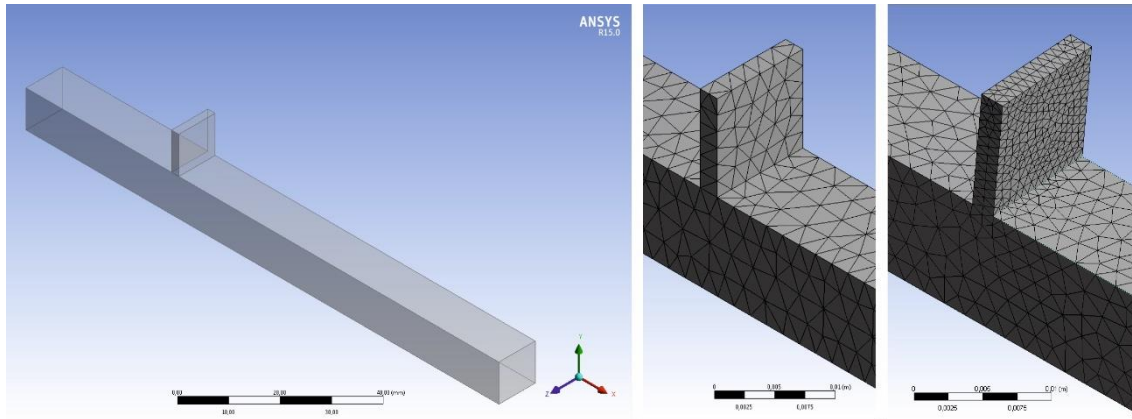


Figure 44: An example of mesh refinement (entire geometry – left; mesh without refinement – centre; refined mesh –right)

3.5.4.2. Meshing of the lab-scale heat exchanger

For the lab-scale heat exchangers some meshing studies were performed. Therefore, some meshing parameters were varied to determine their influence on the final solution with the solver Ansys® CFX. In Table 12 the setting variations are given.

Table 12: Mesh settings for the lab-scale heat exchanger model

Setting	Mesh type 1	Mesh type 2	Mesh type 3	Mesh type 4
Solver preference	CFX	CFX	CFX	CFX
Relevance center	Fine	Fine	Fine	Fine
Advanced size function	None	Curvature and proximity	Curvature	Curvature and proximity
Smoothing	High	High	High	High
Transition	Slow	Slow	Slow	Slow
Span angle center	Fine	Fine	Fine	Fine
Automatic inflation	None	None	None	Automatic program controlled

For the evaluation, one reference operating point with water on both side was chosen with the following parameters:

- Mass flow hot side: $\dot{m}_h = 0.017 \text{ kg/s}$
- Inlet temperature hot side: $t_h = 54.82 \text{ °C}$
- Mass flow hot side: $\dot{m}_h = 0.036 \text{ kg/s}$
- Inlet temperature hot side: $t_h = 12.83 \text{ °C}$

3.5.4.3. Meshing of the full-scale demonstrator

The full-scale demonstrator was modelled as a two-volume geometry. Based on the experience gained from modelling of the lab-scale heat exchanger only two different meshes were generated for the model of the second demonstrator. For these meshes, the same parameters were as for the lab-scale heat exchanger model.

Four simple operation points with water in both fluid volumes were used for evaluation of the mesh quality. These were measured during preliminary testing of the demonstrator with a demonstrator configuration of six chambers for each hot and cold fluid. As the chambers are parallel to each other, 1/6 of the mass flow was taken for the simulation with the same temperatures. All operation points were simulated for both mesh types. The parameters used for the evaluation solver runs are given in Table 13

Table 13: Parameters of mesh evaluation simulation runs

Operation point	Volume flow, cold	Volume flow, hot	Inlet temperature, cold, $T_{in,c}$	Inlet temperature, hot, $T_{in,h}$	Outlet temperature, cold, $T_{out,h}$	Outlet temperature, hot, $T_{out,h}$
-	l/h	l/h	°C	°C	°C	°C
1	354	356	14,0	62,4	26,4	49,5
2	517	240	13,9	61,2	22,4	43,1
3	565	240	13,7	51,0	20,4	39,1
4	762	524	13,5	60,7	22,3	47,0

3.5.4.4. Mesh studies

For pure CFD simulations, the standard mesh quality 'fine' was sufficient and provided appropriate results at an acceptable solver run time of between 8 and 24 hours. The element numbers of about 10^6 for the smaller lab-scale geometry or $5 \cdot 10^6$ were manageable. An example of the meshed flow channel on the condensation side of the lab-scale heat exchanger is given in Figure 45.

For more complex, FEM-based or coupled FSI simulations, the standard fine mesh was not sufficient and several parameters had to be changed. This is based on the extremely thin films, which had to be modelled as a 3-D geometry. As already described in section 3.5.4, for pure CFD modelling it was absolutely sufficient to model the thin film as a virtual wall with the corresponding thickness and material properties. For the FEM modelling the structure could not be modelled as a virtual wall, as a virtual wall is non-deformable. Therefore, a very thin solid body was created and had to be meshed according to its dimensions, in order to determine the deformation of the film.

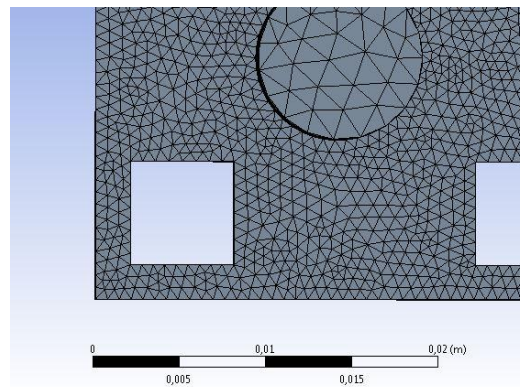


Figure 45: Mesh quality example at the inlet area of the lab-scale heat exchanger

In general, according to the FEM modelling guide provided by Ansys (Ansys Inc. 2014c) the maximum element size for a successful FEM model should be half size of the smallest part of the geometry. In our case, this means that with a film thickness of $100\ \mu\text{m}$ the element size should not be larger than $50\ \mu\text{m}$. Assuming that a standard element then would be a tetrahedron, which is a common shape for mesh elements, this means that for a film area of $A_{\text{full}} = 0,1641\ \text{m}^2$ and a height of $100\ \mu\text{m}$ an element number of approx. $1.11 \cdot 10^9$ would be required. Due to hardware limitations, such element numbers cannot be handled by the used computers, as such a model would need over 1 TB of RAM. Therefore, a mesh size had to be found, when neglecting the recommendation of Ansys to nevertheless provide acceptable results. The main goal herein was to find an element size range that allows minor variations without having any influence on the FEM result. This was done by using a very simple geometry and was supposed to depict one flow canal segment of the large heat exchanger.

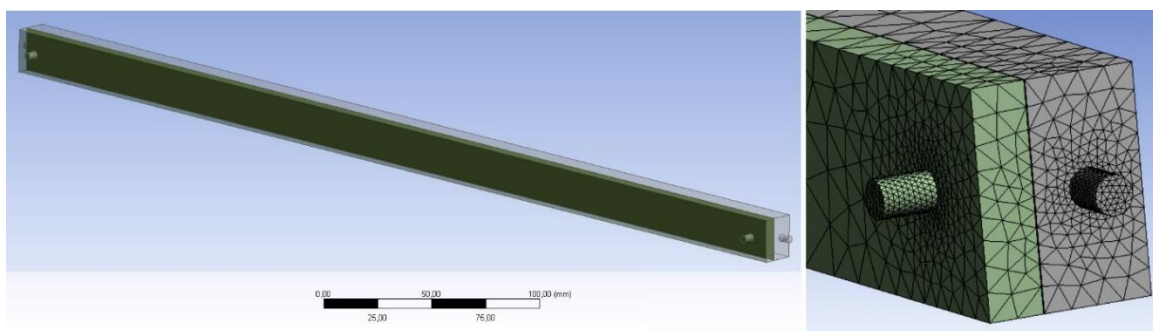


Figure 46: Test geometry and a mesh example for the FEM mesh study (green: hot fluid volume, grey: cooling volume)

In Figure 46, the used test geometry is shown. It consists of two fluid volumes (green and grey) and one solid volume, which depicts the flexible film and is located between the both fluid volumes. Due to its low thickness ($0.1\ \text{mm}$) it is barely visible in Figure 46. The pressure at the inlets as well as the solid material properties were set in way to result in a deformation of the film previously determined experimentally. As no real structural analysis was required and the FEM solver only was meant to generate a deformed body, the used parameters are not given here and can be found the work of

Meyer (Meyer 2014). An overview of the mesh study results is shown in Figure 47. As can be seen, the result, namely the deformation height, remained the same for element sizes between 0.2 and 0.4 mm. For larger elements and hence lower element numbers, the deformation decreased significantly. The encircled values in the chart represent this constant range.

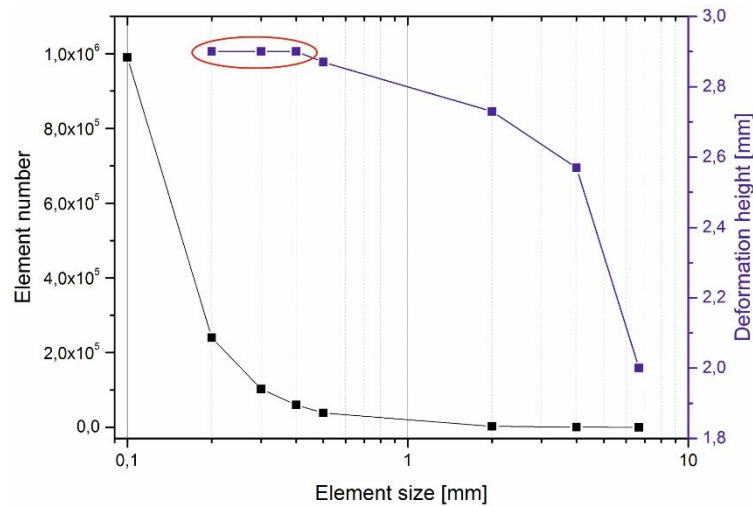


Figure 47: Mesh study results for the FEM modelling

However, the maximum deformation is not the most criterion of the mesh study. The quality of the deformation shape is also essential for a successful modelling. Especially for the later coupling, the shape must be smooth and any sharp edges cannot be accepted, as they would disturb the contacts between the two bodies. Three exemplary shapes are shown in Figure 48. For the left and the middle shapes the relatively sharp edge at the point of the most deformation are such disturbing areas. In case of building a contact area with a fluid body, these areas would lead to free space between the contact areas, which causes errors in the solving process. For the right shape, these errors could be prevented. The surface of the shape is not only visually smooth, but contains enough elements to enable a full contact between the film and the fluid volume.

In summary, it can be said that from the mesh study an acceptable mesh size could be found. Though it didn't match the recommendations of Ansys developers, the result quality was still sufficient and the size of the model problem was manageable. For all the simulation runs described in further sections, the minimum element size of 0.3 mm was used.

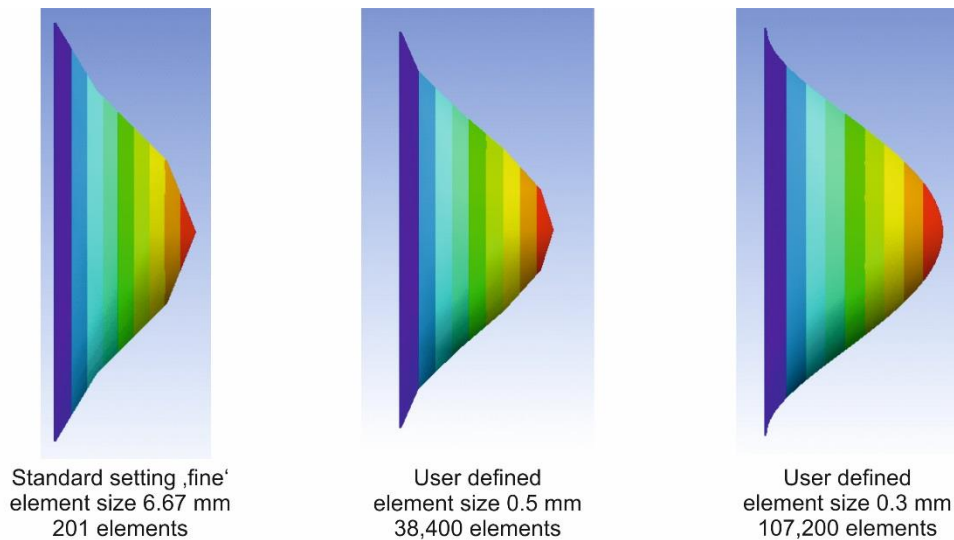


Figure 48: Deformed shapes of the deformed film (side view)

3.5.5. Modelling of the mechanical deformation

This section is based on the Ansys Mechanical User Guide (Ansys Inc. 2014c), all information is taken from it. The software module Ansys Mechanical® is available either as a standalone software package, which includes a pre-processor, a mesher, a solver and a post-processor or as a module within the Ansys Workbench® environment. While the standalone application Ansys Mechanical ADPL® provides the full functionality with extended meshing capabilities and material models, the module integrated in Workbench has a reduced functionality. However, the standalone software cannot be linked to other Ansys packages. The usage of the Ansys Parametric Design Language® (APDL) is also possible in the Workbench environment, but a separate module must be used coupled with the mechanical module.

Ansys Mechanical® was developed for FEM-based structural analysis with advanced modelling possibilities for non-linear material behaviour. In this work, the program was used for linear elastic materials only, therefore only few relevant features are described. For the modelling of the geometry and the meshing same modules can be used as for the CFX®-module. The material model is given by the engineering data, which contains all material properties. Since Ansys solvers perform the computing based on molar properties, at least the values for the molar mass, the Young's modulus and the Poisson's ratio must be set for every material. Some materials, such as structural steel and concrete are already implemented in the data base. For a more complex material behaviour, which can contain non-linearities, dynamic hardening etc. several further options can be used.

The APDL scripting an important part of Ansys Mechanical® as it provides advanced commands and methods for FEM-based analysis. All Ansys Mechanical® functions can be controlled with APDL commands. Some functions, like the export of the deformed mesh, can only be performed with an appropriate script, as the graphic interface doesn't provide it. The language contains several

commands for mathematical operations, solver controls and other features and can also be used for creating macros. A complete list of commands including explanations and syntax can be found in (Ansys Inc. 2011).

3.5.6. Fluid dynamics modelling

3.5.6.1. Domains

Before configuring the boundaries such as inlets, outlets and walls, the fluid volumes were declared as a fluid domains in Ansys CFX®. Four domain types are available: fluid, solid, porous and immersed solids. The both domain types used in this work were the fluid and the solid domains. The domain selection also activates the main settings for the model, such as material assignment, applied physical models and solver controls.

Fluid domain

The fluid domain is primarily used to model flows in gases and liquids. Apart from the material or in this case the fluid assignment, various fluid material model parameters can be set additionally. For single phase fluids and continuous phase transition processes the best suitable morphology is the “Continuous fluid”. For detailed condensation or boiling processes, the “Droplets” morphology can be used too, but it requires a very detailed knowledge of the estimated droplet size and the droplet interaction. Additionally, the reference pressure, the buoyancy vector parameters, motion of the domain and mesh deformation can be set. The last parameter is very important for the coupled fluid-structure-interaction. If the option activated, the deformable mesh regions must be specified as well as some mesh parameters.

Here must be said that a major part of the selectable options are beta-options, which means that they still are being developed and should not be used for reliable modelling. Especially the usage of different fluid materials in different domains of one model was still (Ansys Workbench® 15.0) only possible with activated beta options, as the same fluid material is being used for all domains of one model by default.

Further fluid model settings contain the heat transfer options. The thermal energy equations can be switched off completely; an isothermal simulation with a reference temperature or a heat transfer determination by only thermal energy or even total energy can be selected. The next block consists of turbulence modelling options. Here the available turbulence models, such as k- ϵ -model, the SST, BSL or SSG models. Laminar flows can be set as well. Another setting, which can be relevant for the heat transfer is the thermal radiation. For this, several models can be used, such as Monte Carlo, discrete transfer or spectral models. Since radiation was neglected in the simulation model presented here, the radiation settings are not explained here.

Solid domain

The solid domain model contains fewer settings than the fluid domain. The most parameters cover possible mesh deformation and heat transfer aspects. For the latter, the thermal conductivity as well as the thermal radiation options can be activated. As for the fluid domains, several mesh deformation settings are beta options and may not provide reliable results.

Inlet types

The selection of the appropriate inlet or outlet type is essential for a successful modelling. As no specified rules exist, according to which the suitable inlet type can be selected, several possibilities had to be tested. As the settings vary depending on the fluid properties and the selected fluid model, all settings, used in this work, will be explained here. For all inlet types, the flow regime can be specified; subsonic and supersonic flows can be studied depending on the selected turbulence model and the fluid material.

Velocity inlets

These boundaries are based on the assumption, that the speed is constant over the entire surface of the inlet. The velocity itself can be declared as orthogonal to the inlet area as well as by the Cartesian or the cylindrical coordinates systems. For all velocity inlet types, the turbulence intensity can be set as well as the inlet temperature, if the thermal energy option is activated in the domain. The turbulence can be adjusted by the intensity setting, in percentage of the entire flow, as well as by setting the values for the k - ϵ -parameters directly. Other turbulence settings are also available, depending on the selected fluid model. Furthermore, radiation settings can also be applied.

Mass flow rate

In this case, an average mass flow can be set either normal to the inlet area or specified by vectors in an appropriate coordinate system. This inlet type appears to be more accurate, as an inhomogeneous velocity distribution is being computed, with respect to the selected turbulence model and the specified wall parameters. It is also often useful for simulations, when the average speed information at the inlet is not available. However, the computation of the velocity profile might cause some errors, which occurred several times, during the model development.

Pressure based inlets

Two pressure based inlet types are available in CFX®: the static pressure and the total pressure. The options for turbulence intensity and heat transfer can also be set here. These inlet types are particularly suitable for gas flows with given pressure.

3.5.6.2. Outlet types

The selection of the appropriate outlet type is in some cases even more important than the choice of the inlet type. For the CFX[®] solver, the outlets must follow some rigid rules, which in fact are contradictory to the real physics and, hence, must be paid explicit attention to. The main principle of the outlet is the specified flow direction. Unless declared otherwise by setting the flow vectors, every flow must be oriented off the fluid domain. In cases when the physics (e.g. pressure) force the fluid to flow backwards into the domain, a wall is being placed on the relevant mesh element in order to prevent the backflow. On one hand, this mechanism can be useful, when the local pressure is computed in a wrong way in one specific iteration. On the other, in the worst case 100% of the outlet could be closed this way, which then leads to solver errors. This aspect is very important for low flow rates and especially for condensation processes, when the density of the fluid decreases significantly. If this behaviour occurs, switching the outlet to a pressureless opening might be a solution.

Velocity based outlets

The settings for the velocity based outlets are very similar to those of the velocity inlets. This setting enforces the solver to compute the velocity according to the setting. The velocity can be set as an average normal speed or by vectors in the Cartesian or cylindrical coordinate systems.

Pressure based outlet

This outlet type uses either an average static pressure in the outlet area or a static pressure condition outside the domain. In first case, several averaging options can best, such as circumferential pressure profiles or a radial pressure equilibrium. Both settings require a very good knowledge of the physical parameters of the outlet, which in many cases are not available.

Mass flow outlet

The explicit mass flow must be specified in this case. It is not possible to use the mass flow inlet and outlet in one domain, as it might lead to divergences. Additionally, a pressure shift option can be activated, which can be useful in case the pressure profile at the outlet is known.

3.5.6.3. Opening types

The opening is a boundary type, which allows the fluid to flow into as well as out of the domain. There are two types of the opening boundaries: the pressure based and the velocity based types. For the first type, the flow direction is computed with respect to the pressure gradient between the domain and

the specified outside pressure. The velocity vector declaration only specifies the direction vectors but not the orientation. For example: a vector [1,0,0] would only force the fluid to flow in x-direction, but does not specify whether it flows the positive or the negative way. Unlike the outlet, no walls are placed in case of an opening if fluid flows back into the domain. In cases when this behaviour is physically valid, the opening can be used as outlet. However, if no backflow is allowed or is physically not possible in the model, an opening could provide wrong results. For each option, any backflows can be easily detected in the solver log, so often a trial-and-error method for the determination of the proper outlet is to be applied.

3.5.6.4. Wall types

The wall boundaries significantly influence the flow; hence, the right settings must be chosen with care. In many cases, a simple adiabatic free slip wall is the right solution, especially if the roughness of the wall material is not known. If more information is available, the wall shear velocities can be set, which could be important for turbulent flows where near-wall areas have an influence on the flow. In cases no slip is expected on the wall, the wall roughness and if known the wall velocity can be specified. More relevant for this work are the heat transfer options. Either heat flux, temperature or a heat transfer coefficient can be set here. For the heat transfer between two domains the declaration of the contact boundaries as a wall is not appropriate, since no material data, e.g. thermal conductivity can be declared here. In this case, interfaces must be used.

3.5.6.5. Interfaces

Interfaces allow the connection between two domains in case of 3D-simulations. Normally, the pre-processor CFX-Pre[®] automatically recognises the relevant contacts between bodies and declares them as simple interfaces. Especially for heat transfer applications the interfaces are inevitable, as they provide the possibility to model heat flux from one domain to another.

All domain types, such as solid, fluid or porous can be connected by appropriate interfaces. For example, a simple two chamber heat exchanger can be modelled with two solid-fluid interfaces in order to imply both fluid bodies and the heat transferring wall as a solid body. Although this modelling type is appropriate and physically valid, a simpler model can also be used. A virtual wall can be added to the interface model. This allows avoiding the third solid body, but it keeps the physically important heat conduction information through the wall. Therefore, additional interface models must be activated with the heat transfer option. Now the interface is considered as a wall with extended heat transfer features. With the option "Conservative heat flux" the thickness of the virtual wall can be set as well as the material, which contains all the necessary thermal conductivity or heat capacity data, relevant for the heat transfer model.

3.5.6.6. Materials

All materials, including solids and fluids can be defined here. Depending on the model requirements, various material properties can be set. These can be either constant or variable. For variable data, mostly temperature or pressure dependent, several input possibilities exist. Apart from tabled data, equations can be used to approximate the values of the properties. Water as the most commonly used fluid is already implemented with constant data, as well as with the IAPWS tabled data and the NASA equations. While no further settings are necessary for the IAPWS data, as all required equation coefficients are already implemented, for the NASA equations the values for the fluid specific parameters must be entered.

For user-defined functions, the specific CFX Expression Language must be used. This consists of common mathematical operators and a set of physical constants, such as the universal gas constant or the dimensionless number π . Apart from that, all flow variables, like the velocity as vector quantity, the pressure or the temperature can also be implemented into expressions. This is important for computing the pressure or temperature dependent fluid properties. Furthermore, logical expressions can be created by use of the common “if-condition”.

3.5.7. Flow and heat transfer modelling

3.5.7.1. Simple, one-phase, stationary heat transfer model

For single-phase simulations with pure liquids, such as water or non-condensing organic solvents, a simple, stationary k - ϵ -model was used for the determination of the flow and the heat transfer. Since the temperature differences between the inlet and the outlet on the cooling side are below 10 K, constant fluid properties (density, specific heat capacity, heat conduction and viscosity) were assumed. For preliminary runs, used for the mesh quality evaluation, constant fluid properties were also used for the hot side, despite much higher temperature differences. For organic solvents, however the temperature differences are much higher, due to lower mass flows. Hence, the relevant liquid properties were modelled by approximation equations taken from (VDI 2006) shown below.

The parameters for the relevant fluids in respect to equations (2.47) to (2.50) (water and hexane) are given in Table 14. For many cases, short equations with parameter sets from ‘A’ to ‘C’ are sufficient (VDI 2006). In this work, the entire equations with the complete parameter set were used in order to achieve the best accurate results.

For the determination of the proper fluid properties, the solver required some more options adjusted. The solver creates a table with all relevant properties, which are being used for further computations of the flow. Therefore, the limits for used variables must be set in the pre-processor, to reduce the

amount of the generated data. As only the temperature was used as an equation variable, these were set to $T_{\min} = 5^{\circ}\text{C}$ and $T_{\max} = 90^{\circ}\text{C}$.

As can be seen in the experimental data, this range is wider than the actual operating range. This was done to avoid undefined variable ranges. Depending on the quality of the mesh, minor errors can occur during the simulation run on a specific cell with the consequence of computed temperatures, which are lower or higher than expected. These minor errors do not affect the overall solution results, as they might only occur at specific iterations, especially at the beginning of the run. By expanding the variable range these errors can be covered.

Table 14: Dimensionless parameters for material property approximation equations (liquid state)

Fluid	Property	A	B	C	D	E
Water	Density	1.5053957	0.03642	617.774	0.05771	-
	Dynamic viscosity	-22.967	3275.79	0.017637	$6.93 \cdot 10^{-7}$	$-1.2933 \cdot 10^{-7}$
	Thermal conductivity	-0.3623	$0.50659 \cdot 10^{-2}$	$-5.705 \cdot 10^{-6}$	$-1.527 \cdot 10^{-9}$	$1.747 \cdot 10^{-12}$
	Specific heat capacity	3092.00	12.327	-0.044504	$5.226 \cdot 10^{-5}$	-
Hexane	Density	3.7550573	0.06603	523.991	0.12451	-
	Dynamic viscosity	-12.493	1027.57	$3.16 \cdot 10^{-3}$	$-2.26 \cdot 10^{-7}$	-
	Thermal conductivity	0.2331	$-4.713 \cdot 10^{-4}$	$7.35 \cdot 10^{-7}$	$-1.733 \cdot 10^{-9}$	$1.67 \cdot 10^{-12}$
	Specific heat capacity	2002.30	-2.177	$1.0473 \cdot 10^{-2}$	$-2 \cdot 10^{-7}$	-

Furthermore, the buoyancy settings must be implemented to consider the gravitation. The relevant buoyancy parameters are vector based, so the direction of the gravitation force can be adjusted with respect to the orientation of the geometry. In addition to that, a reference density of the volume fluid must be set. In this case, the density of the fluid at 1 bar pressure and 20°C was selected.

For the heat conduction through the polymer film modelled as a virtual, contact wall, constant values were used for the thermal conductivity and the density. The reference temperature for these properties was set to 20°C , as most available material data is related to this temperature. Though that, the average temperature of the film during operation of the heat exchanger is about 30°C , the deviations of material properties are negligible. The simulation runs are stationary hence; the specific heat capacity is not necessarily needed for solving this problem. The used solid polymer properties are given in Table 15.

Table 15: Material properties of the PET polymer film

Property at 20°C	Symbol	Value / unit
Molar mass (of one monomer)	M_{poly}	192 kg/kmol
Density	ρ_{poly}	770 kg/m ³
Heat conduction coefficient	λ_{poly}	0.25 W/m K
Specific heat capacity	c_{poly}	1100 J/kg K

3.5.7.2. Extended one-phase model with geometry deformation

This model can be described as one way coupling between the pure fluid dynamics and the structural FEM-analysis which provides a stationary, deformed geometry, bounding the fluid. It was also the first step towards the full two-way coupling.

Determination of the deformation

The Ansys Mechanical Stationary module provides the first part of the model, the stationary FEM-Analysis. For the determination of the deformation, a simple reversible, linear elastic material model with a stationary, evenly distributed load was used. Only two material parameters are used here: the Young's modulus and the Poisson's ratio. Both values were set for the material model, in order to match the experimentally determined deformation results. In this case, the usage of the wrong material property values is legitimate, since only the correct shape of the geometry was needed as the result and the inner tensions are not of interest. In order to describe the relatively low deformation (1-2 mm) compared with the entire geometry (170 x 170 mm) dimensions, very small meshing elements had to be chosen, which caused several problems during the simulation run. This is described in section 4.1.3.

Transferring the deformation to the initial geometry.

After the deformed geometry was computed, the initial geometry had to be updated by the deformation to generate the new deformed shape. For this, Ansys provides the command 'UPGEOM' within the APDL (Ansys Parametric Design Language), which stands for 'UPdate GEOMetry'. In the Ansys Classic environment it is also available as a selectable menu command. In the Workbench environment, the usage is only possible with APDL scripts. It moves each mesh element from the initial position within the geometry to a new position described by its displacement in the relevant coordinate system (Ansys Inc. 2011).

The command contains several options. The first one is the 'Factor', which can be used to magnify the displacement values. The default value is 1.0, which means that the deformation is applied without

any modifications. Furthermore, the load steps and the substeps can be provided. This is relevant for the transient models with non-constant loads. In this case, the model is stationary, hence, the load step doesn't have to be specified. The deformation information is always written to a file, from where it can be determined any time after the export. In this file, the displacements for each element are written for all coordinates in the used coordinate system. To save the file, the name as well as the file extension must be provided. Hereby, it must be said that the file extension must be 'RST', because no other extensions are accepted by the command, but it must be set anyway.

In some cases, especially if the geometry is large or have a complex shape, additional solver controls must be set, to reduce memory, CPU or disk space usage. The first control is the overall complexity of the problem. For complex shapes a value greater than 3 is advisable, the default value is '0'. The next values set the memory, CPU and disk space settings. Detailed information on these can be found in (Ansys Inc. 2011). Furthermore, a new geometry file must be created, for which the command 'CDWRITE' must be used. It creates a new file containing the geometry with displacements. This file must have the extension 'cdb'.

The complete script including the activation command '/prep7' of the pre-processor command module is:

```
PCGOPT,1,--,NO,OFF,ON,AUTO,OFF
```

```
/prep7
```

```
UPGEOM,1,1,1,newgeo,rst
```

```
cdwrite,db,newgeo2,cdb
```

Creating a usable geometry for a CFD-solver

For this, the Workbench module called 'Finite element modeler' must be used. By the previous step, only a collection of the mesh elements with the relevant coordinate are created, but this result does not contain any information about the boundaries and surfaces of the geometry. These are created in the 'Finite element modeler'. The module finds new surfaces with the corresponding edges and splits curved surfaces to match the later requirements for the meshing. It is also possible to export the deformed shape to other CFD or FEM programs, such as NASTRAN or ABAQUS. In our case, a direct export within the Workbench environment was required, therefore, the export to Ansys APDL was used.

Connecting the single steps

In case the model contains two or more bodies, the bodies, which are not supposed to be exported, can be suppressed. The export destination is set by the 'wire' connection (blue) to the next solver module, as shown in Figure 49.

The blue dot at the end of each line indicates the direction, which is used for the export of the information data. Since the entire model is a one-way simulation, the results are exported from left to right.

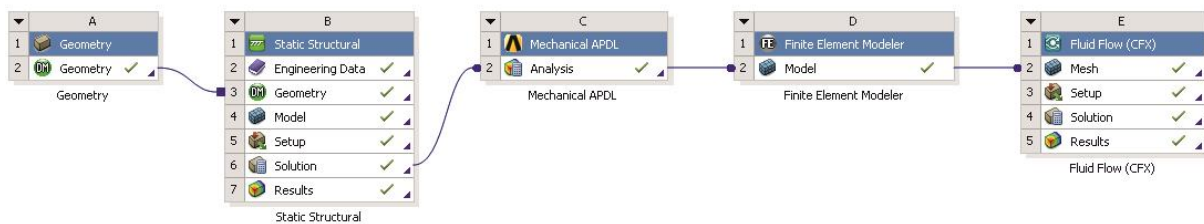


Figure 49: Model scheme for the serial non-coupled model in Ansys Workbench®

3.5.7.3. Coupled fluid-structure-interaction model

General preliminary considerations

The coupled FSI (Fluid-Structure-Interaction) is the most complex model used in this work. In general, it must be said, that this type of coupling possibility is a relatively new feature in Ansys Workbench, which despite excessive work could only be successfully implemented with the Workbench version 15.0. Previous versions either generated too many errors during the execution or the necessary connections between the modules were not allowed by the software environment.

The main principle of the two-way coupling is the exchange of the solution information between two solvers for each iteration step. In this case, the deformation of each cell must be exported to the CFD-solver as a geometry. This deformation itself is caused by the fluid based pressure loads on the structural part of the model, which are exported from the CFD solution. This principle is shown in Figure 50.

Before building up such a coupled model, a complete understanding of this principle and of all consequences for the solver must be fully understood. Several conditions must be fulfilled to create a successful model. First, the contacts between the fluid and the solid (structural) bodies must match exactly. Only if this is the case, the deformation information can be transferred from the structural

body to the fluid. In consequence, this means that both meshes (for the FEM and the CFD parts) must be exactly the same, at least at the contact surfaces.

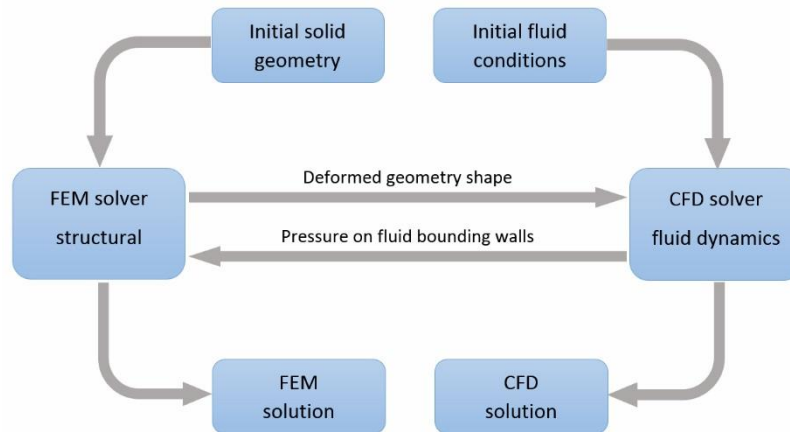


Figure 50: A block diagram of a FSI principle

If the contact surface is not plane, which is the case for most FSI problems, the mesh must be fine enough to eliminate the possibility of intersections of mesh elements or the creation of gaps between deformed shape mesh and the corresponding fluid area.

3.5.7.4. Phase transition heat transfer model

Since the main application of the modelled heat exchanger is the condensation of organic solvents, an attempt to simulate the phase transition was made. In general, a very detailed knowledge of the fluid properties in both phases is absolutely necessary to provide a physically valid model. In case of water (only used for preliminary tests of the model) and of the used organic solvent hexane the relevant physical properties are either obtainable from tables or can be computed by approximation equations, such as the Real-Gas-Equations (RGE). For water, these are already included in the CFX material data base as the IAPWS-data base (Ansys Inc. 2014a). For hexane, they have to be implemented by appropriate expressions. Several possibilities are available for the determination of the fluid properties. For the liquid phase, the same equations and coefficients were used as for the single-phase model (s. 0). For the gaseous phase, similar equations are available. The compressibility of the gas is here taken into account by the density function which has both pressure and temperature as relevant parameter. For pressures below 5 bar the simple Ideal-Gas-Law can be used with sufficient accuracy of the results (VDI 2006). The standard implementation in Ansys CFX, however, is either the Peng-Robinson (equ. 2.45) or Soave-Redlich-Kwong (equ. 2.42) equations.

It is also possible to use constant properties for each phase, but the usage real gas equations has become best practice for such models. In this case, the equations (2.47) to (2.50) were used to

generate a data table for the gas and the liquid phase, as they provide sufficient data for the description of the material behaviour in the relevant temperature and pressure range. The relevant parameters for the gas phase of hexane are given in Table 16.

The phase transition itself is forced by the saturation conditions such as the saturation pressure p_s and the saturation temperature T_s . The corresponding Antoine equation defines the connection between the two phases and enables to determine the thermodynamic condition for the phase transition.

Table 16: Parameters for material property (gas state) approximation equations (2.47) to (2.50)

	Property	A	B	C	D	E
Water	Density	1.505	$3.6 \cdot 10^{-2}$	$6.178 \cdot 10^2$	$5.771 \cdot 10^{-2}$	-
	Dynamic viscosity	$-2.297 \cdot 10^1$	$3.276 \cdot 10^3$	$1.763 \cdot 10^{-2}$	$6.93 \cdot 10^{-7}$	$-1.293 \cdot 10^{-7}$
	Thermal conductivity	$-3.623 \cdot 10^{-1}$	$5.066 \cdot 10^{-3}$	$-5.705 \cdot 10^{-6}$	$-1.527 \cdot 10^{-9}$	$1.747 \cdot 10^{-12}$
	Specific heat capacity	$3.092 \cdot 10^3$	$1.233 \cdot 10^1$	$-4.4 \cdot 10^{-2}$	$5.226 \cdot 10^{-5}$	-
Hexane	Density	3.755	$6.6 \cdot 10^{-2}$	$5.24 \cdot 10^2$	$1.24 \cdot 10^{-1}$	-
	Dynamic viscosity	$-1.249 \cdot 10^1$	$1.028 \cdot 10^3$	$3.16 \cdot 10^{-3}$	$-2.26 \cdot 10^{-7}$	-
	Thermal conductivity	$2.331 \cdot 10^{-1}$	$-4.713 \cdot 10^{-4}$	$7.35 \cdot 10^{-7}$	$-1.733 \cdot 10^{-9}$	$1.67 \cdot 10^{-12}$
	Specific heat capacity	$2.002 \cdot 10^3$	-2.177	$1.047 \cdot 10^{-2}$	$-2 \cdot 10^{-7}$	-

For the determination of the vapour mass fraction x the lever rule (3.1) is being used by the CFX-solver (Ansys Inc. 2013):

$$x = \frac{h_{\text{mix}} - h_{\text{sat,l}}(p)}{h_{\text{sat,g}}(p) - h_{\text{sat,l}}(p)} \quad (3.1)$$

Herein h_{mix} denotes the enthalpy of the gas-liquid mixture and $h_{\text{sat,l}}$ as well as $h_{\text{sat,g}}$ denote the pressure dependent enthalpies of the liquid and the gas phase respectively. In CFX, this connection is being created with the Homogeneous Binary Mixture model. In case of user-defined functions for material properties, the saturation properties must be set either as a function of temperature (Antoine equation) or as a constant value. Despite the inaccuracy of the Antoine equation (VDI 2006) it is the standard equation implemented in CFX. Three material dependent parameters are required for the equation to determine the temperature dependent saturation pressure as follows:

$$p_{\text{sat}} = p_{\text{scale}} \exp\left(A - \frac{B}{T + C}\right) \quad (3.2)$$

with the saturation pressure p_{sat} and the constants C and B.

4. RESULTS AND DISCUSSION

4.1. MECHANICAL STABILITY AND CHEMICAL RESISTANCE

In this section, the results of the experimental studies on the material properties are presented. Since the observed behaviour was different for the static and the dynamic pressure loads this section is split into two subsections for the pressure load type. For static and dynamic static loads a pressure of 6 bar was applied. The static load as well as the pulsating load testing was performed at 90°C. Due to the low boiling point, additional testing was performed at 70°C for hexane and heptane, but no significant difference of the behaviour at this lower temperature could be observed.

4.1.1. Static pressure load

4.1.1.1. Main test results for the polyimide film

Deformation

The main test results for the polyimide film are given in Figure 51. Despite the information on the chemical resistance of the material provided by the manufacturers, toluene and tetrahydrofuran had a major impact on the behaviour of tested films.

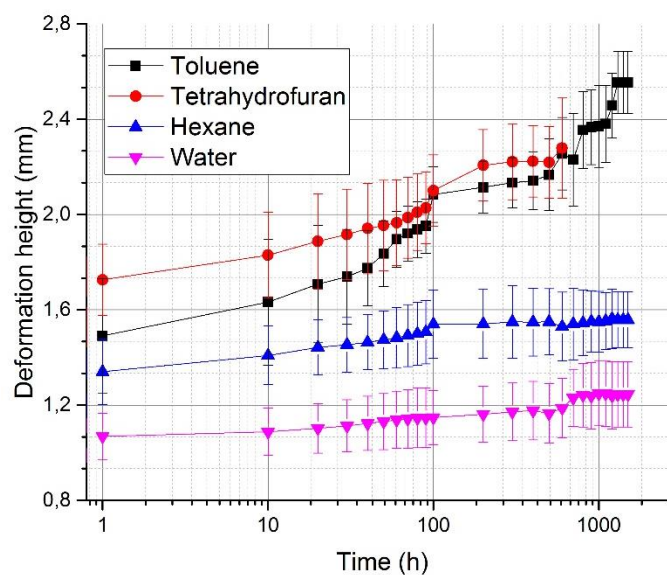


Figure 51: Comparison of the deformation heights for the polyimide film

Neither the simple alkanes such as hexane nor water did affect the mechanical strength of the film severely. While the average deformation height of the samples exposed to water was 1.24 mm, the contact with hexane increased it to 1.56 mm. In both cases, no significant creep could be observed after testing periods between 500 and 700 hours for water and hexane respectively. The graph only shows the results for hexane, the results for heptane are hidden, as they correspond with the hexane results. No difference could be observed between the two alkanes with respect to their influence on

the film behaviour. For this reason, the results of hexane represent both alkane testing procedures. Furthermore, it must be said that the temperature difference for the testing procedures with alkanes, 70°C for hexane and 90°C for heptane did not show any influence on the results.

As mentioned above toluene had a major impact on the mechanical strength of the tested films. In contrast to exposure to hexane a permanent and significant creep could be observed during the entire testing period for all used film samples. From the first hours of the experiment the deformation height of the film was considerably higher with 1.51 mm than with water (1.05 mm) or hexane (1.27 mm). For longer exposure periods the difference increased up to the double deformation height of water. Since the creep was observed during the entire testing period, the deformation height can be expected to continue increasing, which is an important aspect to pay attention to for the apparatus design.

Tetrahydrofuran had an even larger influence on the mechanical strength of the film than toluene. As can be seen in Figure 51, the graph of tetrahydrofuran ends at approx. 700 hours. This represents that all six samples broke a latest after this exposure time. The deformation height was not much larger than with toluene. During the first 30 hours, it was about 0.2 mm and below 0.1 mm afterwards. However, the contact with tetrahydrofuran caused a major damage of the material, which led to the observed premature failure. The failure times of each sample varied highly, too.

Inner material structure changes and inhomogeneities

These deviations between the results of the samples taken from one film were observed for all fluids the films were exposed to and are represented by the error bars in Figure 51. A better overview of the high variety of the deformation results is given in Figure 52. For better visualisation of the different break times, a linear scale was used instead of the usual logarithmic scale.

As can be seen, the break times varied between less than 200 hours for Sample 4 and over 700 hours for Sample 2. Here it must be said, that all samples were taken from one film roll with the size of an A4-sheet. Furthermore, all tested samples were visually checked for damages in the exposed area by a microscope with a 20x magnification.

These deviations can be explained by inhomogeneities in the film material as well as by deviations of the thickness. Although most manufacturers do not provide official information on the accuracy of the thickness of the produced films, it is known that the thickness can vary up to +/- 20% from the nominal. Which in case of the tested 75 µm film leads to a thickness between 0.06 mm and 0.09mm. Therefore, the films were observed under the microscope for possible inhomogeneities or even damages of the inner structure.

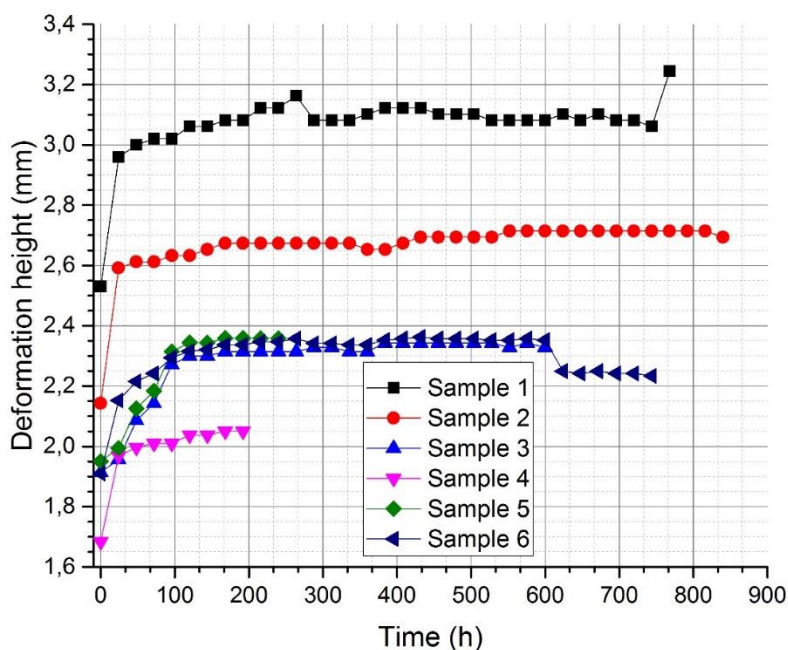


Figure 52: Deformation heights of six polyimide samples exposed to tetrahydrofuran

In Figure 53 the inner structure of the polyimide films at a magnification of 20 before and after the experiment is given. The right side of Figure 53 shows the undamaged part of the film. Apart from the change of colour, no significant changes of the structure could be observed. This colour change was not only observed for the film, but also for the used solvent. In normal condition, tetrahydrofuran is colourless, but after the experiment, it became orange. Similar change of colour was also observed for the contact with toluene. Here the solvent turned light brown after the experiment. Both solvents with the colour change are shown in Figure 54. For toluene, a light turbidity occurred, while tetrahydrofuran remained clear.

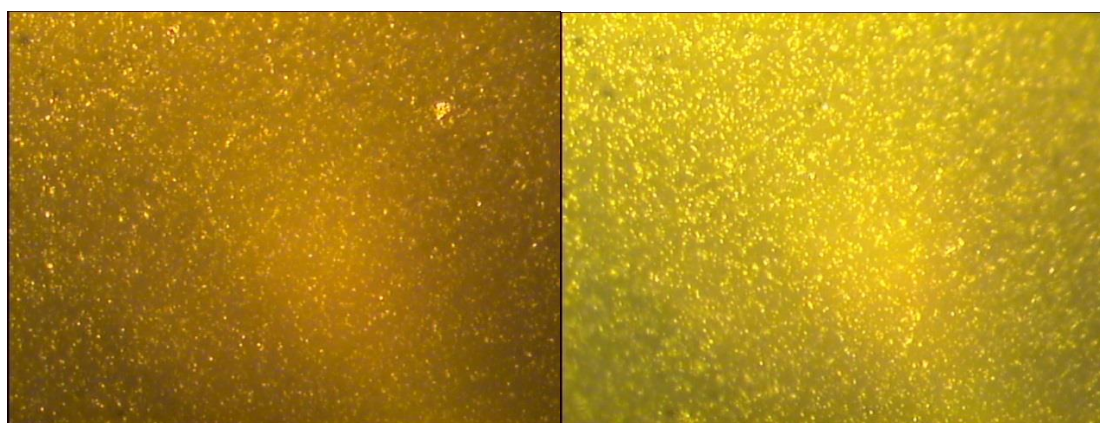


Figure 53: Microscope pictures of the polyimide film before (left) and after the exposure (right)

For polyimide, it can be hence summarised that despite its acclaimed excellent properties it can't be used for application which involve toluene and tetrahydrofurane. For alkanes, such as hexane and

heptane or water it is suitable as it provides a sufficient chemical resistance and the mechanical properties are not severely influenced by the liquid.



Figure 54: Colour change of the solvents: toluene - left, tetrahydrofuran - right

4.1.1.2. Main test results of the PTFE-glass fibre compound

Deformation

The results for the PTFE-glass fibre compound, which are given in Figure 55, show a different behaviour compared to polyimide. First, it was observed that the presence of water does not affect the film at all. Neither creep could be measured nor were any damages or failures of the samples observed. The deformation heights for all fluids are lower than for the polyimide film; the glass fibre enforcement appeared to be effective.

As for polyimide, the results with hexane and heptane for the PTFE-glass fibre film samples show a similar trend (the graph for hexane represents both solvents). While the deformation height was increasing very slowly during the first 500 hours, after that significant creep occurs during the exposure time between 500 and 900 hours. After this period, no creep could be measured until the end of the experiment.

This stepwise behaviour could also be observed during the exposure to toluene. Here the significant creep started after about 100 hours. In contrast to hexane, the creep did not stop but continued until the end of the experiment. Four of six tested samples failed during this period. The two intact samples, however, did not show any damages. The average deformation height was a little higher than with hexane, but still much lower than the corresponding values for polyimide. However, it must be taken into account that the deformation is most probably expected to continue increasing which would lead to higher deformation for longer exposure times.

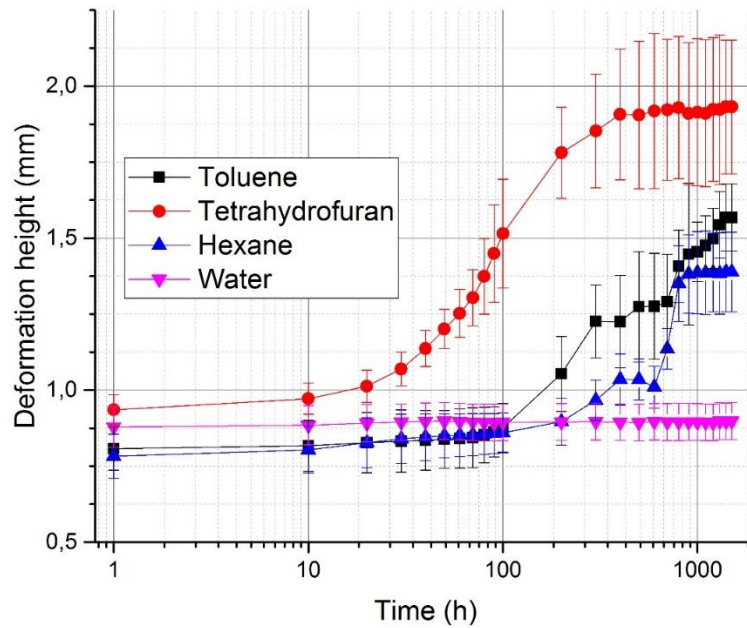


Figure 55: Comparison of the deformation heights for the PTFE-glass fibre film

The highest impact on the mechanical strength of the film samples was caused by tetrahydrofuran. The creep in the material was quite high for the first 200 hours, after that it became lower and finally almost no creep could be measured after 500 to 600 hours. However, the deformation height was the highest (1.9 mm) for the PTFE-glass fibre films, but still below the corresponding values of the polyimide with the maximum height of over 2.2 mm. Furthermore, it must be said, that from the six tested samples three failed after less than 10 hours of exposure. The other three samples remained intact and showed no damage till the end of the experimental time.

Inner material structure changes and inhomogeneities

For the PTFE-glass fibre compound deviations between the used samples occurred too. Especially with tetrahydrofuran, they were extremely high with over +/- 13% from the average value. The break times for the failed samples also varied highly, as can be seen in Figure 56. While the premature break occurred within 200 hours, the deformation height of the intact samples only increased until approx. 500 hours and then no creep could be observed. Hence, it could be said that the time limit of approx. 200 hours is a critical exposure period, after which no breakage occurred. In order to prove this expanded testing has to be performed with a number of samples sufficient for empirically based conclusions.

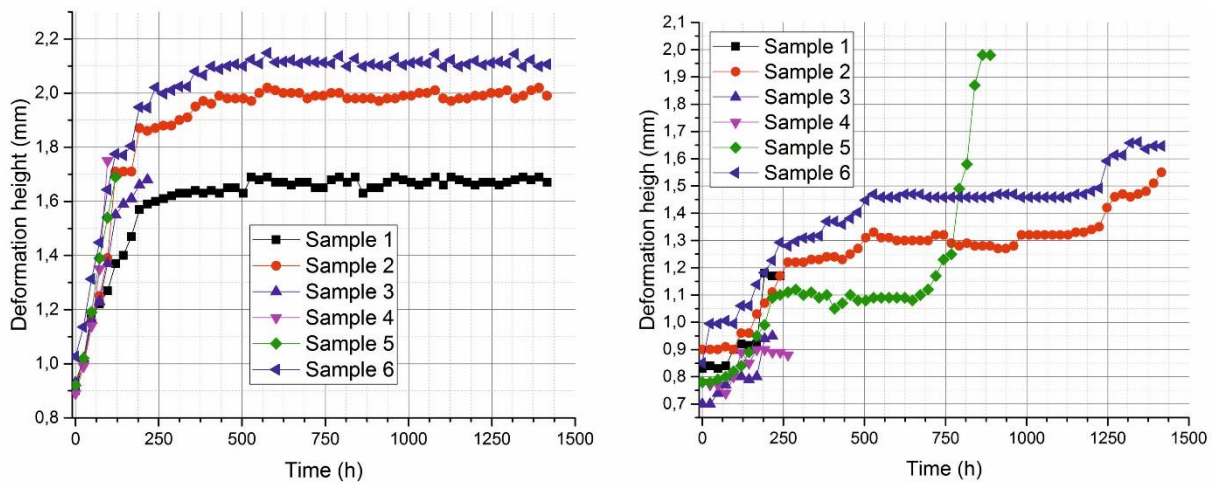


Figure 56: Deformation heights of the PTFE-glass fibre samples exposed to tetrahydrofuran (left) and toluene (right)

The inner structure of the PTFE-glass fibre compound is definitely one of the obvious reasons for this highly deviant behaviour. The glass fibre mesh, which is coated with the PTFE-matrix, is irregular and has many voids. This is shown in Figure 57.

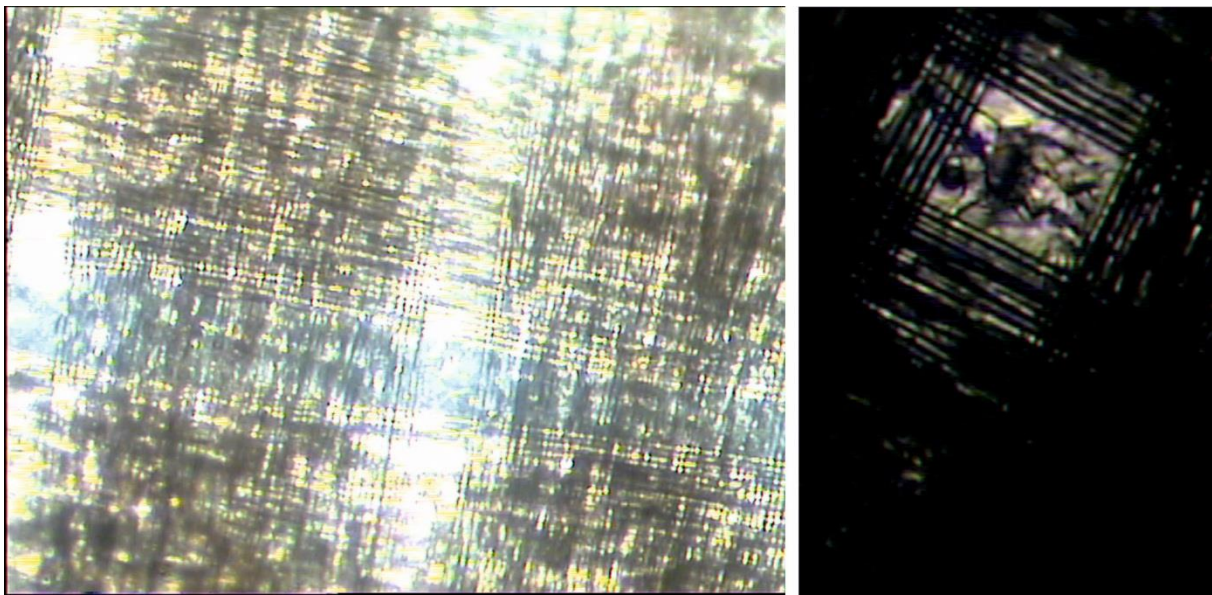


Figure 57: Inner structure of the PTFE-glass fibre compound; left: 20x magnification; right: 100x magnification

Even with the smaller magnification, it is obvious that the glass fibre mesh is highly irregular. The white areas in the picture indicate the low density of the fibres and hence the weaker regions of the film. Though the voids shown on the right side of Figure 57 are about approx. between 100 and 400 μm and hence much larger than the area of the film exposed to fluid and pressure, they surely affect the mechanical strength of the sample and can be the explanation for the highly inhomogeneous behaviour.

Another interesting aspect about the material properties is the stepwise increase of the deformation heights. This also can be explained by the inner structure of the compound. The solvent diffused

through the outer PTFE-layer. This process was very slow and hence for the first 100 hours the deformation was very low too. After is time the diffused molecules of the solvent get through to the contact surface between the PTFE-matrix and the glass fibres and not only reduce the adhesive force between the two compound parts but also between the single glass strings. This weakens the inner structure, makes it more flexible and causes the significantly higher deformation, which was observed after 100 – 200 hours.

Summing up it can be said that both tested materials showed major weakening caused by the organic solvent. However, while for the polyimide the contact with THF and toluene often led to failure of the material, the PTFE - glass fibre – compound was able to withstand the mechanical and thermal loads without any damage to the material. For this reason, the latter is the most favourable material for this application.

4.1.2. Pulsating pressure load

The investigation of the pulsating load was done to determine the influence of alternating loads on the durability of the materials. For the heat exchanger design, the knowledge of the dynamic behaviour is also important, as it provides additional information about the possible number of start-ups.

As already described in section 3.4.4, these testing procedures could only be performed with water. Therefore, the reference for the pulsating pressure load is the constant pressure load in water. In Figure 58 a comparison between the constant load behaviour and the behaviour for the two tested pulsation speeds is given. It covers a time period of 200 hours and visualises the time-based analysis.

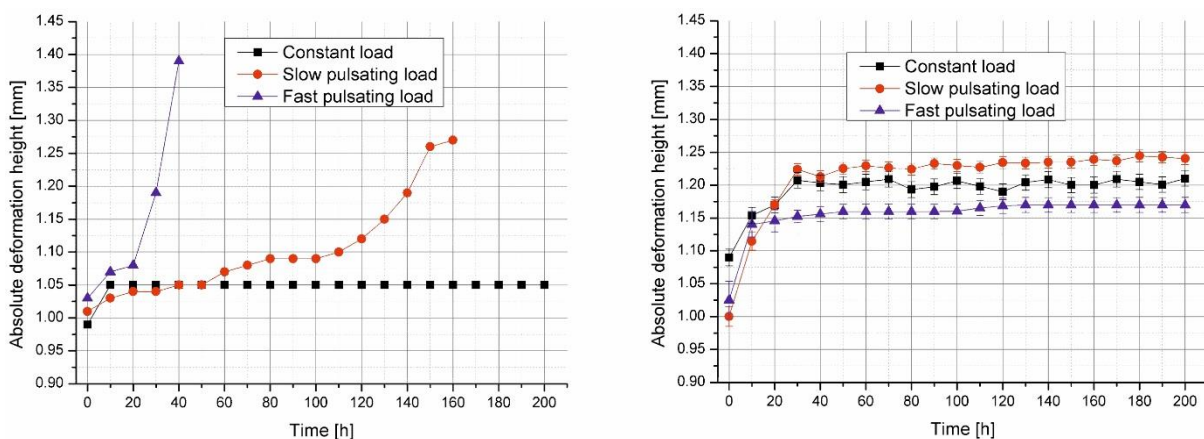


Figure 58: Time-based comparison of the material behaviour for different load types; left: PTFE - glass fibre - compound, right: polyimide

As can be seen in Figure 58, the behaviour for the tested materials is completely different. Polyimide shows a very low affection by the pulsation, either fast or slow. For the PTFE – glass fibre – compound the lifetime of the material was significantly reduced by pulsations.

Polyimide showed a typical hardening of visco-elastic polymeric materials, as the lowest deformation occurs at the fast pulsation speed. This behaviour corresponds with observations made by (Serban et al. 2013) or (Shi et al. 2002). For the low pulsation speed, however, this phenomenon was weaker, which means that the speed was not high enough, and hence the relaxation time was sufficiently long to enable a slightly higher deformation, than at constant load.

As said above, the PTFE – glass fibre – compound appeared to be significantly affected by the pulsating, especially at lower speed. This impact can be explained by the inner structure of the compound. The glass fibres, which are the responsible for the stability within the compound, have a very low ductility. Therefore, they are very sensitive to brittle fracture, which is most like to occur during pulsating loads at higher speeds. The graphs for the low and high pulsation speeds visualise the influence of the pulsation rate. For a better visualisation of this behaviour, a different plot is more appropriate, which contains the number of the load changes in the horizontal axis instead of the time. This is shown in Figure 59.

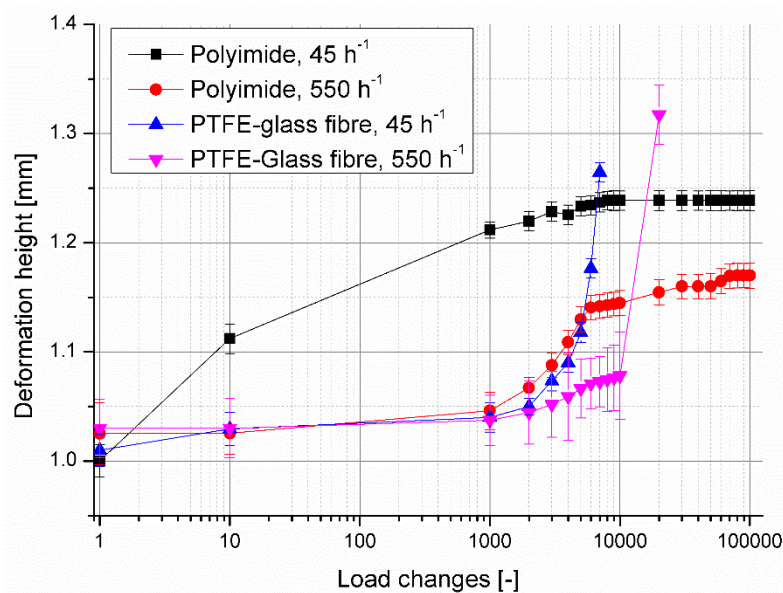


Figure 59: Comparison of the performance of the polyimide film and the PTFE-glass fibre compound at pulsating pressure loads

On the other hand, at the higher pulsation rate of 550 h^{-1} much higher load change numbers could be reached, than at the lower pulsation rate of 45 h^{-1} . As in case of the polyimide, this can be explained by the visco-elastic behaviour of the PTFE, with the increase of the material strength at fast deformations.

The differences between the two materials considering the deviation range of the tested six samples displayed by means of the error bars is also interesting. While for the polyimide film the deviations were insignificant and all six samples showed almost the same deformation, for the PTFE-glass fibre

compound the deviations were much higher. Here again, the inhomogeneous distribution of the glass fibres is primary cause for this, as it is impossible to produce six samples with equal inner structure.

To summarize the results of the investigation of the films, it can be said, that the overall suitability was better for the PTFE-glass fibre compound, due to the much better long-term resistance to organic solvents, especially to toluene and tetrahydrofuran. The polyimide film not only showed significant decomposition, but also caused a colour change of the solvent. And it also failed mechanically at contact with toluene. The dynamic weakness of the PTFE-glass fibre compound is to be considered for the development of the application design. However, for static loads its performance is the best.

4.1.3. Deformation modelling for coupled FSI-models

For both model types, the one-way and the two-way coupling, several problems occurred during pre-processing and solving. First it must be said, that most options that needed for both models also required the activation of the beta features. Especially for the two-way, full fluid-structure interaction, almost the entire model was implemented with the beta features. Second, a full integration of at least liquid-liquid heat transfer was not possible in principle. Though the required sub-models could be activated for the boundaries between the film and the fluids, no heat transfer results could be computed.

In summary, it can be said, that the FSI-functionality within Ansys Workbench (Version 15.0) was still limited to very basic physical models, so only little information could be obtained from the results of the modelling.

In principle, the one-way coupling, as shown in Figure 49, worked fine, and a static deformed shape of the fluid volumes could be obtained with this model, which is shown in Figure 60. The width of the channels is 2 mm and the distance between them is 3mm. Here the hot side of the lab-scale heat exchanger is given, with the deformation caused by the higher pressure on the cold side. As can be seen, a smooth surface was generated, mapped by approx. 2.9 million tetrahedrons. This mesh size was still manageable for the geometry transfer to the CFD module. It also showed no errors or areas with a coarse mesh, which would result a faulty geometry.

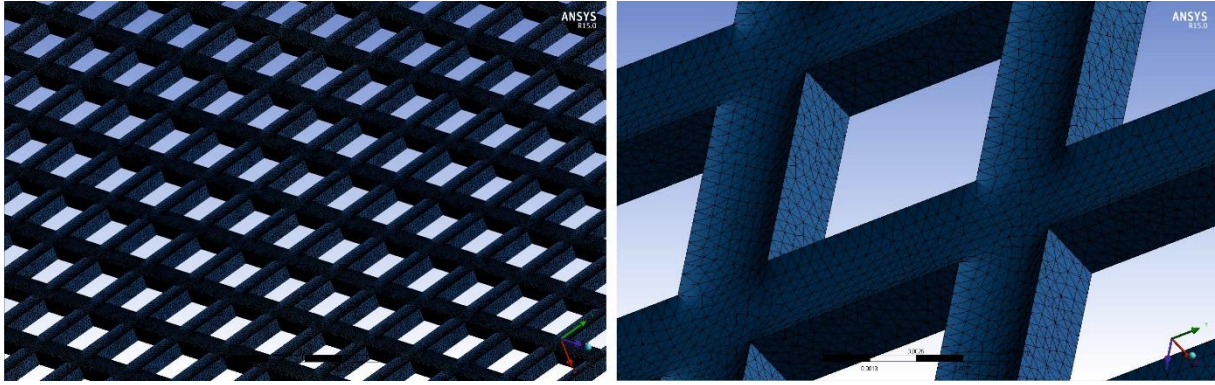


Figure 60: Deformed shape of the lab-scale heat exchanger after FEM analysis

With the next step, the deformed shape was exported to the meshing module included into the CFX model. The result can be seen in Figure 61. At first sight, the mesh transfer seemed to be successful. The deformations were transferred with a similar mesh size and shape. However, several errors occurred too. The right part of Figure 61 shows one of them. For some unexplainable reasons the mesh size was reduced at some areas, which made the surface less smooth. Furthermore, the tetrahedrons became sharp, which means that one angle was less than 10° . According to (Ansys Inc. 2014a) such mesh elements might cause singularities, during computing, which may lead to solver crashes. Even neglecting the latter, the deformations shape was transferred with errors, which has an impact on the result.

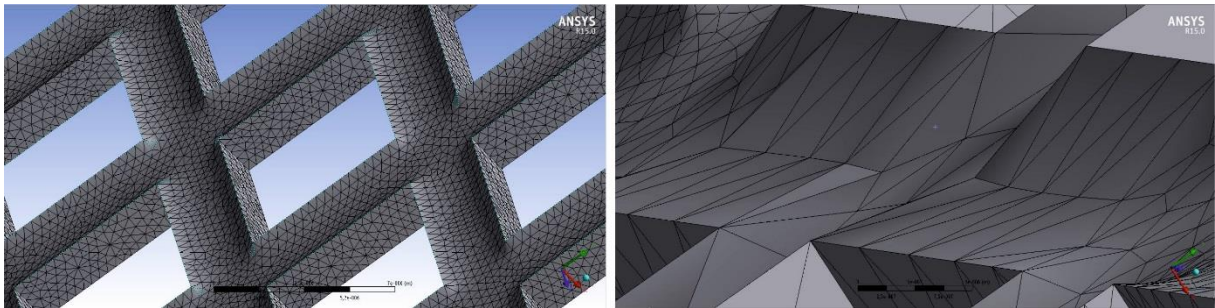


Figure 61: Deformed shape of the mesh received with errors by CFX®

Another problem appeared to be much more severe, than the shape errors. With this method, only one part of the lab-scale heat exchanger could be modelled, due to the huge hardware requirements. The try to model both fluid volumes and the film failed; the FEM solver was not able to compute the deformation with the required accuracy with an available memory of approx. 64 GB. With a coarse mesh, a computation was possible but resulted in an unacceptable shape quality. This is already described in section 3.5.4. A reduction of the problem to two deformable fluid volumes, that included the negligence of the film, delivered the same problems and no satisfying results could be obtained.

For the two-way coupling, showed in Figure 50 the situation was much more complex. First, the mesh size became unmanageable for the entire geometry, leading to elements numbers over 10 million. A

reduction of the mesh number led to FEM errors or to wrong deformation results with intersections between the elements of the fluid bodies. For a proper determination of the deformation, a test section (3 x 3 mm), which is shown in Figure 62 consisted of approx. 22,000 mesh elements. The full-scale heat exchanger contains over 2100 such sections, which leads to an element number of over 43 million per fluid volume. Such a number could not be handled with the given IT-infrastructure.

Apart from that, one additional limitation was discovered during building-up the model. With the used CFX - solver it was only possible to couple an isothermal fluid flow with the structural analysis. Heat transfer through a deformable or moving mesh was available as option, but was not computed. Another important constraint was the inability of the coupling mechanism to use two fluid volumes with a solid volume between them. Hence, all trials to model a complete element, containing the hot, the cool sides and the film resulted in warnings given by the pre-processor and finally in solver crashes.

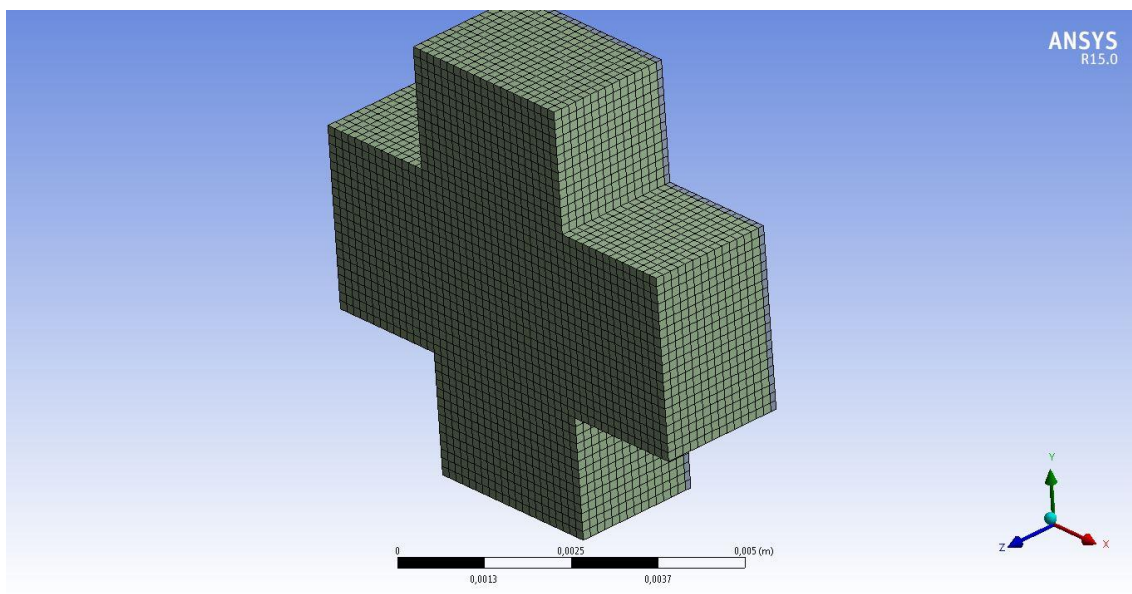


Figure 62: Single element of the full-scale heat exchanger

In summary, it must be said that the coupled models cannot be used as a reliable tool for productive modelling of flexible heat exchangers. In future versions of Ansys Workbench® the used beta features and the coupling algorithms might be improved, which may enhance the functionality and enable a proper modelling. However, the problem of the very thin films, which leads to enormous element numbers, will remain until a significant increase of available RAM memory on basic computers. Now, this means, that such numerical problems can only be solved on high performance clusters.

4.2. RESULTS OF THE HEAT TRANSFER DETERMINATION

For a proper evaluation of the performance and the effectivity of a heat exchanger, several identifiers can be used. In this case, the overall heat transfer coefficient (s. 2.3.4) and the overall efficiency factor was the most appropriate. As the primary purpose of the heat exchanger was the cooling and the condensation of a fluid, the effective enthalpy difference of the hot fluid ΔH_{hot} was used for the determination of the heat transfer coefficient k_{hot} .

The enthalpy difference for the heat transfer without any phase transitions was computed as follows:

$$\Delta H_{\text{hot}} = \dot{m}_{\text{hot}} (c_{p,h,2}(T_{h,2}) \cdot T_{h,2} - c_{p,h,1}(T_{h,1}) \cdot T_{h,1}) \quad (4.3)$$

with the mass flow \dot{m}_{hot} , the heat capacities $c_{p,h,i}$ at the corresponding temperatures $T_{h,i}$, where the index '1' denotes the inlet and the index '2' the outlet.

For phase transitions the expression above was expanded by the condensation enthalpy term, h_{cond} :

$$\Delta H_{\text{hot}} = \dot{m}_{\text{hot}} (c_{p,h,2}(T_{h,2}) \cdot T_{h,2} - c_{p,h,1}(T_{h,1}) \cdot T_{h,1} + h_{\text{cond}}) \quad (4.4)$$

The fluid properties for water were computed with the IAPWS-equations and for hexane the Augnier-Redlich-Kwong equations were used. These are described in section 2.2.3.4.

The overall efficiency η_{hex} the following definition was used:

$$\eta_{\text{hex}} = \frac{\Delta h_{\text{hot}}}{\Delta h_{\text{hot,max}}} = \frac{\dot{m}_{\text{hot}} (c_p(T_{h,2}) \cdot T_{h,2} - c_p(T_{h,1}) \cdot T_{h,1} + h_{\text{cond}})}{\dot{m}_{\text{hot}} (c_p(T_{h,2}) \cdot T_{h,2} - c_p(T_{c,1}) \cdot T_{c,1} + h_{\text{cond}})} \quad (4.5)$$

where the index 'c' denotes the cooling fluid, and $T_{c,1}$ the cooling fluid inlet temperature.

Finally, the overall heat transfer coefficient k_{hot} is computed by

$$k_{\text{hot}} = \frac{\Delta H_{\text{hot}}}{A_H} \quad (4.6)$$

with the heat exchange area A_H .

4.2.1. Lab-scale heat exchanger

To determine some basic heat transfer properties of the polymer films and to compare their performance extensive testing was performed with the lab-scale heat exchanger described in section 3.4.2. These experiments can be split into three stages. For the first, water was used as the hot fluid as well as the cooling fluid. The second stage consisted cooling an organic solvent, namely hexane in liquid state, without a state transition. Moreover, the third stage were experiments with condensation of hexane.

4.2.1.1. Experimental results for water-water heat transfer

In Figure 63 the results for testing of the polyimide (PI) film (Kapton HN) under not condensing conditions are given. The measurement data can be found in Table 19 and Table 20 in Appendix 6.1 . As can be seen, the overall heat transfer coefficient k_{hot} is highly dependent on the mass flows of the both fluids, as it increases with the mass flows. On the one hand, this can be explained mathematically, as the mass flow rate affects the total enthalpy difference directly, s. Eq. (4.3). On the other hand, the significant decrease of the heat transfer coefficient at lower flows rates can also be explained by the formation of trickles on the hot side of the heat exchanger, which reduces the effective heat transfer area. This aspect will be discussed in detail later, considering the deviations between the experimentally and numerically determined heat transfer coefficients.

Despite the non-optimised design of the lab-scale heat exchanger, competitive overall heat transfer coefficients could be reached. Especially for the highest flow rates, heat transfer coefficients over 450 W/m²K could be determined. At these flow rates, the entire heat transfer surface of the heat exchanger was completely covered with the fluids from both sides, which also improved the effectiveness of the heat exchanger.

The logarithmic temperature difference was the highest for the lower mass flows and decreased with the higher mass flows. This is obvious, as the dwell time is much higher for the lower mass flow rates and hence the hot fluid can be cooled more effectively, which leads to a higher temperature difference.

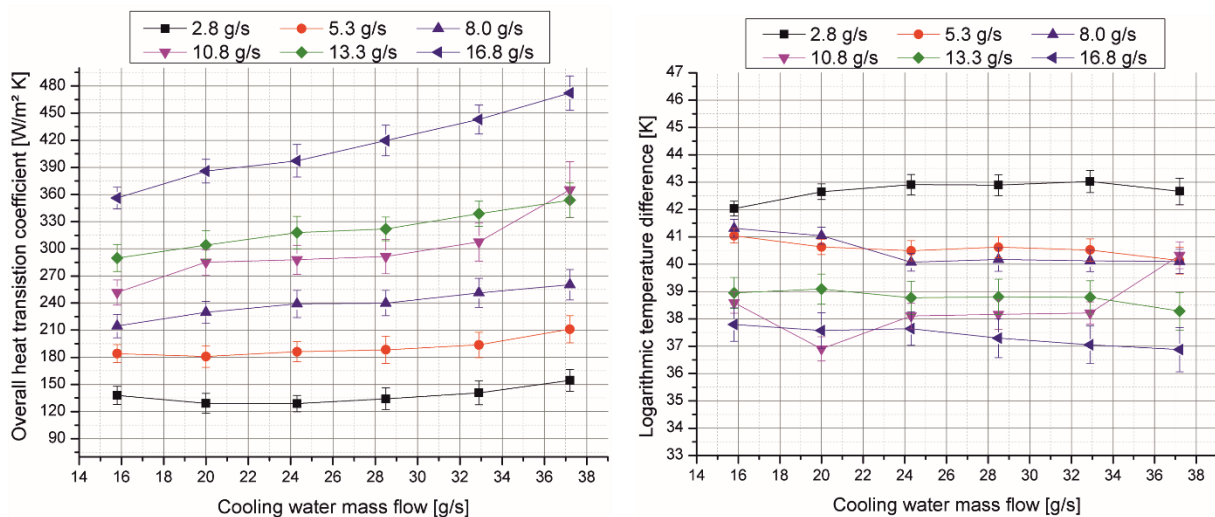


Figure 63: Overall heat transfer coefficients and the corresponding logarithmic temperatures for the experiments with water on the polyimide film in the lab-scale heat exchanger

For the PTFE-glass fibre compound, the overall heat transfer coefficients were much lower than for the PI film (s. Figure 64: Overall heat transfer coefficients and the corresponding logarithmic temperatures for the experiments with water on the PTFE-Glass fibre compound in the lab-scale heat exchanger. The maximum values reached here were approx. 370 W/m² K, which is almost 20% lower, than for the

polyimide. For mid-range operating points however, the difference was not that significant, while for lower flow rates it increased again up to 20%. In general, the increase of the effectiveness of the heat exchanger depended on the flow rates, but the influence is lower than for the PI film. The cooling water mass flow rate did not significantly affect the overall heat transfer.

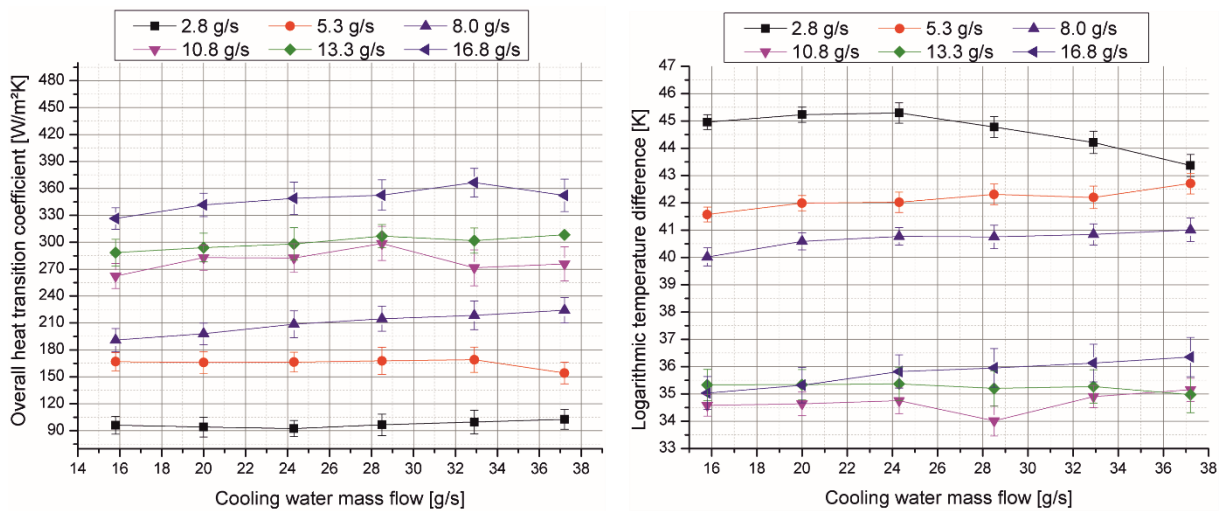


Figure 64: Overall heat transfer coefficients and the corresponding logarithmic temperatures for the experiments with water on the PTFE-Glass fibre compound in the lab-scale heat exchanger

The logarithmic temperature differences on the other hand, were up to 3 K higher for the PTFE-glass fibre compound than for the polyimide for lower flow rates, but also lower at higher flow rates. Since the inlet temperatures were the same for the specified operating points and both tested films, this behaviour can only be explained by the material properties of the films. During the experiments, significant differences of the wetting behaviour were observed. The low surface energy of polytetrafluoroethylene leads to narrower trickles, than with polyimide. This also can be seen in Figure 65, which shows a thermographic image of the temperature distribution within the heat exchanger.

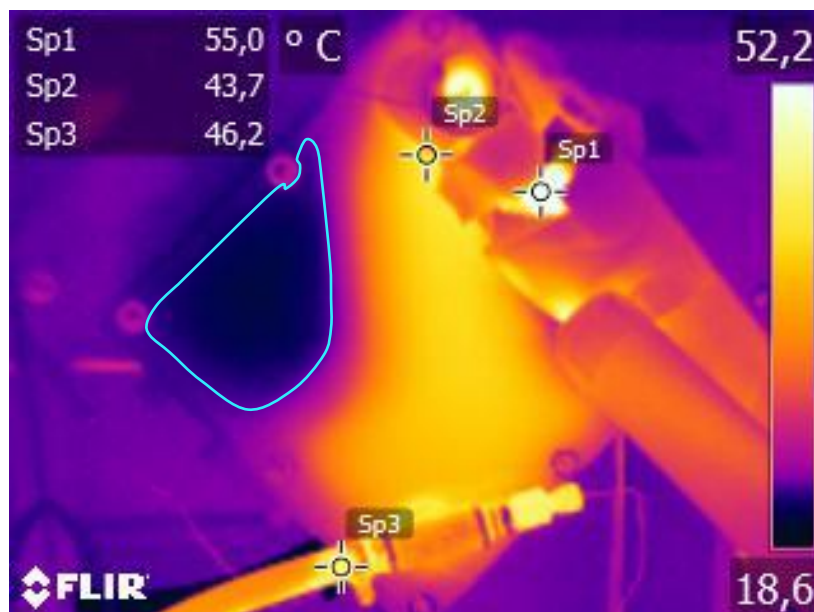


Figure 65: Thermal image of a low rate flow on the hot side with the polyimide film

The cyan marked area shows a not-wetted, cold region in the hot side of the heat exchanger. As the main hot flow forms a trickle the edges on both left and right sides are not covered with the hot fluid and therefore do not participate in the heat exchanging process. The feed pipe covers the corresponding cold area on the right side. Although the quality and especially the resolution of the thermal camera did not allow an exact evaluation, a qualitative comparison between the wetted areas at the same low rate was performed by counting the pixels with the relevant temperature. These results are given in Figure 66.

Though the exact determination of the areas was not possible, the figure shows that, the wetted surface was much larger with the polyimide film, which enhanced the effectiveness of the heat transfer process.

In order to summarise the results for water-water-heat transfer in the lab-scale heat exchanger it can be said, that the polyimide film showed better performance with up to 20% higher overall heat transfer coefficients than with the PTFE-glass fibre film. For the latter, the effectiveness appeared not to have a high dependency on the cooling fluid flow rate, while with the polyimide film it increased significantly with the higher flow rate.

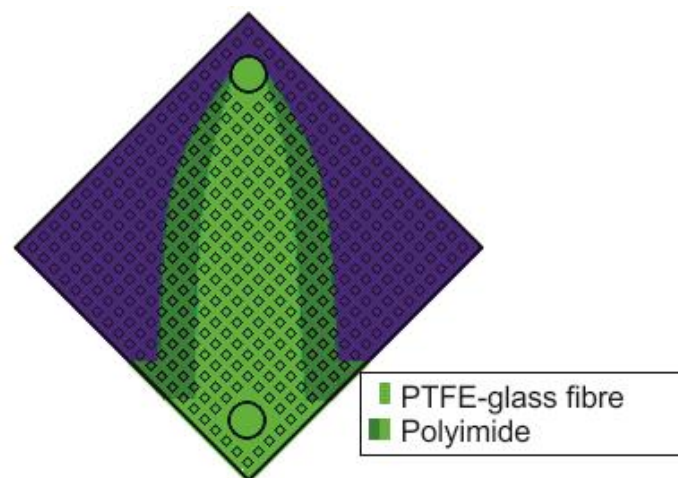


Figure 66: A qualitative comparison of the wetting behaviour of PTFE and PI films

In order to summarise the results for water-water-heat transfer in the lab-scale heat exchanger it can be said, that the polyimide film showed better performance with up to 20% higher overall heat transfer coefficients than with the PTFE-glass fibre film. For the latter, the effectiveness appeared not to have a high dependency on the cooling fluid flow rate, while with the polyimide film it increased significantly with the higher flow rate.

The last aspect to be mentioned was the sealing of the apparatus. While with the polyimide film the sealing with a standard elastomer material (nitrile rubber) was absolutely sufficient. With the PTFE-

glass fibre compound however, some minor leakages occurred at higher flow rates, so a thicker and slightly softer seal had to be used.

4.2.1.2. Experimental results for liquid hexane-water heat transfer

For the non-condensing hexane system, the results were similar. The measurement data for these results can be found in Table 21 and Table 22 in Appedix 6.1. For the polyimide film the significant dependency on the mass flow of the heat transfer coefficient was also determined, which can be seen in Figure 67.

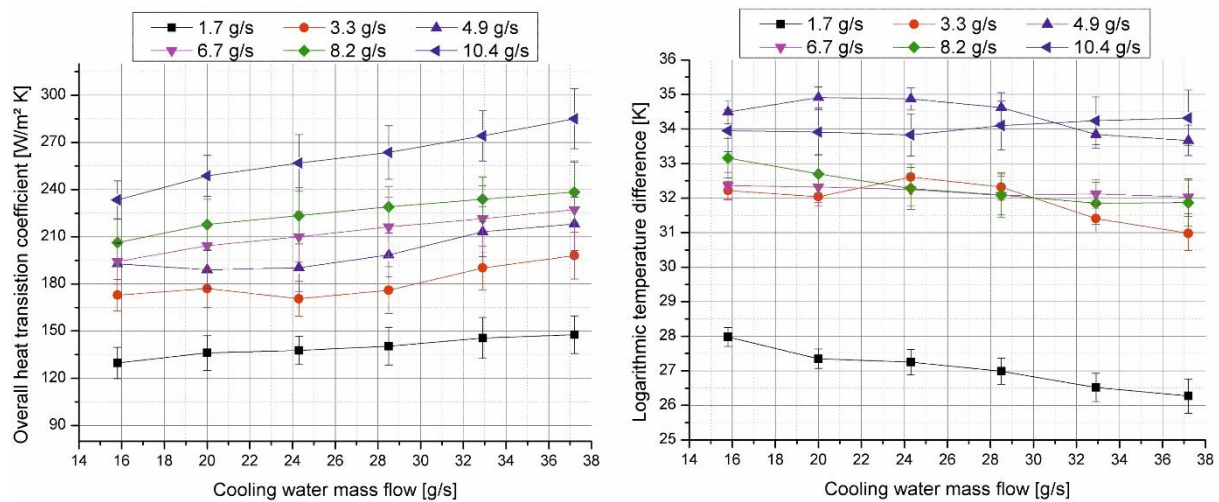


Figure 67: Overall heat transfer coefficients and the corresponding logarithmic temperatures for the experiments with non-condensing hexane on the PI film

As expected, due to the lower heat capacity of hexane, the heat transfer was lower and hence lower heat transfer coefficients between 130 and 285 W/m² K could be determined (s. Figure 68). For the PTFE-glass fibre compound the corresponding values were also lower than for water with the same flow rates. But, the dependency on the cooling water flow rate was much higher here than for water-water results. This can be explained the different surface tensions of the used liquids. While for water the value is high with 72.75 mN/m, for hexane the corresponding value is 18.4 mN/m (CHEMIE.DE Information Service GmbH). A high surface tension enforces the development of trickles, while a low surface tension enhances the wetting of the film. For the PTFE-glass fibre compound, this effect has a much higher influence as can be determined from the comparison of the results for water and hexane. For low flow rates, such as 2.8 g/s the heat transfer results for hexane are even higher than for water, despite the much lower heat capacity of hexane. Here the more intense formation of trickles of water reduced the heat transfer surface significantly. However, for higher low rates the influence of the surface tension decreases, as the formation of trickles becomes less intense.

On the other hand, the differences for higher flow rates were not as significant as for the water-water experiments. For the highest flow rate of 16.8 g/s the heat transfer coefficients were similar for both films with values between 230 W/m²K and 280W/m² K.

For hexane, the heat transfer coefficients for most operating points were lower with the PTFE-glass fibre compound than with the polyimide film. Therefore, these experiments also confirmed that considering the heat transfer the polyimide films are more effective than the PTFE-glass fibre compound.

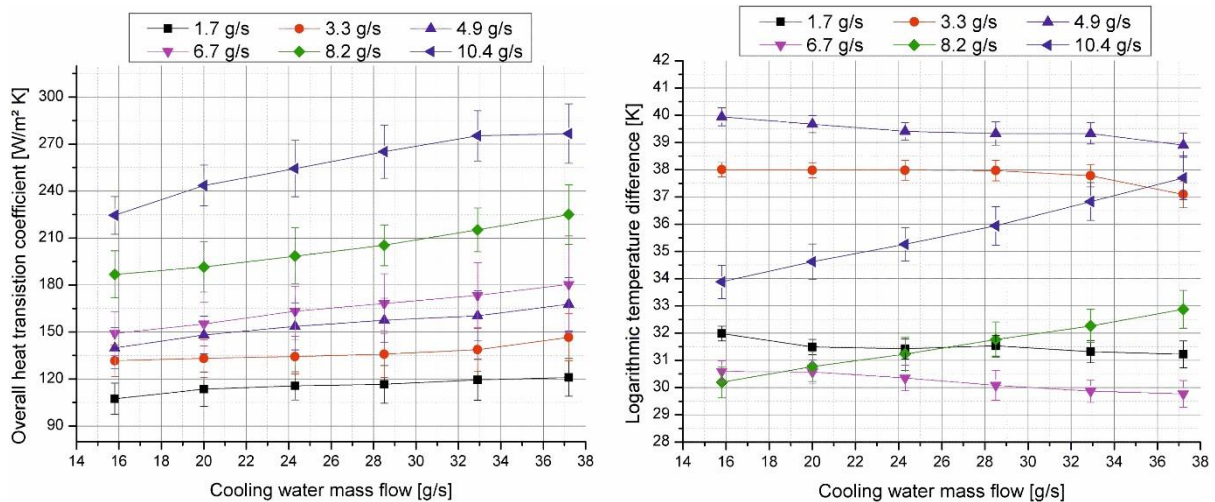


Figure 68: Overall heat transfer coefficients and the corresponding logarithmic temperatures for the experiments with non-condensing hexane on the PTFE-glass fibre compound

4.2.1.3. Experimental results for hexane condensation with water cooling

Compared to the non-condensing heat transfer, the flow rates for the condensing hexane were significantly lower due to the limiting heating power of the evaporator. The flow rates were set in a way to ensure that the hexane is completely gaseous when it enters the condenser. The measurement data is given in Table 23 and in Appendix 6.1. With higher flow rates, above 3.5 g/s the installed evaporator provided a visible gas-liquid mixture. The highest peak values for the overall heat transfer coefficients again were achieved with the polyimide film, as can be seen in Figure 69 and Figure 70.

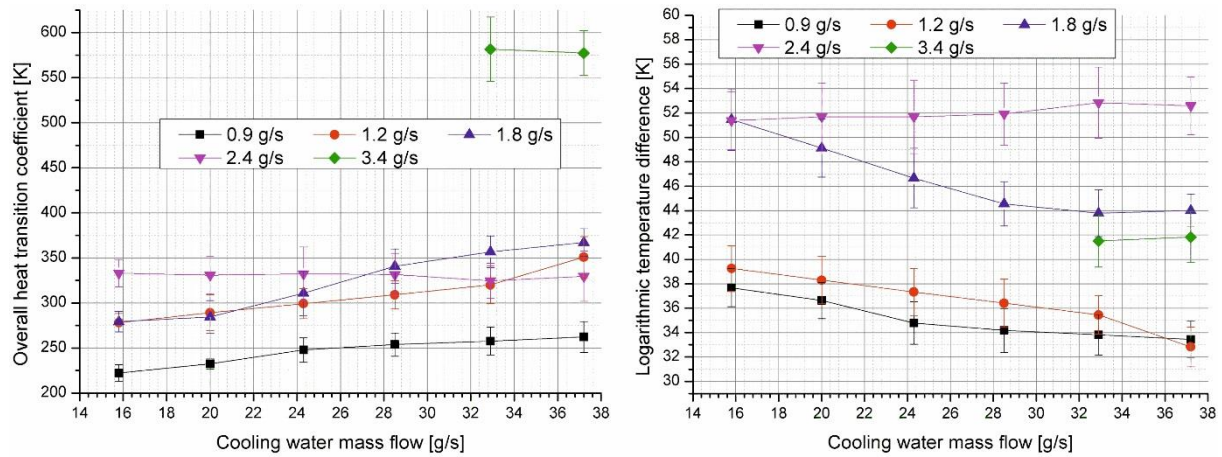


Figure 69: Overall heat transfer coefficients and the corresponding logarithmic temperatures for the experiments with condensing hexane on the polyimide film

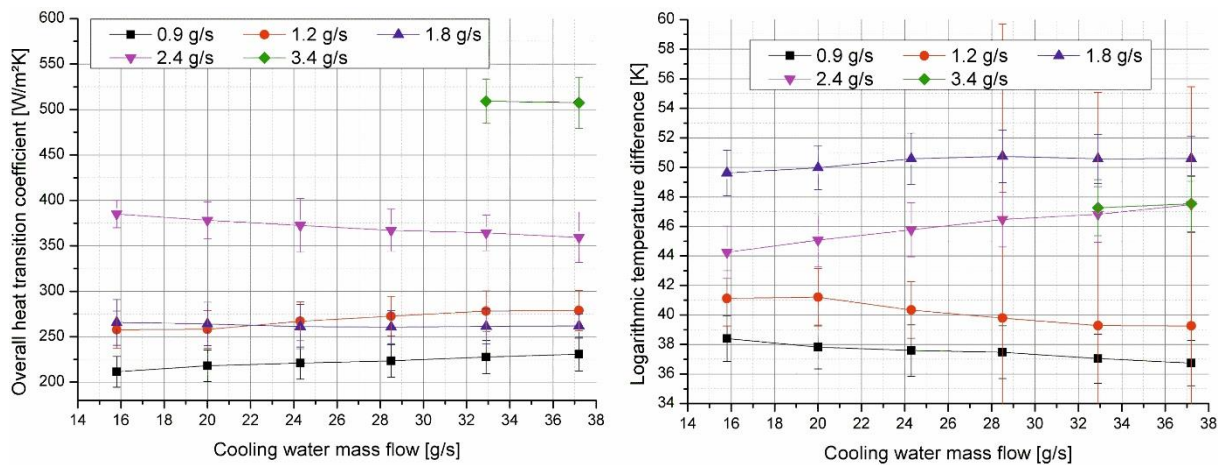


Figure 70: Overall heat transfer coefficients and the corresponding logarithmic temperatures for the experiments with condensing hexane on the PTFE-glass fibre compound

For the PTFE-glass-fibre compound, the maximum heat transfer values are about 100 W/m² K lower than for the polyimide film. The possible reason for this was already explained with the water-water heat transfer. However, the influence of the low surface tension of PTFE is lower for the condensation, than for the liquid-liquid heat transfer.

4.2.1.1. Numerical results of the heat transfer in the lab-scale apparatus

The modelling of the water-water heat transfer was only applied to the lab-scale heat exchanger. The results are shown in Figure 71. Here the flow rates for the curves denote the hot fluid, while the cooling fluid flow rate is given on the horizontal axis. For these simulations, the same operating conditions were used, as for the experimental investigations described in section 4.2.1.1. For the determination of the fluid properties, the integrated NASA coefficients were used.

For the middle flow range between 6.7 and 8.2 g/s the used SST-model provided acceptable accuracy and hence could depict the real heat transfer. A variation of different fluid flow models, such as k- ϵ ,

SST and laminar could not enhance the accuracy, in case of the laminar model the deviation was about 30% and for the k- ϵ -model about 20%. Hence, the SST-model was proved as the most suitable, and was also used for the full-scale heat exchanger.

For higher and lower flow rates, the deviations became much more significant. For the lowest flow rate of the hot fluid (1.7 g/s) only the first operating point with the lowest cooling water flow rate could match the experiment. For higher cooling water flow rates, the overall heat transfer coefficient was about twice as high. For 3.3 g/s the deviation from the experiment was between 27% and 86%.

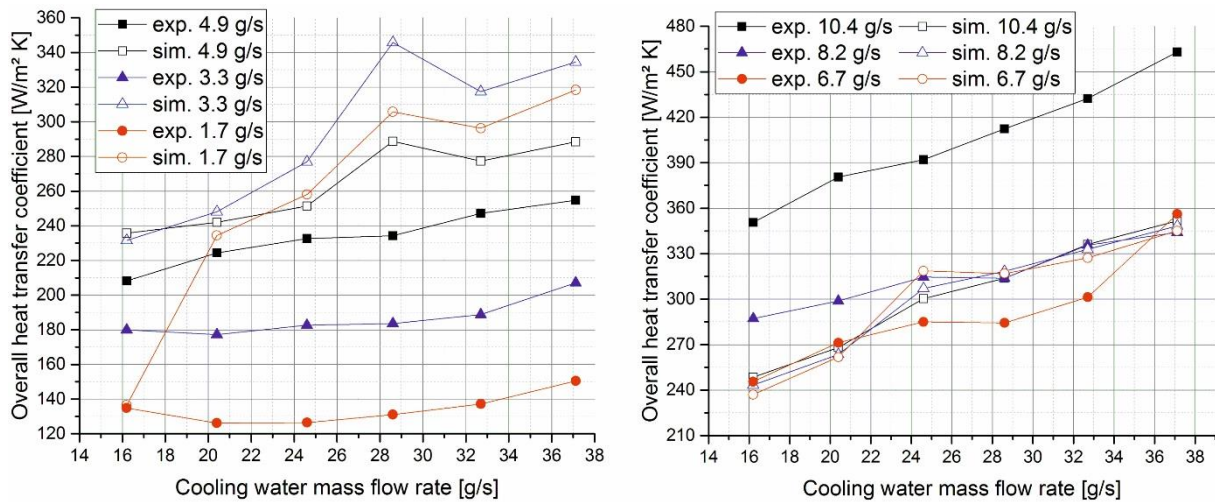


Figure 71: Comparison of the simulated and experimental results for water-water heat transfer in the lab-scale heat exchanger

The most obvious reason for this model behaviour is the formation of trickles at lower flow rates, which was also observed in earlier experiments (s. 4.2.1.1). The used models did not depict these trickles. Hence, the solver tried to spread the fluid over the entire heat transferring surface of the apparatus. This led to a significant increase of the heat transfer, which explains the deviations.

However, the significant deviation for the highest hot flow rate (10.4 g/s) cannot be explained by the trickles. Here, the numerically determined value about 30% lower than the experimental one. The result of the variation of the different fluid flow models is shown in Figure 72. Here, the operating point '1' depicts the hot flow rate of 8.2 g/s and the second depicts the flow rate of 10.4 g/s. While for the first point, the k- ϵ -model was the closest to the experiment with about 30% deviation, for the second point the SST-model was the most accurate, but still had a deviation of 31%. From the physical point of view, the SST-model appeared to be more plausible, as it follows the qualitative increase of the heat transfer coefficient with the higher flow rate. For the k- ϵ -model however, the heat transfer coefficient decreases dramatically, which is not correct physically. Although the laminar model also described an increase of the heat transfer, the error was over 400%, which is not acceptable.

A possible reason could be the insufficient depiction of the turbulence intensity. It was tried to solve this by tuning the turbulence parameters of the SST-model, but without any significant effect on the result.

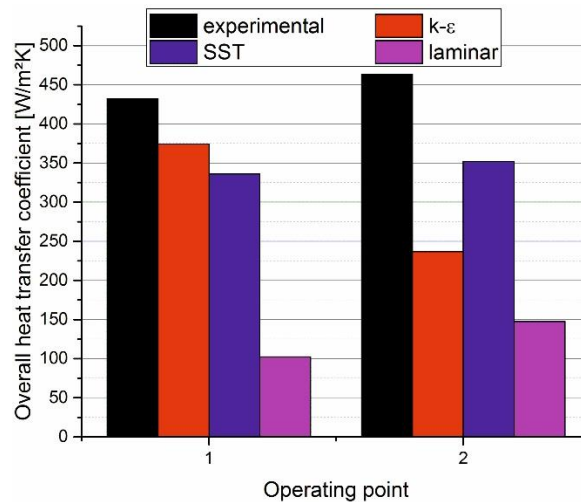


Figure 72: Comparison of the heat transfer results at the highest flow rates with different fluid flow models

4.2.2. Full-scale demonstrator

4.2.2.1. Experimental results for the water - water heat transfer

Due to massive sealing problems, only two operating points could be measured with the first demonstrator. With this configuration two operating points were investigated with a 5-stack apparatus. On a test rig of Calorplast GmbH, which consisted of two heat metres and used the regular house water supply. This means, that the heat exchanger consisted of five modules with a hot and a cold chamber. The corresponding results are given in Table 17.

As can be seen with this apparatus a good overall heat transfer coefficients depending on the cooling fluid flow rate could be achieved. However, these results cannot be taken into account, as not only the sealing to the outside failed, but a mass transfer between the hot and the cold chambers occurred too. Hence, the experiments were continued with the enhanced second demonstrator.

Table 17: Testing results for demonstrator 1

Operating Point	Hot flow			Cooling flow			Heat transfer coefficient
	\dot{V}	t_{inlet}	t_{outlet}	\dot{V}	t_{inlet}	t_{outlet}	
	l/min	°C	°C	l/min	°C	°C	W/m ² K
1	5.2	42.1	32.4	21.5	16.1	17.1	640
2	5.2	50.3	37.7	15	15.8	18.7	387

For the water-water heat transfer with the demonstrator 2, a normal in-house water supply was used. Therefore, the inlet temperatures varied between 55°C and 65°C for the hot side and between 13°C and 17°C for the cooling side. Since the entire research was focused on the condensation processes, only few experiments with liquid-liquid heat transfer were performed. The measurement data is given in Table 25 in Appendix 6.2.

As can be seen from Figure 73 the heat transfer efficiency was directly dependent on the flow rate and overall heat transfer coefficients up to almost 1000 W/m K (for the reduced area) could be achieved. As expected, with the consideration of the full film area the coefficients were lower, with about 600 W/m² K. Compared to the average heat transfer coefficients for plate heat exchangers even the results with the reduced area are at a higher performance level. In the (VDI 2006) corresponding values between 350 and 1200 W/m² K are given for the liquid-liquid heat transfer in a plane plate heat exchanger. With profiled plates, much higher values up to 4000 W/m² K can be reached.

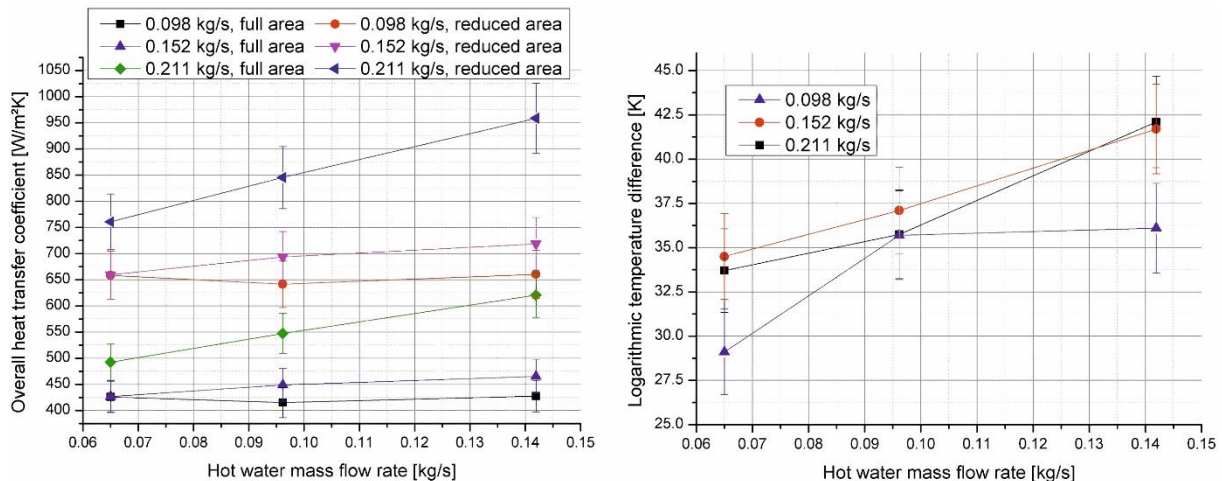


Figure 73: Overall heat transfer coefficients and the corresponding logarithmic temperature differences for testing procedures with water in demonstrator 2

Nevertheless, it must be said that because of the entirely new geometry of the heat exchanger it is not possible to find comparable designs with the corresponding efficiency values. On the one hand, the only reference, which can be used are the results in (Christmann et al. 2012), where a similar stabilising structure was used. Although in this case the stabilisers were much smaller (steel grid) and the ratio of the reduced and the full surface area was negligible. On the other hand, despite the fact that Christmann investigated the condensation of gases, he used a fall film design in his work, thus his results are not comparable due to the design used in this work.

4.2.2.2. Experimental results for hexane condensation heat transfer

The measurement data for these results are given in Table 26 in the Appendix 6.2. In Figure 74 the result summary for the condensation testing is given. In summary, it can be said that even taking the

entire film surface into account competitive heat transfer coefficients up to $1100\text{W}/\text{m}^2\text{K}$ could be achieved. Obviously, for the reduced area these values were higher, up to $1700\text{W}/\text{m}^2\text{K}$. According to (VDI 2006) for condensation of steam overall heat transfer coefficients between 900 and 3500 are common. With both surface area assumptions, the condenser operated at a lower level. For the falling film condensation Christmann was able to reach up to $3000\text{W}/\text{m}^2\text{K}$, which is comparable with the performance of the conventional apparatus design made of metals (Christmann et al. 2012)

Surprisingly, the heat transfer coefficient decreased significantly at higher mass flow rates of hexane. This could be caused by several factors. First, the quality of the evaporated hexane gas was not measured. Therefore, the mass flow rates were set to ensure at least a visible absence of any liquid drops in the gas, which was assumed to be saturated. At higher flow rates, it was possible, that the evaporation was not complete at the inlet of the condenser and hence the condensation enthalpy was lower than assumed. To reduce the influence of this aspect the enthalpy difference of the cooling water was taken into account, neglecting the heat losses to the environment.

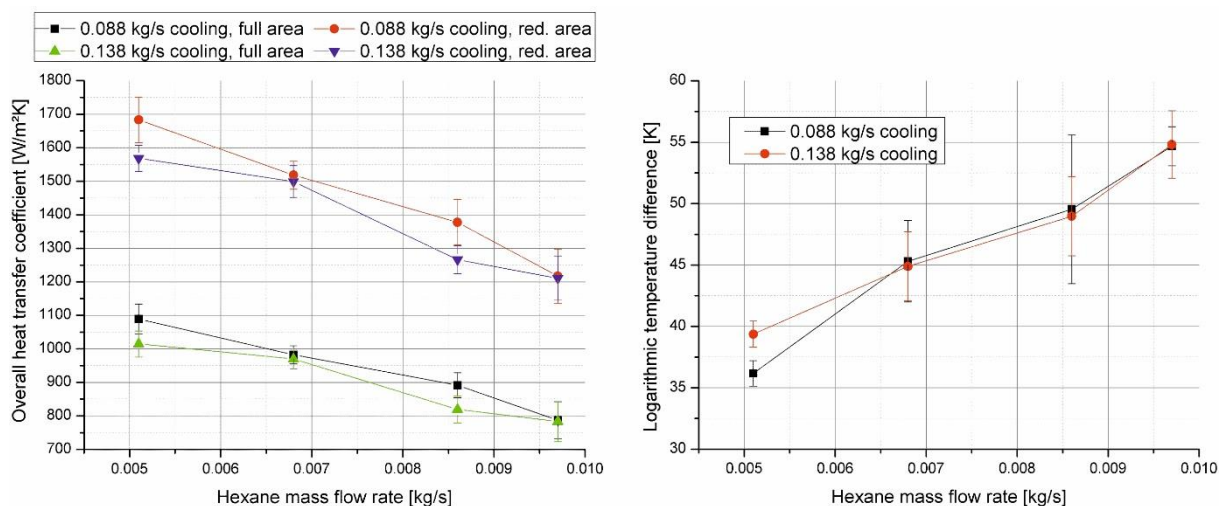


Figure 74: Overall heat transfer coefficients and the corresponding logarithmic temperature differences for testing procedures with hexane condensation in demonstrator 2

Second, mathematically the heat transfer coefficient was influenced by the higher logarithmic temperature difference, which increased significantly. This is based on the much higher outlet temperatures on the hot side. While for lower mass flow rates, a remarkable supercooling (30 K below the boiling point) was observed, for the highest flow rate the outlet temperature was only 10K below the boiling point. Hence, the logarithmic temperature difference varied between 36 K and 55 K, which significantly reduced the value of the heat transfer coefficient.

4.2.2.3. Design and sealing difficulties

As already mentioned in the sections above the sealing of the heat exchanger remained an unsolved issue when using the PTFE-glass fibre compound. With the PET or PI films, a sealing for pressures below

two bar could be maintained. Although this solution did not match the initial project requirements including the demand of maximum pressure of six bar, limited testing could be performed to obtain the effectivity results of the apparatus design.

The sealing itself appeared to have two weak points. The first one was the low surface tension and mechanical strength of PTFE. As can be seen in Table 2, PTFE is a mechanically very weak material, which causes permanent and significant creep. This inevitably led to leakages. The attempts to increase the pressing tension between the film and the sealing only led to an even greater deformation of the compound and finally to its destruction.

The second issue was the material of the sealing itself. Because of the very special demands of the process of condensing organic solvents to the apparatus, the material selection was limited to only few materials. On the other hand, the sealing material had to be soft enough, in order not to damage the sensitive surface of the PTFE-glass fibre compound. In most cases, soft seals are used for such purposes, which are made of elastomers with or without hardeners. In most cases these are not chemically resistant. The only possibility here was the usage of foamed PTFE or other fluorine polymers. However, these materials also suffered from their mechanical weakness and did not provide a leakage free operation.

Therefore, a widely used material finally was selected, by usage of which a functioning sealing could be achieved with the PET-film. The selected material was VITON[®] developed by DuPont. Though this polymer contains fluorine, which in most cases increases the chemical resistance and the thermal stability, the sealing was able to operate at six bar for only two weeks of daily testing, which was in total about only 40 hours. As can be seen in Figure 75 the sealing failure is obvious. Especially the temperature appeared to be to most problematic factor, as the damage was much less severe at the outlet of the condensation side, where the material was also in contact with the hexane. This is shown in Figure 76.

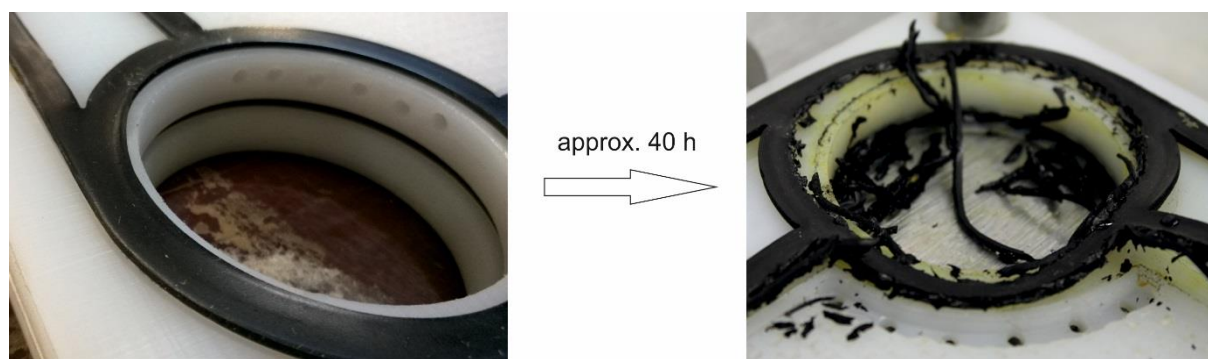


Figure 75: Damaging of the sealing material at the gas inlet

These results are of special interest since the material is known as thermally stable up to 200°C. According to the manufacturer and several other sources the chemical resistance for hexane is also given (Mark 2007). Based on these observations, it can be said, that the excellent thermal and chemical stability is definitely not the case, and therefore this material cannot be used for sealing.

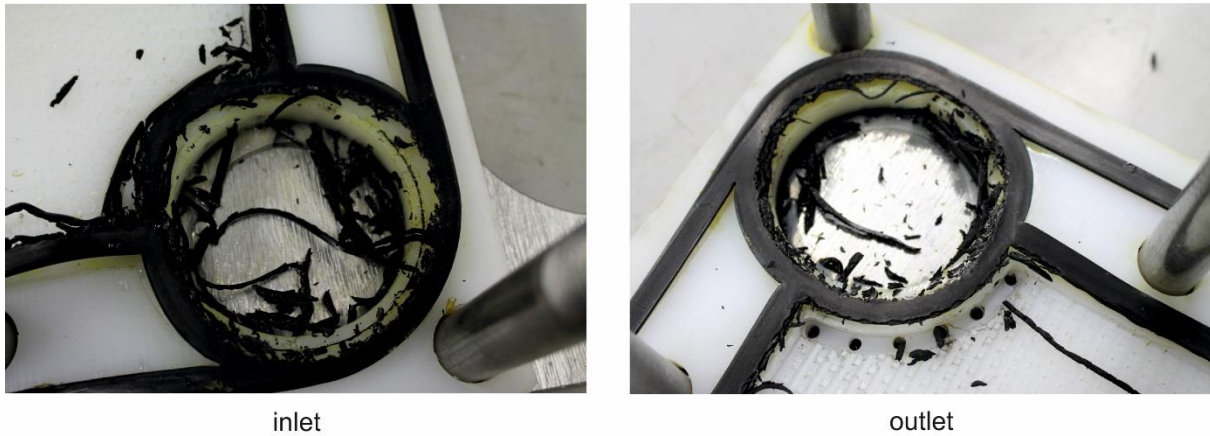


Figure 76: A comparison of the sealing damage at the inlet (left) and at the outlet (right)

Another important aspect for the testing procedures was the type of the used polymer film. As the research results of the chemical stability showed a clear advantage of the PTFE-glass fibre compound, it was tried to test the performance with this film. However, due to major sealing problems, this was not possible and the investigation continued with a simple PET film with a thickness of 100 μm . With it, the sealing was sufficient for pressures up to two bar and the testing could be performed. This aspect is discussed in detail in section 4.2.2.3. Overall, it must be said, that the sealing issue remains unsolved and major research work must be done to find an appropriate material.

4.2.2.4. Results of the numerical modelling of the condensation process

To determine the most suitable fluid properties model, a comparison of the models described in 2.2.3.4 was performed. For the validation of experimental values from (VDI 2006) were taken. For this comparison, values of four fluid properties were computed for the saturation state in the relevant temperature range from 300 to 400 K. The fluid properties were selected according to their relevance for the flow and heat transfer determination.

In principle, the computation of the values could be performed with any mathematical software and of course with Excel®. However, since Ansys CFX® is a commercial software the implementation of the models cannot be checked by reviewing the source code. The computation hence was performed with Ansys CFX® on a simple steady state model, to receive reliable information on the modelling results with this software.

An overview of the results is shown in Figure 77. Herein the relative deviation from the experimental values (VDI 2006), which is marked as a horizontal black line at the value of '1' on the vertical axis, is given. In general, it can be said that the models deliver almost the same values, especially for the dynamic viscosity and the heat conductivity. For these two properties, the difference between the models is so low, that it cannot be displayed with the used graph resolution. For the density and the heat capacity, the deviation between the models of 1 to 2% could be determined.

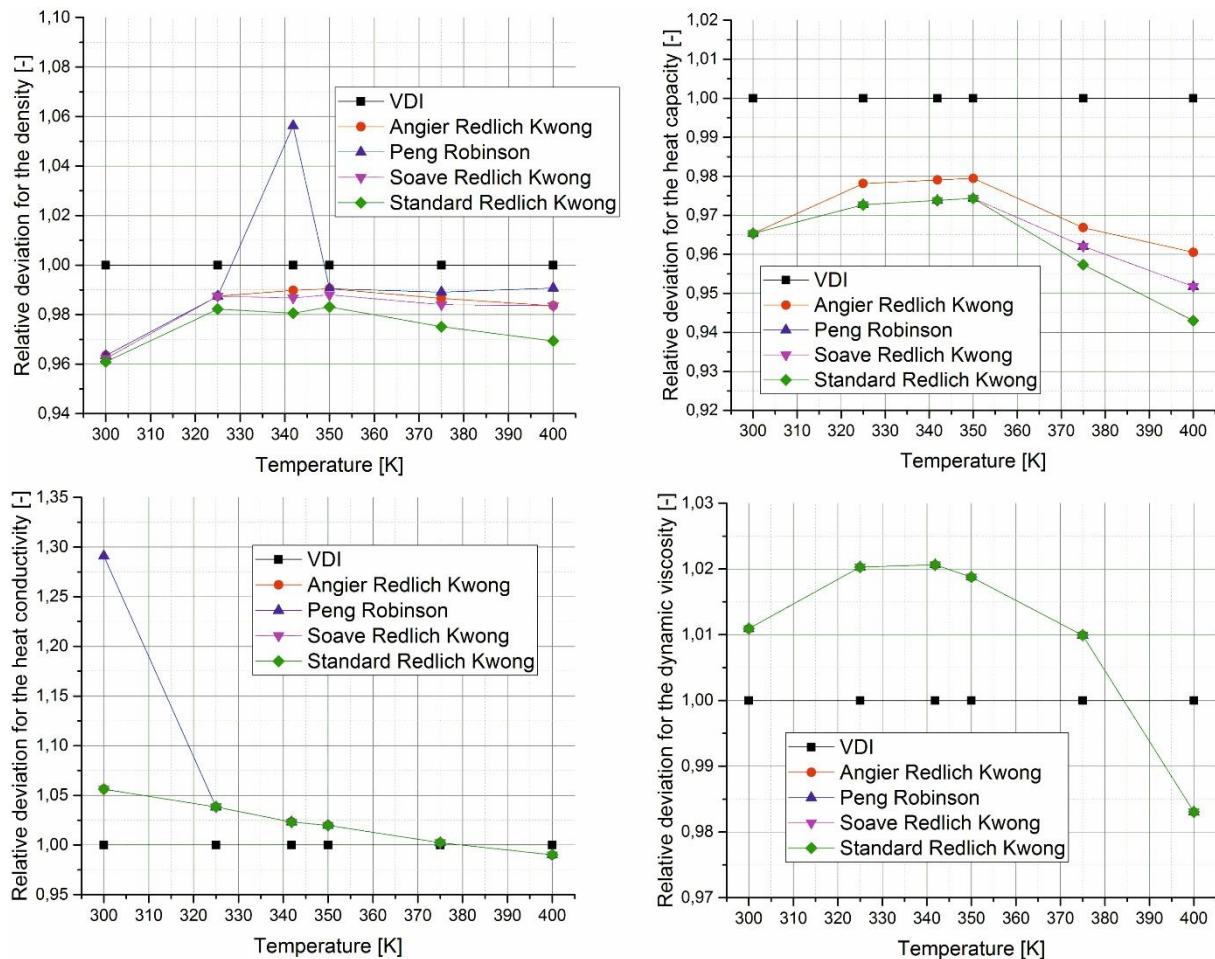


Figure 77: Comparison of the available fluid models

For the precision of the models, it must be said that the Peng Robinson model provided the lowest accuracy. For the density, the deviation was up to 6% and for the heat conductivity up to 30%. Considering all fluid properties, the Aungier Redlich Kwong model provided the best accuracy with the lowest deviations from the experimental values. Therefore, this one was used for the determination of the hexane properties for the condensation as well as for the non-condensing models. For water, the implemented NASA coefficients model (s. 2.2.3.4) was used.

The modelling of the condensation process was performed for the demonstrator 2 on the static geometry. Since the film was modelled as a virtual wall, to reduce the element number of the mesh, the reduced film surface area (s. 3.4.3.2) was used for the validation of the simulation results.

Due to the numerous difficulties and errors, which occurred during building up the model and the solver runs, only one operating point was computed successfully and could be evaluated. It also must be said, that this type of simulation was only possible after activating the so called 'Beta options', for which Ansys does not provide any guarantee of functioning. The results are given in Table 18.

Table 18: Results of the condensation modelling with Ansys CFX®

Method	$T_{cw,out}$	$T_{hex,out}$	k_{sim}
Experimental	21.73 °C	58.94 °C	947.17 W/m ² K
k-ε, λ = 0.25W/mK	47.582 °C	47.584 °C	6525.39 W/m ² K
k-ε, λ = 0.05W/mK	47.575 °C	47.585 °C	6508.71 W/m ² K
k-ε, λ = 0.05W/mK, additional heat transfer wall function	47.578 °C	47.858 °C	6508.70 W/m ² K
SST	Solver run not possible		
Laminar	No condensation occurred		

As can be seen, the simulated heat transfer coefficients were significantly higher, than the experimentally determined ones. The cooling water temperature at the outlet was over 20 K higher and the condensate temperature about 10 K higher. Nevertheless, this difference does not explain the enormous difference between the experimental and the simulated values for the heat transfer coefficient.

For this modelling a variation of the fluid flow models was performed, but only the k-ε-model delivered physically valid results. With the SST-model no solver run was possible, as the solver crashed after few iterations. Moreover, for the laminar flow, no condensation occurred, though the temperature of the hexane gas was low enough.

As an attempt to reduce the heat transfer, the heat conductivity of the virtual wall was decreased from 0.25 W/m² K to 0.05 W/m² K. This was the only changeable parameter, neglecting the geometry changes, as the fluid properties were computed with each iteration with respect to the temperature and the pressure. However, this significant modification neither affected the temperatures at the outlet nor the overall heat transfer coefficient. The only effect was the dislocation of the condensation lines, as can be seen in Figure 78, which describes the mass fraction distribution of the gaseous hexane.

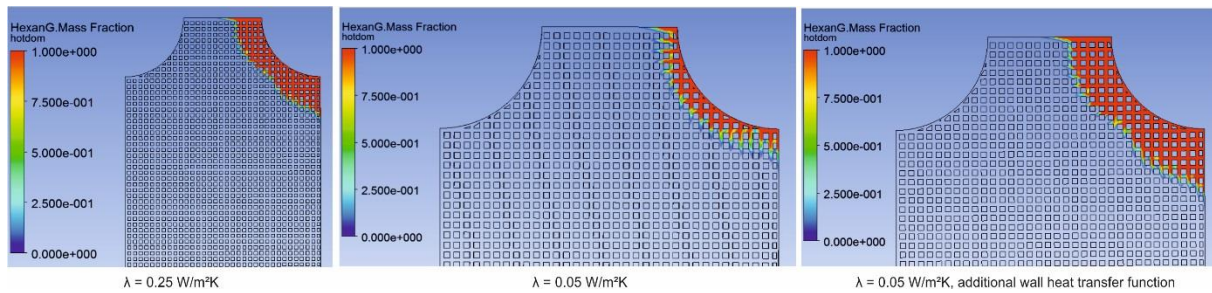


Figure 78: Condensation lines for the used models

Despite expectations based on physical laws the reduction of the thermal conductivity of the polymer led to a faster condensation. This obvious error could be corrected by including an additional wall heat transfer function, which describes the near wall heat transfer in a more precise way. However, the conductivity of the film then appeared not to affect the result at all and the mass fraction distribution remained unchanged.

In the following three figures, the temperature distribution for the condensation side of the heat exchanger is shown. On the left sides, the contact surface with the film and hence with the cooling fluid is shown, while the right sides show the outer walls, which were set as adiabatic.

The temperature distribution in Figure 75 corresponds with the condensation lines shown in Figure 78. While the equilibrium temperature of 47.5 °C was already reached almost at the very inlet for the reduced thermal conductivity, for the two other models it was located closer to the centre of the apparatus.

From the theoretical point of view, the temperature distribution with the reduced conductivity in Figure 80 and the additional wall heat transfer model in Figure 81 was the best. Here, an area with the condensation temperature (approx. 341 K) was visualised, as shown in Figure 81. In comparison with the results with the real conductivity, shown in Figure 79, the shape of the condensation area is very similar, but the temperature lies a few degrees below the condensation point.

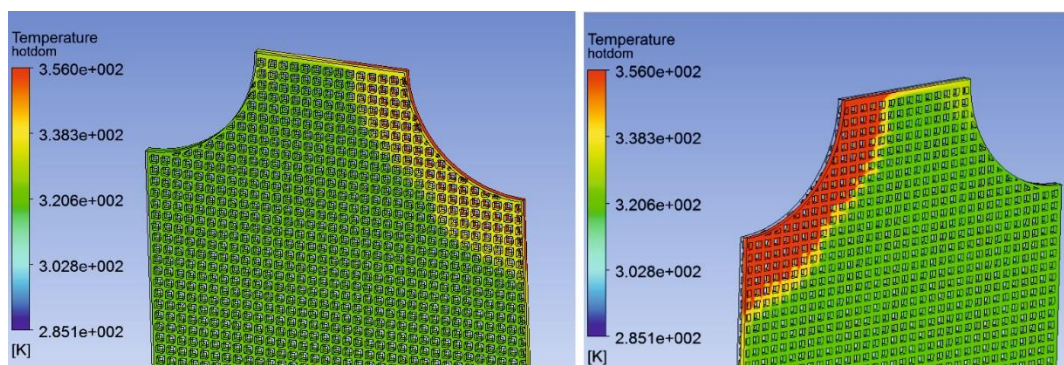


Figure 79: Temperature distribution with $\lambda=0.25 \text{ W/m}^2\text{K}$

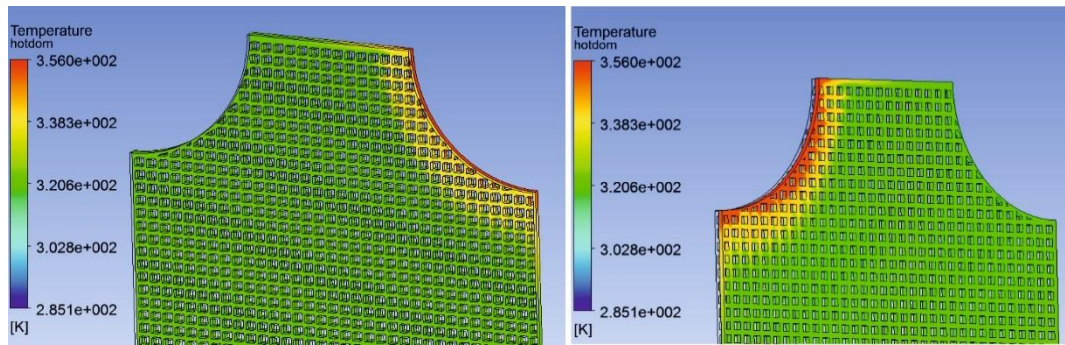


Figure 80: Temperature distribution with $\lambda=0.05 \text{ W/m}^2\text{K}$

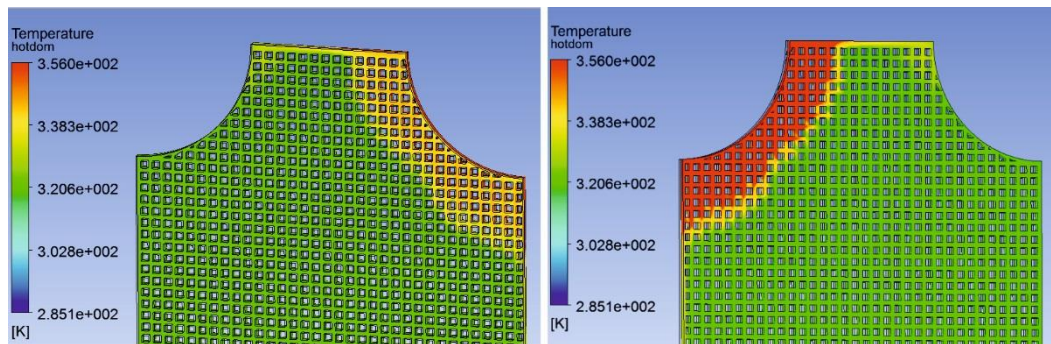


Figure 81: Temperature distribution with $\lambda=0.05 \text{ W/m}^2\text{K}$ and additional wall heat transfer model

However, for all three models it must be said, that the cooling of the hot hexane condensate was much more effective than in the experiment. The reasons for this can be of various origin. Neglecting the beta status of the functionality and the corresponding errors in the implementation of the model, the condensation type also might have an impact on the result. The only possible condensation model implemented in CFX[®] was the thermal energy based mass fraction changed of a continuous fluid. This means, that the gas-liquid mixture was considered as a homogeneous fluid with averaged flow properties. Based on this assumption, the formation of drops and the corresponding changes in the flow, contact areas essential for the heat transfer were neglected. Therefore, no explicit contact of the drops with the film was taken in to account, which is crucial for a correct depiction of the condensation process. Although a droplet condensation model is integrated in CFX[®], it first requires the exact knowledge of the formed droplet size and several other parameters. Secondly, it is also a beta feature, and could not be combined with a fluid with non-constant properties, like density or thermal conductivity.

In summary, it can be said that the modelling of the phase transition with Ansys CFX[®] has not yet reached a satisfying level. On the one hand, it is possible to model the condensation process itself and to generate a physically legitimate mass fraction distribution of the condensed liquid in a gas-liquid mixture. On the other hand, the energy balance of the process was not computed correctly, which led to enormous errors. The fact, that the used functionality is still being developed (referred to Ansys Workbench 15.0) additionally proves that the software cannot yet be used for productive modelling.

This includes also the simulation of the heat transfer between two different fluids, because Ansys CFX® only accepts the same fluid for all fluid domains by default and the usage of different fluid is only possible after activating the 'beta features'.

5. SUMMARY AND OUTLOOK

5.1. CONCLUSIONS

In this thesis, the suitability of high performance polymer films for applications in the chemical industry was investigated. The performed studies consisted of the determination of the mechanical, thermal and chemical properties of the films as well as the numerical and experimental investigations of the polymer film heat exchanger performance. The aim was to find the limits in application with condensation of organic solvents, like hexane, heptane, toluene and tetrahydrofuran in comparison to water.

Hence, the first ultimate topic was the exact determination of the mechanical strength of the used polymer films at the specific operation conditions, such as high temperatures (up to 100 °C), high pressure loads (up to 6 bar) and the permanent presence of organic solvents (hexane, heptane, toluene and tetrahydrofuran). Furthermore, the influence of dynamic, pulsating pressure loads was also studied. For this, a test rig was build, which enabled the long-term testing of the films at specified conditions and extensive testing procedures were performed. Each of the tested samples was exposed for at least two months to the chemical, thermal and mechanical loads. For the pulsating loads, up to 100,000 load changes were executed.

From a preliminary literature based research and several tests at the partner in industry, two film types were selected due to their acclaimed chemical and thermal resistance: a polyimide film with a thickness of 75 µm and a polytetrafluoroethylene-glass fibre compound, which was 150 µm thick. According to numerous lists and tables on the chemical resistance these two materials appeared to show the best performance at the specified conditions.

The investigations showed that despite the information provided by manufacturers or suppliers the polyimide film was not able to withstand the defined pressure and temperature during permanent contact with tetrahydrofuran. Furthermore, a change of colour occurred for the tetrahydrofuran, which additionally proved that polyimide was not suitable. Similar behaviour was observed with toluene. For both cases, the film samples were either seriously damaged or even destroyed during the testing procedure. With hexane and heptane however, the polyimide film performed well, and all samples were able to withstand the exposure.

The polytetrafluoroethylene-glass fibre compound showed a much better behaviour, as at least some of the sampled could perform without any visible damage with all four organic solvents. Here the chemical stability of the polytetrafluoroethylene in combination with the glass fibre enforcement showed less irreversible deformation, and did not affect the solvent in a visible manner.

For the pulsating loads, an advantageous behaviour of the polyimide film was determined, as it appeared not to be affected by the fast pulsations (550 / h) and only weakly affected by the slow pulsations (45 / h). For the PTFE-glass fibre compound a major weakening of the inner structure was observed and in contrast to the polyimide film it could only withstand about 20,000 load changes, while for the polyimide over 100,000 load changes could be achieved.

In summary of all researched properties of the films, the PTFE-glass fibre compound showed a better overall performance, especially considering the chemical resistance. The weakness at frequent load changes can be faced with over dimensioning of thickness of the films, as soon as the chemical resistance is guaranteed.

No big differences between the films could be observed during the study of the heat transfer. The polyimide film showed a marginally better performance. Only for the liquid-liquid heat transfer with water the polyimide film was significantly better with up to $470 \text{ W/m}^2\text{K}$ compared to $360 \text{ W/m}^2\text{K}$ with the PTFE-glass fibre compound. With liquid hexane, the performance of the films was equal with about $270 \text{ W/m}^2\text{K}$ to $280 \text{ W/m}^2\text{K}$. For the condensation process of hexane, for the polyimide film heat transfer coefficients of approx. $570 \text{ W/m}^2\text{K}$ could be achieved, while with the PTFE-glass fibre compounds the corresponding values (approx. $510 \text{ W/m}^2\text{K}$) were slightly lower.

Due to massive sealing problems, the PTFE-glass fibre compound could not be tested in the full-scale heat exchanger. Here, the very low mechanical strength of the PTFE matrix and the low surface energy of the material made it impossible to find an appropriate sealing material, which also provided the required thermal and chemical stability. Therefore, the testing with the full-scale heat exchanger was performed with a widely used polyethylene terephthalate, with a thickness of $100 \mu\text{m}$. For this film, a standard FKM (fluoro-elastomer) could be used for pressures below three bar.

With the developed full-scale heat exchanger, overall heat transfer coefficients between $700 \text{ W/m}^2\text{K}$ for liquid-liquid operation and $1700 \text{ W/m}^2\text{K}$ for the condensation of hexane could be reached. These values proved that the usage of thin polymer films lead to a competitive apparatus performance. Unfortunately, the used sealing material showed a much weaker chemical stability, and therefore could not be used for a time period over two weeks. Here additional research work is required in order to find an appropriate and durable material for the sealing.

In addition to the experimental research, the heat transfer was modelled with the commercial multiphysics software Ansys Workbench® for the lab-scale and for the full-scale apparatuses. The first stage of the modelling was a simple liquid-liquid simulation for water. The second stage contained the modelling of the condensation process. In addition, the third stage was an attempt to include the pressure based geometry deformations into the main model.

For the liquid-liquid heat transfer a close agreement with the experimental results could be reached for a limited range of the flow rates. For very low flow rates, the numerical results of the heat transfer coefficient were up to 2.5 times higher. This is most likely based on the trickles within the flow, which occurred in experiments and could not be modelled. Therefore, a much larger effective heat transfer area was used for the numerical determination, which enhanced the heat transfer. A comparison of the laminar modelling with two turbulence models (k - ϵ and SST) revealed, that the SST model met the experimental results best and hence had the lowest deviations. Although, it must be said, that all models provided physically valid solutions. This behaviour was observed for both geometries (lab-scale and full-scale), hence a geometry size dependency of the model could not be determined.

The condensation study was very challenging. In order to describe the fluid properties, especially for mixtures with variable gas-liquid ratios, several fluid property models were tested in order to find the most reliable one. For the properties of hexane, the Aungier-Redlich-Kwong models provided the lowest deviations from experimental data taken from literature and hence was used for the modelling of the condensation process. The cooling water was also modelled as variable properties fluid with the same fluid model. As for the single-phase simulations, the laminar model was compared with the two most popular turbulence models, mentioned above. However, here the differences between the models were enormous. With the laminar flow model, no condensation occurred, although the temperatures were low enough to enable a phase transition. The k - ϵ model crashed for every operating point after few iterations. Only the SST-model provided physically correct results. However, even with this model, the simulation was not stable and the default convergence criteria were not reached. Furthermore, though the condensation could be modelled successfully, the determination of the energy balance was faulty, which led to very high heat transfer coefficient values over $6000 \text{ W/m}^2\text{K}$. Compared with the experiment, where corresponding values below $1000 \text{ W/m}^2\text{K}$ were determined, this meant a deviation of over 600%, which cannot be accepted. Nevertheless, it must be said that the modelling of the condensation was performed with so called 'beta features' in CFX[®], as this was the only possibility to model phase transitions and different fluids in one problem case. These 'beta features' should not be used for reliable modelling and are still being developed (Ansys Workbench 15.0).

For the last stage of the numerical study, the geometry deformation was modelled with the fluid-structure-interaction. Two methods were used here. The first method was a non-coupled model. Therefore, a deformed static geometry was created with the FEM-module of Ansys with assumed static pressure loads. Afterwards, the deformed shape was exported as a new geometry to the CFX[®] module, where it was normally used. Unfortunately, both models revealed significant weak points based on the size of the numerical problem and on the restrictions of the used software. First the low thickness (0.1

mm) and the width of the flow channels (2 mm) required very fine meshes, which resulted in unmanageable mesh element numbers.

The second method was a direct two-way coupling between the FEM and the CFD solvers. Here the fluid volume with the higher pressure caused a deformation of the separating film, and hence deformed the both fluid volumes. While for all previous models, the film was defined as a virtual wall, in this case the film had to be a separate solid body. In principle, this method did work, which could be shown with small test geometries. However, even for the smaller lab-scale heat exchanger the solving of the problem became unmanageable due to its mesh element number. According to structural considerations the mesh size had to set to a value below the thickness of the film (0.1 mm). The best practice for the FEM analysis is a mesh element with the half size of the smallest dimension of the body.

Following this practice, the mesh size element was set to 0.05 mm, which led to huge numbers of mesh elements over 10 million only for the film. For the fluid volumes, the elements with the same size had to be used at least at the boundaries to the film. This provided another 10 million mesh elements. Hence, the total mesh size was about 30 or even more million. Such problem sizes could not be solved on the computers available for this work, and therefore no validation of the model based on experimental values could be performed.

The second problem were the inability of CFX to compute the heat transfer through a deforming or moving contact between two bodies. Hence, for the manageable small detail section of the full-scale model, only the flow could be modelled, but not the heat transfer and the energy balance.

Overall, with this work the suitability of polymer film heat exchangers for chemical applications could be proven, as sufficient mechanical, chemical and thermal stability could be fulfilled by at least one tested film. Furthermore, a competitive heat transfer performance could also be observed.

5.2. OUTLOOK

According to the results achieved in this work, the further research should be focused on the following topics. The first is the determination of appropriate sealing materials and geometries. On the one hand, several polymeric materials still have to be tested for their suitability, especially for the chemical and thermal resistance. On the other hand, attempts should be performed to enhance the design of the seals, which might enable the usage of chemically stable PTFE-based foamed seal materials.

The second topic should be the improvement of the numerical models for the heat transfer, especially with condensation. As already mentioned, the functions of Ansys CFX® used for this work are still in the beta status, which means that they are not fully developed yet. Since Ansys is working on it, with

later versions the modelling of different fluids and mixtures might be improved in a way to provide reliable models, which could be used effectively. As an alternative, the open source software package OpenFOAM could also be tried out. The main advantage of OpenFOAM is the possibility to review and if necessary to modify solver code, in order to achieve better results. Apart from that, additional user defined functions can also be added to the solver. Although this is also possible in Ansys, no control over the interaction of these user defined functions with the commercial solver is possible.

Considering the fluid-structure interaction it can be said, that with more powerful computers or even computer clusters an attempt of solving the numerical problems for the full-scale geometries. Especially the random access memory (RAM) have to increase to over 128 GB in order to manage the required mesh element numbers.

Publication bibliography

Altair Engineering, Inc (2014): Website of the Altair Hyperworks software. Available online at <http://www.altairhyperworks.co.uk>, accessed on 02.06.14.

Ansys Inc. (2011): ANSYS Parametric Design Language Guide. Rel. 12.0. Ansys Inc. Available online at http://orange.engr.ucdavis.edu/Documentation12.0/120/ans_apdl.pdf, accessed on 23.05.13.

Ansys Inc. (2012): Automotive Fluid-Structure Interaction (FSI) Concepts, Solutions and Applications. With assistance of Laz Foley. Edited by Ansys Inc. Available online at [http://easc.ansys.com/staticassets/ANSYS/staticassets/resourcelibrary/presentation/Auto_Sim_World_Conf_LFOLEY_FSI%20\(1\).pdf](http://easc.ansys.com/staticassets/ANSYS/staticassets/resourcelibrary/presentation/Auto_Sim_World_Conf_LFOLEY_FSI%20(1).pdf), accessed on 28.03.15.

Ansys Inc. (2014a): Ansys CFX-Solver Modelling Guide. Rel. 15.0. Edited by Ansys Inc. Ansys Inc. Available online at <http://orange.engr.ucdavis.edu/Documentation12.1/121/CFX/xmod.pdf>, accessed on 19.02.12.

Ansys Inc. (2014b): Ansys CFX-Solver Theory Guide. Rel. 15.0. Edited by Ansys Inc. Ansys Inc. Available online at <http://orange.engr.ucdavis.edu/Documentation12.1/121/CFX/xthry.pdf>, accessed on 03.02.15.

Ansys Inc. (2014c): Ansys Mechanical User Guide. Rel. 15.0. Ansys Inc. Available online at <http://148.204.81.206/Ansys/150/ANSYS%20Mechanical%20Users%20Guide.pdf>, accessed on 03.02.15.

Ansys Inc. (2014d): Workbench Help System. Version 15: Ansys Inc.

Baehr, Hans-Dieter; Kabelac, Stephan (2012): Thermodynamik. Berlin, Heidelberg: Springer Vieweg.

Baehr, Hans-Dieter; Stephan, Karl (2008): Wärme- und Stoffübertragung 6. neu bearbeitete Auflage Wärme- und Stoffübertragung. 6th ed. Berlin, Heidelberg: Springer-Verlag.

BMBF (2010): Technologies for Sustainability and Climate Protection. Federal Ministry of Education and Research. Available online at <http://chemieundco2.de/en/index.php>, accessed on 24.02.15.

Böhme Kunststofftechnik GmbH & Co. KG: Official website of Böhme Kunststofftechnik. Available online at <http://boehme-kunststoff.de/>, accessed on 13.03.14.

Burcat, Alexander; Ruscic, Brank (2005): Third Millennium Ideal Gas and Condensed Phase Thermochemical Database for Combustion. with updates from Active Thermochemical Tables. Available online at <http://garfield.chem.elte.hu/Burcat/burcat.html>, accessed on 22.01.15.

Bürckle GmbH (2011): Chemische Beständigkeit von Kunststoffen. Available online at https://www.buerkle.de/media/files/Downloads/Liste_chemische_Bestaendigkeiten_DE_2015.pdf, accessed on 17.05.11.

Burkey, Daniel (2014): Simulation der Strömung und des Wärmeübergangs in einem Wärmeübertrager mit Hyperworks. Studienarbeit. Kaiserslautern.

Calorplast GmbH: Official website. Available online at <http://www.calorplast-waermetechnik.de/>, accessed on 25.05.15.

Campbell, J. M. (1992): Gas conditioning and processing, Volume 1: Fundamentals. 7th ed. Norman: Campbell Petroleum Series.

CHEMIE.DE Information Service GmbH: Chemie.de Information Service website - Oberflächenspannung. Available online at <http://www.chemie.de/lexikon/Oberfl%C3%A4chenspannung.html>, accessed on 26.10.15.

Christmann, J. B. P.; Krätz, L. J.; Bart, H.-J. (2012): PEEK Film Heat Transfers Surfaces for Multi-effect Distillation: A Mechanical Investigation. In *Applied Thermal Engineering* 28, pp. 175–181.

CPS Chemical Process Solutions Ltd.: Official website. Available online at <http://www.cps-plastics.co.uk/>, accessed on 25.05.15.

Czichos, Horst; Skrotzki, Birgit; Simon, Franz-Georg (2014): Das Ingenieurwissen Werkstoffe. Berlin, Heidelberg: Springer-Verlag.

Derieth, T.; Bandlamundi, G.; Beckhaus, P.; Heinzl, A.; Kreuz, C.; Mahlendorf, F. (2008): Development of highly filled graphite compounds as bipolar plate material for low and high temperature PEM fuel cells. In *Journal of New Materials for Electrochemical Systems* 11, pp. 21–29.

DuPont Teijin Films: Mylar A data sheet. With assistance of DuPont Teijin Films. Available online at <http://www.dupontteijinfilms.com/filmenterprise/Datasheet.asp?ID=302&Version=US>, accessed on 30.05.15.

DuPont Teijin Films (2013): Kapton - Polyimidfolie - Zusammenfassung der Eigenschaften. Available online at http://www.goba.de/pics/service_support/c/Eigenschaften%20und%20Daten%20-%20Kapton.pdf, accessed on 28.06.13.

Elsner, Peter, Peter; Hirth, Eyerer; Thomas (2005): Die Kunststoffe und ihre Eigenschaften. 6th ed. Berlin, Heidelberg: Springer-Verlag.

Elsner, Peter; Eyerer, Peter; Hirth, Thomas (Eds.) (2012): Kunststoffe. Eigenschaften und Anwendungen. Berlin, Heidelberg: Springer-Verlag.

Frenkel, Michael; Kabo, G. J.; Marsch, K. N.; Roganov, G. N.; Wilhoit, R. C. (1994): Thermodynamics of Organic Compounds in the Gas State. Volume II. 2 volumes. Boulder: The Texas A&M System.

Gehr GmbH: Material information on PET. Available online at <http://www.gehr.de/>, accessed on 18.07.15.

German Federal Environment Agency (2015): Emissionsquellen. Available online at <http://www.umweltbundesamt.de/themen/klima-energie/klimaschutz-energiepolitik-in-deutschland/treibhausgas-emissionen/emissionsquellen>, accessed on 11.10.15.

GESTIS (2015): Substance Database. Edited by German Social Accident Insurance (DGUV). Available online at [http://gestis-en.itrust.de/nxt/gateway.dll?f=templates\\$fn=default.htm\\$vid=gestiseng:sdbeng](http://gestis-en.itrust.de/nxt/gateway.dll?f=templates$fn=default.htm$vid=gestiseng:sdbeng), accessed on 19.07.15.

Gleich (2015): EN AW 5083. Edited by Gleich Aluminiumwerk GmbH & Co. KG. Available online at <http://gleich.de/de/produkte/aluminium-walzplatten/al-walzplatten---en-aw/en-aw-5083?pdf>, accessed on 19.07.15.

Gooch, Jan W. (Ed.) (2007): Encyclopedic Dictionary of Polymers: Springer Science+Business Media, LLC.

Goodfellow GmbH: Product information database for polymer films. Available online at <http://www.goodfellow.com/catalogue/GFCatalogue.php?Language=G>, accessed on 19.07.15.

HERA AG: Die chemische Beständigkeit der Kunststoffe. Einflüsse und Verhalten. Available online at www.heratech.ch, accessed on 10.01.12.

Herwig, Heinz; Moschallski, Andreas (2014): Wärmeübertragung. Physikalische Grundlagen – Illustrierende Beispiele – Übungsaufgaben. 3rd ed.: Springer Vieweg.

Herwig, Heinz; Schmandt, Bastian (2015): Strömungsmechanik. Physik - mathematische Modelle - thermodynamische Aspekte. 3rd ed.: Springer Vieweg.

Hornbogen, Erhard; Eggeler, Gunther; Werner, Ewald (2012): Werkstoffe. Aufbau und Eigenschaften von Keramik-, Metall-, Polymer- und Verbundwerkstoffen. 10th ed. Berlin, Heidelberg: Springer-Verlag.

IAPWS (2014): Revised Release on the IAPWS Formulation 1995 for the Thermodynamic Properties of Ordinary Water Substance for General and Scientific Use. Edited by The International Association for the Properties of Water and Steam. The International Association for the Properties of Water and Steam. Moscow. Available online at <http://www.iapws.org/relguide/IAPWS95-2014.pdf>, accessed on 01.05.15.

Johnson, Richard (1998): *The Handbook of Fluid Dynamics*. Boca Raton: CRC Press LLC.

Laurien; Prof. Dr.-Ing. habil. E. Oertel; Prof. Prof. e.h. Dr.- Ing.habil. H.: (2011): *Numerische Strömungsmechanik*: Springer-Verlag.

Lechler, Stefan (2011): *Numerische Strömungsberechnung*. Berlin, Heidelberg: Springer-Verlag.

Mark, James E. (Ed.) (2007): *Physical Properties of Polymers Handbook*. 2nd ed.: Springer Science&Business Media, LLC.

Martin, Helmut (2011): *Numerische Strömungssimulation in der Hydrodynamik. Grundlagen und Methoden*. 1st ed. Berlin, Heidelberg: Springer-Verlag.

McBride, Bonnie J.; Sanford, Gordon (1992): *NASA Reference Publication 1271, Computer Program for Calculating and Fitting Thermodynamic Functions*. Cleveland: NASA.

McBride, Bonnie J.; Sanford, Gordon; Reno, Martin M. (1993): *NASA Technical Memorandum 4513, Coefficients for Calculating Thermodynamic and Transport Properties of Individual Species*. Cleveland: NASA.

Mchaweh, A.; Alsaygha, A.; Nasrifarb, Kh.; Moshfeghianc, M.: A simplified method for calculating saturated liquid densities. In : *Fluid Phase Equilibria*, vol. 6, pp. 157–167.

Menerga GmbH: Official website. Available online at <http://www.menerga.com/en/>, accessed on 25.05.15.

Menter, F. R. (1994): Two-Equation Eddy-Viscosity Turbulence Models for Engineering Applications. In *AIAA Paper 32 (8)*, pp. 1598–1605.

Meyer, Wolfgang (2014): *Numerische Untersuchung der Strömung in einem polymeren Wärmeübertrager*. Diplomarbeit. Kaiserslautern: TU Kaiserslautern.

Oertel, Herbert jr.; Böhle, Martin; Reviol, Thomas (2014): *Strömungsmechanik. für Ingenieure und Naturwissenschaftler*. 7th ed.: Springer Vieweg.

OpenCFD Ltd. (2015): *OpenFOAM Software package*: OpenCFD Ltd. Available online at <http://openfoam.com>, accessed on 23.05.14.

Perry, Clifford R.; Dietz, Lloyd H; Shannon, Roger L.: Heat exchange apparatus having thin film flexible sheets. App. no. US 06/200,510. Patent no. US 4411310 A.

Reichelt Chemietechnik GmbH u. Co. (2015): *Product information for THOMASANN-PTFE Adhesive based on Synthetic Rubber (Contact Adhesive)*. Available online at <http://en.rct-online.de/detail/index/sArticle/15915>, accessed on 31.05.15.

Rotert GmbH: Beständigkeitsliste der Kunststoffe. Available online at <http://www.rotert.com/WebRoot/Rotert/Shops/Rotert/MediaGallery/Dokumente/Bestaendigkeitsliste.pdf>, accessed on 17.02.12.

Schäfer, Jan (2013): CFD-Simulation der Strömung in einem Wärmeübertrager mit OpenFOAM. Studienprojekt. Kaiserslautern: TU Kaiserslautern.

Serban, Dan Andrei; Weber, Glenn; Marsavina, Liviu; Silberschmidt, Vadim V.; Hufenbach, Werner (2013): Tensile properties of semi-crystalline thermoplastic polymers: Effects of temperature and strain rates. In *Polymer Testing* 32, pp. 413–425.

Shi, X. Q.; Wang, Z. P.; Pang, H.L. J.; Zhang, X. R. (2002): Investigation of effect of temperature and strain rate on mechanical properties of underfill material by use of microtensile specimens. In *Polymer Testing* 21, pp. 725–733.

Soave, Giorgio (Ed.) (1972): Equilibrium constants from a modified Redlich-Kwong equation of state (Chemical Engineering Science, 27).

StrykerTECH LLC: Official website of StrykerTECH LLC. Available online at <http://www.stryker-tech.com>, accessed on 20.05.15.

T'Joen, C.; Park, Y.; Wang, Q.; Sommers, A.; Han, X.; Jacobi, A. (2009): A Review on polymer heat exchangers for HVAC&R applications. In *International Journal of Refrigeration* (32), pp. 763–779.

Taralov, M.; Taralova, V.; Popov, P.; Iliev, O.; Latz, A.; Zausch, J. (2012): Report on Finite Element Simulations of Electrochemical Processes in Li-ion Batteries with Thermic Effects. Edited by Fraunhofer TTWM. Available online at http://www.itwm.fraunhofer.de/fileadmin/ITWM-Media/Zentral/Pdf/Berichte_ITWM/2012/bericht_221.pdf, accessed on 28.03.16.

Thermoquick Engineering: Material data for PET. No longer available online, accessed on 17.02.12.

ThyssenKrupp: Werkstoffdatenblatt 16Mo3. Edited by ThyssenKrupp Materials International. Available online at http://www.thyssenkrupp-stahlkontor.de/tl_files/ThyssenKrupp/pdf/16Mo3.pdf, accessed on 19.07.15.

United Nations (2015): Framework Convention on Climate Change. Available online at http://unfccc.int/meetings/paris_nov_2015/meeting/8926.php, accessed on 20.12.15.

VDI (2006): VDI Wärmeatlas. 10th ed. Berlin, Heidelberg: Springer-Verlag.

von Böckh, Peter; Wetzel, Thomas (2014): Wärmeübertragung. Grundlagen und Praxis. 5th ed. Berlin: Springer Vieweg.

WilTec Wildanger Technik GmbH (2015): Official website. WilTec Wildanger Technik GmbH. Available online at <http://www.wiltec.de/>, accessed on 12.04.15.

Yang, Yong (2007): Thermal Conductivity. In James E. Mark (Ed.): *Physical Properties of Polymers Handbook*. 2nd ed.: Springer Science+Business Media, LLC, pp. 155–162.

Zaheed, L.; Jachuck, R.J.J. (2004): Review of polymer compact heat exchangers, with special emphasis on a polymer film unit. In *Applied Thermal Engineering* 24, pp. 2323–2358.

Zaheed, L.; Jachuck, R.J.J. (2005): Performance of a square, cross-corrugated, polymer film, compact, heat-exchanger with potential application in fuel cells. In *Journal of Power Sources* 140, pp. 304–310.

Zehe, Michael; Sanford, Gordon; McBride, Bonnie J. (2001): CAP: A computer Code for Generating Tabular Thermodynamic Functions from NASA Lewis Coefficients. Cleveland: NASA.

6. APPENDIX

6.1. EXPERIMENTAL DATA OBTAINED WITH THE LAB-SCALE HEAT EXCHANGER

Table 19: Experimental data obtained with the lab-scale heat exchanger: liquid water - water with polyimide film

Code of operating point	Flow cooling side		Flow hot side		Temperatures cooling side		Temperatures hot side	
	Inlet	Outlet	Inlet	Outlet	Inlet	Outlet	Inlet	Outlet
-	l/s	kg/s	l/min	kg/s	°C	°C	°C	°C
Water.Polyimide.70.170.20	0,016	0,016	0,17	0,0028	15,87	16,4	66,63	50,64
Water.Polyimide.70.170.25	0,020	0,020	0,17	0,0028	15,77	16,2	66,66	51,46
Water.Polyimide.70.170.30	0,024	0,024	0,17	0,0028	15,48	15,76	66,59	51,34
Water.Polyimide.70.170.35	0,029	0,029	0,17	0,0028	15,24	15,51	66,68	50,80
Water.Polyimide.70.170.40	0,033	0,033	0,17	0,0028	14,82	15,02	66,81	50,12
Water.Polyimide.70.170.45	0,037	0,037	0,17	0,0028	14,35	14,53	66,82	48,64
Water.Polyimide.70.320.20	0,016	0,016	0,32	0,0053	14,87	16,22	62,28	51,27
Water.Polyimide.70.320.25	0,020	0,020	0,32	0,0053	14,58	15,72	61,32	50,61
Water.Polyimide.70.320.30	0,024	0,024	0,32	0,0053	14,3	15,52	61,09	50,10
Water.Polyimide.70.320.35	0,029	0,029	0,32	0,0053	14,24	15,15	61,1	49,95
Water.Polyimide.70.320.40	0,033	0,033	0,32	0,0053	14,09	14,75	60,9	49,46
Water.Polyimide.70.320.45	0,037	0,037	0,32	0,0053	14,05	14,73	60,98	48,63
Water.Polyimide.70.480.20	0,016	0,016	0,48	0,008	13,11	14,96	59,72	51,16
Water.Polyimide.70.480.25	0,020	0,020	0,48	0,008	12,82	14,58	59,4	50,29
Water.Polyimide.70.480.30	0,024	0,024	0,48	0,008	12,57	14,08	58,14	48,89
Water.Polyimide.70.480.35	0,029	0,029	0,48	0,008	12,47	13,78	58,08	48,77
Water.Polyimide.70.480.40	0,033	0,033	0,48	0,008	12,37	13,49	58,07	48,33
Water.Polyimide.70.480.45	0,037	0,037	0,48	0,008	12,20	13,16	57,99	47,91
Water.Polyimide.70.650.20	0,016	0,016	0,65	0,0108	12,73	15,10	56,03	49,08
Water.Polyimide.70.650.25	0,020	0,020	0,65	0,0108	14,62	15,55	55,85	48,32
Water.Polyimide.70.650.30	0,024	0,024	0,65	0,0108	12,47	14,52	55,60	47,75
Water.Polyimide.70.650.35	0,029	0,029	0,65	0,0108	12,47	14,32	55,62	47,66
Water.Polyimide.70.650.40	0,033	0,033	0,65	0,0108	12,44	13,93	55,70	47,29
Water.Polyimide.70.650.45	0,037	0,037	0,65	0,0108	12,48	13,55	58,80	48,26
Water.Polyimide.70.790.20	0,016	0,016	0,79	0,0131	13,23	16,12	56,99	50,33
Water.Polyimide.70.790.25	0,020	0,020	0,79	0,0131	13,01	15,31	56,80	49,79
Water.Polyimide.70.790.30	0,024	0,024	0,79	0,0131	12,90	15,18	56,50	49,23
Water.Polyimide.70.790.35	0,029	0,029	0,79	0,0131	12,83	14,92	56,42	49,05

Water.Polyimide.70.790.40	0,033	0,033	0,79	0,0131	12,77	14,54	56,39	48,64
Water.Polyimide.70.790.45	0,037	0,037	0,79	0,0131	12,73	14,42	55,94	47,95
Water.Polyimide.70.1010.20	0,016	0,016	1,01	0,0168	13,41	16,81	56,01	49,82
Water.Polyimide.70.1010.25	0,020	0,020	1,01	0,0168	13,21	16,24	55,66	48,99
Water.Polyimide.70.1010.30	0,024	0,024	1,01	0,0168	13,08	15,65	55,49	48,61
Water.Polyimide.70.1010.35	0,029	0,029	1,01	0,0168	13,00	15,51	55,19	47,99
Water.Polyimide.70.1010.40	0,033	0,033	1,01	0,0168	12,89	15,01	54,84	47,29
Water.Polyimide.70.1010.45	0,037	0,037	1,01	0,0168	12,83	14,90	54,82	46,81

Table 20: Experimental data obtained with the lab-scale heat exchanger: liquid water - water with PTFE film

Code of operating point	Flow cooling side		Flow hot side		Temperatures cooling side		Temperatures hot side	
	l/s	kg/s	l/min	kg/s	Inlet °C	Outlet °C	Inlet °C	Outlet °C
Water.PTFE.70.170.20	0,016	0,016	0,17	0,0028	16,05	16,98	67,65	55,74
Water.PTFE.70.170.25	0,020	0,020	0,17	0,0028	16,1	16,59	67,67	55,94
Water.PTFE.70.170.30	0,024	0,024	0,17	0,0028	16,24	16,51	67,67	56,13
Water.PTFE.70.170.35	0,029	0,029	0,17	0,0028	16,54	16,74	67,64	55,72
Water.PTFE.70.170.40	0,033	0,033	0,17	0,0028	17,01	17,13	67,63	55,48
Water.PTFE.70.170.45	0,037	0,037	0,17	0,0028	17,72	17,81	67,55	55,28
Water.PTFE.70.320.20	0,016	0,016	0,32	0,0053	14,95	16,94	62,7	52,59
Water.PTFE.70.320.25	0,020	0,020	0,32	0,0053	14,72	16,31	62,73	52,57
Water.PTFE.70.320.30	0,024	0,024	0,32	0,0053	14,63	15,93	62,55	52,36
Water.PTFE.70.320.35	0,029	0,029	0,32	0,0053	14,46	15,56	62,66	52,31
Water.PTFE.70.320.40	0,033	0,033	0,32	0,0053	14,45	15,14	62,38	51,98
Water.PTFE.70.320.45	0,037	0,037	0,32	0,0053	14,63	15,02	62,5	52,90
Water.PTFE.70.480.20	0,016	0,016	0,48	0,008	14,91	17,13	59,79	52,41
Water.PTFE.70.480.25	0,020	0,020	0,48	0,008	14,83	16,86	60,38	52,62
Water.PTFE.70.480.30	0,024	0,024	0,48	0,008	14,57	16,32	60,41	52,20
Water.PTFE.70.480.35	0,029	0,029	0,48	0,008	14,49	16,09	60,36	51,91
Water.PTFE.70.480.40	0,033	0,033	0,48	0,008	14,38	15,57	60,24	51,62
Water.PTFE.70.480.45	0,037	0,037	0,48	0,008	14,18	15,26	60,29	51,41
Water.PTFE.70.650.20	0,016	0,016	0,65	0,0108	19,21	22,13	58,53	52,04
Water.PTFE.70.650.25	0,020	0,020	0,65	0,0108	19,16	21,63	58,59	51,58
Water.PTFE.70.650.30	0,024	0,024	0,65	0,0108	19,18	21,44	58,62	51,60
Water.PTFE.70.650.35	0,029	0,029	0,65	0,0108	14,27	16,25	56,30	48,39
Water.PTFE.70.650.40	0,033	0,033	0,65	0,0108	19,67	21,14	58,76	51,98
Water.PTFE.70.650.45	0,037	0,037	0,65	0,0108	19,38	20,72	58,74	51,80
Water.PTFE.70.790.20	0,016	0,016	0,79	0,0131	17,81	20,96	57,74	51,73
Water.PTFE.70.790.25	0,020	0,020	0,79	0,0131	17,84	20,55	57,63	51,50
Water.PTFE.70.790.30	0,024	0,024	0,79	0,0131	17,99	20,30	57,66	51,44
Water.PTFE.70.790.35	0,029	0,029	0,79	0,0131	18,34	20,35	57,77	51,40
Water.PTFE.70.790.40	0,033	0,033	0,79	0,0131	18,60	20,25	57,89	51,61
Water.PTFE.70.790.45	0,037	0,037	0,79	0,0131	18,96	20,42	57,90	51,54

Water.PTFE.70.1010.20	0,016	0,016	1,01	0,0168	17,53	20,75	56,81	51,55
Water.PTFE.70.1010.25	0,020	0,020	1,01	0,0168	17,10	19,85	56,59	51,04
Water.PTFE.70.1010.30	0,024	0,024	1,01	0,0168	16,73	19,17	56,67	50,92
Water.PTFE.70.1010.35	0,029	0,029	1,01	0,0168	16,43	18,66	56,44	50,61
Water.PTFE.70.1010.40	0,033	0,033	1,01	0,0168	16,19	18,08	56,35	50,26
Water.PTFE.70.1010.45	0,037	0,037	1,01	0,0168	16,01	17,63	56,16	50,27

Table 21: Experimental data obtained with the lab-scale heat exchanger: liquid hexane - water with polyimide film

Code of operating point	Flow cooling side		Flow hot side		Temperatures cooling side		Temperatures hot side	
	l/s	kg/s	l/min	kg/s	Inlet °C	Outlet °C	Inlet °C	Outlet °C
Hexane.Polyimide.70.170.20	0,016	0,016	0,17	0,0017	17,54	17,91	68,14	31,07
Hexane.Polyimide.70.170.25	0,020	0,020	0,17	0,0017	17,43	17,77	68,14	30,14
Hexane.Polyimide.70.170.30	0,024	0,024	0,17	0,0017	17,26	17,72	68,14	29,83
Hexane.Polyimide.70.170.35	0,029	0,029	0,17	0,0017	17,2	17,7	68,13	29,46
Hexane.Polyimide.70.170.40	0,033	0,033	0,17	0,0017	17,11	17,37	68,1	28,71
Hexane.Polyimide.70.170.45	0,037	0,037	0,17	0,0017	17,1	17,34	68,01	28,44
Hexane.Polyimide.70.320.20	0,016	0,016	0,32	0,0033	17,64	18,93	67,21	37,83
Hexane.Polyimide.70.320.25	0,020	0,020	0,32	0,0033	17,44	18,62	67,14	37,24
Hexane.Polyimide.70.320.30	0,024	0,024	0,32	0,0033	17,23	18,49	67,12	37,79
Hexane.Polyimide.70.320.35	0,029	0,029	0,32	0,0033	17,17	18,19	67,13	37,14
Hexane.Polyimide.70.320.40	0,033	0,033	0,32	0,0033	17,17	17,92	67,16	35,68
Hexane.Polyimide.70.320.45	0,037	0,037	0,32	0,0033	17,05	17,65	67,16	34,83
Hexane.Polyimide.70.480.20	0,016	0,016	0,48	0,0049	17,89	19,57	66,21	42,55
Hexane.Polyimide.70.480.25	0,020	0,020	0,48	0,0049	17,56	19,08	66,11	42,63
Hexane.Polyimide.70.480.30	0,024	0,024	0,48	0,0049	17,41	19,01	66,03	42,43
Hexane.Polyimide.70.480.35	0,029	0,029	0,48	0,0049	17,26	18,60	66,04	41,61
Hexane.Polyimide.70.480.40	0,033	0,033	0,48	0,0049	17,19	18,38	65,90	40,26
Hexane.Polyimide.70.480.45	0,037	0,037	0,48	0,0049	17,02	17,98	65,76	39,67
Hexane.Polyimide.70.650.20	0,016	0,016	0,65	0,0067	22,57	24,08	64,44	48,06
Hexane.Polyimide.70.650.25	0,020	0,020	0,65	0,0067	22,41	23,91	64,71	47,51
Hexane.Polyimide.70.650.30	0,024	0,024	0,65	0,0067	22,26	23,95	64,83	47,19
Hexane.Polyimide.70.650.35	0,029	0,029	0,65	0,0067	22,17	23,79	64,79	46,72
Hexane.Polyimide.70.650.40	0,033	0,033	0,65	0,0067	21,98	23,39	64,82	46,30
Hexane.Polyimide.70.650.45	0,037	0,037	0,65	0,0067	21,89	23,05	64,79	45,84
Hexane.Polyimide.70.790.20	0,016	0,016	0,79	0,0082	20,81	22,50	62,51	47,95
Hexane.Polyimide.70.790.25	0,020	0,020	0,79	0,0082	20,71	22,60	62,38	47,23
Hexane.Polyimide.70.790.30	0,024	0,024	0,79	0,0082	20,81	22,83	62,23	46,89
Hexane.Polyimide.70.790.35	0,029	0,029	0,79	0,0082	20,90	22,71	62,20	46,57
Hexane.Polyimide.70.790.40	0,033	0,033	0,79	0,0082	21,16	22,55	62,17	46,33
Hexane.Polyimide.70.790.45	0,037	0,037	0,79	0,0082	21,18	22,48	62,36	46,20

Hexane.Polyimide.70.1010.20	0,016	0,016	1,01	0,0104	20,20	22,23	62,13	48,83
Hexane.Polyimide.70.1010.25	0,020	0,020	1,01	0,0104	19,83	21,69	62,12	47,97
Hexane.Polyimide.70.1010.30	0,024	0,024	1,01	0,0104	19,50	21,78	62,13	47,55
Hexane.Polyimide.70.1010.35	0,029	0,029	1,01	0,0104	19,12	21,14	62,19	47,11
Hexane.Polyimide.70.1010.40	0,033	0,033	1,01	0,0104	18,78	20,40	62,18	46,44
Hexane.Polyimide.70.1010.45	0,037	0,037	1,01	0,0104	18,40	19,89	62,20	45,80

Table 22: Experimental data obtained with the lab-scale heat exchanger: liquid hexane – water with PTFE film

Code of operating point	Flow cooling side		Flow hot side		Temperatures cooling side		Temperatures hot side	
	l/s	kg/s	l/min	kg/s	Inlet °C	Outlet °C	Inlet °C	Outlet °C
-	l/s	kg/s	l/min	kg/s	°C	°C	°C	°C
Hexane.PTFE.70.170.20	0,016	0,016	0,17	0,0017	14,96	15,6	67,84	32,75
Hexane.PTFE.70.170.25	0,020	0,020	0,17	0,0017	14,51	15,07	67,88	31,38
Hexane.PTFE.70.170.30	0,024	0,024	0,17	0,0017	14,21	14,69	67,89	30,80
Hexane.PTFE.70.170.35	0,029	0,029	0,17	0,0017	13,92	14,2	67,93	30,41
Hexane.PTFE.70.170.40	0,033	0,033	0,17	0,0017	13,7	13,94	67,97	29,79
Hexane.PTFE.70.170.45	0,037	0,037	0,17	0,0017	13,54	13,69	67,96	29,40
Hexane.PTFE.70.320.20	0,016	0,016	0,32	0,0033	13,82	15,15	67,06	40,65
Hexane.PTFE.70.320.25	0,020	0,020	0,32	0,0033	13,71	14,95	67,07	40,37
Hexane.PTFE.70.320.30	0,024	0,024	0,32	0,0033	13,62	14,64	67,03	40,11
Hexane.PTFE.70.320.35	0,029	0,029	0,32	0,0033	13,54	14,41	67,07	39,84
Hexane.PTFE.70.320.40	0,033	0,033	0,32	0,0033	13,51	14,21	67,06	39,40
Hexane.PTFE.70.320.45	0,037	0,037	0,32	0,0033	13,48	14,15	66,99	38,31
Hexane.PTFE.70.480.20	0,016	0,016	0,48	0,0049	13,82	15,65	65,29	45,42
Hexane.PTFE.70.480.25	0,020	0,020	0,48	0,0049	13,65	15,26	65,35	44,45
Hexane.PTFE.70.480.30	0,024	0,024	0,48	0,0049	13,54	14,94	65,27	43,74
Hexane.PTFE.70.480.35	0,029	0,029	0,48	0,0049	13,37	14,61	65,25	43,21
Hexane.PTFE.70.480.40	0,033	0,033	0,48	0,0049	13,20	14,30	65,25	42,82
Hexane.PTFE.70.480.45	0,037	0,037	0,48	0,0049	13,17	14,12	65,21	42,00
Hexane.PTFE.70.650.20	0,016	0,016	0,65	0,0067	24,71	26,98	62,63	50,75
Hexane.PTFE.70.650.25	0,020	0,020	0,65	0,0067	24,74	26,56	62,70	50,34
Hexane.PTFE.70.650.30	0,024	0,024	0,65	0,0067	24,83	26,54	62,83	49,92
Hexane.PTFE.70.650.35	0,029	0,029	0,65	0,0067	24,95	26,41	62,73	49,55
Hexane.PTFE.70.650.40	0,033	0,033	0,65	0,0067	25,13	26,45	62,82	49,33
Hexane.PTFE.70.650.45	0,037	0,037	0,65	0,0067	25,33	26,54	63,16	49,17
Hexane.PTFE.70.790.20	0,016	0,016	0,79	0,0082	25,07	28,06	62,98	50,97
Hexane.PTFE.70.790.25	0,020	0,020	0,79	0,0082	24,59	26,88	63,06	50,51
Hexane.PTFE.70.790.30	0,024	0,024	0,79	0,0082	23,86	26,12	63,14	49,94
Hexane.PTFE.70.790.35	0,029	0,029	0,79	0,0082	23,16	24,95	63,14	49,25
Hexane.PTFE.70.790.40	0,033	0,033	0,79	0,0082	22,30	23,94	63,21	48,43
Hexane.PTFE.70.790.45	0,037	0,037	0,79	0,0082	21,29	22,76	63,28	47,54

Hexane.PTFE.70.1010.20	0,016	0,016	1,01	0,0104	20,27	23,96	62,58	49,81
Hexane.PTFE.70.1010.25	0,020	0,020	1,01	0,0104	19,39	22,22	62,81	48,66
Hexane.PTFE.70.1010.30	0,024	0,024	1,01	0,0104	18,68	21,37	63,17	48,12
Hexane.PTFE.70.1010.35	0,029	0,029	1,01	0,0104	18,23	20,20	63,60	47,61
Hexane.PTFE.70.1010.40	0,033	0,033	1,01	0,0104	17,35	19,04	64,06	47,05
Hexane.PTFE.70.1010.45	0,037	0,037	1,01	0,0104	16,72	18,00	64,39	46,89

Table 23: Experimental data obtained with the lab-scale heat exchanger: gaseous hexane – water with polyimide film

Code of operating point	Flow cooling side		Flow hot side		Temperatures cooling side		Temperatures hot side	
	l/s	kg/s	l/min	kg/s	Inlet °C	Outlet °C	Inlet °C	Outlet °C
Hexane.Cond.Polyimide.90.90.20	0,016	0,0158	0,094	0,0009	14,05	17,92	79,37	35,04
Hexane.Cond.Polyimide.90.90.25	0,020	0,0200	0,094	0,0009	13,91	16,42	79,8	32,64
Hexane.Cond.Polyimide.90.90.30	0,024	0,0243	0,094	0,0009	13,78	17,62	79,93	30,66
Hexane.Cond.Polyimide.90.90.35	0,029	0,0285	0,094	0,0009	13,74	16,95	79,90	29,63
Hexane.Cond.Polyimide.90.90.40	0,033	0,0329	0,094	0,0009	13,67	16,15	79,84	28,84
Hexane.Cond.Polyimide.90.90.45	0,037	0,0372	0,094	0,0009	13,44	15,35	79,91	27,85
Hexane.Cond.Polyimide.90.110.20	0,016	0,0158	0,116	0,0012	14,38	18,74	78,75	38,33
Hexane.Cond.Polyimide.90.110.25	0,020	0,0200	0,116	0,0012	14,01	17,85	78,81	36,11
Hexane.Cond.Polyimide.90.110.30	0,024	0,0243	0,116	0,0012	13,89	18,13	78,82	34,79
Hexane.Cond.Polyimide.90.110.35	0,029	0,0285	0,116	0,0012	14,07	17,88	78,84	33,62
Hexane.Cond.Polyimide.90.110.40	0,033	0,0329	0,116	0,0012	14,5	16,84	78,9	32,32
Hexane.Cond.Polyimide.90.110.45	0,037	0,0372	0,116	0,0012	15,05	17,51	79,01	29,90
Hexane.Cond.Polyimide.90.170.20.1	0,016	0,0158	0,174	0,0018	14,97	21,74	77,61	66,94
Hexane.Cond.Polyimide.90.170.20.2	0,016	0,0158	0,174	0,0018	14,68	21,17	77,9	64,98
Hexane.Cond.Polyimide.90.170.20.3	0,016	0,0158	0,174	0,0018	17,86	25,09	78,00	66,80
Hexane.Cond.Polyimide.90.170.20.4	0,016	0,0158	0,174	0,0018	22,29	28,25	77,56	68,20
Hexane.Cond.Polyimide.90.170.25	0,020	0,0200	0,174	0,0018	15,00	22,21	77,69	61,39
Hexane.Cond.Polyimide.90.170.25	0,020	0,0200	0,174	0,0018	14,68	20,2	77,99	57,93
Hexane.Cond.Polyimide.90.170.25.1	0,020	0,0200	0,174	0,0018	18,55	24,97	77,94	66,76
Hexane.Cond.Polyimide.90.170.25.2	0,020	0,0200	0,174	0,0018	20,54	26,81	78,1	59,83
Hexane.Cond.Polyimide.90.170.30.1	0,024	0,0243	0,174	0,0018	14,83	20,46	77,9	54,58
Hexane.Cond.Polyimide.90.170.30.2	0,024	0,0243	0,174	0,0018	15,24	20,99	77,99	54,77
Hexane.Cond.Polyimide.90.170.30.3	0,024	0,0242	0,174	0,0018	19,54	25,6	77,9	64,32
Hexane.Cond.Polyimide.90.170.30.4	0,024	0,0242	0,174	0,0018	19,19	25,09	78,15	52,55
Hexane.Cond.Polyimide.90.170.35.1	0,029	0,0285	0,174	0,0018	15,01	20,28	77,97	51,89
Hexane.Cond.Polyimide.90.170.35.2	0,029	0,0285	0,174	0,0018	20,23	25,5	77,91	58,57
Hexane.Cond.Polyimide.90.170.35.3	0,029	0,0285	0,174	0,0018	18,57	23,56	78,23	50,25
Hexane.Cond.Polyimide.90.170.40.1	0,033	0,0329	0,174	0,0018	15,4	19,24	78,01	49,00
Hexane.Cond.Polyimide.90.170.40.2	0,033	0,0329	0,174	0,0018	15,08	19,02	78	47,37
Hexane.Cond.Polyimide.90.170.40.3	0,033	0,0328	0,174	0,0018	21,4	25,83	77,94	53,73
Hexane.Cond.Polyimide.90.170.40.4	0,033	0,0328	0,174	0,0018	18,11	22,03	78,21	45,97

Hexane.Cond.Polyimide.90.170.45.1	0,037	0,0372	0,174	0,0018	16,91	20,58	77,77	47,17
Hexane.Cond.Polyimide.90.170.45.2	0,037	0,0372	0,174	0,0018	14,86	18,28	78,04	43,60
Hexane.Cond.Polyimide.90.170.45.3	0,037	0,0372	0,174	0,0018	22	25,68	77,89	51,97
Hexane.Cond.Polyimide.90.170.45.4	0,037	0,0372	0,174	0,0018	17,09	20,6	78,31	42,45
Hexane.Cond.Polyimide.90.230.20	0,016	0,0158	0,23	0,0024	14,11	20,56	69,31	68,19
Hexane.Cond.Polyimide.90.230.25	0,020	0,0200	0,23	0,0024	13,95	20,19	69,31	68,27
Hexane.Cond.Polyimide.90.230.30	0,024	0,0243	0,23	0,0024	13,74	19,95	69,37	67,74
Hexane.Cond.Polyimide.90.230.35	0,029	0,0285	0,23	0,0024	13,66	19,31	69,35	67,50
Hexane.Cond.Polyimide.90.230.40	0,033	0,0329	0,23	0,0024	13,55	17,87	69,29	67,85
Hexane.Cond.Polyimide.90.230.45	0,037	0,0372	0,23	0,0024	13,38	17,31	69,32	66,56
Hexane.Cond.Polyimide.90.320.40	0,033	0,0328	0,328	0,0034	25,39	29,52	69,29	68,68
Hexane.Cond.Polyimide.90.320.45	0,037	0,0371	0,328	0,0034	25,39	28,99	69,36	68,70

Table 24: Experimental data obtained with the lab-scale heat exchanger: gaseous hexane – water with PTFE film

Code of operating point	Flow cooling side		Flow hot side		Temperatures cooling side		Temperatures hot side	
	l/s	kg/s	l/min	kg/s	Inlet °C	Outlet °C	Inlet °C	Outlet °C
Hexane.Cond.PTFE.90.90.20	0,016	0,0158	0,094	0,0009	14,05	17,92	79,37	35,04
Hexane.Cond.PTFE.90.90.25	0,020	0,0200	0,094	0,0009	13,91	16,42	79,8	32,64
Hexane.Cond.PTFE.90.90.30	0,024	0,0243	0,094	0,0009	13,78	17,62	79,93	30,66
Hexane.Cond.PTFE.90.90.35	0,029	0,0285	0,094	0,0009	13,74	16,95	79,90	29,63
Hexane.Cond.PTFE.90.90.40	0,033	0,0329	0,094	0,0009	13,67	16,15	79,84	28,84
Hexane.Cond.PTFE.90.90.45	0,037	0,0372	0,094	0,0009	13,44	15,35	79,91	27,85
Hexane.Cond.PTFE.90.110.20	0,016	0,0158	0,116	0,0012	14,38	18,74	78,75	38,33
Hexane.Cond.PTFE.90.110.25	0,020	0,0200	0,116	0,0012	14,01	17,85	78,81	36,11
Hexane.Cond.PTFE.90.110.30	0,024	0,0243	0,116	0,0012	13,89	18,13	78,82	34,79
Hexane.Cond.PTFE.90.110.35	0,029	0,0285	0,116	0,0012	14,07	17,88	78,84	33,62
Hexane.Cond.PTFE.90.110.40	0,033	0,0329	0,116	0,0012	14,5	16,84	78,9	32,32
Hexane.Cond.PTFE.90.110.45	0,037	0,0372	0,116	0,0012	15,05	17,51	79,01	29,90
Hexane.Cond.PTFE.90.170.20.1	0,016	0,0158	0,174	0,0018	14,97	21,74	77,61	66,94
Hexane.Cond.PTFE.90.170.20.2	0,016	0,0158	0,174	0,0018	14,68	21,17	77,9	64,98
Hexane.Cond.PTFE.90.170.20.3	0,016	0,0158	0,174	0,0018	17,86	25,09	78,00	66,80
Hexane.Cond.PTFE.90.170.20.4	0,016	0,0158	0,174	0,0018	22,29	28,25	77,56	68,20
Hexane.Cond.PTFE.90.170.25.1	0,020	0,0200	0,174	0,0018	15,00	22,21	77,69	61,39
Hexane.Cond.PTFE.90.170.25.2	0,020	0,0200	0,174	0,0018	14,68	20,2	77,99	57,93
Hexane.Cond.PTFE.90.170.25.3	0,020	0,0200	0,174	0,0018	18,55	24,97	77,94	66,76
Hexane.Cond.PTFE.90.170.25.4	0,020	0,0200	0,174	0,0018	20,54	26,81	78,1	59,83
Hexane.Cond.PTFE.90.170.30.1	0,024	0,0243	0,174	0,0018	14,83	20,46	77,9	54,58
Hexane.Cond.PTFE.90.170.30.2	0,024	0,0243	0,174	0,0018	15,24	20,99	77,99	54,77
Hexane.Cond.PTFE.90.170.30.3	0,024	0,0242	0,174	0,0018	19,54	25,6	77,9	64,32
Hexane.Cond.PTFE.90.170.30.4	0,024	0,0242	0,174	0,0018	19,19	25,09	78,15	52,55
Hexane.Cond.PTFE.90.170.35.1	0,029	0,0285	0,174	0,0018	15,01	20,28	77,97	51,89
Hexane.Cond.PTFE.90.170.35.2	0,029	0,0285	0,174	0,0018	20,23	25,5	77,91	58,57
Hexane.Cond.PTFE.90.170.35.3	0,029	0,0285	0,174	0,0018	18,57	23,56	78,23	50,25
Hexane.Cond.PTFE.90.170.40.4	0,033	0,0329	0,174	0,0018	15,4	19,24	78,01	49,00
Hexane.Cond.PTFE.90.170.40.1	0,033	0,0329	0,174	0,0018	15,08	19,02	78	47,37
Hexane.Cond.PTFE.90.170.40.2	0,033	0,0328	0,174	0,0018	21,4	25,83	77,94	53,73
Hexane.Cond.PTFE.90.170.40.3	0,033	0,0328	0,174	0,0018	18,11	22,03	78,21	45,97

Hexane.Cond.PTFE.90.170.45.1	0,037	0,0372	0,174	0,0018	16,91	20,58	77,77	47,17
Hexane.Cond.PTFE.90.170.45.2	0,037	0,0372	0,174	0,0018	14,86	18,28	78,04	43,60
Hexane.Cond.PTFE.90.170.45.3	0,037	0,0372	0,174	0,0018	22	25,68	77,89	51,97
Hexane.Cond.PTFE.90.170.45.4	0,037	0,0372	0,174	0,0018	17,09	20,6	78,31	42,45
Hexane.Cond.PTFE.90.230.20	0,016	0,0158	0,23	0,0024	14,11	20,56	69,31	68,19
Hexane.Cond.PTFE.90.230.25	0,020	0,0200	0,23	0,0024	21,31	27,08	69,77	68,85
Hexane.Cond.PTFE.90.230.30	0,024	0,0242	0,23	0,0024	21,19	26,00	69,91	68,87
Hexane.Cond.PTFE.90.230.35	0,029	0,0285	0,23	0,0024	20,89	24,90	69,92	68,84
Hexane.Cond.PTFE.90.230.40	0,033	0,0328	0,23	0,0024	20,64	24,45	69,91	68,85
Hexane.Cond.PTFE.90.230.45	0,037	0,0372	0,23	0,0024	20,28	23,53	69,96	68,83
Hexane.Cond.PTFE.90.320.40	0,033	0,0328	0,328	0,0034	20,07	23,81	69,37	69,10
Hexane.Cond.PTFE.90.320.45	0,037	0,0372	0,328	0,0034	20,12	22,87	69,31	68,78

6.2. EXPERIMENTAL DATA OBTAINED WITH THE FULL-SCALE DEMONSTRATOR 2

Table 25: Experimental data obtained with the full-scale heat demonstrator 2: water – water with PET film

Code of operating point	Flow cooling side		Flow hot side		Temperatures cooling side		Temperatures hot side	
	l/s	kg/s	l/min	kg/s	Inlet °C	Outlet °C	Inlet °C	Outlet °C
Water.PET.70.170.20	0,016	0,016	0,17	0,0028	15,87	16,4	66,63	50,64
Water.PET.70.170.25	0,020	0,020	0,17	0,0028	15,77	16,2	66,66	51,46
Water.PET.70.170.30	0,024	0,024	0,17	0,0028	15,48	15,76	66,59	51,34
Water.PET.70.170.35	0,029	0,029	0,17	0,0028	15,24	15,51	66,68	50,80
Water.PET.70.170.40	0,033	0,033	0,17	0,0028	14,82	15,02	66,81	50,12
Water.PET.70.170.45	0,037	0,037	0,17	0,0028	14,35	14,53	66,82	48,64
Water.PET.70.320.20	0,016	0,016	0,32	0,0053	14,87	16,22	62,28	51,27
Water.PET.70.320.25	0,020	0,020	0,32	0,0053	14,58	15,72	61,32	50,61
Water.PET.70.320.30	0,024	0,024	0,32	0,0053	14,3	15,52	61,09	50,10
Water.PET.70.320.35	0,029	0,029	0,32	0,0053	14,24	15,15	61,1	49,95
Water.PET.70.320.40	0,033	0,033	0,32	0,0053	14,09	14,75	60,9	49,46
Water.PET.70.320.45	0,037	0,037	0,32	0,0053	14,05	14,73	60,98	48,63
Water.PET.70.480.20	0,016	0,016	0,48	0,008	13,11	14,96	59,72	51,16
Water.PET.70.480.25	0,020	0,020	0,48	0,008	12,82	14,58	59,4	50,29
Water.PET.70.480.30	0,024	0,024	0,48	0,008	12,57	14,08	58,14	48,89
Water.PET.70.480.35	0,029	0,029	0,48	0,008	12,47	13,78	58,08	48,77
Water.PET.70.480.40	0,033	0,033	0,48	0,008	12,37	13,49	58,07	48,33
Water.PET.70.480.45	0,037	0,037	0,48	0,008	12,20	13,16	57,99	47,91
Water.PET.70.650.20	0,016	0,016	0,65	0,0108	12,73	15,10	56,03	49,08
Water.PET.70.650.25	0,020	0,020	0,65	0,0108	14,62	15,55	55,85	48,32
Water.PET.70.650.30	0,024	0,024	0,65	0,0108	12,47	14,52	55,60	47,75
Water.PET.70.650.35	0,029	0,029	0,65	0,0108	12,47	14,32	55,62	47,66
Water.PET.70.650.40	0,033	0,033	0,65	0,0108	12,44	13,93	55,70	47,29
Water.PET.70.650.45	0,037	0,037	0,65	0,0108	12,48	13,55	58,80	48,26
Water.PET.70.790.20	0,016	0,016	0,79	0,0131	13,23	16,12	56,99	50,33
Water.PET.70.790.25	0,020	0,020	0,79	0,0131	13,01	15,31	56,80	49,79
Water.PET.70.790.30	0,024	0,024	0,79	0,0131	12,90	15,18	56,50	49,23
Water.PET.70.790.35	0,029	0,029	0,79	0,0131	12,83	14,92	56,42	49,05
Water.PET.70.790.40	0,033	0,033	0,79	0,0131	12,77	14,54	56,39	48,64

Water.PET.70.790.45	0,037	0,037	0,79	0,0131	12,73	14,42	55,94	47,95
Water.PET.70.1010.20	0,016	0,016	1,01	0,0168	13,41	16,81	56,01	49,82
Water.PET.70.1010.25	0,020	0,020	1,01	0,0168	13,21	16,24	55,66	48,99
Water.PET.70.1010.30	0,024	0,024	1,01	0,0168	13,08	15,65	55,49	48,61
Water.PET.70.1010.35	0,029	0,029	1,01	0,0168	13,00	15,51	55,19	47,99
Water.PET.70.1010.40	0,033	0,033	1,01	0,0168	12,89	15,01	54,84	47,29
Water.PET.70.1010.45	0,037	0,037	1,01	0,0168	12,83	14,90	54,82	46,81

Table 26: Experimental data obtained with the full-scale heat demonstrator 2: gaseous hexane – water with PET film

Code of operating point	Flow cooling side		Flow hot side		Temperatures cooling side		Temperatures hot side	
	l/s	kg/s	l/min	kg/s	Inlet °C	Outlet °C	Inlet °C	Outlet °C
-								
Hexane.Cond.PET.90.90.20	0,016	0,0158	0,094	0,0009	14,05	17,92	79,37	35,04
Hexane.Cond.PET.90.90.25	0,020	0,0200	0,094	0,0009	13,91	16,42	79,8	32,64
Hexane.Cond.PET.90.90.30	0,024	0,0243	0,094	0,0009	13,78	17,62	79,93	30,66
Hexane.Cond.PET.90.90.35	0,029	0,0285	0,094	0,0009	13,74	16,95	79,90	29,63
Hexane.Cond.PET.90.90.40	0,033	0,0329	0,094	0,0009	13,67	16,15	79,84	28,84
Hexane.Cond.PET.90.90.45	0,037	0,0372	0,094	0,0009	13,44	15,35	79,91	27,85
Hexane.Cond.PET.90.110.20	0,016	0,0158	0,116	0,0012	14,38	18,74	78,75	38,33
Hexane.Cond.PET.90.110.25	0,020	0,0200	0,116	0,0012	14,01	17,85	78,81	36,11
Hexane.Cond.PET.90.110.30	0,025	0,0243	0,116	0,0012	13,89	18,13	78,82	34,79
Hexane.Cond.PET.90.110.35	0,029	0,0285	0,116	0,0012	14,07	17,88	78,84	33,62
Hexane.Cond.PET.90.110.40	0,033	0,0329	0,116	0,0012	14,5	16,84	78,9	32,32
Hexane.Cond.PET.90.110.45	0,037	0,0372	0,116	0,0012	15,05	17,51	79,01	29,90
Hexane.Cond.PET.90.170.20	0,016	0,0158	0,174	0,0018	14,97	21,74	77,61	66,94
Hexane.Cond.PET.90.170.20	0,016	0,0158	0,174	0,0018	14,68	21,17	77,9	64,98
Hexane.Cond.PET.90.170.20	0,016	0,0158	0,174	0,0018	17,86	25,09	78	66,80
Hexane.Cond.PET.90.170.20	0,016	0,0158	0,174	0,0018	22,29	28,25	77,56	68,20
Hexane.Cond.PET.90.170.25	0,020	0,0200	0,174	0,0018	15	22,21	77,69	61,39
Hexane.Cond.PET.90.170.25	0,020	0,0200	0,174	0,0018	14,68	20,2	77,99	57,93
Hexane.Cond.PET.90.170.25	0,020	0,0200	0,174	0,0018	18,55	24,97	77,94	66,76
Hexane.Cond.PET.90.170.25	0,020	0,0200	0,174	0,0018	20,54	26,81	78,1	59,83
Hexane.Cond.PET.90.170.30	0,024	0,0243	0,174	0,0018	14,83	20,46	77,9	54,58
Hexane.Cond.PET.90.170.30	0,024	0,0243	0,174	0,0018	15,24	20,99	77,99	54,77
Hexane.Cond.PET.90.170.30	0,024	0,0242	0,174	0,0018	19,54	25,6	77,9	64,32
Hexane.Cond.PET.90.170.30	0,024	0,0242	0,174	0,0018	19,19	25,09	78,15	52,55
Hexane.Cond.PET.90.170.35	0,029	0,0285	0,174	0,0018	15,01	20,28	77,97	51,89
Hexane.Cond.PET.90.170.35	0,029	0,0285	0,174	0,0018	20,23	25,5	77,91	58,57
Hexane.Cond.PET.90.170.35	0,029	0,0285	0,174	0,0018	18,57	23,56	78,23	50,25
Hexane.Cond.PET.90.170.40	0,033	0,0329	0,174	0,0018	15,4	19,24	78,01	49,00
Hexane.Cond.PET.90.170.40	0,033	0,0329	0,174	0,0018	15,08	19,02	78	47,37
Hexane.Cond.PET.90.170.40	0,033	0,0328	0,174	0,0018	21,4	25,83	77,94	53,73
Hexane.Cond.PET.90.170.40	0,033	0,0328	0,174	0,0018	18,11	22,03	78,21	45,97

Hexane.Cond.PET.90.170.45	0,037	0,0372	0,174	0,0018	16,91	20,58	77,77	47,17
Hexane.Cond.PET.90.170.45	0,037	0,0372	0,174	0,0018	14,86	18,28	78,04	43,60
Hexane.Cond.PET.90.170.45	0,037	0,0372	0,174	0,0018	22	25,68	77,89	51,97
Hexane.Cond.PET.90.170.45	0,037	0,0372	0,174	0,0018	17,09	20,6	78,31	42,45
Hexane.Cond.PET.90.230.20	0,016	0,0158	0,23	0,0024	14,11	20,56	69,31	68,19
Hexane.Cond.PET.90.230.25	0,020	0,0200	0,23	0,0024	13,95	20,19	69,31	68,27
Hexane.Cond.PET.90.230.30	0,024	0,0243	0,23	0,0024	13,74	19,95	69,37	67,74
Hexane.Cond.PET.90.230.35	0,029	0,0285	0,23	0,0024	13,66	19,31	69,35	67,50
Hexane.Cond.PET.90.230.40	0,033	0,0329	0,23	0,0024	13,55	17,87	69,29	67,85
Hexane.Cond.PET.90.230.45	0,037	0,0372	0,23	0,0024	13,38	17,31	69,32	66,56
Hexane.Cond.PET.90.320.40	0,033	0,0328	0,328	0,0034	25,39	29,52	69,29	68,68
Hexane.Cond.PET.90.320.45	0,037	0,0371	0,328	0,0034	25,39	28,99	69,36	68,70

SUPERVISED THESES

- E. Mwiseneza (2015) "Numerische Untersuchung des Wärmeübergangs in einem Polymerfilm-Wärmeübertrager", Diplomarbeit
- D. Momoyie (2015) „Untersuchung von Polymerfolien mittels Raman-Spektroskopie“, Forschungsarbeit
- W. Meyer (2014) "Numerische Untersuchung der Strömung in einem polymeren Wärmeübertrager", Diplomarbeit
- D. Döring (2014), "Ermittlung von Wärmedurchgangskoeffizienten eines kompakten Polymerwärmeübertragers", Projektarbeit
- J. P. Klein / A. Hoffmann (2014), "Simulation der Kondensation in einem Polymerfilm-Wärmeübertrager mit Ansys® CFX und Fluent®", Forschungsprojekt
- A. Keller (2014) "Experimentelle Untersuchung des Wärmeübergangs in einem Polymerfolien-Wärmeübertrager", Studienarbeit
- L. Hartmann (2014) "Simulation der Strömung und des Wärmeübergangs in einem Wärmeübertrager mit Ansys CFX", Projektarbeit
- D. Burkey (2014) "Simulation der Strömung und des Wärmeübergangs in einem Wärmeübertrager mit Hyperworks", Studienarbeit
- J. Bartmann (2013) "Langzeitverhalten von Kunststoffen bei Kontakt mit organischen Lösungsmitteln", Studienprojekt
- C. Berger (2013) "Entwicklung und Aufbau eines Kleinwärmeübertragers aus Kunststoff", Bachelorarbeit
- J. Schäfer (2013) "CFD-Simulation der Strömung in einem Wärmeübertrager mit OpenFOAM", Studienprojekt
- D. Schwarz (2013) "Untersuchung der mech. Eigenschaften von Polymeren bei Kontakt mit organischen Lösungsmitteln", Studienprojekt
- M. D. Lujan Rico (2013) "Investigation of the influence of hot water on mechanical properties of polymers", Final degree project.
- M. Ogurcan (2013) "CFD-Simulation der Strömung in einem Wärmeübertrager mit Ansys Fluent", Bachelorarbeit
- V. Pahl (2012) "FEM-Berechnung der Stützstruktur eines Polymerwärmeübertragers", Studienarbeit

CURRICULUM VITAE

Family name: Laaber

Surname: Dmitrij

Scientific experience

Since 2015 **Project engineer**, synlight group, Institute for Solar Research, German Aerospace Center, Jülich

2011 – 2014 **Research assistant**, Chair of Separation Science and Technology, University of Kaiserslautern

Education

2002 – 2009 **Diploma degree in Mechanical Engineering** (equivalent to M.Sc.), Technical University of Hamburg-Harburg